Advances in donor-based spin qubits in silicon: spin relaxation and flip-flop qubits

Author:
Tenberg, Stefanie

Publication Date:
2019

DOI:
https://doi.org/10.26190/unsworks/21129

UNIVERSITY OF NEW SOUTH WALES

DOCTORAL THESIS

Advances in donor-based spin qubits in silicon: spin relaxation and flip-flop qubits

Author:
Stefanie TENBERG

Supervisor:
Prof. Andrea MORELLO
Co-Supervisor:
Dr. Vivien SCHMITT

A thesis submitted in fulfilment of the requirements for the degree of

Doctor of Philosophy

in the

School of Electrical Engineering and Telecommunications
Faculty of Engineering

March 15, 2019

Thesis/Dissertation Sheet

Surname/Family Name	:	**Tenberg**
Given Name/s	:	**Stefanie Birgit**
Abbreviation for degree as give in the University calendar	:	**PhD**
Faculty	:	**Engineering**
School	:	**Electrical Engineering and Telecommunications**
Thesis Title	:	**Advances in donor-based spin qubits in silicon: spin relaxation and flip-flop qubits**

Abstract 350 words maximum: (PLEASE TYPE)

Donor spins in silicon allow for extremely long storage of quantum information and provide accurate single spin control. While these properties make them attractive for quantum computation, to build a large-scale quantum computer some major challenges still need to be addressed.

One key issue is coupling two donor quantum bits (qubits) with high fidelity, in a scalable manner, without requiring extremely accurate donor placement. In this thesis, we propose a new type of qubit, the flip-flop qubit, a combination of the electron-nuclear spin states of the phosphorus donor, that can be controlled by microwave electric fields. A dipole is created when separating the donor electron from the nucleus, allowing two-qubit gates mediated by electric dipole-dipole interaction at donor distances of several hundred nanometres. Gate fidelities are predicted to be within fault-tolerance thresholds for quantum error correction codes, using realistic charge noise values. Strong coupling of the qubit to superconducting resonators can also be achieved. This idea can be extended to couple nuclear spins to electric fields by adding a magnetic drive, applied simultaneously with the electric drive in a Raman-like configuration. Both qubits can be incorporated in a large scale quantum processor.

Two types of flip-flop qubit prototypes, one suited for direct dipole-dipole coupling and one for coupling to a resonator, have been designed, fabricated and measured. Fundamental functionalities have been established and the coupling of a charge qubit to a resonator has been observed.

When building a large scale quantum computer, precise knowledge of the fundamental physics of the donor system is of key importance. To this end, we analyse the electron spin relaxation. We find that the spin relaxation is caused by phonon emission at high magnetic fields (>3 T), but becomes dominated by evanescent-wave Johnson noise at lower fields. We also find evidence of spurious spin relaxation caused by electron tunnelling to a charge reservoir, preventable by appropriate tuning of the donor electrochemical potential.

Overall, the achievements made in this thesis bring us a step closer to achieving a scalable spin-based quantum computer in silicon.

FOR OFFICE USE ONLY Date of completion of requirements for Award:

ORIGINALITY STATEMENT

‘I hereby declare that this submission is my own work and to the best of my knowledge it contains no materials previously published or written by another person, or substantial proportions of material which have been accepted for the award of any other degree or diploma at UNSW or any other educational institution, except where due acknowledgement is made in the thesis. Any contribution made to the research by others, with whom I have worked at UNSW or elsewhere, is explicitly acknowledged in the thesis. I also declare that the intellectual content of this thesis is the product of my own work, except to the extent that assistance from others in the project's design and conception or in style, presentation and linguistic expression is acknowledged.’

Signed …….....

Date …….....

INCLUSION OF PUBLICATIONS STATEMENT

UNSW is supportive of candidates publishing their research results during their candidature as detailed in the UNSW Thesis Examination Procedure.

Publications can be used in their thesis in lieu of a Chapter if:

- The student contributed greater than 50% of the content in the publication and is the "primary author", ie. the student was responsible primarily for the planning, execution and preparation of the work for publication
- The student has approval to include the publication in their thesis in lieu of a Chapter from their supervisor and Postgraduate Coordinator.
- The publication is not subject to any obligations or contractual agreements with a third party that would constrain its inclusion in the thesis

Please indicate whether this thesis contains published material or not.

☐ *This thesis contains no publications, either published or submitted for publication (if this box is checked, you may delete all the material on page 2)*

☒ *Some of the work described in this thesis has been published and it has been documented in the relevant Chapters with acknowledgement (if this box is checked, you may delete all the material on page 2)*

☐ *This thesis has publications (either published or submitted for publication) incorporated into it in lieu of a chapter and the details are presented below*

CANDIDATE'S DECLARATION

I declare that:

- I have complied with the Thesis Examination Procedure
- where I have used a publication in lieu of a Chapter, the listed publication(s) below meet(s) the requirements to be included in the thesis.

Name	Signature	Date (dd/mm/yy)
Stefanie Tenberg		**15/03/19**

Postgraduate Coordinator's Declaration (to be filled in where publications are used in lieu of Chapters)

I declare that:

- the information below is accurate
- where listed publication(s) have been used in lieu of Chapter(s), their use complies with the Thesis Examination Procedure
- the minimum requirements for the format of the thesis have been met.

PGC's Name	PGC's Signature	Date (dd/mm/yy)

COPYRIGHT STATEMENT

Signed …….....

Date …….....

AUTHENTICITY STATEMENT

‘I certify that the Library deposit digital copy is a direct equivalent of the final officially approved version of my thesis. No emendation of content has occurred and if there are any minor variations in formatting, they are the result of the conversion to digital format.’

Signed …….....

Date …….....

"Poetry is not only dream and vision; it is the skeleton architecture of our lives. It lays the foundations for a future of change, a bridge across our fears of what has never been before."

Audre Lorde

UNIVERSITY OF NEW SOUTH WALES

Abstract

Faculty of Engineering
School of Electrical Engineering and Telecommunications

Doctor of Philosophy

Advances in donor-based spin qubits in silicon: spin relaxation and flip-flop qubits

by Stefanie TENBERG

Donor spins in silicon allow for extremely long storage of quantum information and provide accurate single spin control. While these properties make them attractive for quantum computation, to build a large-scale quantum computer some major challenges still need to be addressed.

One key issue is coupling two donor quantum bits (qubits) with high fidelity, in a scalable manner, without requiring extremely accurate donor placement. In this thesis, we propose a new type of qubit, the flip-flop qubit, a combination of the electron-nuclear spin states of the phosphorus donor, that can be controlled by microwave electric fields. A dipole is created when separating the donor electron from the nucleus, allowing two-qubit gates mediated by electric dipole-dipole interaction at donor distances of several hundred nanometres. Gate fidelities are predicted to be within fault-tolerance thresholds for quantum error correction codes, using realistic charge noise values. Strong coupling of the qubit to superconducting resonators can also be achieved. This idea can be extended to couple nuclear spins to electric fields by adding a magnetic drive, applied simultaneously with the electric drive in a Raman-like configuration. Both qubits can be incorporated in a large scale quantum processor.

Two types of flip-flop qubit prototypes, one suited for direct dipole-dipole coupling and one for coupling to a resonator, have been designed, fabricated and measured. Fundamental functionalities have been established and the coupling of a charge qubit to a resonator has been observed.

When building a large scale quantum computer, precise knowledge of the fundamental physics of the donor system is of key importance. To this end, we analyse the electron spin relaxation. We find that the spin relaxation is caused by phonon emission at high magnetic fields ($> 3\,\mathrm{T}$), but becomes dominated by evanescent-wave Johnson noise at lower fields. We also find evidence of spurious spin relaxation caused by electron tunnelling to a charge reservoir, preventable by appropriate tuning of the donor electrochemical potential.

Overall, the achievements made in this thesis bring us a step closer to achieving a scalable spin-based quantum computer in silicon.

This thesis was accepted upon reviews from A.Prof. Michel Pioro-Ladrière from Université de Sherbrooke and Dr. María José Calderón from the Instituto de Ciencia de Materiales de Madrid.

Acknowledgements

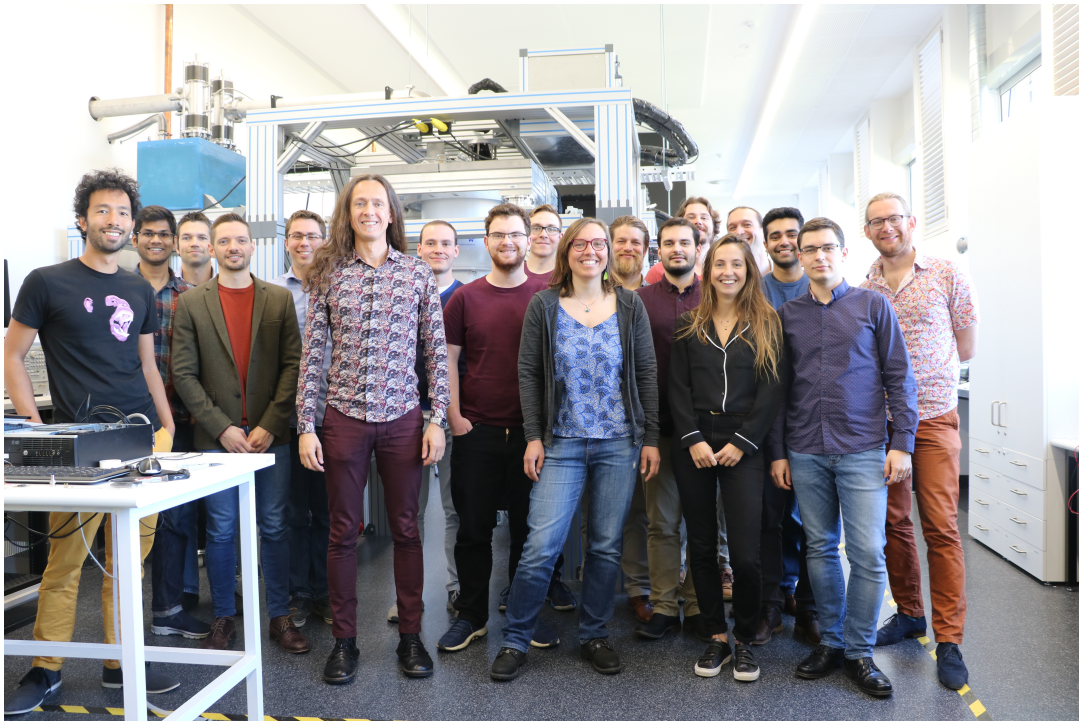

FIGURE 1: Fundamental Quantum Technologies Group - 2018

The last four years of my Ph.D. have been transforming, enlightening, a trial, exhausting, fantastic, liberating and so much more, but mostly they were a journey towards personal and academic growth. I would have not made it to where I stand today without those who have supported me. You were there for the ups and downs, for the successes and the failures and I am eternally grateful.

To my supervisor. Andrea, not only do you know your physics well, but you also know how to present your knowledge and ideas. You make it easy to believe in new pathways and venture into the unknown. Thanks for passing on so much of your knowledge and always caring about the people in your research group. I always felt at home here and well supported, even when things were not going as planned. I learned so much and never regretted coming to Sydney - I would do it again in heartbeat.

To all my group members. You were the most amazing friends one could wish for during a Ph.D. When help was needed, it was never hard to find someone. When it was time to celebrate, fun exploits were easily had. To Guilherme, who started the project from scratch. During the many hours we spent discussing flip-flop theory and the many days we were in the clean room, both learning how to fabricate devices, I always felt like you were giving your best to be a good supervisor and friend. To Vivien. When Gui left, you took over my supervision without a stride, always telling me what was (but mostly wasn't) important. You taught me a lot about fabrication and electronics. To Serwan. Thanks for all the debugging of SilQ, the many nice lunch breaks and all the fun times on conferences. I always felt like I could discuss any issue with you - it kept me sane when I needed it most! To Mateusz. I really appreciate all the clean room discussions and the office banter. To Arne. I could always count on your advice whether it was physics-related or not. To Tim. Thanks for actually joining me here from Aachen. Working together with

you again was a blast. To Vincent. Without you the group would not have been the same!

Thank you also to Andrew, Fay, Kok Wai and the rest of the Dzurak group for the support regarding fabrication and measurement equipment. Special thanks for Dave, Rodrigo, Otte, Gordon, Joanna and Andrew S. who kept the labs running.

To all my outdoors and dive friends. UNWSOC and UNSW UWC have had a major impact on my life. Through you I learned new skills and found new hobbies. My life has changed a lot since the day I joined and my adventures provided the balance I needed to keep going when Ph.D life was hard. I now have so many dreams of adventures all over the world and am planning to fulfil some of them as soon as I submit this document. Sam, Damon and Laura, we had so many great adventures, you were my mentors. Angela, Che, Jason, you always made my time in the mountains legendary. Maria and Kieran, learning with you was the best. Chris, thanks for all the great dive adventures and for trusting me to drive the boat.

To Hendrik, my Master thesis supervisor. You were the one who set me on this path. Without your suggestion I would never have come to Sydney. For that, I am grateful!

Finally, to my parents and my grandparents. I love you. My full confidence, that you will always support me no matter what, has enabled me to venture out of my comfort zone and achieve what I have so far. I owe you everything.

Publications

Peer reviewed journal articles

G. Tosi, F. A. Mohiyaddin, V. Schmitt, **S. Tenberg**, R. Rahman, G. Klimeck, A. Morello.
"Silicon quantum processor with robust long-distance qubit couplings", *Nature communications* Vol. 8, 450 (2017).

G. Tosi, F. A. Mohiyaddin, **S. Tenberg**, A. Laucht, A. Morello.
"Robust electric dipole transition at microwave frequencies for nuclear spin qubits in silicon", *Physical Review B* Vol. 98, 075313 (2018).

Conference article

A. Morello, G. Tosi, F. A. Mohiyaddin, V. Schmitt, V. Mourik, T. Botzem, A. Laucht, J. J. Pla, **S. Tenberg**, R. Savytskyy, M. Madzik, F. Hudson, A. S. Dzurak, K. Itoh, A. M. Jakob, B. C. Johnson, J. C. McCallum, D. Jamieson
"Scalable Quantum Computing with Ion-Implanted Dopant Atoms in Silicon", *IEEE International Electron Devices Meeting (IEDM) 2018*

Articles in submission

S. Tenberg, S. Asaad, M. Madzik, M.A.I. Johnson, B. Jöcker, A. Laucht, F.E. Hudson, D.N. Jamieson, J.C. McCallum, A.S. Dzurak, R. Joynt, A. Morello.
"Electron spin relaxation of single phosphorus donors in metal-oxide-semiconductor nanoscale devices." arXiv:1812.06644 (2018).

Conference Presentations

S. Tenberg, G. Tosi, F. A. Mohiyaddin, V. Schmitt, R. Rahman, G. Klimeck, A. Morello.
"A donor based silicon quantum processor with robust long-distance qubit couplings."
Presented at:
- IEEE Technologies of Future 2015. Sydney, Australia (Poster)
- Silicon Quantum Electronics Workshop 2015. Takamatsu, Japan (Poster)
- Silicon Quantum Electronics Workshop 2016. Delft, Netherlands (Oral)
- Conference on Optoelectronic and Microelectronic Materials and Devices 2017, Sydney, Australia (Oral)
- Centre for Quantum Computation and Communication Workshop 2017. Sunshine Coast, Australia (Oral)
- Silicon Quantum Electronics Workshop. Portland, USA, August 2017 (Poster)
- Army Research Office Quantum Computing Program Review 2017. San Diego, USA (Poster)

S. Tenberg, S. Asaad, M. Johnson, A. Laucht, F. Hudson, D. Jamieson, J. McCallum, A. Dzurak, A. Morello.
"Low magnetic field anomalies of donor electron spin relaxation in silicon at low temperatures".

Presented at:
- American Physical Society March Meeting 2017. New Orleans, USA (Oral)
- Army Research Office Quantum Computing Program Review 2017. San Diego, USA (Poster)
- Silicon Quantum Electronics Workshop 2017. Portland, USA (Poster)
- UNSW Engineering Postgraduate Research Symposium 2017. Sydney, Australia (Oral)

S. Tenberg
"Harness the quantum to revolutionise computing."
Presented at:
- UNSW Three Minute Thesis Competition Engineering 2016. Sydney, Australia (Oral, Winner Public Choice Award)
- UNSW Three Minute Thesis Competition Interfaculty Finals 2016. Sydney, Australia (Oral)

Contents

List of Figures

List of Abbreviations

2D	2-dimensional
2DEG	2-dimensional electron gas
AC	Alternating current
Al	Aluminium
Al_2O_3	Aluminium oxide
ALD	Atomic layer deposition
AWG	Arbitrary waveform generator
CNOT	Controlled-NOT
CPWR	Coplanar waveguide resonator
CT	Clock transition
CQCT	Charge qubit clock transition
cQED	circuit quantum electrodynamics
DC	Direct current
DOS	Density of states
EBL	Electron beam lithography
EBPVD	Electron beam physical vapour deposition
ESD	Electrostatic discharge
EDSR	Electron dipole spin resonance
ESR	Electron spin resonance
EWJN	Ewanescent wave Johnson noise
ff	Flip-flop
FGA	Forming gas anneal
IPA	Isopropyl alcohol
Ge	Germanium
MIBK	Methyl isobutyl ketone
MMCX	Micro-miniature coaxial
MOS	Metal-oxide-semiconductor
MW	Microwave
Nb	Niobium
NEMO	Nanoelectronic Modelling
NMP	N-methyl-2-pyrollidone
NMR	Nuclear magnetic resonance
P	Phosphorus
PCB	Printed circuit board
PMMA	Polymethyl methacrylate)
rms	Root mean square
RF	Radio frequency
RTA	Rapid thermal anneal
SEM	Scanning electron microscope
SET	Single electron transistor
Si	Silicon
SIM	Small instrumentation module
SiO_2	Silicon dioxide

SMA	Sub-Miniature version A
so	Spin-orbit
STM	Scanning tunnelling microscope
TCAD	Technology computer aided design
VNA	Vector network analyser
VTI	Variable-temperature insert

To my grandparents
Irmgard, Heinz, Agnes and Ludger.
A little piece of forever.

Chapter 1

Introduction: A different form of computation

"Nature isn't classical, [...], and if you want to make a simulation of nature, you'd better make it quantum mechanical, and [...] it's a wonderful problem, because it doesn't look so easy."

– Richard Feynman, 1982

1.1 The quantum revolution of computation

Ever since the invention of the abacus around $2700 - 2300$ BC in Babylon [1] computation has been a fundamental pillar of human societies. Over centuries calculus and mathematics have evolved and become more and more relevant in all aspects of our lives. When in the second half of the 20th century the digital computer was invented, data processing and storage capabilities grew exponentially [2]. In the last decades digital computing has revolutionized many aspects of modern life, ranging from logistics to medicine, banking and many more. Not only is the computing power developing though, but computing is constantly reinventing itself. New technologies emerge, enveloping their predecessors. A powerful example is the invention of the internet in the late 1980s [3] which enabled networking, collaboration and open-source culture. Nowadays computing is deeply embedded in everyday life. We, as a society and as individuals, rely on the ever increasing and evolving technology. However, we have been approaching a critical turning point in computation history in recent years. Not only has the processing power growth started to saturate since device feature size reached atomistic distances, but also is the complexity of modern society's challenges increasing to a point where many of these challenges are fundamentally unsolvable with classical computation. One of these challenges is the understanding of advanced molecules and quantum systems to engineer chemical processes and nanotechnology. We find ourself at the "frontier of complexity" [4], when the next evolution of computation is necessary - the quantum revolution.

Quantum systems are inherently complex once many particles are involved. For instance in quantum chemistry, to find the stable electron configuration of a molecule, the ground state, one needs to perform configuration interaction (CI) calculations. Many-particle molecular wave functions are represented by single-particle atomic orbitals, where the number of orbitals is proportional to the number of electrons (corresponding to the number of atoms) in a molecule [5]. Depending on the desired accuracy, a basis set is chosen and then the CI matrix is computed. The calculation time and resources scale exponentially with the molecule size on a classical computer. For instance, even today's largest supercomputers cannot accurately simulate the molecule cholesterol $C_{27}H_{46}O$, an essential component for all animal and human life. To describe the interactions of the 84 electrons, we chose a correlation consistent basis, which gives around 1500 spatial basis functions which in turn yields 10^{162} configurations - more than atoms in the universe [5], [6]. We find that the complexity of this quantum system prevents any precise predictions. However, if we cannot conquer this complexity with current means, why not harness it instead?

Already in 1982, physicist Richard Feynman suggested to harness the inherent complexity of quantum systems to simulate other quantum systems when he said *"Nature isn't classical, [...], and if you want to make a simulation of nature, you'd better make it quantum mechanical, and [...] it's a wonderful problem, because it doesn't look so easy."* [7] The complexity of quantum systems and the power of information encoded in quantum particles arises from two inherent quantum mechanical properties of all quantum particles: superposition and entanglement [8]. The former allows the quantum particle to be in exclusive states at the same time. The latter describes the correlation between different states - fully entangled states cannot be described independently, they are not separable.

A quantum computer consists of many such quantum particles that have only two available states (quantum bits or qubits), equivalent to the classical bits 0 and 1. On such a computer, the exponential scaling of resources needed to simulate quantum systems on classical computers turns into a more favourable polynomial

overhead [6], [9]. For instance, for cholesterol only around 1000 qubits are required to store the molecules wave function and calculate its ground state. Efficient quantum simulation of a molecule's ground-state energies with a variational quantum eigensolver has already been demonstrated for smaller molecules such as H_2 and LiH [10]. Many more quantum algorithms for condensed matter physics, chemistry, math and computer science have been developed and promise quantum speed-up [11], [12].

The foundation of such a quantum computer is a single qubit: a well-defined two-level system, that can interact strongly with another qubit but does not interact with the environment, except when being measured. These requirements stand in conflict with each other and already give us an indication that building a quantum computer is indeed a challenging task, just as Feynman suggested.

As the stakes in this "quantum race" are high, in the last years not only researchers but also companies like IBM, Intel, Microsoft and Google have started to participate. Billions of dollars have been invested for the potential to push past the frontier of complexity and many different paths are being explored.

There exist a myriad of physical systems that promise good qubits, ranging from microscopic systems such as trapped atoms, photons and spins in semiconductors to macroscopic systems such as superconducting qubits [13]. As it stands, trapped ions and superconducting qubits are leading in the number of connected qubits, reaching 53 and 72 respectively [14], [15] (as of December 2018). However, these system do not represent universal quantum computers yet. The former lacks universality as only specific problems like the Ising model can be simulated, while the latter has yet to proof full control of its qubits. If these platforms will establish themselves in the long run is still in question as trapped ions are challenging to scale up to large qubit networks and superconducting qubits struggle with relatively short coherence times [13], [16].

Another promising and growing sector are semiconductor spin qubits, specifically silicon based ones. Firstly, they can draw from the experience and technology of the billion dollar semiconductor industry, and secondly, they have a good potential for large scale quantum computing as they are small and adjustable with long coherence times [17]. D. DiVincenzo and D. Loss first proposed a single spin qubit in 1998 [18]. Shortly thereafter, the first GaAs spin qubit was build [19] and has seen huge development since [20], [21]. However, the inevitable presence of nuclear spins in GaAs makes the qubits challenging to work with. In silicon, this noise source is strongly reduced and superior industry nano-fabrication techniques are available. Consequently, already in 1998 Kane envisioned a silicon based quantum computer [22]. Nevertheless, it took until 2007 for the first single electron occupation silicon quantum dot to be realised [23]. Since then donor based qubits [24], quantum dot qubits [25], [26], SiGe qubits [27] and CMOS qubits [28] have been devised, reaching high levels of accuracy and control [17]. The current state of the art is a programmable two-qubit quantum processor in Si/SiGe quantum dots [29].

UNSW has pioneered this era of silicon qubits. Since Kane made his silicon quantum processor proposal here at UNSW [22], our researches have worked to achieve this goal. A. Morello and his research group have pursued the path to silicon quantum computing by using implanted phosphorus donors in silicon. Both the electron and the nucleus spin perform well as qubits with exceptional coherence times of over 30 s and single qubit gate fidelities of 99.99 % for the nucleus [30]. Nevertheless, integrating donor qubits into a scalable quantum computer architecture remains a formidable challenge and many effects in the quantum system remain little understood.

1.2 Scope of this thesis

In this thesis, I continue on the path towards a donor based silicon quantum processor by proposing a new way to not only couple donor spin qubits over distances of several hundred nanometres but also entangle them with photons in a superconducting resonator. To this end, the quantum information is encoded in a novel electrically accessible qubit, the flip-flop qubit, which is formed by both the electron and the nuclear spin together. The flip-flop qubit relies on the formation of a charge qubit by separating the electron from the donor nucleus. The resulting large electric dipole enables electric driving and two-qubit coupling. I have devised, built and measured devices, which support the flip-flop qubit for both coupling two qubits via dipole-dipole interaction and coupling a qubit to a superconducting resonator. For the first time, I show the coupling of the donor charge qubit to a single photon.

Another important factor in advancing donor qubits is the full understanding of the qubit system. To this end, I have measured the electron spin relaxation of a donor in silicon extensively. This work has expanded the general understanding of the relaxation processes involved and compliments other studies of relaxation times in silicon [24], [31]–[33].

To fully understand all concepts in this thesis, **Chap. 2** gives an overview of the fundamental knowledge on which this thesis is based. Starting with the basics of qubits, it then moves to properties of donors in silicon, such as orbital structure, valleys and effective mass. This is followed by an explanation how quantum information can be encoded in both the donor electron and nuclear spin and how those qubits are controlled and measured. Qubit decoherence is also discussed briefly. Then the fundamentals of circuit quantum electrodynamics (cQED) are laid out. The representation of a quantized electromagnetic field by an harmonic oscillator is derived. This oscillator can be created by a superconducting resonator circuit. It is explained how the resonator couples to the transmission lines and its fields are measured through the scattering matrix. Finally the coupling of a qubit to such a resonator, described by the Jaynes-Cummings Hamiltonian, is elaborated.

Chap. 3 introduces the flip-flop qubit, where the quantum information is encoded in the joined electron-nuclear states $\{|\downarrow\Uparrow\rangle, |\uparrow\Downarrow\rangle\}$. It can be controlled by microwave electric fields with error rates of 10^{-3} and coupled to photons of a superconducting resonator with a coupling rate of 3 MHz. Furthermore, its second-order electric dipole-dipole interaction allows for long range two-qubit coupling with a SWAP frequency of 2 MHz and an error rate below 10^{-2}. The qubit exhibits clock transitions, regions where the qubit is protected from charge noise and the dephasing can be as slow as $1/T_2^* \approx 3 \times 10^3\,\mathrm{s}^{-1}$. These properties show the flip-flop qubit to be compatible with quantum error correction and open up the pathway for a scalable donor qubit quantum processor.

Chap. 4 expands the concepts of the flip-flop qubit and shows that a strong electric dipole (> 100 D) for the nuclear spin can be created by applying a magnetic drive in addition to the electric flip-flop control. This dipole can then be employed to couple the nuclear spin to a superconducting resonator at a megahertz rate. Two-qubit nuclear spins transitions can be driven at a frequency of 1 MHz while 400 nm apart. The nuclear spin remains resilient against charge noise when at a clock-transition, where the dephasing rate is below $10 \times 10^3\,\mathrm{s}^{-1}$. The nuclear spin, equipped with the artificial electric dipole, can then be incorporated into large hybrid quantum architectures.

Chap. 5 gives a brief introduction to quantum error correction and explores ideas how both the flip-flop and the nuclear qubit can be incorporated in large quantum

computing architectures, capable of quantum error correction. Moreover, a small qubit array design for short term proof-of principle measurements is discussed.

Chap. 6 presents the device design, fabrication, the experimental setup and measurement apparatus. First, the design for the flip-flop qubit aimed at direct two-qubit dipole-dipole coupling is laid out. This is followed by the discussion of the superconducting resonator, designed to incorporate the flip-flop qubit. Next, fabrication procedures are detailed. Finally the experimental setups for each type of experiment, ranging from electron qubit to flip-flop measurements and cQED analysis, are shown, including cabling, filtering and measurement apparatus.

Chap. 7 provides measurements to determine the functionalities of the flip-flop qubit devices and observations of both the flip-flop resonance and coupling of the charge qubit to a resonator. Moreover, the designed resonators are characterized. Difficulties, preventing proper operation of the flip-flop qubit and coherent control, are discussed.

Chap. 8 contains a detailed analysis of the electron spin relaxation in donors. After a review of the theory of relaxation in donors, the relaxation rate as a function of magnetic field for multiple devices is presented. The measurement shows that at low magnetic fields evanescent wave Johnson noise (EWJN) is responsible for an increase of the electron spin relaxation. At high magnetic fields, phonon-induced relaxation is dominant, but is modulated by different strain in the various samples. Additionally, direct tunnelling is found to increase relaxation when the donor electrochemical potential is close to SET electrochemical potential.

Finally, **Chap. 9** presents an overview of the achievements reported in this thesis and their limitations. The outlook for donor quantum computation is discussed. The thesis concludes with a brief personal viewpoint.

Chapter 2

Fundamentals: Donor qubits in silicon and circuit QED

"The world used to be a much simpler place. A hundred years or so ago, we lived in a very normal, classical universe where everything made sense, and nothing behaved strangely. Then along came quantum theory."
– Michael Brooks

In this chapter, the concepts of quantum computation with a focus on donor qubits in silicon are presented as well as the fundamentals of circuit quantum electrodynamics.

2.1 The quantum bit

A qubit is a well-defined quantum two-level system. The quantum system is defined by its Hamiltonian, a Hermitian operator which corresponds to the total energy of the system. The two levels are described by the eigenstates of this system, ground state $|0\rangle$ and excited state $|1\rangle$, analogous to a classical bit with states 0 and 1. The qubit can be in any superposition state

$$|\psi\rangle = \alpha\,|0\rangle + \beta\,|1\rangle = \begin{pmatrix}\alpha\\ \beta\end{pmatrix} \tag{2.1}$$

with $\alpha, \beta \in \mathbb{C}$ and $|\alpha^2| + |\beta^2| = 1$. Whenever a quantum state is measured directly, the part of the wave function associated with that state collapses into an eigenstate, in this case either $|0\rangle$ or $|1\rangle$ if measured along the quantization axis. The probability to collapse into these states is respectively $|\alpha|^2$ and $|\beta|^2$. Thus, to readout a quantum state, it is measured repeatedly to determine the state probability.

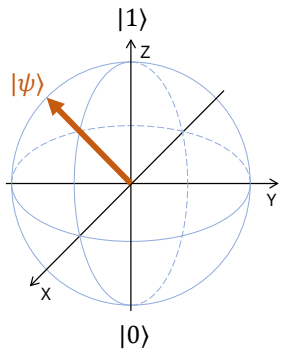

FIGURE 2.1: **Bloch sphere.** The qubit state $|\psi\rangle$ is represented by a vector inside a sphere with radius unity.

A qubit state can be represented geometrically as a vector in a three-dimensional sphere, where the mutually orthogonal eigenstates $|0\rangle, |1\rangle$ are typically positioned on the north and south pole respectively. All points on the surface of the sphere symbolize pure superpositions of the eigenstates while interior points signify mixed states, statistical ensembles of different qubit states. This visual construct is called Bloch sphere (Fig. 2.1). The basis of this vector space are the Pauli matrices

$$\sigma_x = \begin{pmatrix}0 & 1\\ 1 & 0\end{pmatrix},\ \sigma_y = \begin{pmatrix}0 & -i\\ i & 0\end{pmatrix},\ \sigma_z = \begin{pmatrix}1 & 0\\ 0 & -1\end{pmatrix}. \tag{2.2}$$

We can express the qubit Hamiltonian in its general form as

$$\mathcal{H} = \frac{\epsilon}{2}\sigma_z + \frac{\Delta}{2}\sigma_x, \tag{2.3}$$

where $\frac{\epsilon}{2}\sigma_z$ describes the unperturbed qubit system with eigenenergies $\pm\frac{\epsilon}{2}$ while $\frac{\Delta}{2}\sigma_x$ is the coupling term between the two eigenstates. The energy splitting between ground and excited state of the coupled Hamiltonian is then

$$E_Q = \sqrt{\epsilon^2 + \Delta^2}. \tag{2.4}$$

When $\mathcal{H}$ is time-independent, the time-evolution of the qubit state is given by the Schrödinger equation

$$\mathcal{H}\,|\psi(t)\rangle = i\hbar\frac{\partial}{\partial t}\,|\psi(t)\rangle \tag{2.5}$$

to

$$|\psi(t)\rangle = \boldsymbol{U}\,|\psi(t_0)\rangle = \exp\left(\frac{-i\mathcal{H}t}{\hbar}\right),|\psi(t_0)\rangle \tag{2.6}$$

where $\boldsymbol{U}$ is the time-evolution operator.

Qubit implementation Quantum two-level systems exist in many different physical systems. However, to viably implement a qubit a number of criteria need to be fulfilled at a minimum, the DiVincenzo criteria [34]. The qubit itself must be well-defined and therefore describable by a Hamiltonian. Moreover, it must possess a well-defined known initial state in which it can be prepared with high precision. Furthermore, the qubit's state needs to be measurable, such that we can determine its value precisely at any time. Additionally, a universal set of quantum gates has to exist for one and two qubits to execute quantum algorithms. Nonetheless, the qubit needs to be isolated from its environment to prevent fluctuations on the outside to change the quantum state, leading to a loss of quantum information. The rate of information loss needs to be much smaller than the longest gate operation time. Lastly the qubits have to form a scalable architecture where many qubits can interact with each other, long distance transport of qubit states is possible and errors can be corrected.

Note that while qubits are the most common way to attempt building a quantum computer, quantum d-state systems or continuous quantum variables are viable alternatives [13].

2.2 Phosphorus dopants in silicon

In the last decade, silicon has become popular for qubits and quantum computation as spins in silicon are well decoupled from their environment, leading to long coherence times. Moreover, it is an attractive material as technologies and knowledge from the large semiconductor industry can be harnessed.

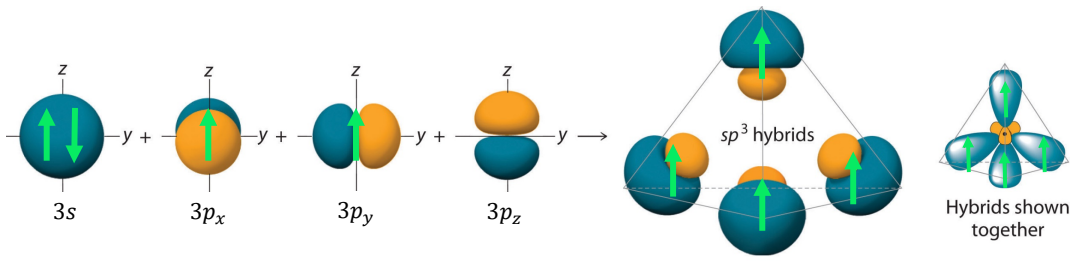

FIGURE 2.2: **Silicon orbital structure**. Combining one s-type and three p-type atomic orbitals results in four sp^3 hybrid orbitals which are oriented at 109.5° to one another in a tetrahedral structure. The arrows represent the electron spin state. The figure is adapted from Ref. [35].

Silicon is a group-IV semiconductor with 14 protons and consequently 14 electrons in its atomic shell. In an isolated atom, the electrons fill the orbitals successively, complying with Hund's rule. Hund's rule states that the ground state of the

atom has the biggest total spin that complies with the Pauli principle. With its 14 electrons, silicon has an electron configuration of $1s^2 2s^2 2p^6 3s^2 3p^2$. In a crystal, the 4 valence electrons with the orbitals $3s^2 3p^2$ of neighbouring atoms hybridize with one electron each and sp^3 hybrid orbitals are formed instead, resulting in a tetrahedral structure (Fig. 2.2).

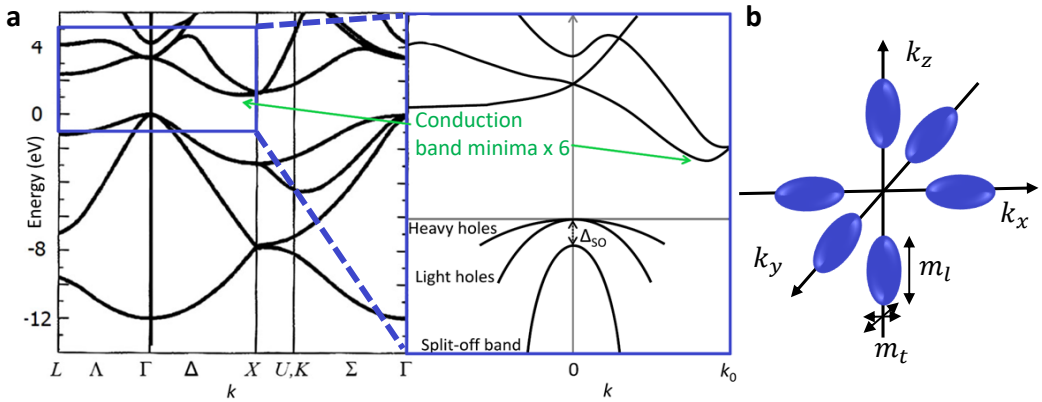

FIGURE 2.3: **Silicon band structure and valley properties.** **a** Band structure of bulk silicon. The conduction band minimum is at finite crystal momentum $k = 0.85\,k_0$ and six-fold degenerate. **b** 6 constant energy surfaces at the conduction band minimum in k-space represent the 6 valleys. The anisotropic energy dispersion results in the longitudinal m_l and transverse m_t effective masses. Fig. **a** is taken from Ref. [17].

As the crystal lattice contains a large number of silicon atoms and the Pauli principle prevents any electrons to have the same quantum number, the molecular orbitals are very tightly spaced in energy and can be considered a continuum, an energy band. The band structure of a silicon crystal (Fig. 2.3a) exhibits a band gap of 1.12 eV with a minimum of the conduction band at a finite crystal momentum $k = 0.85k_0$ ($k_0 = 1/a$ is the Brillouin zone boundary and a is the lattice constant) and as such has an indirect band gap. This conduction band minimum consists of 6 degenerate valleys with two valleys along each k_x, k_y and k_z (Fig.2.3b). The dispersion relation at the band edge is

$$E(k) = E(0) + \frac{\hbar^2 k^2}{2m^*}, \tag{2.7}$$

which determines the effective mass m^* of the electrons in the energy band. For silicon, the dispersion is anisotropic along different crystal directions (Fig.2.3b), which results in a transverse effective mass of $m_t \approx 0.19\,m_e$ along k_x and k_y and a longitudinal effective mass of $m_l \approx 0.98\,m_e$ along k_z, where m_e is the mass of the free electron [36]. This gives a total effective mass of $m^* = \sqrt{m_l^2 + 2m_t^2}/3 \approx 0.33 m_e$.

Group-V elements such as P, As, Sb and Bi are single electron donors for silicon. However, this thesis focusses on phosphorus donors only. When incorporating a donor into the silicon crystal, the extra positive charge of the donor nucleus creates a Coulomb binding potential for the outermost weakly bound electron of the donor

$$V(r) = \frac{1}{4\pi\epsilon_0\epsilon_r}\frac{-Ze}{r}, \tag{2.8}$$

where Z is the excess charge of the dopant, ϵ_0 the permittivity of vacuum and ϵ_r the relative dielectric constant (Fig. 2.4a). In the environment of the silicon crystal the

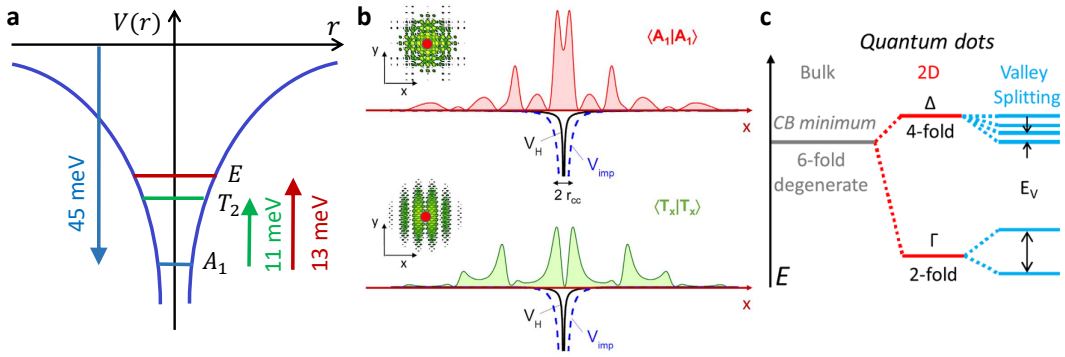

FIGURE 2.4: **Donor Coulomb potential and wave function.** **a** Donor Coulomb potential $V(r)$ with ground state (A_1) and excited states (T_2, E) indicated. The valley degeneracy has been lifted by the strong confinement due to the dopant atom. **b** Wave function and charge distribution of the donor electron states A_1 (top panel) and T_x (bottom panel), exhibiting valley oscillations. **c** Valley splitting of quantum dots. The degeneracy of the 6 valleys is lifted by strong electric fields and the z-confinement. Fig. **b** is taken from Ref. [37] and Fig. **c** from Ref. [17].

donor can be treated analogous to a hydrogen atom in vacuum, where the effective electron mass is m^*, according to the dispersion relation of the conduction band electrons, and $\epsilon_r = 11.9$ due to silicon screening the Coulomb force. Thus, the donor has a Bohr radius of $a_\mathrm{d} = a_0\epsilon_r/m^* \approx 20\,\text{Å}$, where a_0 is the Bohr radius in vacuum [17].

Central-cell corrections due to the strong donor confinement potential split the six valleys into a singlet with A_1 symmetry (ground state, $-45.6\,\text{meV}$ below the conduction band minimum), a triplet with T_2 symmetry ($11\,\text{meV}$ above A_1) and a doublet with E symmetry ($13\,\text{meV}$ above A_1), see Fig. 2.4a [36]. For each of these states $i \in (A_1, T_2^x, T_2^y, T_2^z, E^{xy}, E^z)$, the corresponding donor wave function $\Psi_i = \sum_{j=1}^{6} \alpha_i^{(j)} \psi^{(j)}$ is a linear combination of the envelope-modulated Bloch functions $\psi^{(j)}$ of the $1s$ orbital from the six valleys j [36], [37], where the coefficients

$$\alpha_{A_1}^{(j)} = \frac{1}{\sqrt{6}}(1,1,1,1,1,1), \tag{2.9a}$$

$$\alpha_{T_2^x}^{(j)} = \frac{1}{\sqrt{2}}(1,-1,0,0,0,0), \tag{2.9b}$$

$$\alpha_{T_2^y}^{(j)} = \frac{1}{\sqrt{2}}(0,0,1,-1,0,0), \tag{2.9c}$$

$$\alpha_{T_2^z}^{(j)} = \frac{1}{\sqrt{2}}(0,0,0,0,1,-1), \tag{2.9d}$$

$$\alpha_{E^{xy}}^{(j)} = \frac{1}{2}(1,1,-1,-1,0,0), \tag{2.9e}$$

$$\alpha_{E^z}^{(j)} = \frac{1}{2}(1,1,0,0,-1,-1), \tag{2.9f}$$

denote the relative contribution from each of the individual valleys. For instance, the singlet ground state A_1 is a symmetric combination of all 6 valleys. Its wave function is symmetric but exhibits oscillations within a_d (Fig. 2.4b, taken from Ref. [37]). These oscillations arise from the donor confinement and the finite momentum k_0 of the valley states and are called valley oscillations. All donor states exhibit valley oscillations which can strongly influence interactions related to wave function

overlap, like the exchange interaction.

Note that, in quantum dots the valley degeneracy is also lifted (Fig. 2.4c). Large electric fields and the triangular quantum well confinement at the Si/SiO_2 interface increase the energy of the in-plane $k_{\pm x}, k_{\pm y}$ valleys and split the two-fold degeneracy the $k_{\pm z}$ valleys [17].

2.3 A donor spin qubit

Spin is an intrinsic quantum mechanical property of elementary particles and atomic nuclei that describes how the particle is deflected when moving in magnetic fields. It gives the particle angular momentum and a small magnetic moment. Spin is quantized, thus can only take the discrete values $-s, -s+1, ..., s-1, s$ where $s = n/2$ is the spin quantum number with $n \in \mathbb{N}_0$. This property makes spin $s = 1/2$ ideal for quantum computation, being a natural two level system.

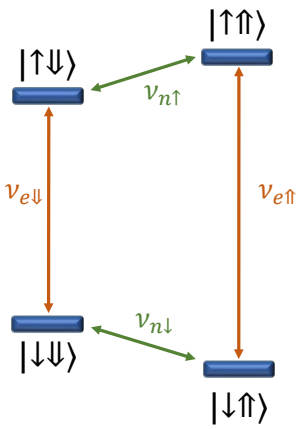

FIGURE 2.5: **Electron-nucleus level diagram.** Electron and nuclear spin energy levels with magnetic transitions indicated.

Both the donor electron and the phosphorus nucleus carry a spin of $1/2$. Consequently, both the electron spin $\{|\uparrow\rangle, |\downarrow\rangle\}$ and the nuclear spin $\{|\Uparrow\rangle, |\Downarrow\rangle\}$ can be used to encode quantum information. Unperturbed, the spin states have the same energy - they are spin-degenerate. However, if an external magnetic field B_0 is applied, they split by the Zeeman energy $E_Z = h\gamma B_0$, with γ being the corresponding gyromagnetic ratio (Fig. 4.3). The quantization of the spin happens along the direction of B_0, which we set in the z-direction unless otherwise indicated. The Hamiltonian describing the uncoupled electron-nuclear system is

$$\mathcal{H}_Z = h\gamma_e B_0 \boldsymbol{S}_z - h\gamma_n B_0 \boldsymbol{I}_z \tag{2.10}$$

with $\boldsymbol{S}_z = \frac{1}{2}\sigma_z$ and $\boldsymbol{I}_z = \frac{1}{2}\sigma_z$ as the spin operators in z-direction of the electron and nucleus respectively and $\gamma_e = 27.97\,\mathrm{GHz/T}$, $\gamma_n = 17.23\,\mathrm{MHz/T}$ as the respective gyromagnetic ratios.

However, the electron and the nucleus are not isolated from each other. They interact intrinsicly due to the Fermi contact hyperfine interaction A. The hyperfine interaction arises from the overlap of the electron wave function and the nucleus. The singlet ground state wave function ψ_{A_1} has a finite probability at the position of the nucleus (Fig. 2.4b) while for the excited states ψ_{T_2}, ψ_E the probability is zero.

Consequently, only the A_1 state enables the hyperfine interaction. There is no dipolar interaction between the electron and the nucleus as the ground state is a symmetric 1s state. Note, that any other nuclei in the vicinity contribute to the contact hyperfine interaction. These nuclei also have a finite dipolar contribution as they are positioned off-centre of the wave function. The hyperfine interaction Hamiltonian is

$$\mathcal{H}_{\mathrm{A}} = hA\boldsymbol{S}\cdot\boldsymbol{I}, \tag{2.11}$$

where $\boldsymbol{S} = \boldsymbol{S}_x + \boldsymbol{S}_y + \boldsymbol{S}_z$ and $\boldsymbol{I} = \boldsymbol{I}_x + \boldsymbol{I}_y + \boldsymbol{I}_z$ with $\boldsymbol{S}_i/\boldsymbol{I}_i$ as the spin operator in direction $i = x, y, z$. This interaction leads to the Hamiltonian of the coupled electron-nuclear system

$$\mathcal{H} = \mathcal{H}_{\mathrm{Z}} + \mathcal{H}_{\mathrm{A}} = h\gamma_e B_0 \boldsymbol{S}_z - h\gamma_n B_0 \boldsymbol{I}_z + hA\boldsymbol{S}\cdot\boldsymbol{I}. \tag{2.12}$$

For $\gamma_e B_0 \gg \gamma_N B_0 > A$ the detuning between the coupled states $|\uparrow\Downarrow\rangle, |\downarrow\Uparrow\rangle$ is much larger than A and the electron and nuclear states can be separated. The eigenstates of the Hamiltonian $\{|\uparrow\Uparrow\rangle, |\uparrow\Downarrow\rangle, |\downarrow\Uparrow\rangle, |\downarrow\Downarrow\rangle\}$ (Fig. 4.3) are then the tensor products of the individual spin states ($|\uparrow\Uparrow\rangle = |\uparrow\rangle \otimes |\Uparrow\rangle$ etc.) with eigenenergies

$$E_{\downarrow\Uparrow}/h = \frac{-\sqrt{(\gamma_+ B_0)^2 + A^2} - A/2}{2}, \tag{2.13a}$$

$$E_{\downarrow\Downarrow}/h = \frac{-\gamma_- B_0 + A/2}{2}, \tag{2.13b}$$

$$E_{\uparrow\Downarrow}/h = \frac{\sqrt{(\gamma_+ B_0)^2 + A^2} - A/2}{2}, \tag{2.13c}$$

$$E_{\uparrow\Uparrow}/h = \frac{-\gamma_- B_0 - A/2}{2}, \tag{2.13d}$$

where $\gamma_\pm = \gamma_e \pm \gamma_N$.

2.3.1 Electric field influence

Electric fields, arising from strain, surface charges, confinement effects or an external voltage bias, influence the electron orbital, the valley states and the hyperfine interaction significantly.

If an electric field is applied to the donor, the electron is slowly separated from nucleus, until the donor is ionized and the electron is confined at the Si/SiO_2 interface in form of a quantum dot (Fig. 2.6a insets). When transitioning from donor to dot, the 6 valley states' energies shift when the electric field increases and the confinement transitions from the strong symmetric donor potential to a triangular potential well at the Si/SiO_2 interface. As a consequence the valley splitting between the first and excited state decreases (Fig. 2.6a, As donor, taken from Ref. [38]) and valley mixing may have to be considered.

As an electric field distorts the wave function, the hyperfine interaction will change, creating a Stark shift of the spectral line (Fig. 2.6b, taken from Ref. [39]).

These electric effects are both very relevant for our qubit experiments, where large electric fields are present.

2.3.2 Qubit control

As spins possess a magnetic moment, they can be controlled via magnetic resonance, where an external oscillating magnetic field is applied in resonance with the spin states energy splitting.

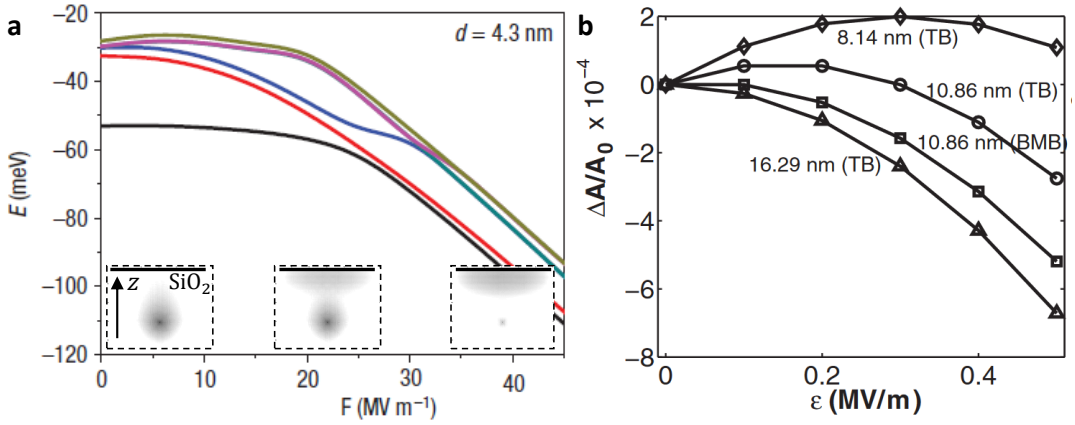

FIGURE 2.6: **Effect of electric fields on the donor electron.** **a** First six eigenlevels of an As donor electron at depth $d = 4.3$ nm as a function of electric field, calculated in a tight-binding approximation. Insets show a sketch of the electron wave function for three different electric fields. **b** Change of the hyperfine interaction as a function of electric field for different donor depths, calculated with tight-binding (TB) and band minima basis (BMB) methods. Fig. **a** is adapted from Ref. [38] and Fig. **b** is taken from Ref. [39].

Within a static magnetic field $B_0\hat{z}$, a spin precesses around the magnetization axis $\hat{z}$ at the Larmor frequency $\omega_0 = \gamma B_0$ (Fig. 2.7a). It is convenient to change our reference frame from the laboratory to a rotating frame which rotates at angular frequency ω (Fig. 2.7b). This corresponds to a basis transformation of

$$|\psi_r\rangle = \exp\left(\frac{i\omega t}{2}\sigma_z\right)|\psi\rangle\,. \tag{2.14}$$

In this reference frame, the spin state appears to precess with the angular frequency $\Delta\omega = \omega_0 - \omega$.

We apply a magnetic pulse $2B_{\mathrm{ac}}\cos(\omega_{\mathrm{ac}}t)\hat{x}$, perpendicular to $B_0\hat{z}$, oscillating at an angular frequency ω_{ac} in the laboratory frame. As $\cos(\omega_{\mathrm{ac}}t) = \frac{1}{2}[\exp(i\omega_{\mathrm{ac}}t) + \exp(-i\omega_{\mathrm{ac}}t)]$, we find two magnetic field components of amplitude B_{ac} in the rotating frame: one rotating with the frame at $\Delta\omega_{\mathrm{ac}} = \omega - \omega_{\mathrm{ac}}$ and one against at $\Delta'\omega_{\mathrm{ac}} = \omega + \omega_{\mathrm{ac}}$. We now choose $\omega = \omega_{\mathrm{ac}}$. If $\omega_{\mathrm{ac}} \approx \omega_0$, the counter-rotating part can be neglected, as it is far detuned from resonance. This is called the rotating wave approximation (RWA). The spin will then precess around the effective magnetization axis with $\omega_{\mathrm{eff}} = \Delta\omega + \omega_{\mathrm{R}}$, where $\omega_{\mathrm{R}} = \gamma B_{\mathrm{ac}}$ (Fig. 2.7c). If $\Delta\omega = \omega_{\mathrm{ac}} - \omega_0 = 0$, the spin rotates at ω_{R} in the yz-plane of the Bloch sphere. These oscillations are called Rabi oscillations and their angular frequency ω_{R} is the Rabi frequency. If $\Delta\omega \neq 0$, the evolution of the spin state $|\psi(t)\rangle$ is described by the Rabi formula which gives the probability that the state is found in $|\uparrow\rangle$, when initially in $|\downarrow\rangle$, to

$$|\langle\uparrow|\psi(t)\rangle|^2 = \frac{\omega_{\mathrm{R}}^2}{\omega_{\mathrm{R}}^2 + \Delta\omega^2}\sin^2\left(\frac{\sqrt{\omega_{\mathrm{R}}^2 + \Delta\omega^2}}{2}t\right). \tag{2.15}$$

When this magnetic resonance technique is applied to the electron, we speak of electron spin resonance (ESR) and, when it is applied to the nucleus, of nuclear magnetic resonance (NMR). In figure 4.3 these magnetic transitions and their resonance

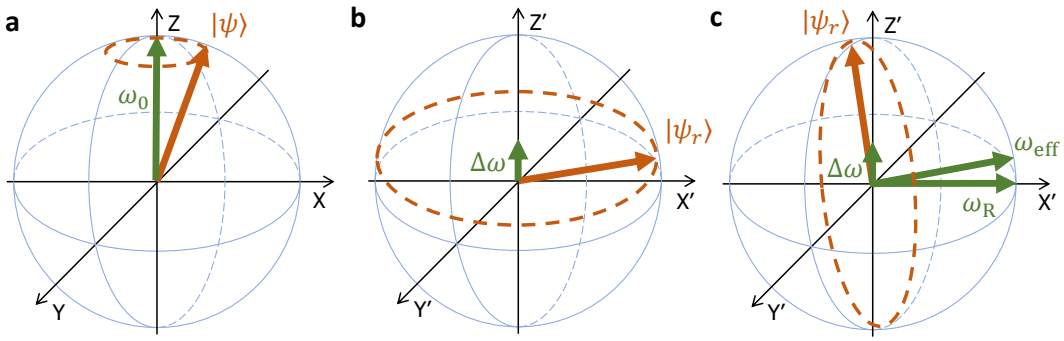

FIGURE 2.7: **Spin qubit in the rotating frame. a** In the laboratory frame, the spin precesses around $B_0\hat{z}$ with an angular frequency of ω_0. **b** In a rotating frame with angular frequency ω, the magnetic field along the z-direction is reduced and the spin now precesses at $\Delta\omega = \omega_0 - \omega$. **c** When an oscillating magnetic field with ω_{ac} is applied, it appears static in a rotating frame with $\omega_{\text{R}} = \gamma B_{\text{ac}}$ for $\omega = \omega_{\text{ac}}$. The spin precesses around the effective magnetic field axis with $\omega_{\text{eff}} = \Delta\omega + \omega_{\text{R}}$. At zero detuning $\omega_{\text{ac}} = \omega_0$, the spin perfectly oscillates between $|0\rangle$ to $|1\rangle$ at frequency ω_{R}.

frequencies

$$\begin{aligned}
\nu_{e\Uparrow} &= \gamma_e B_0 + A/2, \\
\nu_{e\Downarrow} &= \gamma_e B_0 - A/2, \\
\nu_{n\uparrow} &= A/2 - \gamma_n B_0, \\
\nu_{n\downarrow} &= A/2 + \gamma_n B_0
\end{aligned}$$

are illustrated.

For a single phosphorus donor electron qubit, spin control was first demonstrated in 2012 [40] and for the nuclear qubit in 2013 [41]. When implanting the donor in purified ^{28}Si, which contains only 800 ppm ^{29}Si with nuclear spin 1/2, control fidelities of 99.94 % and 99.99 % respectively have been achieved [30], [42].

2.3.3 Qubit initialization and measurement

To successfully operate a spin system as a qubit, we need to be able to determine in which spin state it is at any given time. Therefore, we employ spin-to-charge conversion, which turns the electron spin signal into a charge signal and use a single electron transistor (SET) to detect small charge changes in its vicinity.

A SET consists of a small island of accumulated electrons which is capacitively coupled to a top gate TG and tunnel coupled to two electron reservoirs, the source S and the drain D (Fig. 2.8a). The energy of this island is

$$\begin{aligned}
E &= \frac{Q^2}{2C} \\
&= \frac{e^2 N^2}{2C} \\
&= E_C N^2,
\end{aligned} \tag{2.16}$$

where Q is the charge on the island which consists out of N electrons, C is the total capacitance of the island and E_C is the charging energy. To add one electron to the

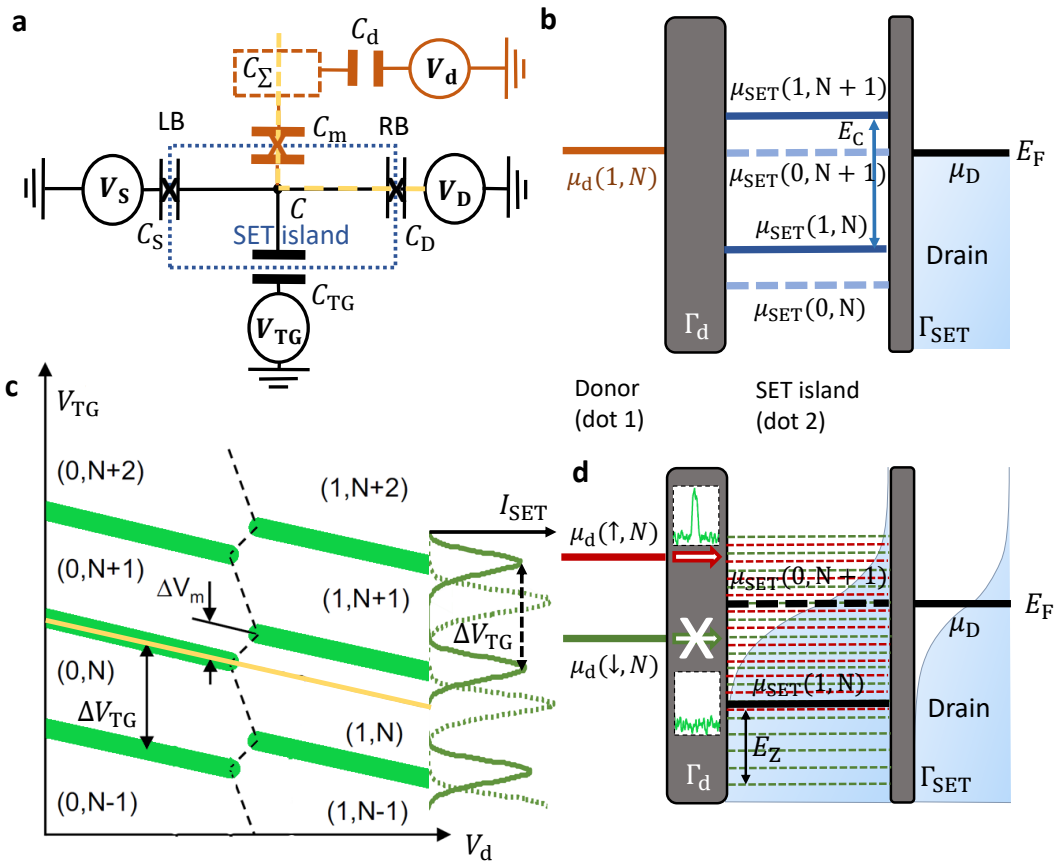

FIGURE 2.8: **Electron readout with spin-dependent tunnelling.** **a** The SET consists out of an island with a total capacitance C. The island is tunnel coupled to S and D with capacitances C_S and C_D respectively and capacitively coupled to a top gate TG with C_{TG}. Additionally the SET is tunnel coupled to any donor in the vicinity with capacitance C_m. The total capacitance of the donor C_Σ depends on its surroundings. Tunnel coupled junctions are indicated with X. **b** Sketch of the electrochemical potentials along the dashed yellow line in panel **a**. The SET island and the donor form a parallel double dot such that μ_{SET} depends on the charge state of the donor. **c** Charge stability diagram where the green lines represent the SET Coulomb peaks, as shown in the inset, spaced by ΔV_{TG}. μ_{SET} can be kept fixed by biasing V_d and V_{TG} along the yellow line. **d** Sketch of the electrochemical potentials at finite B_0, where all spin states are split by E_Z. Only $|\uparrow\rangle$ can tunnel into the SET and enable current flow, while $|\downarrow\rangle$ stays confined and the current blocked. Fig. **c** is adapted from Ref. [43].

island one needs the energy

$$\begin{aligned}\Delta E(N) &= E(N+1) - E(N) \\ &= E_C\left(N + \frac{1}{2}\right) \\ &\equiv \mu_{SET}(N),\end{aligned} \tag{2.17}$$

called the electrochemical potential. The SET island exhibits a ladder of these potentials $\mu_{SET}(N), \mu_{SET}(N+1), \ldots$ (Fig. 2.8b).

In our qubit devices, the diameter of the SET island is usually $d_{SET} \approx 50 - 100\,\text{nm}$ which corresponds to a capacitance of $C = 2\pi\epsilon_0\epsilon_r d_{SET} = 33 - 65\,\text{aF}$ and a charging energy of $E_C = 2.4 - 1.2\,\text{meV}$. For charging effects to be relevant, the temperature needs to be small in comparison to the charging energy ($E_C \gg k_B T_e$ with T_e as the electron temperature).

Assuming zero bias between S and D, the corresponding electrochemical potentials μ_S and μ_D align ($\mu_S = \mu_D$). When a voltage bias V_{TG} is applied on TG, $\mu_{SET}(N)$ is shifted. For $\mu_{SET}(N) \geq \mu_D$, the Nth electron cannot be added to the SET island and no current can flow from S to D - the SET is in Coulomb blockade. Only when $\mu_{SET}(N) = \mu_D$, electrons can tunnel on and off the SET island one at a time at no energy cost - the blockade is lifted and a current is observed. Hence, when continuously increasing V_{TG}, the current oscillates between high and low values and we observe Coulomb oscillations (Fig. 2.8c, inset). The spacing between the peaks corresponds to

$$\Delta V_{TG} = \frac{E_C}{e\alpha_{TG}}, \tag{2.18}$$

where

$$\alpha_{TG} = \frac{C_{TG}}{C} \tag{2.19}$$

is the lever arm between TG and the SET island with C_{TG} as their mutual capacitance. The finite width of the peaks arises from the thermal broadening of the occupied states at the Fermi level E_F, the bias between S and D and the tunnel rate Γ_{SET} of an electron through the barrier ("lifetime broadening").

When a donor is in the vicinity of the SET, it is tunnel coupled with a capacitance of C_m to the island (Fig. 2.8a). The SET island and the donor then form a parallel double quantum dot. Thus, both $\mu_{SET}(N)$ and $\mu_d(N)$, the donor electrochemical potential, depend on the charge state of the donor and the SET island respectively (Fig. 2.8b). We tune the SET such that $\mu_{SET}(0, N+1) = \mu_D < \mu_{SET}(1, N+1)$. We shift μ_d by applying a voltage V_d on the donor top gate. During this process we keep the SET energy levels fixed by compensating with V_{TG} such that we follow the angle of the Coulomb peaks (yellow line in Fig. 2.8c). As long as the donor is neutral, the SET stays in Coulomb blockade. However, when $\mu_d \geq \mu_{SET}(1, N+1)$, the donor becomes ionized and the SET potential shifts from $\mu_{SET}(1, N+1)$ to $\mu_{SET}(0, N+1)$ - Coulomb blockade is lifted and current flows. This allows us to detect a change of the donor charge state. When we measure the SET current both as a function of V_{TG} and V_d, we record a 2D map of Coulomb peaks, the charge stability diagram (Fig. 2.8c). Charges, e.g. donors, can easily be identified by discontinuities in the Coulomb peaks that appear when the donor is loaded. This charge transfer signal is given by

$$\frac{\Delta q}{e} = \frac{\Delta V_m}{\Delta V_{TG}} = \frac{C_m}{C_\Sigma}, \tag{2.20}$$

where C_Σ is the total donor capacitance. $\Delta q/e$ approaches one, the closer the donor is positioned to the SET.

At finite B_0, all spin states are split by E_Z. When $E_Z \ll k_B T_e$, we can exploit this splitting to link the spin state to the charge state and distinguish between an electron in spin state $|\uparrow\rangle$ and $|\downarrow\rangle$. To this end, we carefully tune the donor potential such that $\mu_d(\uparrow, N) = \mu_{SET}(0, N+1) + E_Z/2$ and $\mu_d(\downarrow, N) = \mu_{SET}(0, N+1) - E_Z/2$ (Fig. 2.8d). In this case, an electron in spin state $|\downarrow\rangle$ always stays confined at the donor and the SET remains in Coulomb blockade. Thus, we associate a $|\downarrow\rangle$ electron with a low current signal. On the contrary, an electron in spin state $|\uparrow\rangle$ can tunnel to the SET. Coulomb blockade is lifted and a high current flows until another electron in spin state $|\downarrow\rangle$ tunnels onto the donor and blocks the current again. Hence, we associate a $|\uparrow\rangle$ electron with a high current blip (Fig. 2.8d). The blip duration is determined by the tunnel rate $\Gamma_{d,\downarrow}$ of an electron in spin state $|\downarrow\rangle$ from the SET to the donor. Note, that the electron spin states in the SET are also split by E_Z. Nevertheless,

the tunnel rate for both electron spin states remains equal as long as the number of available states around E_F is the same for both spin states. Moreover, assuming the SET island to be a quasi-continuum of states serves only as an approximation. In fact, mostly we operate our SETs with around 100 electrons. In this regime we observe some remaining many-electron quantum-dot behaviour [44]. As a consequence the density of states in the SET is not fully continuous and $\Gamma_{d,\downarrow}$ and $\Gamma_{d,\uparrow}$ can slightly vary for different voltages and are not necessarily equal.

This measurement process can also be used to initialize the qubit into a well known state, a vital feature for qubit operation. When tuned for read out, any electron in spin state $|\uparrow\rangle$ will eventually escape and be replaced by an electron in spin state $|\downarrow\rangle$. Thus, after a time $t > \Gamma_{d,\downarrow}^{-1} + \Gamma_{d,\uparrow}^{-1}$, the electron is initialized in the spin state $|\downarrow\rangle$.

This type of single-shot donor electron spin readout has been first demonstrated in 2010 by A. Morello *et. al.* [24]. The nuclear spin state can also be readout via this mechanism as its state can be mapped onto the electron spin via NMR pulses [41].

2.3.4 Qubit decoherence

Small amounts of information loss from the qubit to the environment can lead to the destruction of a coherent quantum state. This process is called decoherence.

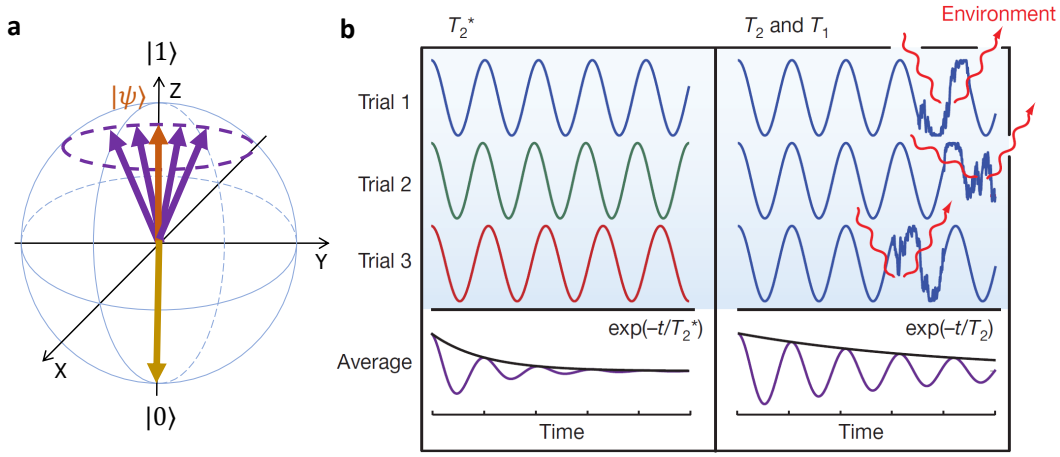

FIGURE 2.9: **Qubit decoherence. a** An initially coherent state $|\psi\rangle$ decoheres through dephasing, relaxation and excitation. Dephasing corresponds to a diffusion of the qubit's phase when the Larmor frequency slowly changes (purple arrows). Relaxation (yellow arrow) corresponds to a transition from $|1\rangle$ to $|0\rangle$ while excitation leads to a transition from $|0\rangle$ to $|1\rangle$. **b** Slow noise along σ_z changes the qubit Larmor frequency over time. Thus a temporal ensemble dephases on a time scale T_2^* (left panel). Interactions with the environment also can change the qubits phase in a single trail, causing decoherence of the temporal ensemble on the time scale T_2 (right panel). Energy exchange with the environment leads to relaxation on the time scale of T_1 (right panel). Fig. **b** is taken from Ref. [13].

Any external noise source that couples to the qubit system leads to fluctuations in the qubit Hamiltonian $\mathcal{H}_0$ (Eq. 2.3) resulting in a perturbed Hamiltonian of

$$\mathcal{H}(t) = \mathcal{H}_0 + \mathcal{H}'. \tag{2.21}$$

$\mathcal{H}'$ is the noise perturbation which can be divided into longitudinal noise along the z-direction with

$$\mathcal{H}'_z = \delta\epsilon(t)\sigma_z \tag{2.22}$$

and perpendicular noise along the x-direction with

$$\mathcal{H}'_x = \delta\Delta(t)\sigma_x. \tag{2.23}$$

Here $\delta\epsilon(t)$ and $\delta\Delta(t)$ are the energy shifts caused by noise sources in z- and x-direction respectively.

$\mathcal{H}'_z$ causes fluctuations in the qubit frequency $\omega_0(t)$. Consequently, when taking a temporal ensemble measurement, the qubit precesses with a different angular frequency around its quantization axis at each trial. Hence, the phase at a specific time t' of the qubit oscillation is different for each trail. This causes an apparent damping of the oscillation on a time scale called T_2^* (Fig. 2.9). A single qubit oscillation can retain its phase coherence much longer, although it will still interact with the environment. The interaction may result in a phase shift of the qubit and the qubit coherence will dephase on a time scale T_2 (Fig. 2.9).

Longitudinal noise for donors in silicon can arise from Overhauser field fluctuations of ^{29}Si nuclear spins, thermal Johnson-Nyquist radiation and instability of B_0 [30]. The dephasing time can be extended by dynamical decoupling techniques where clever pulse sequences cancel slow noise [45]. The longest coherence time for a single spin in silicon was measured to $T_2 = 35.6\,\mathrm{s}$ for the phosphorus nuclear spin while employing such techniques [30]. For the electron spin $T_2 = 1\,\mathrm{s}$ was achieved [46].

Fluctuations in the off-diagonal elements of the qubit Hamiltonian due transverse noise sources, as expressed in $\mathcal{H}'_x$, create an energy exchange with the environment and cause transitions between the qubit eigenstates. On the time scale T_1 the qubit system will then relax into thermal equilibrium (Fig. 2.9).

Perpendicular noise for donors in silicon is weak and mostly caused by phonons. Relaxation times can reach $T_1 = 30\,\mathrm{s}$ for the electron spin and exceed hours for the nuclear spin [47]. Refer to Chap. 8 for a detailed discussion of relaxation in donors.

2.4 Circuit Quantum Electrodynamics

In cQED a single photon inside a cavity, comprised of an on-chip resonator, coherently couples to a quantum system. In quantum computation, cQED can be employed to measure qubits, couple qubits over long distances and to connect different types of quantum systems.

2.4.1 A quantized electric field

To describe the coupled system of a cavity electric field and the quantum system, we need to find a quantum mechanical treatment of the electric field to understand its interaction with single quantum particles. Therefore we first determine the energy contained by an electromagnetic field and then quantize the field, following Refs. [48], [49].

For any electromagnetic field Maxwell's equations apply

$$\vec{\nabla} \times \vec{E} = -\frac{\partial \vec{B}}{\partial t} \text{ (Faradays Law)}, \tag{2.24}$$

$$\frac{1}{\mu_0}\vec{\nabla} \times \vec{B} = \epsilon_0 \frac{\partial \vec{E}}{\partial t} + \vec{J} \text{ (Amperes Law)}, \tag{2.25}$$

$$\epsilon_0 \cdot \vec{\nabla}\vec{E} = \sigma \text{ (Gauss Law)}, \tag{2.26}$$

$$\vec{\nabla}\vec{B} = 0 \text{ (Gauss Law)}, \tag{2.27}$$

where $\vec{E}(t)$ is the electric field, $\vec{B}(t)$ the magnetic field, μ_0 the magnetic permeability in vacuum, ϵ_0 the electric permittivity in vacuum, σ is the charge density and $\vec{J}$ the current density. In free space $\sigma = 0$, $\vec{J} = 0$. We introduce the vector potential

$$\vec{B} = \vec{\nabla} \times \vec{A}(r,t), \tag{2.28}$$

$$\vec{E} = -\vec{\nabla}\phi(r,t) - \frac{\partial \vec{A}(r,t)}{\partial t}, \tag{2.29}$$

where ϕ is the scalar potential, and apply the Coulomb gauge $\vec{\nabla}\vec{A} = 0$. This leads to the wave equation

$$\vec{\nabla}^2 \vec{A}(\vec{r},t) = \frac{1}{c^2}\frac{\partial^2 \vec{A}(\vec{r},t)}{\partial^2 t}, \tag{2.30}$$

that describes the propagation of the vector potential in free space.

In a cubic cavity with length L and volume $V = L^3$, the solution for an electromagnetic field with periodic boundary conditions is

$$\vec{A} = \sum_k \left\{ \vec{A}_k e^{-i\omega_k t + i\vec{k}\cdot\vec{r}} + \vec{A}_k^* e^{i\omega_k t - i\vec{k}\cdot\vec{r}} \right\}, \tag{2.31}$$

where $\vec{k} = 2\pi n_i / L$ is the wave vector with $n_i \in \mathbb{N}_0$ for $i = x, y, z$, $\omega_k = c_0\vec{k}$ is the angular frequency and $c = 1/\sqrt{\mu_0\epsilon_0}$ the speed of light in vacuum. The energy contained in the kth mode of the electromagnetic field is given by the Poynting vector to

$$\begin{aligned} S_k &= \frac{1}{2}\int_{\text{cavity}} \left(\epsilon_0 |\vec{E}_k|^2 + \frac{1}{\mu_0}|\vec{B}_k|^2 \right) dV \\ &= 2\epsilon_0 V \omega_k^2 |\vec{A}_k|^2. \end{aligned} \tag{2.32}$$

We can express the vector potential in form of the 'momentum' p_k and the 'position' q_k of mode k as

$$A_k = \frac{1}{2\sqrt{\epsilon_0 L \omega_k^2}} \left(\omega_k q_k + i p_k\right) \vec{\epsilon}_k, \tag{2.33a}$$

$$A_k^* = \frac{1}{2\sqrt{\epsilon_0 L \omega_k^2}} \left(\omega_k q_k - i p_k\right) \vec{\epsilon}_k \tag{2.33b}$$

with $\vec{\epsilon}_k$ as the polarization direction. Then the field energy follows to

$$S_k = \frac{1}{2}\left(p_k^2 + \omega_k^2 q_k^2\right). \tag{2.34}$$

We identify this energy as the energy of an harmonic oscillator.

Now we quantize the electromagnetic field by replacing the classical position and momentum with their quantum operators $\boldsymbol{p}_k$ and $\boldsymbol{q}_k$, leading to a Hamiltonian of

$$\mathcal{H} = \sum_k \frac{1}{2} \left(\boldsymbol{p}_k^2 + \omega_k \boldsymbol{q}_k^2 \right). \tag{2.35}$$

We call this quantization "Second Quantization". This terminology arises as the quantization of discrete modes, e.g. of a particle in a cavity, is considered the first quantization and then the integer number of excitations of each of these modes is considered the second quantization.

We introduce the annihilation $\boldsymbol{a}$ and creation $\boldsymbol{a}^\dagger$ operators for each wave vector k which destroy and create a quantum of energy $\hbar\omega_k$ in the electromagnetic field mode k:

$$\boldsymbol{a}_k = \frac{1}{\sqrt{2\hbar\omega_k}} \left(\omega_k \boldsymbol{q}_k + i\boldsymbol{p}_k \right), \tag{2.36a}$$

$$\boldsymbol{a}_k^\dagger = \frac{1}{2\sqrt{\hbar\omega_k}} \left(\omega_k \boldsymbol{q}_k - i\boldsymbol{p}_k \right) \tag{2.36b}$$

with the commutator

$$[\boldsymbol{a}_k, \boldsymbol{a}_k^\dagger] = \delta_{k,k'}. \tag{2.37}$$

Thus the Hamiltonian transforms into the standard harmonic oscillator Hamiltonian of

$$\mathcal{H}_{\mathrm{HO}} = \sum_k \hbar\omega_k \left(\boldsymbol{a}_k^\dagger \boldsymbol{a}_k + \frac{1}{2} \right). \tag{2.38}$$

$\mathcal{H}_{\mathrm{HO}}$ indicates that an electromagnetic field consists out of many independent quantum mechanical systems: each mode k is represented by one harmonic oscillator with energy $E_k = \hbar\omega_k$. The nth excitation of the kth harmonic oscillator is interpreted as having n particles. Thus we introduce the number operator

$$\boldsymbol{n}_k = \boldsymbol{a}_k^\dagger \boldsymbol{a}_k, \tag{2.39}$$

with its eigenvectors $|n_k\rangle$, which counts the number n_k of excitations (and hence particles) in each mode k. The eigenenergy of each mode with n_k particles is given by

$$E_{n,k} = \hbar\omega_k \left(n_k + \frac{1}{2} \right). \tag{2.40}$$

The ground state $n = 0$, also called vacuum state as no excitations are present, contains the energy $E_{0,k} = \frac{1}{2}\hbar\omega_k$. While being an eigenstate of $\mathcal{H}_{\mathrm{HO}}$, the vacuum state is not an eigenstate of the electric and magnetic field operators $\boldsymbol{E} = \sum_k \boldsymbol{E}_k$ and $\boldsymbol{B} = \sum_k \boldsymbol{B}_k$, where

$$\boldsymbol{E}_k = i\boldsymbol{E}_{0,k} \left\{ \boldsymbol{a}_k e^{-i\omega_k t + i\boldsymbol{k}\cdot\boldsymbol{r}} - \boldsymbol{a}_k^\dagger e^{i\omega_k t - i\boldsymbol{k}\cdot\boldsymbol{r}} \right\}, \tag{2.41}$$

$$\boldsymbol{B}_k = \frac{i}{c} \boldsymbol{B}_{0,k} \left\{ \boldsymbol{a}_k e^{-i\omega_k t + i\boldsymbol{k}\cdot\boldsymbol{r}} - \boldsymbol{a}_k^\dagger e^{i\omega_k t - i\boldsymbol{k}\cdot\boldsymbol{r}} \right\} \tag{2.42}$$

with $\boldsymbol{E}_{0,k} = \sqrt{\frac{\hbar\omega_k}{2\epsilon_0 V}} \boldsymbol{\epsilon}_k$ and $\boldsymbol{B}_{0,k} = \sqrt{\frac{\hbar\omega_k}{2\epsilon_0 V}} \boldsymbol{k} \times \boldsymbol{\epsilon}_k$. Thus, the electric and magnetic fields do not have definite values in this state and fluctuate around their mean value of zero. These fluctuations are called zero-point fluctuations and can be interpreted as pairs of virtual photons that are continuously appearing and disappearing.

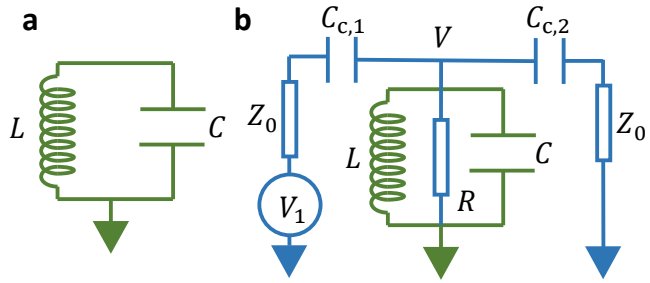

FIGURE 2.10: **LC resonator.** **a** Harmonic oscillator formed by an LC resonator with capacitance C and inductance L. **b** The resonator is coupled via capacitors $C_{c,1}$ and $C_{c,2}$ to transmission lines with impedance Z_0. A resistor R represents internal losses of the resonator.

2.4.2 Superconducting resonators

The simplest harmonic oscillator in superconducting circuits is the lumped element LC resonator, which consists of a capacitor C and an inductance L (Fig. 2.10a). Following Ref. [50], [51], this section gives an overview over important properties of superconducting resonators.

The LC resonator is described by the Hamiltonian

$$\mathcal{H} = \frac{Q^2}{2C} + \frac{\mathbf{\Phi}^2}{2L}, \tag{2.43}$$

where $\mathbf{\Phi}$ is the flux in the inductor and Q the charge accumulated on the capacitor. The system can be represented as a harmonic oscillator $\mathcal{H}_{\mathrm{HO}}$ with resonance frequency $\omega_{\mathrm{r}} = 1/\sqrt{LC}$ and creation and annihilation operators

$$\boldsymbol{a}^{\dagger} = \frac{1}{\sqrt{2\hbar Z_{\mathrm{r}}}} \left(\mathbf{\Phi} - iZ_r \boldsymbol{Q}\right), \tag{2.44}$$

$$\boldsymbol{a} = \frac{1}{\sqrt{2\hbar Z_{\mathrm{r}}}} \left(\mathbf{\Phi} + iZ_r \boldsymbol{Q}\right), \tag{2.45}$$

where $Z_{\mathrm{r}} = \sqrt{L/C}$ is the resonator impedance. The voltage $\boldsymbol{V}$ across the capacitor and the current $\boldsymbol{I}$ in the inductor can be expressed as

$$\boldsymbol{V} = \frac{\boldsymbol{Q}}{C} = iV_{\mathrm{rms}} \left(\boldsymbol{a}^{\dagger} - \boldsymbol{a}\right), \tag{2.46}$$

$$\boldsymbol{I} = \frac{\mathbf{\Phi}}{L} = \omega_{\mathrm{r}} \frac{V_{\mathrm{rms}}}{Z_r} \left(\boldsymbol{a}^{\dagger} + \boldsymbol{a}\right) \tag{2.47}$$

$$\tag{2.48}$$

with $V_{\mathrm{rms}} = \omega_{\mathrm{r}} \sqrt{\frac{\hbar Z_r}{2}}$ as the root-mean-square vacuum fluctuations of the voltage. The voltage and current then generate an electric and magnetic field

$$\boldsymbol{E}(\boldsymbol{r}) = i\boldsymbol{E}_{\mathrm{rms}}^{\mathrm{vac}}(\boldsymbol{r}) \left(\boldsymbol{a} - \boldsymbol{a}^{\dagger}\right), \tag{2.49}$$

$$\boldsymbol{B}(\boldsymbol{r}) = i\boldsymbol{B}_{\mathrm{rms}}^{\mathrm{vac}}(\boldsymbol{r}) \left(\boldsymbol{a} + \boldsymbol{a}^{\dagger}\right) \tag{2.50}$$

with $\boldsymbol{E}_{\mathrm{rms}}^{\mathrm{vac}}$ and $\boldsymbol{B}_{\mathrm{rms}}^{\mathrm{vac}}$ as their respective vacuum rms fluctuations at position $\boldsymbol{r}$.

Coupling to the transmission lines

In an experiment, the resonator is coupled to measuring lines and exhibits losses. We examine the situation where the resonator is coupled by capacitances $C_{c,1}$ and $C_{c,2}$ to two transmission lines with impedance Z_0 (Fig. 2.10b). The capacitances create a strong impedance mismatch, confining the electromagnetic field inside the resonator. The new effective capacitance is

$$C' = C + \frac{C_{c,1}}{1+(C_{c,1}\omega_r Z_0)^2} + \frac{C_{c,2}}{1+(C_{c,2}\omega_r Z_0)^2} \approx C + C_{c,1} + C_{c,1}. \tag{2.51}$$

Hence, coupling the resonator to transmission lines changes its resonance frequency and impedance to $\omega_r = 1/\sqrt{LC'}$ and $Z_r = \sqrt{L/C'}$. A resistance R in the resonator represents the internal losses, which gives an effective resistance of

$$\frac{1}{R'} = \frac{1}{R} + \frac{1}{R_{ext,1}} + \frac{1}{R_{ext,2}}, \tag{2.52}$$

where $R_{ext,i} = [1/(C_{c,i}Z_0\omega_r)^2 + 1]Z_0$ for $i = 1, 2$. The total losses are expressed by the resonator's quality factor

$$Q_{tot}^{-1} = \frac{Z_r}{R'} = Q_{ext,1}^{-1} + Q_{ext,2}^{-1} + Q_{int}^{-1}, \tag{2.53}$$

with the contributions $Q_{int}^{-1} = R\sqrt{L/C'}$ describing the internal losses and $Q_{ext,i}^{-1} = R_{ext,i}\sqrt{L/C}$ the losses to the transmission lines. The corresponding damping rates are $\kappa_L = \omega_r'/Q_{int}$ and $\kappa_i = \omega_r'/Q_{ext,i}$.

For $C_{c,i} \ll C$ ($Q \gg 1$), we can approximate

$$\omega_r' \approx \omega_r,\ Z_r' \approx Z_r,\ R_{ext,i} \approx 1/Z_0 C_{c,i}^2 \omega_r^2 \tag{2.54}$$

and

$$\kappa_i = \omega_r^3 C_{c,i}^2 Z_0 Z_r \tag{2.55}$$

with $C_{c,i} = 1/\sqrt{Q_{ext,i} Z_0 Z_r \omega_r^2}$.

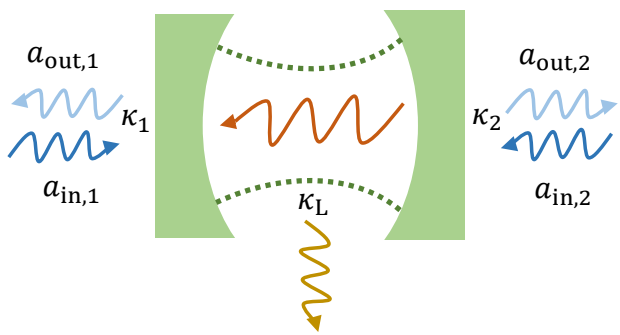

FIGURE 2.11: **Probing a resonator from the outside**. When measuring a resonator with classical microwave fields, the input and output electromagnetic fields of the resonator can be determined with a scattering matrix approach, using the classical input and output waves a. To account for quantum back-action, input-output theory is applied, considering an intra-resonator field $\boldsymbol{a}(t)$, coupled to external fields with coupling strengths κ.

When measuring the resonator from the outside with classical microwave fields, it is connected to voltage sources through the transmission lines. The input and

output electromagnetic fields of the resonator can be attained through the scattering matrix S [52]. We probe a resonator coupled to two ports with capacitors $C_{c,1}$ and $C_{c,2}$ (Fig. 2.10b, 2.11) with a Vector Network Analyser (VNA) to determine the scattering matrix coefficients

$$S_{ij} = \frac{a_{\text{out,i}}}{a_{\text{in,j}}}, \tag{2.56}$$

where $a_{\text{out,i}}$ ($a_{\text{in,j}}$) is the classical output (input) wave at port $i = 1,2$ ($j = 1,2$). To account for quantum back-action, we apply a quantum mechanical treatment where these classical waves are replaced by coherent electromagnetic waves. Input-output theory [53] gives

$$S_{21}(\omega) = \frac{2\sqrt{\kappa_1\kappa_2}}{\kappa_1 + \kappa_2 + \kappa_L - 2i(\omega - \omega_0)} \tag{2.57}$$

for the transmitted signal and

$$S_{ii}(\omega) = \frac{\kappa_i - \kappa_j - \kappa_L + 2i(\omega - \omega_0)}{\kappa_i + \kappa_j + \kappa_L - 2i(\omega - \omega_0)} \tag{2.58}$$

for the reflection.

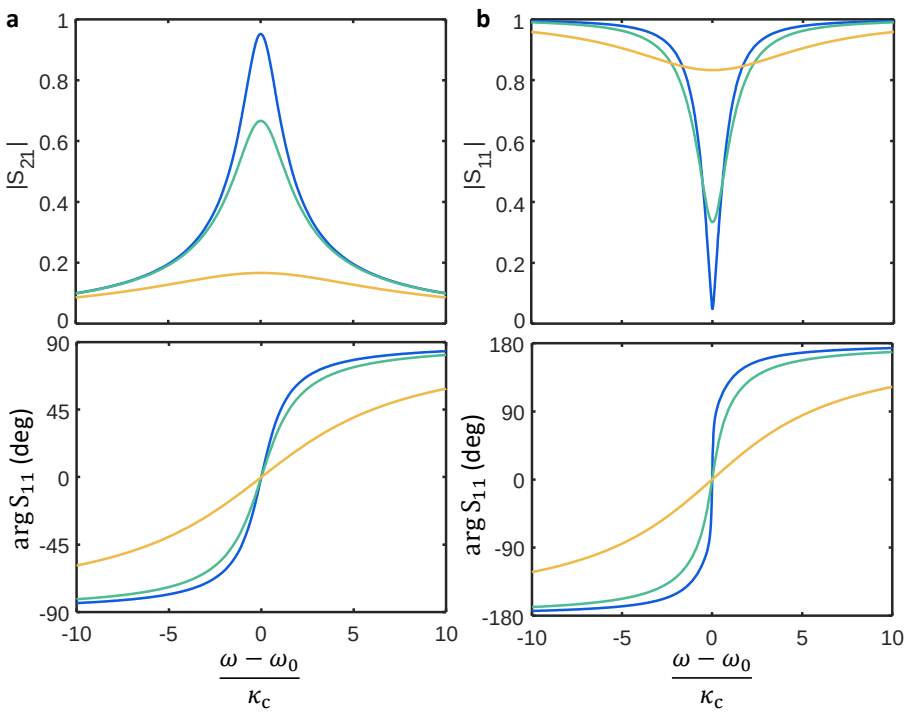

FIGURE 2.12: **Transmission and reflection measurements**. Amplitude and phase of the scattering matrix components for $\kappa_c = 10\kappa_L$ (blue, over-coupled regime), $\kappa_c = \kappa_L$ (green, critical regime), $\kappa_c = 0.1\kappa_L$ (yellow, under-coupled regime).

Depending on the strength of the internal damping rate κ_L in comparison with the external coupling rate $\kappa_c = \kappa_1 + \kappa_2$, we can identify three distinct regimes in which the resonator can be operated (Fig. 2.12):

- **The under-coupled regime**, where $\kappa_L \gg \kappa_c$ (yellow curves). The peak width is mostly determined by κ_L.
- **The critical coupling regime**, where $\kappa_L = \kappa_c$ (green curves).

- **The over-coupled regime**, where $\kappa_L \ll \kappa_c$ (blue curves). Both the amplitude and phase response at resonance is maximum for S_{11} and S_{21}.

2.4.3 Coupling a qubit to a quantized field: Jaynes-Cummings Hamiltonian

To understand how a two-level system, in our case the qubit with Hamiltonian

$$\mathcal{H}_Q = \frac{\hbar\omega_0}{2}\sigma_z \tag{2.59}$$

(Sec. 2.1), interacts with a single mode resonator of frequency ω_r with the free field Hamiltonian

$$\mathcal{H}_{HO} = \hbar\omega_r\left(\boldsymbol{a}^\dagger\boldsymbol{a} + \frac{1}{2}\right) \tag{2.60}$$

(Sec. 2.4.1), we explore the source of their interaction, the Lorentz force.

When a charged particle travels through an electromagnetic field, it experiences the Lorentz force

$$\vec{F} = q\left(\vec{E} + \vec{v}\times\vec{B}\right), \tag{2.61}$$

where $\vec{v}$ is the velocity and q the charge of the particle. The corresponding Lagrangian of this motion is

$$L = \frac{1}{2}m\dot{\vec{q}}^2 - q\phi + q\vec{A}\cdot\dot{\vec{q}}, \tag{2.62}$$

where m is the mass of the particle. The classical Hamiltonian of the system is then given by

$$\begin{aligned} H(\vec{q},\vec{p}) &= \vec{p}\dot{\vec{q}} - L(\vec{p},\dot{\vec{q}}) \\ &= \frac{1}{2m}\left(\vec{p} - q\vec{A}\right)^2 + q\phi. \end{aligned} \tag{2.63}$$

Following Refs. [48], [49], we quantize the system by replacing the classical variables with their quantum operators and get the quantum mechanical Hamiltonian of

$$\mathcal{H}(\boldsymbol{r},t) = \frac{1}{2m}\left(\boldsymbol{p} - q\boldsymbol{A}(\boldsymbol{r},t)\right)^2 + q\phi(\boldsymbol{r},t) \tag{2.64}$$

$$= \frac{\boldsymbol{p}^2}{2m} - \frac{q}{m}\boldsymbol{p}\boldsymbol{A}(\boldsymbol{r},t) + \frac{q^2}{2m}\boldsymbol{A}(\boldsymbol{r},t)^2 + q\phi(\boldsymbol{r},t) \tag{2.65}$$

$$= \mathcal{H}_0 + \mathcal{H}_{int}, \tag{2.66}$$

where $\mathcal{H}_0 = \frac{p^2}{2m}$ and

$$\mathcal{H}_{int} = \frac{q}{m}\boldsymbol{p}\boldsymbol{A}(\boldsymbol{r},t) + \frac{q^2}{2m}\boldsymbol{A}(\boldsymbol{r},t)^2 + q\phi(\boldsymbol{r},t) \tag{2.67}$$

$$\approx \frac{q}{m}\boldsymbol{p}\boldsymbol{A}(\boldsymbol{r},t). \tag{2.68}$$

We have neglected the diamagnetic term $\sim \boldsymbol{A}^2$ as we are only considering small fields. Furthermore, the term $q\phi$ only creates a global phase and thus can be ignored.

If the wavelength of the field photons is much larger than the relevant distances ($\boldsymbol{kr} \ll 1$), we can approximate the electromagnetic field's spacial component as constant $e^{i\boldsymbol{kr}} \approx 1$ (dipole approximation). The interaction Hamiltonian is then given by the dipole interaction

$$\mathcal{H}_{\text{int}} = -\boldsymbol{d}\boldsymbol{E}(t), \tag{2.69}$$

where $\boldsymbol{d} = q\boldsymbol{r}$ is the dipole moment of the qubit.

We consider a single mode cavity field (Eq. 2.41) of

$$\boldsymbol{E} = E_0 \left(\boldsymbol{a} + \boldsymbol{a}^\dagger\right) \sin(kz), \tag{2.70}$$

leading to an interaction of

$$\mathcal{H}_{\text{int}} = \boldsymbol{d}\lambda \left(\boldsymbol{a} + \boldsymbol{a}^\dagger\right) \tag{2.71}$$

with $\lambda = -E_0 \sin(kz)$.

We introduce the raising and lowering operators of the qubit

$$\sigma_+ = |e\rangle\langle g|, \tag{2.72}$$

$$\sigma_- = |g\rangle\langle e| = \sigma_+^\dagger, \tag{2.73}$$

which obey the Pauli spin algebra.

For the dipole operator, it holds that $\langle e|\boldsymbol{d}|g\rangle = \langle g|\boldsymbol{d}|e\rangle = 0$ because the operator changes sign under parity and parity is conserved in the electromagnetic interaction. Thus only the off-diagonal elements are non-zero and the dipole operator can be expressed as

$$\boldsymbol{d} = d|g\rangle\langle e| + d^*|e\rangle\langle g| = d\sigma_- + d^*\sigma_+, \tag{2.74}$$

which leads to

$$\mathcal{H}_{\text{int}} = \hbar g \left(\boldsymbol{\sigma}_+ + \boldsymbol{\sigma}_-\right) \left(\boldsymbol{a} + \boldsymbol{a}^\dagger\right) \tag{2.75}$$

with $g = d\lambda/\hbar$ as the coupling between the qubit and the electric field with $d = \langle e|\boldsymbol{d}|g\rangle = d^*$ as the qubit dipole moment.

The operators of both, the qubit and the resonator field, evolve as plane waves with ω_0 and ω_r respectively. Hence, we can employ the rotating wave approximation and eliminate the counter-rotating terms $\boldsymbol{\sigma}_+\boldsymbol{a}, \boldsymbol{\sigma}_-\boldsymbol{a}$ which gives

$$\mathcal{H}_{\text{int}} = \hbar g \left(\boldsymbol{\sigma}_+\boldsymbol{a} + \boldsymbol{\sigma}_-\boldsymbol{a}^\dagger\right). \tag{2.76}$$

The total Hamiltonian, that describes the qubit-cavity system, known as the Jaynes-Cummings Hamiltonian, then follows to

$$\begin{aligned}\mathcal{H} &= \mathcal{H}_\text{Q} + \mathcal{H}_\text{HO} + \mathcal{H}_{\text{int}} \\ &= \frac{\hbar\omega_0}{2}\sigma_z + \hbar\omega_\text{r}\left(\boldsymbol{a}^\dagger\boldsymbol{a} + \frac{1}{2}\right) + \hbar g\left(\boldsymbol{\sigma}_+\boldsymbol{a} + \boldsymbol{\sigma}_-\boldsymbol{a}^\dagger\right).\end{aligned} \tag{2.77}$$

When analysing the interaction between the qubit and the cavity we need to take into account the dissipation in the system (Fig. 2.13a). Firstly, the cavity states decay with rate $\kappa\omega_\text{r}/Q_\text{tot}$, where $\kappa = \kappa_\text{c} + \kappa_\text{L}$, caused by the coupling of the cavity to the continuum. Secondly, the qubit's coupling to modes other than the cavity mode

leads to a decay of rate γ. These effects can be included by a master equation approach. However, here we will only consider stationary dynamics when the number of excitations in the system remains constant, following Ref. [54].

In the basis of the uncoupled states

$$|\Psi_{1n}\rangle = |e\rangle|n\rangle, \tag{2.78}$$
$$|\Psi_{2n}\rangle = |g\rangle|n+1\rangle \tag{2.79}$$

we calculate the eigenvalues to

$$E_{\pm}(n) = (n+1)\,\hbar\omega_{\mathrm{r}} \pm \hbar\Omega_n(\Delta) \tag{2.80}$$

with $\Omega_n(\Delta) = \sqrt{\Delta^2 + 4g^2(n+1)}/2$ as the Rabi frequency, where $\Delta = \omega_0 - \omega_{\mathrm{r}}$ is the detuning between the qubit and the cavity. The corresponding eigenstates (also called the dressed states or Jaynes Cummings doublet) are

$$|n,+\rangle = \cos(\Phi_n)|\Psi_{1n}\rangle + \sin(\Phi_n)|\Psi_{2n}\rangle, \tag{2.81}$$
$$|n,-\rangle = -\sin(\Phi_n)|\Psi_{1n}\rangle + \cos(\Phi_n)|\Psi_{2n}\rangle \tag{2.82}$$

with $\Phi_n = \tan^{-1}\left(\frac{\Omega_n(0)}{\Delta}\right)/2$. The two states are split by the Rabi frequency due the AC Stark shift of the resonator.

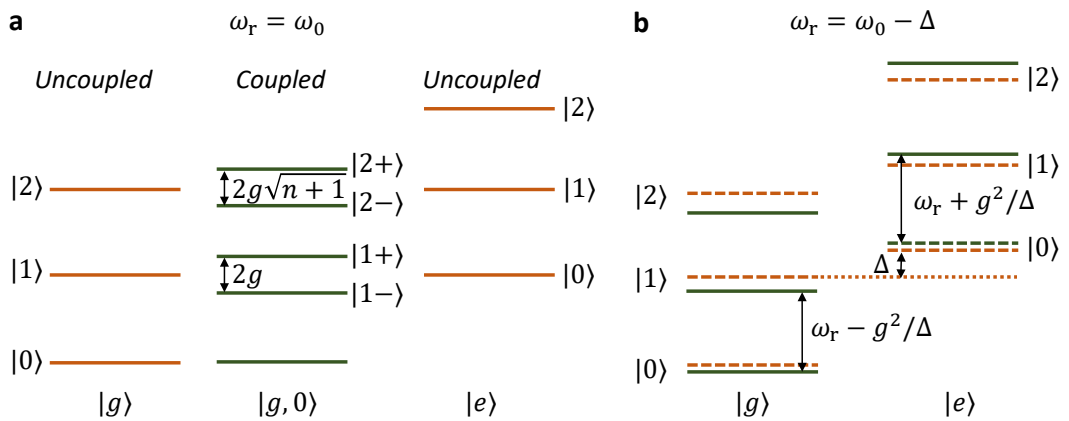

FIGURE 2.13: **Jaynes-Cummings ladder.** **a** Energy levels of the uncoupled (left and right) and dressed (center) qubit-photon states when the qubit and the resonator are in resonance ($\Delta = 0$). The coupling g between the qubit and the resonator lifts the degeneracy of the uncoupled states by $2g\sqrt{n+1}$. **b** Energy levels of the uncoupled (orange lines) and the perturbed states in the dispersive regime. The resonator energy levels are shifted, depending on the qubit state by $\pm g^2/\Delta$.

When the qubit and the resonator are in resonance ($\Delta = 0$), the uncoupled states are degenerate. However, the dressed states are split by $2g\sqrt{n+1}$ due to the qubit-photon interaction (Fig. 2.13a). The splitting increases for an increasing photon number n, making the level spacing anharmonic. This causes non-linear effects at high drive powers when the average photon number in the resonator is large $\langle n\rangle > 1$. In the single photon limit, the eigenstates are maximally entangled and form the dressed states $|0,\pm\rangle = (|e,0\rangle \pm |g,1\rangle)/\sqrt{2}$. An initial state with an excited qubit and zero photons $|e,0\rangle$ evolves into a photon and a qubit in the ground state $|g,1\rangle$ and then back, at the vacuum Rabi frequency $\frac{g}{\pi}$. As one excitation is shared between the qubit and the photon, the decay rate of $|0,\pm\rangle$ is $b = \frac{\kappa+\gamma}{2}$. The pair of states $|0,\pm\rangle$

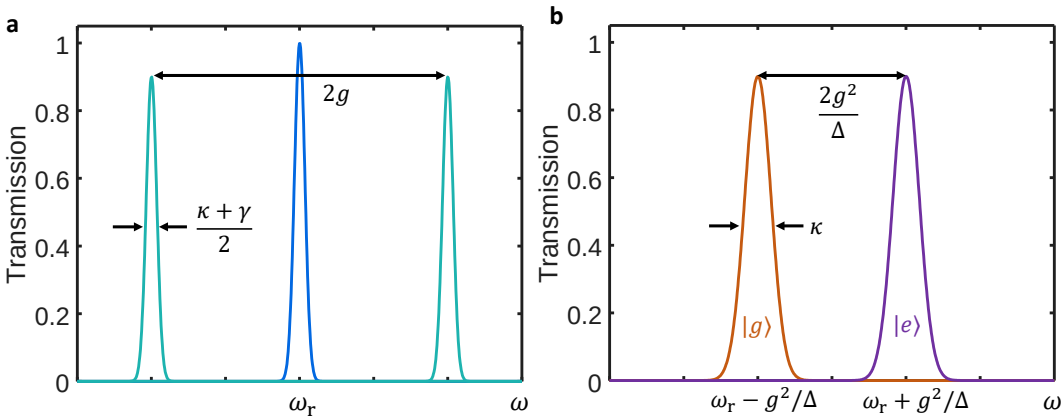

FIGURE 2.14: **Transmission spectrum of the resonator in the strong coupling and dispersive regime. a** When the resonator and the qubit are in resonace ($\omega_r = \omega_0$) the resonance is split into two peaks, separated by twice the coupling strength $2g$. They can be resolved when the qubit and the resonator are in the strong coupling regime with $g \gg \kappa, \gamma$. **b** In the dispersive regime $g \ll \Delta$ when the resonator and the qubit are far detuned, the resonance is AC Stark shifted depending on the qubit state.

can be resolved in the transmission or reflection of the cavity if their splitting $2g$ is larger than the linewidth b (Fig. 2.14a). The coupling strength g is determined by the strength of the transition dipole moment d and the rms zero-point electric field of the resonator mode E_{rms}. Strong coupling is achieved when $g \gg \kappa, \gamma$.

When the detuning is large, such that direct qubit transitions do not occur and only dispersive interactions between the qubit and the cavity field are allowed, we speak of the dispersive regime with $g \ll \Delta$. A Taylor expansion of Eq. (2.80) gives

$$E_{\pm}(n) = \left(n + \frac{1}{2}\right)\hbar\omega \pm \hbar\Delta\left(1 + \frac{2g^2(n+1)}{\Delta^2} + \ldots\right). \tag{2.83}$$

This expansion breaks down when n approaches the critical photon number $n_{\text{crit}} = \frac{\Delta^2}{4g^2}$, setting an upper limit for the photon number in the dispersive regime. The corresponding eigenstates are

$$|n,-\rangle = |g,n\rangle - \frac{g\sqrt{n}}{\Delta}|e,n-1\rangle, \tag{2.84}$$

$$|n,+\rangle = \frac{g\sqrt{n}}{\Delta}|g,n\rangle + |e,n-1\rangle \tag{2.85}$$

and the decay rates

$$\Gamma_{n,-} \approx \kappa - \frac{g\sqrt{n}}{\Delta}\gamma, \tag{2.86}$$

$$\Gamma_{n,+} \approx \frac{g\sqrt{n}}{\Delta}\kappa + \gamma. \tag{2.87}$$

For small $\frac{g}{\Delta}$, the coupling between the qubit and the cavity can be treated as a perturbation. Applying the uniform transformation

$$\boldsymbol{U} = \exp\left[\frac{g}{\Delta}\left(\boldsymbol{a}\sigma_+ - \boldsymbol{a}^\dagger\sigma_-\right)\right] \tag{2.88}$$

yields the perturbed Hamiltonian

$$\mathcal{H}' = \boldsymbol{U}\mathcal{H}\boldsymbol{U}^\dagger \approx \hbar\left[\omega_\mathrm{r} + \frac{g^2}{\Delta}\boldsymbol{\sigma}_z\right]\boldsymbol{a}^\dagger\boldsymbol{a} + \frac{\hbar}{2}\left[\omega_0 + \frac{g^2}{\Delta}\right]\boldsymbol{\sigma}_z. \tag{2.89}$$

We can interpret the perturbation as an AC Stark shift of the qubit transition by $\frac{g^2}{\Delta}(n+\frac{1}{2})$ or a dispersive shift of the resonator resonance by $\pm\frac{g^2}{\Delta}$, depending on the qubit state (Fig. 2.13b, 2.14b).

Chapter 3

The flip-flop qubit

"Physics is the only profession in which prophecy is not only accurate but routine. "
–Neil deGrasse Tyson

Building a quantum computer in silicon demands high-fidelity, low power long-distant qubit interactions. In this chapter we introduce the flip-flop qubit, a combination of the electron-nuclear spin states of a phosphorus donor that can be controlled by microwave electric fields and meets these demands. A second-order electric dipole-dipole interaction allows for robust two-qubit coupling at separations of hundreds of nanometers. Moreover, it enables coupling to microwave resonators that can extend qubit entanglement to macroscopic distances. We predict gate fidelities within fault-tolerance thresholds using realistic noise models, opening up a pathway to a scalable silicon quantum computer.

A condensed version of the work presented in this chapter has been published in:
G. Tosi, F. A. Mohiyaddin, V. Schmitt, **S. Tenberg**, R. Rahman, G. Klimeck, A. Morello. "Silicon quantum processor with robust long-distance qubit couplings", *Nature communications* Vol. 8, 450 (2017).

The author acknowledges G. Tosi for the conception of the idea and large parts of the simulation work, F. A. Mohiyaddin for tight-binding simulations and electric modelling and V. Schmitt for assistance with pulse shaping and noise influences. The author helped develop the project, interpret the results, assisted with simulations and constructed parts of the theoretical framework.

3.1 Introduction

To successfully implement quantum algorithms, a quantum processor has to be able to run quantum error correction codes [55] that deal with the fragile nature of qubits (see Sec. 5.1). The highest tolerances in error rates of 10^{-3} to 10^{-2} are found when using nearest-neighbour topological codes [56], [57], long-distance entanglement links [58] or a combination of both [59]. Therefore a large number of qubits have to be constructed in expandable arrays to form a scalable, universal quantum processor.

To implement such a quantum processor, one not only needs excellent single qubits but also two-qubit logic gates that posses fault-tolerant fidelities and allow for the interconnection of many qubits.

Silicon is a desirable platform for qubits due to its connection to the Metal-Oxide-Semiconductor (MOS) industry and the nanometric qubit unit size [17]. Single qubits with high state preservation and precise qubit control have been established in silicon for many different physical systems such as donor spin ensembles [60], MOS quantum dots [25], SiGe quantum dots [27], [61] and phosphorus donors [42], [47]. While two-qubit gates have been performed [26], [62]–[64], fault-tolerance has not yet been demonstrated.

Out of these different silicon qubit approaches, donor spin qubits are especially appealing as they are extremely well isolated from their environment. By using isotopically enriched ^{28}Si as the substrate material [65], coherence times can reach around a second (for the electron) and a minute (for the nucleus) [30], up to hours in bulk ensembles [60], and control error rates as small as 10^{-4} [42]. However, integrating several of these qubits in a scalable architecture remains a formidable challenge - their good isolation is here a major drawback as it makes reliable two-qubit gates difficult to achieve.

The seminal Kane proposal [22] for a nuclear-spin quantum computer in silicon described the use of short-range exchange interactions J between donor-bound electrons, to mediate an effective inter-nuclear coupling of order $\sim$ 100 kHz at a $\sim$ 15 nm distance. The exchange interaction has an exponential and oscillatory spatial behaviour that can result in an order of magnitude variation in strength upon displacement by a single lattice site [66], [67]. Notwithstanding, plenty of research has explored the inter-donor exchange [68]–[70] and recently a two-qubit gate has been achieved in donor devices fabricated with scanning tunnelling microscopy (STM) lithography [63]. Nevertheless, the stringent requirements of the donor placement make large-scale device fabrication extremely difficult. Slightly relaxed requirements on donor placement can be found when using a hyperfine-controlled exchange interaction between electron spin qubits [71], or a slower magnetic dipole-dipole coupling effective at $\sim$ 30 nm distances [72]. Other proposals space donors further apart by introducing some intermediate coupler, *e.g.* donor chains [73], [74], charge-coupled devices [75], ferromagnets [76], probe spins [77] or quantum dots [78].

Our proposal, presented in this chapter, to avoid the issues related to using the exchange coupling for two-qubit gates, is to employ electric dipole-dipole coupling instead. Not only is this interaction robust against imprecise donor placement but it also allows for fast, fault-tolerant two-qubit gates at spacings of $150 - 500$ nm. This distance leaves sufficient space to intersperse classical control and readout devices, while retaining some of the compactness of atomic-size qubits, making it ideal for a large quantum processor.

To create an electric dipole for the phosphorus donor qubit and make it accessible to electric fields, we introduce a new type of qubit, the flip-flop qubit.

3.2 A new electrically accessible qubit, the flip-flop qubit

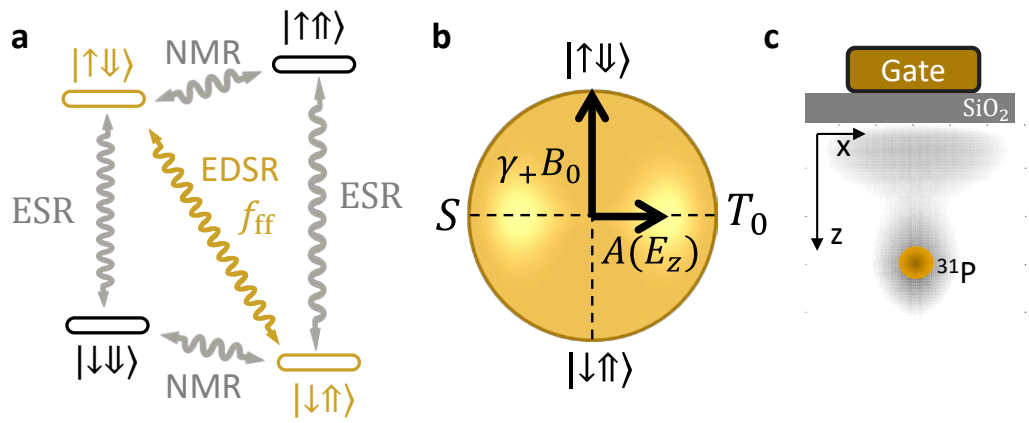

FIGURE 3.1: **Coupling donor spin qubits to electric fields via hyperfine modulation. a** Level diagram of the electron-nucleus spin states in an external magnetic field B_0 with the magnetic transitions (ESR, NMR) and the electric flip-flop transition (EDSR) indicated. The flip-flop basis is coloured in yellow. **b** Bloch sphere of a flip-flop spin qubit in an external magnetic field B_0 coupled to a vertical electric field E_z via the hyperfine interaction A. Electron-nuclear singlet and triplet states are denoted by $S = (|\downarrow\Uparrow\rangle - |\uparrow\Downarrow\rangle)/\sqrt{2}$ and $T_0 = (|\downarrow\Uparrow\rangle + |\uparrow\Downarrow\rangle)/\sqrt{2}$. **c** Donor qubit where a vertical electric field supplied by a metallic gate modifies the hyperfine interaction.

The new qubit is based on the phosphorus donor qubit (Sec. 2.3, Fig. 3.1a). Instead of encoding the quantum information in just the electron or the nuclear spin and control the qubit with magnetic resonance (ESR, NMR), we define a new qubit with the anti-aligned electron-nuclear spin states $\{|\downarrow\Uparrow\rangle, |\uparrow\Downarrow\rangle\}$ as the basis, the flip-flop qubit. The transition between these two eigenstates is not magnetically accessible as the total z-angular momentum is constant. However, the hyperfine interaction A is a transverse term in the flip-flop basis since its eigenstates are $S = (|\downarrow\Uparrow\rangle - |\uparrow\Downarrow\rangle)/\sqrt{2}$ and $T = (|\downarrow\Uparrow\rangle + |\uparrow\Downarrow\rangle)/\sqrt{2}$ (Fig. 3.1b). Therefore, modulating A at frequency

$$\epsilon_{\mathrm{ff}}(A)/h = \sqrt{(\gamma_+ B_0)^2 + A^2}, \tag{3.1}$$

corresponding to the flip-flop qubit energy splitting ϵ_{ff}, causes an electric dipole spin resonance (EDSR) transition between the $|\downarrow\Uparrow\rangle, |\uparrow\Downarrow\rangle$ basis states (Fig. 3.1a).

We can modify A by applying an electric field. For a donor in silicon, A is dominated by the Fermi contact hyperfine interaction between the electron and the nucleus which depends on the overlap of the electron wave function Ψ with the nucleus. The overlap can be altered by applying an electric field on the donor that pulls the electron away from the donor to the Si/SiO_2 interface, where the electron then behaves like a quantum dot after ionization (Fig. 3.1c, see also Sec. 2.3.1). The electron charge position is described by its orbital degree of freedom. In this way, the electric field couples the orbital degree of freedom to the spin states via the hyperfine interaction - an artificial spin-orbit coupling is created which can be employed to drive flip-flop qubit transitions.

3.2.1 Manipulating the orbital degree of freedom: the charge qubit

When the electron is at the donor, the ground orbital wavefunction $|d\rangle$ is a symmetric combination of the six valleys $k_{\pm x}$, $k_{\pm y}$, $k_{\pm z}$ (A_1 like, see Sec. 2.2). The next excited valley-orbit states (T_2 like) are split off by 11 meV and thus can be neglected.

When a strong electric field with potential $V_E = E_z r$ is applied on the donor, the conduction band edge is lowered and a triangular quantum well is formed at the Si/SiO_2 interface in which the electron is confined, a quantum dot is formed (inset Fig. 3.2). The applied electric fields split off the $k_{\pm x}, k_{\pm y}$ valleys so that the wave function is composed of z valleys $k_{\pm z}$, where the remaining two-fold degeneracy is lifted by the abrupt potential of the interface into a lower valley $|i\rangle$ and a higher valley $|v\rangle$, separated by the valley splitting V_s. The remainder of the excited donor and dot states are well above the ground states by several meV [79], [80]. Thus, close to electric field where the donor electron is ionized from the donor E_z^0 (ionization point), the lowest-energy states of the system are $|d\rangle$, $|i\rangle$, $|v\rangle$.

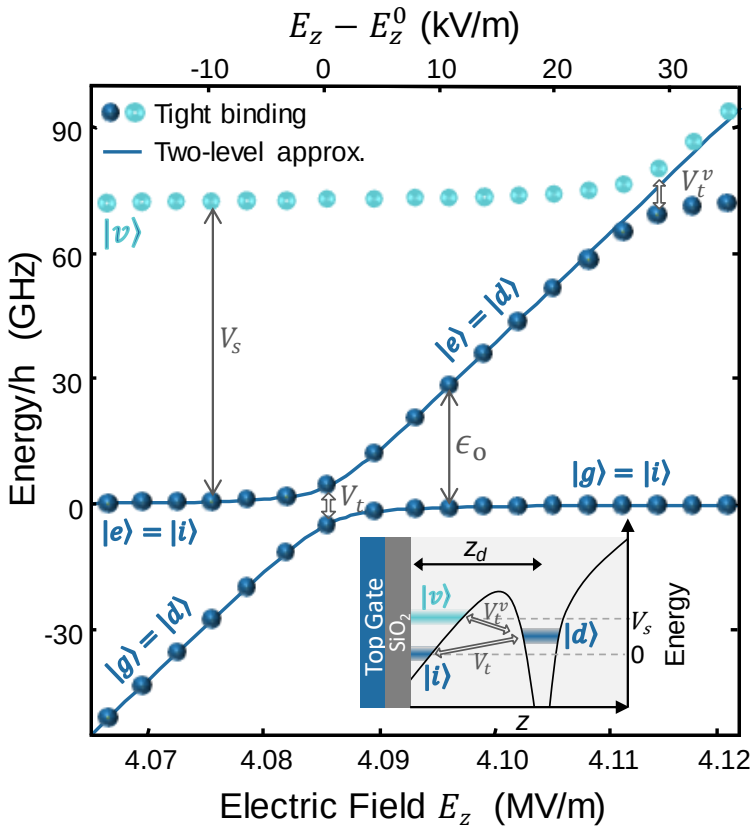

FIGURE 3.2: **Orbital and valley states.** The lowest orbital energy levels of the donor-interface system, with respect to the lower valley interface state $|i\rangle$ (set as the zero-energy reference). The donor is assumed $z_d = 15.2$ nm below a Si/SiO_2 interface. The dots correspond to the energy levels obtained from a full-scale tight-binding calculation with NEMO-3D. Solid lines represent the energy levels obtained from the two level charge qubit approximation (Eq. 3.2). Inset: Potential profile as a function of depth, illustrating the donor $|d\rangle$, lower $|i\rangle$ and upper $|v\rangle$ valley interface states. The donor ground state is tunnel-coupled to the lower and upper valley interface states by V_t and V_t^v respectively.

These levels can be computed with atomistic tight binding calculations using the package NEMO-3D [81], [82]. Fig. 3.2 shows the dependence of the energy levels on the applied electric field E_z with the dots indicating the tight binding simulations,

calculated with a donor depth $z_d = 15.2\,\text{nm}$ below the Si/SiO_2 interface and the donor biased close to ionization.

We find that the electron orbital degree of freedom can be approximated by a two-level system, a charge qubit, with ground state $|g\rangle$ and excited state $|e\rangle$. These charge qubit eigenstates are combinations of the donor ground state $|d\rangle$ and the lower valley interface state $|i\rangle$ which are coupled by the tunnel coupling V_t. This approximation holds as long as the third valley state $|v\rangle$ can be neglected.

When $E_z \ll E_z^0$, the charge qubit ground state $|g\rangle$ consists of the electron wavefunction being localized at the donor, $|d\rangle$, whereas the first excited state $|e\rangle$ corresponds to the lower valley interface state $|i\rangle$. With increasing E_z, the two states approach and anti-cross at the ionization point $E_z = E_z^0$ due to V_t. For $E_z \gg E_z^0$, $|d\rangle$ is the excited state, until it eventually anti-crosses with the upper valley interface state $|v\rangle$ at an electric field of E_z^v, where the two-level approximation breaks down.

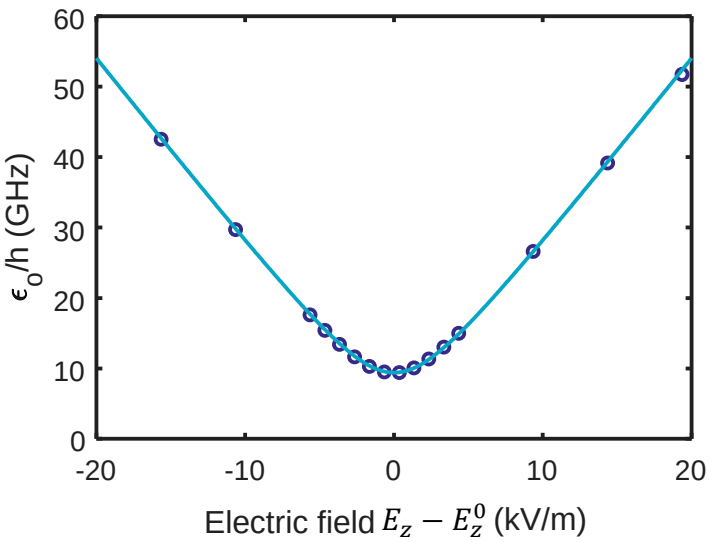

FIGURE 3.3: **Charge qubit dispersion relation.** Charge qubit dispersion relation ϵ_o as a function of vertical electric field E_z, for $V_t/h = 9.3\,\text{GHz}$, $d = 11\,\text{nm}$ and $E_z^0 = 4.0856\,\text{MV/m}$. The dots are obtained by NEMO-3D full-scale tight binding simulation while the line corresponds to the two-level charge-qubit approximation (Eq. 3.3).

Choosing $|d\rangle = \begin{pmatrix} 0 \\ 1 \end{pmatrix}, |i\rangle = \begin{pmatrix} 1 \\ 0 \end{pmatrix}$ as the basis states, we can describe the charge qubit with the Hamiltonian

$$\mathcal{H}_{\text{orb}} = \frac{V_t \sigma_x - \left[e(E_z - E_z^0)d\right] \sigma_z}{2} \tag{3.2}$$

(eigenvalues are shown as solid lines in Fig. 3.2) with a transition energy (Fig. 3.3) of

$$\epsilon_o = \sqrt{V_t^2 + \left[e(E_z - E_z^0)d\right]^2}, \tag{3.3}$$

where d is the length of the induced dipole which represents the separation between the center-of-mass positions of the donor $|d\rangle$ and interface $|i\rangle$ orbitals. For the case of $z_d = 15.2\,\text{nm}$, we find $V_t/h = 9.3\,\text{GHz}$, $E_z^0 = 4.0856\,\text{MV/m}$ and $d = 11\,\text{nm}$, which is expectedly lower than the donor depth z_d.

The charge qubit eigenstates can be expressed as (see App. A for the derivation)

$$|e\rangle = \beta\,|i\rangle + \alpha\,|d\rangle = \begin{pmatrix}\beta\\ \alpha\end{pmatrix}, \tag{3.4a}$$

$$|g\rangle = -\alpha\,|i\rangle + \beta\,|d\rangle = \begin{pmatrix}-\alpha\\ \beta\end{pmatrix} \tag{3.4b}$$

with

$$\alpha = \frac{\phi}{\sqrt{1+\phi^2}}, \tag{3.5a}$$

$$\beta = \frac{1}{\sqrt{\phi^2+1}}, \tag{3.5b}$$

where

$$\phi = \frac{\left(E_z - E_z^0\right) ed + \epsilon_0}{V_t}. \tag{3.6}$$

At E_z^0, we find

$$|e_i\rangle = \frac{1}{\sqrt{2}}\left(|i\rangle + |d\rangle\right) = \frac{1}{\sqrt{2}}\begin{pmatrix}1\\ 1\end{pmatrix}, \tag{3.7a}$$

$$|g_i\rangle = \frac{1}{\sqrt{2}}\left(|i\rangle - |d\rangle\right) = \frac{1}{\sqrt{2}}\begin{pmatrix}1\\ -1\end{pmatrix}, \tag{3.7b}$$

when $\epsilon_0 = V_t$.[1]

The interaction between a ^{31}P donor electron and an electron in a MOS quantum dot has been demonstrated in Ref. [83] for a two electron system, where a qubit was encoded in the spin singlet and triplet states. The tunnel coupling of the singlet and triplet was measured to 4.6 GHz and 7.5 GHz respectively. Even though these tunnel couplings do not directly correspond to the single electron tunnel coupling of our charge qubit, they give a good indication and are similar to the estimates of our model.

3.2.2 Modulating the hyperfine interaction

The state of the charge qubit affects the effective electron-nuclear hyperfine interaction, since it depends on the overlap of the electron wavefunction at the nuclear site. The hyperfine interaction is maximum when the charge qubit is in state $|d\rangle$ (electron fully on the donor), and drops to zero when the charge qubit is in state $|i\rangle$ (electron fully displaced at the interface dot). Thus, we can describe the orbital dependent hyperfine Hamiltonian as

$$\mathcal{H}_A^{\text{orb}} = hA\left(\frac{1-\sigma_z}{2}\right)\mathbf{S}\cdot\mathbf{I}. \tag{3.8}$$

We determine the effective hyperfine strength with applied electric field with tight-binding simulations (dots in Fig. 3.4). Our two-level approximation yields good agreement with these simulations when we calculate the expectation value of

[1] One can also express the charge qubit in the basis of $|g_i\rangle, |e_i\rangle$. Therefore, we apply the unitary transformation $\boldsymbol{U} = \frac{1}{2}\left(\sigma_z + \sigma_x\right) = \frac{1}{2}\begin{pmatrix}1 & 1\\ 1 & -1\end{pmatrix}$. This transforms any operator $\boldsymbol{O}$ to $\boldsymbol{O}' = \boldsymbol{U}^\dagger \boldsymbol{O}\boldsymbol{U}$, giving $\sigma_z \to -\sigma_x$ and $\sigma_x \to \sigma_z$.

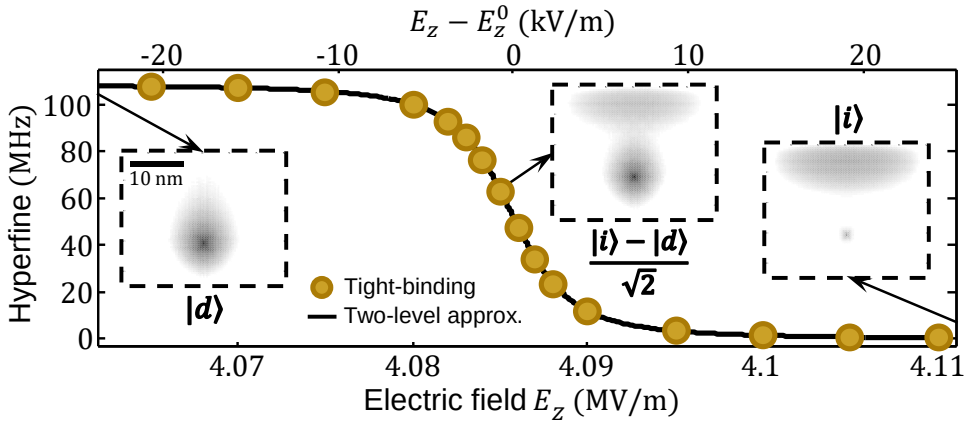

FIGURE 3.4: **Hyperfine interaction change with electric field.** Atomistic tight-binding simulations [81], [82] (dots) of the effective electron-nucleus hyperfine interaction for $z_d = 15.2\,\text{nm}$, as a function of vertical electric field. The solid line is a fit using the simplified two-level Hamiltonian $\mathcal{H}_{\text{orb}} + \mathcal{H}_A^{\text{orb}}$. The insets show the electron ground-state wavefunction $|g\rangle$ for three different vertical electric fields.

$\mathcal{H}_A^{\text{orb}}$ (line in Fig. 3.4) for the charge qubit ground state $|g\rangle$

$$\begin{aligned} A(E_{\text{dc}}) &= \langle g|A\left(\frac{1-\sigma_z}{2}\right)|g\rangle \\ &= A|\beta|^2 \\ &= \frac{A}{2}\left(1 - \frac{e\left(E_z - E_z^0\right)d}{\epsilon_0}\right). \end{aligned} \tag{3.9}$$

To find the spin-orbit coupling between the charge qubit and the flip-flop spin states $|\downarrow\Uparrow\rangle$, $|\uparrow\Downarrow\rangle$, we calculate the matrix transition element

$$\begin{aligned} g_{\text{so}} &= \langle g\uparrow\Downarrow|H_A^{\text{orb}}|e\downarrow\Uparrow\rangle \\ &= \frac{A}{4}\langle g|\sigma_z|e\rangle \\ &= A\alpha\beta \\ &= \frac{hA}{4}\frac{V_t}{\epsilon_0}. \end{aligned} \tag{3.10}$$

As $V_t = \epsilon_0$ at the ionization point, the coupling is the strongest there, allowing for fast driving.

Here we have assumed that the hyperfine coupling between the electron spin and ^{31}P nucleus is purely isotropic [84], i.e. dominated by the Fermi contact hyperfine term. This assumption may no longer exactly hold when the donor electron wave function is distorted from its spherical symmetry in the presence of the strong vertical electric field, whereby a small dipolar component can be created (a related case, where the electron is shared between two proximal phosphorus donors, has been recently studied [85]). However, it is known that the Fermi contact component of the hyperfine coupling for donors in silicon is always the dominant term. This holds even for an electron centred on a phosphorus donor, coupled to ^{29}Si nuclei which are placed off-center with respect to the symmetry point of the wavefunction [86]. Therefore, we expect the isotropic approximation to capture the main physics of the problem.

3.2.3 The flip-flop qubit

To lift the degeneracy of the spin states, we apply an external magnetic field B_0. The Zeeman energy splitting of the electron and nuclear spins depends on the respective gyromagnetic ratio γ. However, the electron gyromagnetic ratio γ_e changes when the electron is confined at the Si/SiO_2 interface, up to $\Delta_\gamma = 0.7\%$ from the donor-bound electron [79]. We include this change in the Zeeman Hamiltonian

$$\mathcal{H}_{B_0}^{\text{orb}} = \gamma_e h B_0 \left[1 + \left(\frac{1+\sigma_z}{2}\right)\Delta_\gamma\right] S_z - \gamma_n h B_0 I_z. \tag{3.11}$$

Hence, the full physics - orbital and spin effects - of the flip-flop qubit, are described by the Hamiltonian

$$\mathcal{H}_{\text{ff}} = \mathcal{H}_{B_0}^{\text{orb}} + \mathcal{H}_A^{\text{orb}} + \mathcal{H}_{\text{orb}}. \tag{3.12}$$

The flip-flop qubit system is composed of three degrees of freedom: charge, electron spin and nuclear spin. This results in an eight-dimensional Hilbert space

$$\mathbb{H}_{\text{ff}} = \mathbb{H}_{\text{orb}} \otimes \mathbb{H}_{\text{e}} \otimes \mathbb{H}_{\text{n}} \tag{3.13}$$

with the basis states of the uncoupled charge, electron and nuclear system $\{|g\rangle, |e\rangle\} \otimes \{|\Uparrow\rangle, |\Downarrow\rangle\} \otimes \{|\uparrow\rangle, |\downarrow\rangle\}$. As long as the Zeeman energy exceeds the hyperfine coupling, characterized by $A/4$, the latter is a perturbation only and the energy eigenstates of $\mathcal{H}_{\text{ff}}$ remain the approximate products of the uncoupled basis states.

To calculate the flip-flop qubit transition energy we numerically determine the eigenvectors of $\mathcal{H}_{\text{ff}}$ and find the ones with the largest overlap to the flip-flop states $|g \Downarrow\uparrow\rangle, |g \Uparrow\downarrow\rangle$ where the charge qubit remains unexcited. We then compute the flip-flop qubit transition energy by calculating the difference of the corresponding eigenvalues (yellow line in Fig. 3.5).

When we compare these results to the bare flip-flop energy $\epsilon_{\text{ff}}(A, \gamma_e)$ (Eq. 3.1, dotted grey in Fig. 3.5) we find a large deviation around the ionization point. $\epsilon_{\text{ff}}(A, \gamma_e)$ shows a steep slope, mostly caused by the E_z-dependence of γ_e as $\gamma_+ B_0 \gg A$, while $\mathcal{H}_{\text{ff}}$ sees a dip. This dip is a dispersive shift of the flip-flop transition for $V_t > \epsilon_{\text{ff}}$ as the charge qubit states $|g\rangle, |e\rangle$ and the flip-flop spin states $|\downarrow\Uparrow\rangle, |\uparrow\Downarrow\rangle$ are detuned by

$$\delta_{\text{so}} = \epsilon_{\text{o}} - \epsilon_{\text{ff}} \tag{3.14}$$

(inset Fig. 3.5) but transversely coupled by the hyperfine interaction with g_{so}.

For small detuning, the coupling hybridizes the charge and spin states (Fig. 3.6) where the ground state and two hybridized charge-spin excited states are given by

$$|\tilde{g}\rangle = |g \downarrow\Uparrow\rangle, \tag{3.15a}$$
$$|\tilde{e}_1\rangle = \beta_{\text{so}} |g \uparrow\Downarrow\rangle + \alpha_{\text{so}} |e \downarrow\Uparrow\rangle, \tag{3.15b}$$
$$|\tilde{e}_2\rangle = -\alpha_{\text{so}} |g \uparrow\Downarrow\rangle + \beta_{\text{so}} |e \downarrow\Uparrow\rangle \tag{3.15c}$$

with (see App. A)

$$\alpha_{\text{so}} = \frac{1}{\sqrt{1+\phi_{\text{so}}^2}}, \tag{3.16a}$$
$$\beta_{\text{so}} = \frac{\phi_{\text{so}}}{\sqrt{\phi_{\text{so}}^2+1}}, \tag{3.16b}$$

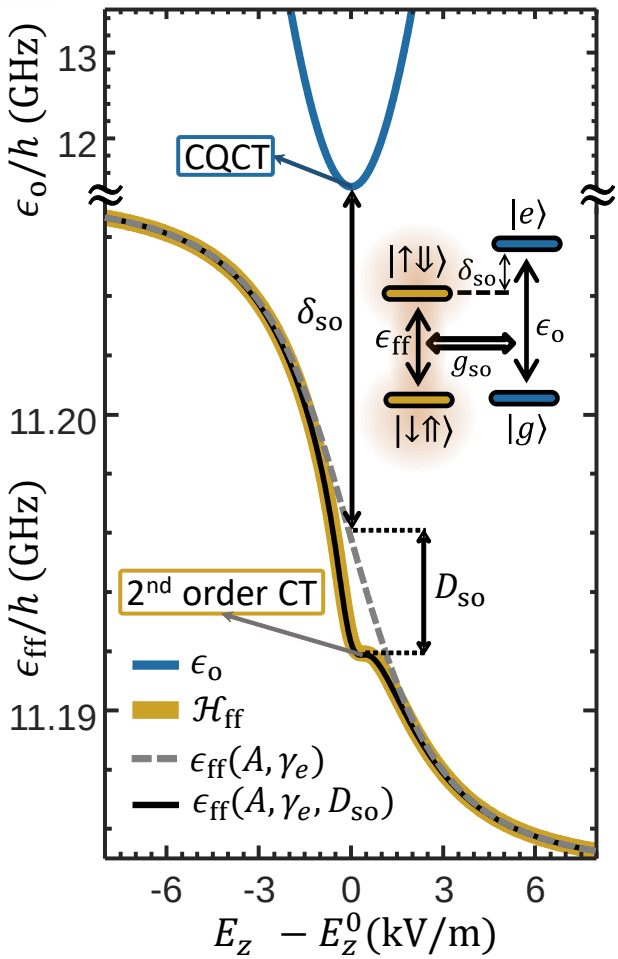

FIGURE 3.5: **Flip-flop qubit dispersion relation.** Charge, ϵ_o, and flip-flop, ϵ_{ff}, qubit transition frequencies as a function of vertical electric field E_z, for $B_0 = 0.4$ T, $A = 117$ MHz, $d = 15$ nm, $\Delta_\gamma = -0.2\%$ and $V_t/h = 11.44$ GHz. The inset shows the level diagram of flip-flop states coupled to charge states. CT stands for 'clock transition' and CQCT for 'charge qubit clock transition'.

where

$$\phi_{so} = \frac{\delta_{so} + \sqrt{\delta_{so}^2 + 4g_{so}^2}}{2g_{so}}. \tag{3.17}$$

For $g_{so} \ll \delta_{so}$, the charge and spin states are dispersively coupled and the flip-flop transition is a second-order process. The dispersive shift of the transition can be calculated with second order perturbation theory to[2]

$$\begin{aligned} D_{so}(E_z) &= \frac{\left|\langle\uparrow\Downarrow g|H_{orb}^A|e\downarrow\Uparrow\rangle\langle e\downarrow\Uparrow|H_{orb}^A|g\uparrow\Downarrow\rangle\right|}{E_{e\downarrow\Uparrow} - E_{g\uparrow\Downarrow}} \\ &= \frac{[g_{so}(E_z)]^2}{\delta_{so}(E_z)}, \end{aligned} \tag{3.18}$$

reducing the flip-flop qubit frequency to

$$\epsilon_{ff}(A, \gamma_e, D_{so}) = \epsilon_{ff}(A, \gamma_e) - D_{so}(E_z), \tag{3.19}$$

[2]Generally, it is expected to observe a dispersive shift of g^2/Δ, where g is the coupling and Δ the detuning, for two coupled systems in the dispersive regime [54]. Compare Sec. 2.4.3 for details.

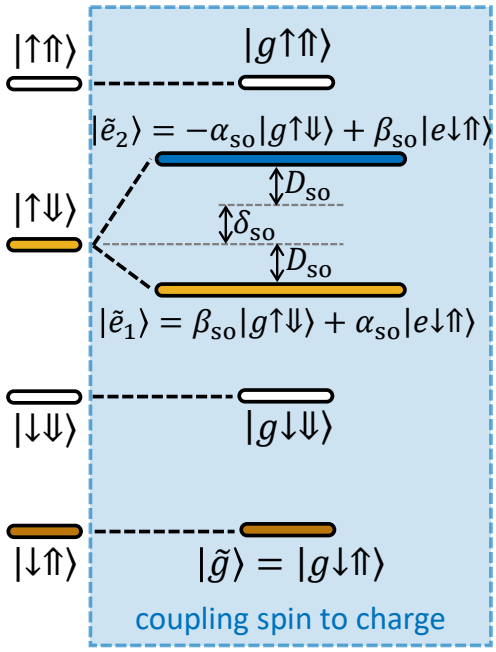

FIGURE 3.6: **Hybridized charge-flip-flop states.** Level diagram showing the hybridization of the charge and flip-flop states due to the coupling g_{so} when the detuning δ_{so} is small.

when the charge qubit is in the ground state.

Around $E_z \approx E_z^0$ the charge qubit comes closest to the flip-flop qubit (Fig. 3.5) while g_{so} is highest. Consequently, $D_{so}(E_z)$ is largest at this point. Eq. (3.19) (thin black line in Fig. 3.5) agrees with the full numerical simulations of the Hamiltonian in Eq. (3.12).

3.3 Decoherence and relaxation due to electrical noise

3.3.1 Dephasing

Since we are coupling the flip-flop spin states to electric fields, the presence of electric noise is a concern for the longevity of our qubit states. Generally, to achieve a high qubit performance one needs a high ratio of qubit coherence time to qubit gate operation time.

For the charge qubit we find that at the ionization point, the transition frequency exhibits a local minimum $\epsilon_0 = V_t$ and is thus first order insensitive to electrical noise $\partial\epsilon_o/\partial E_z = 0$ (Fig. 3.3). Such a tuning point is called a clock transition (CT).

Conveniently, the flip-flop qubit also exhibits a noise insensitive region close to the ionization point. The properties of this region depend on V_t (Fig. 3.7). For low V_t the dispersive shift is strong due to the proximity of the charge qubit and thus creates two first order clock transitions. These merge into one for $V_t/h = 11.44\,\text{GHz}$, which is second-order insensitive to electrical noise $\partial^2\epsilon_{\text{ff}}/\partial E_z^2 = 0$ - dephasing is strongly suppressed at this point. Finally, for high V_t the dispersive shift is not strong enough and does not yield a minimum.

We estimate the dephasing from quasi-static E_z noise. This is noise with a spectral weight centred at frequencies smaller than the qubit resonance and Rabi frequency, that acts on the qubit operators along σ_z. We assume $E_{z,\text{rms}}^{\text{noise}} = 100\,\text{V/m}$ which corresponds to $1.5\,\mu\text{eV}$ charge detuning noise for $d = 15\,\text{nm}$. For details

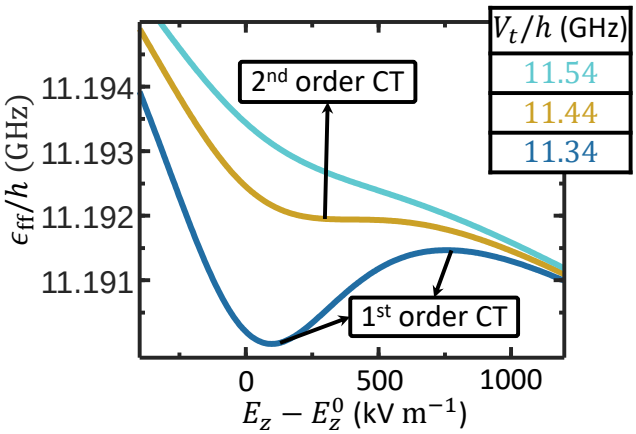

FIGURE 3.7: **Flip-flop dispersion for different tunnel couplings.** E_z-dependence of flip-flop precession frequency for the three indicated tunnel coupling values.

about the noise in the flip-flop devices, consult Sec. 3.7 which discusses the noise effects extensively.

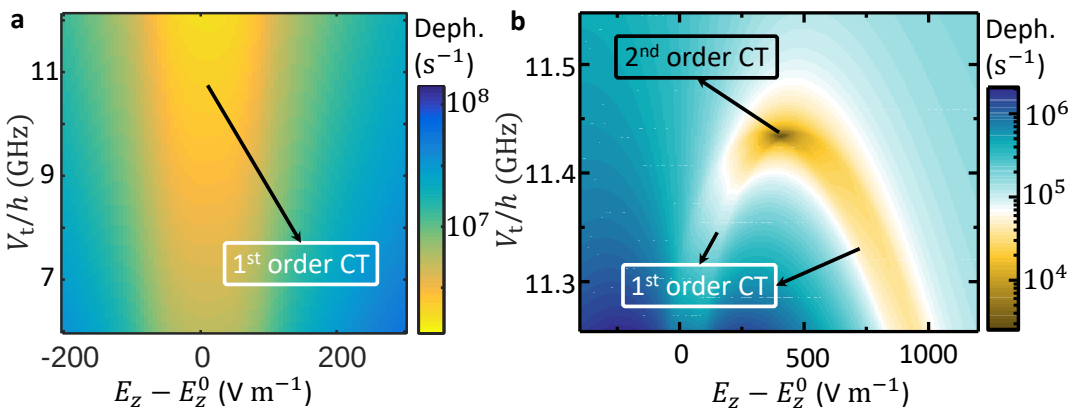

FIGURE 3.8: **Charge and flip-flop qubit dephasing.** Estimated charge (**a**) and flip-flop (**b**) qubit dephasing rate, assuming electric field noise $E_{z,\mathrm{rms}}^{\mathrm{noise}} = 100$ V/m.

To estimate the dephasing resulting from this charge noise, we calculate the difference between the qubit transition frequency ϵ and the transition frequencies ϵ^n that result when applying a uniformly distributed noise in the range $E_z^n = \sqrt{3}[-E_{z,\mathrm{rms}}^{\mathrm{noise}}, E_{z,\mathrm{rms}}^{\mathrm{noise}}]$. This gives

$$\text{Dephasing rate} = \sum_n |\epsilon - \epsilon^n| \, / N_n, \tag{3.20}$$

where N_n is the number of sampled E_z^n and ϵ^n is calculated for each value of E_z^n.

The resulting dephasing rates for both the charge and the flip-flop qubit are shown in Fig. 3.8. We do not intend to operate the charge qubit as its dephasing rate is expected to exceed $10^6\,\mathrm{s}^{-1}$, even at its clock transition. However, for the flip-flop qubit, the dephasing can be as low as $1/T_2^* \approx 3 \times 10^3\,\mathrm{s}^{-1}$ at the second order clock transition. This value is comparable to the dephasing of $1/T_2^* \approx 1 \times 10^3\,\mathrm{s}^{-1}$ of the electron due to magnetic noise from the superconducting magnet which creates B_0 [30].

3.3.2 Relaxation

Relaxation can also inhibit qubit performance (see Sec. 2.3.4). For donors in silicon the electron spin lattice relaxation time is $T_1 > 1\,\mathrm{s}$ due to very weak coupling between the phonons and the spins. However, according to Ref. [87], for the charge and the flip-flop qubit the difference in valley population between the interface and donor state causes an effective electron-phonon coupling which leads to relaxation. Firstly, the relaxation is enhanced by the first excited charge state $|e\rangle$ which creates a strong interaction between the flip-flop qubit and phonon-induced deformation potentials. Secondly, the relaxation is "valley-enhanced" due to the non-trivial valley structure of the electron-phonon interaction and the orbital states.

The charge qubit relaxation rate is given by [87]

$$1/T_{1,\mathrm{c}} = \frac{\Xi_u^2}{60\pi\hbar^4\rho}\left(\frac{2}{3v_l^5}+\frac{1}{v_t^5}\right)\epsilon_o V_t^2, \tag{3.21}$$

where $\Xi_u = 8.77\,\mathrm{eV}$ is the uniaxial deformation potential, $\rho = 2330\,\mathrm{kg/m^3}$ the density of silicon and $v_l = 9330\,\mathrm{m/s}$, $v_t = 5420\,\mathrm{m/s}$ the longitudinal and transverse sound velocity. At the ionization point ($\epsilon_o = V_t$) we find $1/T_{1,c} \approx 0.49 \times 10^6\,\mathrm{s}^{-1}$. The charge qubit relaxation rate increases with higher ϵ_o, away from the clock transition.

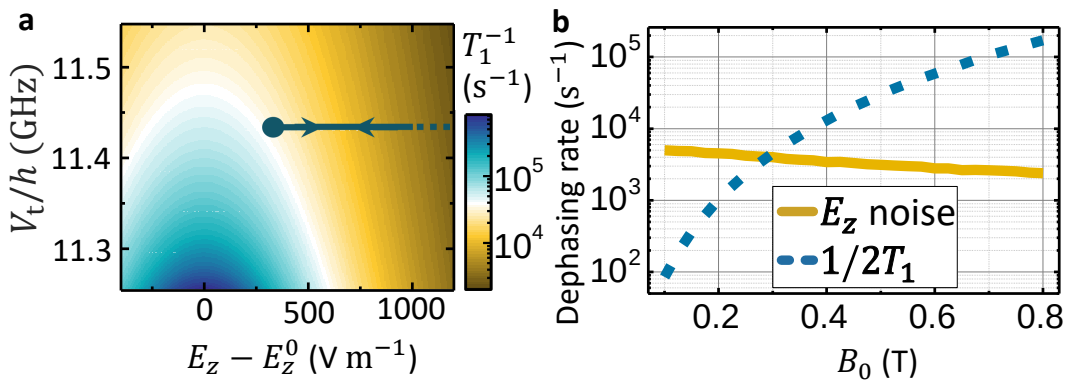

FIGURE 3.9: **Flip-flop relaxation rate.** **a** Flip-flop qubit relaxation rate at $B_0 = 0.4\,\mathrm{T}$, with arrows indicating the adiabatic path used for z-gates. **b** Flip-flop qubit dephasing rate due to E_z noise and relaxation rate, at the 2nd-order clock transition as a function of B_0.

In the dispersive regime $\delta_{\mathrm{so}} \gg g_{\mathrm{so}}$ the flip-flop relaxation directly relates to the charge qubit relaxation. It is equal to the amount of charge excited state in the flip-flop eigenstates times the charge qubit relaxation rate which gives [87]

$$1/T_{1,\mathrm{ff}} = \left(g_{\mathrm{so}}/\delta_{\mathrm{so}}\right)^2/T_{1,\mathrm{c}}. \tag{3.22}$$

The larger the detuning δ_{so}, the smaller is the component of admixed excited eigenstate $|e\downarrow\Uparrow\rangle$ and consequently the relaxation (Fig. 3.9a). At our proposed operating point, the second order flip-flop clock transition, the relaxation rate is $1/T_{1,\mathrm{ff}} \sim 10^4\,\mathrm{s}^{-1}$ for $B_0 = 0.4\,\mathrm{T}$. This indicates that the qubit dephasing will be relaxation limited $1/T_2^* = 1/(2T_1)$. However, the relaxation rate depends on the external magnetic field with the power-law relation $1/T_{1,\mathrm{ff}} \sim B^3$ [87]. Thus reducing the magnetic field, suppresses the relaxation strongly (Fig. 3.9b). We find that for $B_0 < 0.3\,\mathrm{T}$, the dephasing is no longer T_1 dominated. Note though, that when using spin-dependent tunnelling into a SET reservoir as a readout mechanism, we cannot operate the qubit

at this low fields (see Sec. 2.3.3 for details on qubit readout with an SET). Readout via a superconducting resonator is possible however (see Sec. 3.9).

3.4 Tunnel coupling tuning

Tuning the flip-flop qubit, e.g. into a clock transition, requires the ability to tune the tunnel coupling V_t. Moreover, V_t can exhibit oscillations at the atomic scale [80], which previously have been ignored, arising from a similar valley interference effect as the one afflicting the exchange interaction [66]. However, V_t is difficult to control at the fabrication stage, given its exponential dependence on donor depth.

The vertical uncertainty of ion-implanting a donor at $z_d \approx 15$ nm below the interface is of the order ± 10 nm [88], resulting in more than 2 orders of magnitude uncertainty in V_t [80]. Therefore, it is crucial to implement a method to tune V_t *in situ*.

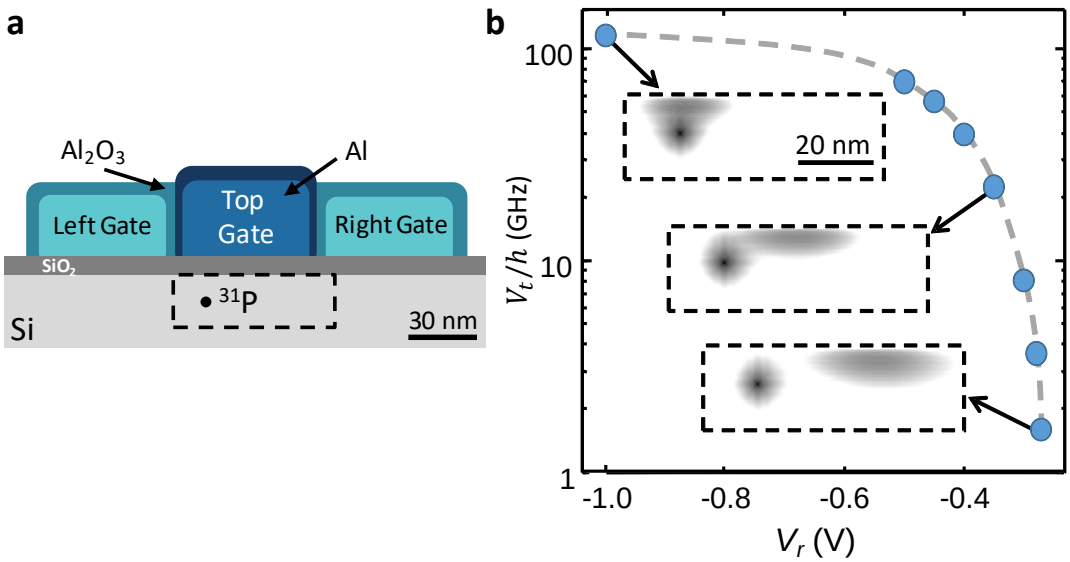

FIGURE 3.10: **Tunnel coupling tuning. a** Device structure to tune the tunnel coupling V_t of the charge qubit by applying lateral voltages. **b** V_t as a function of right gate voltage, calculated using a finite element Poisson solver (Synopsis® TCAD) and atomistic tight biding simulations (NEMO-3D [81], [82]). The insets illustrate the NEMO-3D wavefunctions for three right gate voltages $V_r = -1, -0.35$ and -0.27 V. The left gate voltage is $V_l = -0.5$ V for all the simulations, and the top gate is biased such that the position of the electron is in between the donor and interface. The donor is assumed to be $z_d = 9.2$ nm below the Si/SiO_2 interface.

A possible solution is to displace the location of the interface wavefunction laterally, which in turn modifies the overlap between the donor and interface wavefunctions and therefore reduces V_t. This can be done by adding two gates on either side of the donor top gate (Fig. 3.10a), which pulls the donor electron to the interface, in such a way that a relative voltage between the gates can modify the interface lateral potential landscape. This gate stack is identical to the well-established scheme for the confinement of single electrons in silicon quantum dots [25]. This technique allows V_t to be reduced by at least 2 orders of magnitude when displacing the wavefunction by around 30 nm (Fig. 3.10b), therefore circumventing the uncertainty in donor depth and V_t arising from ion-implantation.

Note that, when moving the interface wavefunction laterally to tune V_t, the electric dipole acquires some horizontal component. In this case, the detuning noise is caused by the noise component along the donor-interface state direction.

3.5 Adiabatic phase control

To incorporate flip-flop qubits in a quantum processor, the presence of slow dephasing regions is important to control the qubit phase with high fidelity and extend the qubit lifetime. Therefore, idle qubits are decoupled from electric fields by fully displacing the electron either to the interface or to the donor to minimize dephasing. Operations are performed close to the ionization point. Consequently, we need to displace the electron, which in turn changes its precession frequency (Fig. 3.5). As a result, the accumulated phase must be corrected after quantum operations.

Optimally, the phase is corrected by moving the electron to the 2nd-order clock transition, therefore minimizing dephasing errors. At this point, the flip-flop qubit phase precesses $\sim \Delta_\gamma \gamma_e B_0/2 - D_{\text{orb}}/h \sim$ 20 MHz faster than at its idle point, and therefore any phase correction in a 2π period can be applied within tens of nanoseconds. The dephasing rate at the clock transition, on the order of $10^3\,\text{s}^{-1}$, would cause very small errors ($< 10^{-4}$). However, while moving the electron from the interface towards the donor, the flip-flop qubit goes through regions of fast dephasing (Figs. 3.8, 3.9), and therefore this operation has to be performed as quickly as possible.

Moving the electron also has to be slow enough to avoid errors due to non-adiabaticity, which include *e.g.* leakage to unwanted high-energy states. These errors depend on the adiabatic factor K, which quantifies the fractional rate of change of the system's eigenstates (the higher the value of K, the more adiabatic and slower is the process). K is defined, in units of rad/s, as

$$K = \left|\frac{\omega_{\text{eff}}}{\dot{\alpha}}\right| \gg 1, \tag{3.23}$$

given a time-dependent Hamiltonian in a two-dimensional Hilbert space,

$$\mathcal{H}_2 = \Delta(t)\sigma_z + \Omega(t)\sigma_x, \tag{3.24}$$

where $\omega_{\text{eff}} = \sqrt{\Delta^2 + \Omega^2}$ is the instantaneous transition angular frequency between eigenstates, and $\dot{\alpha}_K$ is the rate of change of the orientation of $\omega_{\text{eff}}(\alpha_K)$ with $\alpha_K = \arctan(\Omega/\Delta)$ [89]. Following from Eq. 3.23, the adiabaticity is given by

$$K = \frac{\left(\Delta^2 + \Omega^2\right)^{3/2}}{|\dot{\Delta}\Omega - \dot{\Omega}\Delta|} \gg 1. \tag{3.25}$$

To determine the change in E_z per ns that satisfies the adiabatic condition at any given point, we calculate (from Eq. 3.25)

$$\frac{dt}{dE_z} = K\frac{|d\Delta/dE_z \cdot \Omega - d\Omega/dE_z \cdot \Delta|}{\left(\Delta^2 + \Omega^2\right)^{3/2}}. \tag{3.26}$$

Although the transition process involves multiple levels, we apply Eq. 3.25 as an approximation of adiabaticity. This is confirmed to be always valid by checking that the leakage errors are kept below a target level.

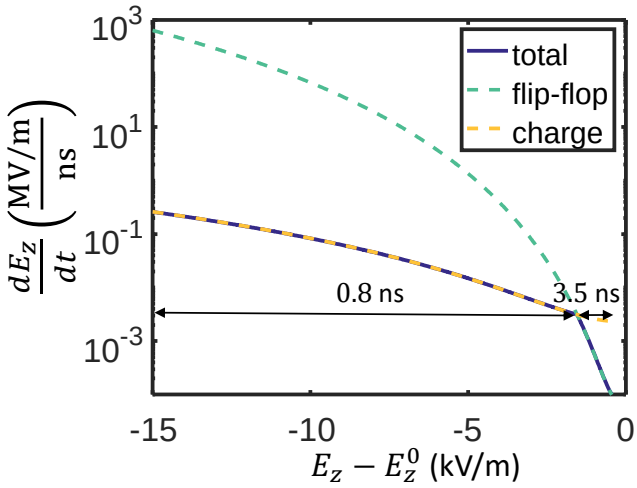

FIGURE 3.11: **Sweep characteristic to adhere to adiabacity**. dE_z/dt for each E_z that fulfils the adiabaticity criterion from Eq. (3.25) for $K = 50$.

For the charge qubit, the σ_z-coefficient is given by $\Delta_c = \pi e(E_z - E_z^0)d/h$ (in angular frequency units) and the Rabi angular frequency is $\Omega_c = \pi V_t/h$. For the flip-flop qubit we find accordingly $\Delta_{so} = \pi\delta_{so}/h$ and $\Omega_{so} = 2\pi g_{so}/h$. For an adiabatic factor K, we then calculate dE_z/dt for each E_z by satisfying the condition

$$dE_z/dt(\text{total}) = \min\left[dE_z/dt(\text{charge}), dE_z/dt(\text{flip-flop})\right]. \tag{3.27}$$

For $K = 50$ (Fig. 3.11), E_z is initially swept quickly for 0.8 ns, allowed by the large charge qubit splitting when $E_z \gg E_z^0$, followed by a slower sweep for 3.5 ns, limited by the proximity of excited charge states to the flip-flop qubit when $E_z \approx E_z^0$. This gives a total setup time of 4.3 ns due to the adiabatic ramp. The electron then remains at the clock transition for a time

$$\begin{aligned} t_\pi &= \frac{\alpha_{\text{rot}}/2\pi - 2\pi \int_{E_s}^{E_f} \left(\epsilon_{\text{ff}}[E_z(t)] - \epsilon_{\text{ff}}[E_z(t_0)]\right) \cdot (dE_z/dt)^{-1} h^{-1} dE_z}{\epsilon_{\text{ff}}[E_z(t_{\text{end}})]/h - \epsilon_{\text{ff}}[E_z(t_0)]/h} \\ &= 60\,\text{ns}, \end{aligned} \tag{3.28}$$

where $\alpha_{\text{rot}} = \pi$ is rotation angle we aim to perform for the gate and $E_{s,f}$ are the start and final electric field values. This time t_π is then the time necessary to perform the gate to correct for the phase shift, after the incurred phase shift during the adiabatic ramp has been subtracted.

To determine the time dynamics of an initial state $|\psi(t_0)\rangle = |g\rangle \otimes (|\downarrow\Uparrow\rangle + |\uparrow\Downarrow\rangle)/\sqrt{2}$, while sweeping E_z adiabatically to move the electron from the interface to the 2nd-order clock transition and back in order to realize a π z-gate, we compute its time evolution

$$|\psi(t)\rangle = e^{-i\mathcal{H}_{\text{ff}}t/\hbar}\,|\psi(t_0)\rangle\,. \tag{3.29}$$

We then find the expectation values, according to $\langle\#\rangle = \langle\psi(t)|\,\#\,|\psi(t)\rangle$, of the flip-flop z-state

$$\sigma_z^{\text{ff}} = |\uparrow\Downarrow\rangle\langle\uparrow\Downarrow| - |\downarrow\Uparrow\rangle\langle\downarrow\Uparrow|\,, \tag{3.30}$$

the flip-flop x-state

$$\sigma_x^{\text{ff}} = |+_x^{\text{ff}}\rangle\langle+_x^{\text{ff}}| - |-_x^{\text{ff}}\rangle\langle-_x^{\text{ff}}|\,, \tag{3.31}$$

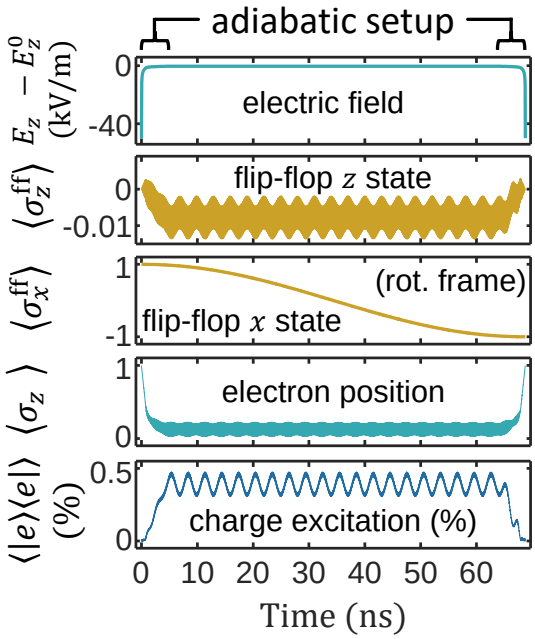

FIGURE 3.12: **High-fidelity adiabatic z-gates.** Time-evolution of an adiabatic ($K = 50$) π z-gate on state $|g\rangle \otimes (|\downarrow\Uparrow\rangle + |\uparrow\Downarrow\rangle)/\sqrt{2}$, showing applied electric field, flip-flop and charge states.

where

$$|+_x^{\rm ff}\rangle = \frac{1}{\sqrt{2}}\left(|\uparrow\Downarrow\rangle + \exp\left(-i2\pi\epsilon_{\rm ff}^{t=0}/h\right)|\downarrow\Uparrow\rangle\right), \tag{3.32a}$$

$$|-_x^{\rm ff}\rangle = \frac{1}{\sqrt{2}}\left(|\uparrow\Downarrow\rangle + \exp\left(-i2\pi\epsilon_{\rm ff}^{t=0}/h - i\pi\right)|\downarrow\Uparrow\rangle\right), \tag{3.32b}$$

the electron position σ_z and the charge qubit excitation $|e\rangle\langle e|$. We find that indeed during the 69 ns the flip-flop phase π-gate is performed while keeping both the flip-flop and charge excitation minimal (Fig. 3.12). Fast oscillations between the charge and flip-flop states are due to small deviations from perfect adiabaticity.

Overall, we find that moving the electron fast, when the different qubit states are far detuned, and slowly when they are close to resonance, allows for minimal errors while switching between the different operation modes.

Adiabatic phase gate error rates

The adiabatic errors (without noise) of an adiabatic unitary process $U_{\rm ideal}$, expressing leakage to other states, can be calculated by averaging the fidelity of the actual process U over a set of initial states $|j\rangle$,

$$\text{Adiabatic error} = 1 - \sum_{|j\rangle}\left|\langle j|\, U^\dagger U_{\rm ideal}\, |j\rangle\right|^2 / N_j, \tag{3.33}$$

where N_j is the number of initial states.

For the z-gate, we choose the 1-qubit ($N_j = 4$) states $|j\rangle = \{|g\downarrow\Uparrow\rangle_e, |g\uparrow\Downarrow\rangle_e, (|g\downarrow\Uparrow\rangle_e + |g\uparrow\Downarrow\rangle_e)/\sqrt{2}, (|g\downarrow\Uparrow\rangle_e + i\,|g\uparrow\Downarrow\rangle_e)/\sqrt{2}\}$, which closest correspond to the uncoupled eigenstates.

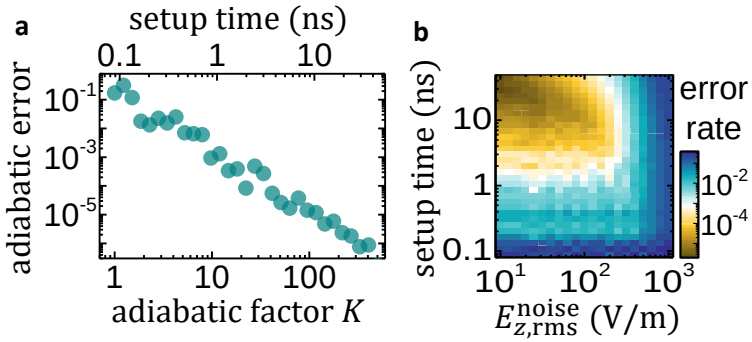

FIGURE 3.13: **Adiabatic z-gates error rates**. **a** π z-gate leakage error for different adiabatic setup times, which are set by the factor K. **b** π z-gate error due to quasi-static E_z noise, at the 2nd-order CT at $B_0 = 0.4$ T, for different noise amplitudes and adiabatic setup times.

The adiabatic errors can be controlled with the factor K, which determines the setup time (see Fig. 3.13a). The longer the setup time, the smaller are the adiabatic errors.

Quasi-static E_z noise can increase errors, due to dephasing (Fig. 3.13b). At realistic noise levels (100 V/m), the gate error rate is found to be $< 10^{-4}$ for setup times of several nanoseconds. Similar error levels arise due to relaxation, which remains below $3 \cdot 10^4$ Hz (arrow in Fig. 3.9).

3.6 Electric drive

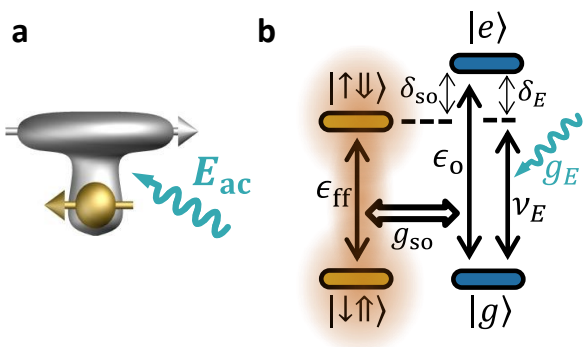

FIGURE 3.14: **Electric drive of the flip-flop qubit.** **a** Spatial representation for an electric drive of the flip-flop qubit, showing the partially ionized electron wavefunction and spin arrows. **b** Level diagram of the detuned charge and spin states.

High-fidelity one-qubit $x(y)$-gates can be achieved when addressing the flip-flop qubit electrically (Fig. 3.14a). A vertical microwave electric field of amplitude E_{ac} is applied in resonance with the flip-flop qubit, *i.e*, $\nu_E = \epsilon_{\text{ff}}/h$, which modulates the hyperfine interaction, rendering $\mathcal{H}_A(t)$ time-dependent. The flip-flop qubit is then driven via a second order process (Fig. 3.14b). The fastest 1-qubit gates are obtained when the electron is at the ionization point, where $\partial A/\partial E_z$ is maximum and thus the spin-orbit coupling $g_{\text{so}} = hA/4$ (Fig. 3.4, Eq. 3.10).

Note that the presence of clock transitions does not affect the ability to use E_{ac} to resonantly drive the qubit, since the transverse term $A(E_z)$ still responds fully to the electric field (this is similar to the case of magnetic clock transitions, e.g. in Si:Bi [90]).

For a linearly polarized electric field, the electric drive of a dipole of size d is described by the Hamiltonian

$$\mathcal{H}_{\mathrm{E}} = edE_{\mathrm{ac}} \cos(2\pi\nu_E t)\sigma_z. \tag{3.34}$$

The coupling of this electric field to the charge qubit is then determined (with Eq. 3.10) by[3].

$$\begin{aligned} g_{\mathrm{E}} &= \langle g| \mathcal{H}_{\mathrm{E}} |e\rangle \\ &= \frac{eE_{\mathrm{ac}}d}{4} \langle g| \sigma_z |e\rangle \\ &= \frac{eE_{\mathrm{ac}}d}{4} \frac{V_t}{\epsilon_{\mathrm{o}}}. \end{aligned} \tag{3.35}$$

A large detuning $\delta_{\mathrm{so}} \gg g_{\mathrm{so}}$ between the charge and flip-flop qubit ensures the least amount of the charge excited state $|e\rangle$ in the flip-flop qubit eigenstates (Eq. 3.16a), minimizing qubit relaxation via charge-phonon coupling. The flip-flop qubit is still driven, via a second-order process, at a rate:

$$g_{\mathrm{E}}^{\mathrm{ff}} = \frac{g_{\mathrm{so}} g_E}{2} \left(\frac{1}{\delta_{\mathrm{so}}} + \frac{1}{\delta_E} \right), \tag{3.36}$$

where $\delta_E = h\nu_E - \epsilon_{\mathrm{o}}$ is the detuning between the electric drive and the charge qubit. Here, we see again that the fastest 1-qubit gates are obtained when the electron is at the ionization point: δ_{so} and δ_E are minimum (ϵ_{o} is minimum), and g_{so} and g_E are maximum (Eqs. 3.10 and 3.35).

3.6.1 Optimized pulse shaping: adiabatic gates

The electrical drive can cause some excitation of the charge qubit. This has to be avoided as both the dephasing and the relaxation rates of the charge qubit are expected to be on the order of $10^6\,\mathrm{s}^{-1}$. It is therefore convenient to turn E_{ac} on/off adiabatically to make sure that any small amount of charge excitation is de-excited at the end of the gate. As for the adiabatic z-gate, we find the adiabatic increase of $E_{\mathrm{ac}}(t)$ (Fig. 3.15 top panel) with Eq. (3.25) where $\Delta_E = \pi\delta_E/h$ and $\Omega_E = 2\pi g_E/h$. We assume an adiabatic factor $K = 30$, which is sufficient for leakage errors $< 10^{-3}$.

To determine the time dynamics of the gate, we employ Floquet theory to efficiently calculate the time evolution of the time-dependent Hamiltonian. For a periodically driven open quantum system with a Hamiltonian

$$\mathcal{H}(t) = \mathcal{H}(t+T) \tag{3.37}$$

with period T, the Floquet theorem states [91], [92] that the time evolution operator $\boldsymbol{K}(t, t_0)$ of the system, defined by

$$|\psi(t)\rangle = \boldsymbol{K}(t, t_0) |\psi(t_0)\rangle, \; \boldsymbol{K}(t_0, t_0) = 1, \tag{3.38}$$

[3] We adapt a definition of the coupling rates consistent with the Jaynes-Cummings model (see Sec. 2.4.3). As such, g corresponds to half the Rabi frequency in the one-photon limit. Furthermore, in every case of resonant driving we assume a linearly polarized field, resulting in a Rabi frequency that equals the dipole matrix element times half the driving field amplitude (RWA, see Sec. 4.3.1, Eq. 4.11). This explains the factors of 4 appearing in all the formulas for coupling rates of driving fields.

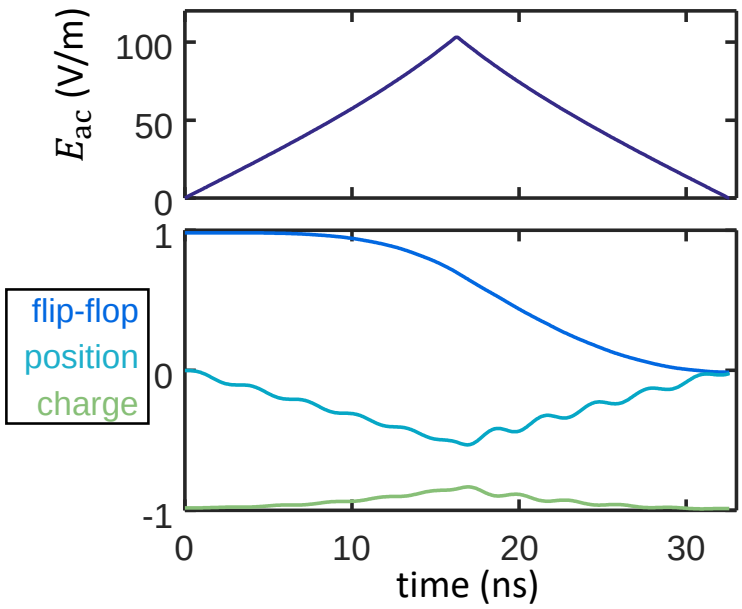

FIGURE 3.15: **Adiabatic $\pi/2$ x-gate.** Time-dependent adiabatic drive amplitude (top panel) and qubit dynamics (bottom panel) of a $\pi/2$ x-gate, for $K = 30$, $B_0 = 0.4$ T, $E_z = E_z^0$ and $V_t/h = 11.5$ GHz. Bottom plot shows flip-flop z state, $\langle \sigma_z^{\mathrm{ff}} \rangle$, electron position, $\langle |d\rangle \langle d| \rangle - \langle |i\rangle \langle i| \rangle$, and charge qubit state, $\langle |e\rangle \langle e| - |g\rangle \langle g| \rangle$.

can be factorized as

$$\boldsymbol{K}(nT, 0) = [\boldsymbol{K}(T, 0)]^n, \tag{3.39}$$

where we use the propagator over a full period $\boldsymbol{K}(T, 0)$ to construct the time evolution over many multiples n of the fundamental period. This formalism effectively renders our time-dependent Hamiltonian time-independent. Additionally, we deconstruct the adiabatic ramp into a few coarse time steps to account for large changes in the driving parameters.

In this way we calculate the time-evolved eigenstate of $\mathcal{H}_{\mathrm{ff}} + \mathcal{H}_{\mathrm{E}}$ and then determine the expectation values of flip-flop z-state $\langle \sigma_z^{\mathrm{ff}} \rangle$, the electron position $\langle |d\rangle \langle d| \rangle - \langle |i\rangle \langle i| \rangle$ and the charge qubit state $\langle |e\rangle \langle e| \rangle - \langle |g\rangle \langle g| \rangle$ (Fig. 3.15 bottom panel).

To perform a $\pi/2$ x-gate, E_{ac} increases steadily until a $\pi/4$ rotation is completed, after which E_{ac} is gradually switched off to achieve the gate. Meanwhile, an average 4% excitation of the charge qubit causes a $\sim 4 \times 10^4$ s^{-1} relaxation rate of the encoded quantum state (Eq. 3.21), or error levels close to 10^{-3}.

This shows that shaping the electric pulses applied to the qubit, minimizes qubit decoherence.

Adiabatic gate errors

Now we investigate how the total $\pi/2$ x-gate errors depend on the biasing of the electron wavefunction. Therefore we calculate the adiabatic error (Eq. 3.33), the error from quasi-static E_z noise with

$$\text{Noise error} = 1 - \sum_{n,|j\rangle_n} \left| \langle j|_n \, U_n^\dagger U_{n,\text{ideal}} \, |j\rangle_n \right|^2 / (N_j N_n), \tag{3.40}$$

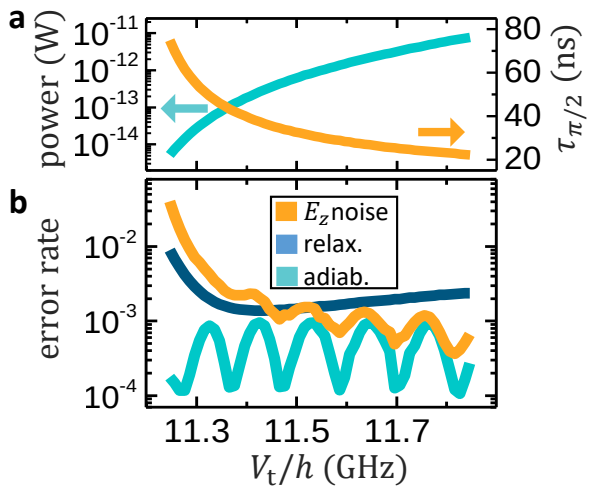

FIGURE 3.16: **Adiabatic gate errors. a** Averaged drive power and gate time for the parameters $K = 30$, $B_0 = 0.4$ T, $E_z = E_z^0$ and $V_t/h = 11.5$ GHz. For the same parameters, **b** the error rates for different V_t. To estimate the drive power, we assumed a 50 Ω line in which a 1 μV AC voltage produces a 10 V/m AC vertical electric field (simulated with Synopsis® TCAD).

where $|j\rangle = \{|g\downarrow\Uparrow\rangle_e, |g\uparrow\Downarrow\rangle_e, (|g\downarrow\Uparrow\rangle_e + |g\uparrow\Downarrow\rangle_e)/\sqrt{2}, (|g\downarrow\Uparrow\rangle_e + i\,|g\uparrow\Downarrow\rangle_e)/\sqrt{2}\}$ and $N_j = 4$, and the relaxation errors with

$$\text{Relax. error} = \left[1 - \exp\left\{-\int_0^{\tau_{\text{gate}}} \left(\sum_{|j(t)\rangle} \langle j(t)|e\rangle\,\langle e|j(t)\rangle\,/N_j\right) dt/T_{1,c}\right\}\right]/2, \quad (3.41)$$

where $|j(t)\rangle$ are the time-evolution of the initial set states $|j\rangle$.

At the ionization point[4], $E_z = E_z^0$, error levels close to 10^{-3} are found over a wide range of V_t (Fig. 3.16b). The $K = 30$ choice ensures adiabatic errors $< 10^{-3}$ with an oscillatory character typical of adiabatic processes [93]. At small V_t (and therefore small detuning δ_{so}), the qubit eigenstates contain a substantial amount of charge, causing more errors due to charge-phonon relaxation. Increasing the detuning δ_E with larger V_t allows for a faster adiabatic sweep and higher powers (Fig. 3.16a), yielding shorter gate times and therefore less errors due to quasi-static noise. Still, the incident power is at least three orders of magnitude lower than the one needed to drive donor electron spin qubits, at the same Rabi frequency, with oscillating magnetic fields [30], [40].

Low error rates for quasi-static noise (Eq. 3.40) are still available away from the ionization point (Fig. 3.17a), even though the best values are found at $E_z = E_z^0$. This is because our gate times are so fast ($\sim$ 20 ns) that dephasing, and therefore clock transitions, do not play a crucial role. Instead, quasi-static E_z noise causes errors mainly by modulating the driving strength g_E^{ff}, causing "gate time jitter". Indeed, the gate time is sensitive to the charge qubit transition frequency ϵ_{o} (Eq. 3.36), and therefore gate errors are minimized close to the charge qubit clock transition (CQCT), where $\partial\epsilon_{\text{o}}/\partial E_z = 0$ (Fig. 3.8).

Finally, lower quasi-static E_z noise can cause less errors, provided that the adiabatic factor K is increased, to reduce leakage errors, up to an optimum value where gate times are still fast as to keep noise errors low (Fig. 3.17b). Relaxation errors could also be reduced by reducing B_0 (recall Fig. 3.9).

[4]Note, that the 2nd clock transition is close but not exactly at E_z^0.

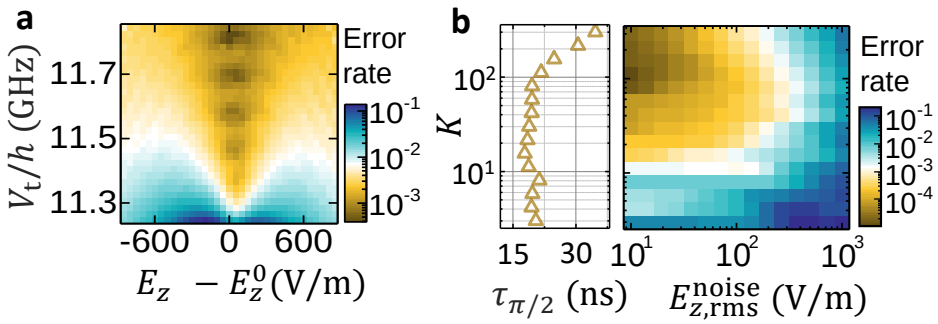

FIGURE 3.17: **Adiabatic gate errors.** **a** Estimated flip-flop qubit $\pi/2$ x-gate error due to quasi-static noise with amplitude $E_{z,\mathrm{rms}}^{\mathrm{noise}} = 100$ V/m. **b** Dependence of the gate error rate on the electric noise r.m.s. amplitude and adiabatic factor K (which sets the gate time).

Overall, we can achieve an electrically driven $\pi/2$ x-gate with a gate time of 30 ns and an error rate of 10^{-3} with an incident power < 1 pW.

3.7 Noise influences

3.7.1 Charge noise

The Si/SiO_2 interface contains a number of defects and electron traps, which can generate charge noise and therefore degrade the operation of qubits sensitive to electric fields. Some experimental studies have extracted the trap density, in the middle of the silicon band gap, for the MOS devices we consider here [94]. It is known, experimentally and theoretically, that these charge fluctuators yield a $1/f$ frequency dependence of the noise spectral density [95]. These models capture the averaged collective effect of many charge fluctuators on the qubit operation. In specific cases, one can occasionally encounter individual charge traps or fluctuators whose effect is more drastic than that of an overall $1/f$ noise. However, it is usually possible experimentally to tune the electrostatic landscape of a nanoscale device in such a way that the individual trap is frozen, *i.e.* does not change its charge state while the qubit is operated. This results in a static shift in the local electric field that can be compensated with other gate voltages. In very rare occasions, a charge trap cannot be frozen while placing the qubit at its optimal operation point. In that case, the qubit will have to be considered faulty, and excluded from participating in the operations of the quantum processor.

In the general case where charge noise can be considered an average collective effect, it can be thought of as a quasi-static drift of the qubit electrostatic environment (noise with a spectral weight centred below the Rabi frequency). Indeed, since individual gates take less than a microsecond, the qubit environment is usually static within a single gate, but fluctuates in between gates. The dephasing time T_2^* characterises the influences of these fluctuations on the qubit (see Sec. 2.3.4).

Experimentally, average quasi-static charge detuning noises around 1-9 μeV are typically found in a range of semiconductor nanodevices, including SiGe [96]–[98], AlGaAs [99] and Si/SiO_2 [83], [98]. In particular, MOS structures were found recently [98] to have a charge noise spectrum similar to SiGe devices, around $(0.5\ \mu\mathrm{eV})^2/\mathrm{Hz}$. Integrating over a quasi-static bandwidth relevant to experimental time scales, say between 1 Hz and 1 MHz ($\sim$ Rabi frequency), yields 1.7 μeV noise. In our simulations, given that the distance between the donor and interface sites is

$\sim$ 10-30 nm, a noise field of 100 V/m would correspond to 1-3 μeV charge detuning noise.

We assume any quasi-static noise to be along the z-direction. However, when we tune V_t by moving the electron wavefunction laterally, the electric dipole acquires some horizontal component (Fig. 3.4). In this case, the detuning noise is caused by the noise component along the donor-interface states direction. At the same time, horizontal noise will also have an effect, albeit minimal, in gate performance. For the parameters at which $V_t/h \approx 10$ GHz in Fig. 3.10b, 10 μV r.m.s. lateral noise would cause less than 0.01% uncertainty in the dipole size, therefore causing negligible gate errors. The same noise causes less than 1% uncertainty in δ_{so} (and therefore in gate time), which translates into maximum 10^{-4} errors due to gate time jitter, and maximum $\sim 10^4\,\mathrm{s}^{-1}$ extra dephasing due to dispersive shifts (Eq. 3.18).

Overall, charge noise is the main source of quasi-static noise (see discussion in the following section) with a typical $1/f$ spectrum. Consistently with recently measured spectral density $S^{\Delta\epsilon}_{\mathrm{SiO2}} = 0.5\,\mu\mathrm{eV}/\sqrt{\mathrm{Hz}}$ for Si/SiO$_2$ interfaces [98], we assume the power spectral density at the donor to be

$$S_{\mathrm{c}}(\omega) = S_{\mathrm{c}}(1\,\mathrm{Hz})/\omega \tag{3.42}$$

with

$$S_{\mathrm{c}}(1\,\mathrm{Hz}) \approx \left(\frac{S^{\Delta\epsilon}_{\mathrm{SiO2}}}{ez_d}\right)^2 \approx 2\times 10^4\,\mathrm{V}^2\,\mathrm{m}^{-2}\,\mathrm{s}. \tag{3.43}$$

3.7.2 Other quasi-static noise sources

Besides quasi-static E_z noise, a number of other noise sources can also affect the qubits.

Johnson-Nyquist noise Another source of electric field noise can be the thermal and electrical noise produced by the metallic gates on top of the qubits, and the room-temperature instruments they connect to. An $R = 50\,\Omega$ resistor at room temperature produces Johnson-Nyquist noise with an r.m.s voltage

$$V^{\mathrm{JN}}_{\mathrm{rms}} = \sqrt{4k_BTR\Delta\nu}. \tag{3.44}$$

The corresponding noise spectral density is

$$S_{\mathrm{JN}}(\omega) = \left(\frac{\partial E_z}{\partial V}\right)^2 \frac{2R\hbar\omega}{\pi}(e^{\hbar\omega/k_BT}-1)^{-1}, \tag{3.45}$$

where we have used $\partial E_z/\partial V = 10^7\,\mathrm{m}^{-1}$, typical in MOS nanostructures (simulated with Synopsis® TCAD).

A quasi-static bandwidth $\Delta\nu \sim 1$ MHz (up to the Rabi frequency) produces $\sim 1\,\mu$V voltage noise, which is equivalent to $E^{\mathrm{noise}}_{z,\mathrm{rms}} \sim 10$ V/m, or errors $< 10^{-5}$ (Fig. 3.17). Furthermore, because of the very low powers required by the electrically-driven 1-qubit gates and adiabatic shuttling, it is possible to insert abundant low-temperature attenuation along the high-frequency lines, and therefore the relevant temperature for the Johnson-Nyquist noise is well below room temperature (as low as several mK, see Sec. 6.4.2).

Evanescent wave Johnson noise Being close to a metallic interface, our qubit will be subject to evanescent wave Johnson noise (EWJN). Here, quantum and thermal fluctuations of the electrical current create electromagnetic field noise which leaks out of the metal in form of evanescent waves (see Sec. 8.2.2). The corresponding electrical noise r.m.s. voltage is [100]

$$V_{\text{rms}}^{\text{EWJN}} = \sqrt{k_B T \Delta\nu / (2 z_d^3 \sigma)} \tag{3.46}$$

and the electrical noise spectral density is [100], [101]

$$S_{\text{EWJN}}(\omega) \approx \frac{\hbar\omega}{4\pi z_d^3 \sigma}, \tag{3.47}$$

where σ is the electric conductivity of the metal gates.

Assuming the qubit is $z_d = 15$ nm under aluminium gates at $T = 100$ mK with $\sigma = 1.6 \times 10^6$ S m^{-1} (Sec. 8.4.1), a quasi-static bandwidth $\Delta\nu \approx 1$ MHz produces $V_{\text{rms}}^{\text{EWJN}} =\sim 0.01$ V/m, which is negligible.

3.7.3 High frequency noise

In general, a driven qubit Rabi-oscillates with a decay envelope function given by [102]

$$P_1(t) = \zeta(t) \exp(-\Gamma_R t), \tag{3.48}$$

where $\zeta(t)$ represents the decay due to quasi-static noise which shifts the qubit resonance frequency and detunes it from resonance. We find $\zeta(t)$ to be on the order of a few kHz, leading to errors below 10^{-3} (Sec. 3.3.1).

$$\Gamma_R = \Gamma_1 + \Gamma_1^{\Delta} + \Gamma_1^{\nu} + \Gamma_{\Omega} \tag{3.49}$$

is the exponential Rabi decay rate which combines various decay mechanisms Γ_i which will be discussed in the following.

Qubit relaxation $\Gamma_1 = 1/T_1$ is the qubit relaxation rate due to an energy exchange with the environment and is around 10^4 s^{-1} which leads to error levels on the order of 10^{-3} (see Ref. [87], Secs. 3.3.2, 3.6.1).

Quasi-static gate time jitter Γ_1^{Δ} is the inverse of the gate time jitter caused by quasi-static noise which modulates the drive strength. This decay leads to error rates around 10^{-3} (Sec. 3.6.1).

Gate time jitter at the drive frequency Γ_1^{ν} is the inverse of the gate time jitter due to noise at the drive frequency.

Vertical (thus parallel to the driving field E_{ac}) noise at the qubit resonance frequency ($\epsilon_{\text{ff}}/h \sim 11$ GHz) would cause transitions between the qubit eigenstates - essentially a spurious excitation/relaxation process driven by noise - at a rate Γ_1^{ν}. This noise can be caused *e.g.* by charges fluctuating in resonance with the qubit or by voltage noise at the metallic gates. This is dominated by vacuum fluctuations, since the qubit frequency is generally higher than the corresponding device temperature. Also, during gate operations, the portion of the noise spectrum around the qubit frequency can add incoherently to the external resonant drive, causing the gate time to fluctuate.

For the flip-flop qubit, the Rabi decay rate is given by

$$\Gamma_1^\nu = \frac{\pi}{2}\left(\frac{\mu_e^{\mathrm{ff}}}{\hbar}\right)^2 S(2\pi\epsilon_{\mathrm{ff}}), \tag{3.50}$$

where $S(2\pi\epsilon_{\mathrm{ff}})$ is the noise power spectral density taken at the qubit angular frequency (in units of $\mathrm{V}^2\,\mathrm{m}^{-2}\,\mathrm{rad}^{-1}\,\mathrm{s}$) and

$$\mu^{\mathrm{ff}} = \langle\frac{g_{\mathrm{so}}}{\delta_{\mathrm{so}}}\rangle ed \tag{3.51}$$

is the average flip-flop qubit electric dipole moment. It is dependent on the amount $g_{\mathrm{so}}/\delta_{\mathrm{so}}$ of charge excitation in the flip-flop states [54] as the charge qubit exhibits the physical dipole with a dipole moment of $\mu^{\mathrm{c}} = ed$ and only acts as a second-order enabler. Because the charge excitation is minimized in our gate schemes (Figs. 3.12a, 3.15 and 3.22a), μ^{ff} is much smaller than the charge dipole, which in turn makes it less susceptible to electrical noise.

In case of charge noise we get $\Gamma_1^\nu \sim 10^4\,\mathrm{s}^{-1}$ with Eq. (3.42). This implies $\pi/2$ x-gate errors[5] of $\sim 10^{-4}$. There could also be vacuum fluctuations of charge traps, which could generate errors due to relaxation. We do not know of any experimental measurement of such a noise for semiconductor nanostructures. For superconducting charge qubits, it has been found that charge noise increases linearly at frequencies beyond the thermal bath [103], [104]. If a similar phenomenon afflicts our qubits, those quantum fluctuations will play an important role beyond ~ 2 GHz (100 mK), implying that, at 10 GHz, relaxation can be up to 25 times enhanced. This can increase relaxation error rates to $\sim 10^{-3}$.

Johnson-Nyquist noise, at a noise temperature $T = 100$ mK with Eq. (3.45), would give $\Gamma_1^\nu < 10^4\,\mathrm{s}^{-1}$, and therefore error rates $< 10^{-4}$.

Finally, for EWJN (Eq. 3.47) at $T = 100$ mK we get $\Gamma_1^\nu < 10^4\,\mathrm{s}^{-1}$, therefore again error rates $< 10^{-4}$.

Note that, in the dressed qubit picture, we find the dephasing of the dressed qubit [105]

$$1/T_{2\rho} = \Gamma_1 + \Gamma_1^\Delta + \Gamma_1^\nu. \tag{3.52}$$

Detuning noise at the Rabi frequency Γ_Ω is the decay rate of the Rabi oscillations due noise at the Rabi frequency ($\Omega_R > 10$ MHz). This type of noise feeds into the driven qubit via fluctuations in the detuning between drive frequency and the qubit precession frequency. The decay rate of the flip-flop qubit is given by

$$\Gamma_\Omega = \frac{\pi}{2}\left(2\pi\sum_{i=x,y,z}\frac{\partial\epsilon_{\mathrm{ff}}}{\partial E_i}\right)^2 S(\Omega_R). \tag{3.53}$$

When performing gate operations while tuned such that we expect low gate errors (Fig. 3.17a), we estimate the change in qubit precession frequency with electric field for vertical E_z-noise to $\partial\epsilon_{\mathrm{ff}}/\partial E_i \sim 10^3$ Hz V^{-1} m (Eq. 3.1). The change in precession due to horizontal electric noise $E_{x,y}$ can be estimated from the change in V_t due to such noise (from Fig. 3.10b) which in turn changes ϵ_{ff}. We find $\partial\epsilon_{\mathrm{ff}}/\partial E_{x,y} \sim 10^2$ Hz V^{-1} m.

$1/f$ charge noise (Eq. 3.42) gives $\Gamma_\Omega < 10^4\,\mathrm{s}^{-1}$, implying $< 10^{-4}$ errors. Johnson-Nyquist noise (Eq. 3.45) from room temperature gives $\Gamma_\Omega = 300\,\mathrm{s}^{-1}$, whereas EWJN

[5] We estimate the error rate as $\Gamma^i \cdot \tau_{\mathrm{gate}}$ where τ_{gate} is the gate duration.

(Eq. 3.47) at 100 mK gives $\Gamma_\Omega = 20\,\mathrm{s}^{-1}$, therefore producing $< 10^{-5}$ and $< 10^{-6}$ errors, respectively.

Note that, in the dressed qubit picture, we find the relaxation of the the dressed qubit [105],[106]

$$1/T_{1\rho} = \Gamma_\Omega. \tag{3.54}$$

3.7.4 Summary

	Error levels at different spectral bandwidths		
Noise source	Quasi-static ($< 1\,\mathrm{MHz}$)	Rabi ($\sim 10\,\mathrm{MHz}$)	Qubit ($\sim 10\,\mathrm{GHz}$)
1/f vertical (E_z)	10^{-3}	$< 10^{-4}$	10^{-4}
1/f horizontal ($E_{x,y}$)	10^{-4}	$< 10^{-5}$	-
Charge-phonon relaxation	-	-	10^{-3}
Johnson-Nyquist	$\ll 10^{-5}$	$< 10^{-5}$	$< 10^{-4}$
EWJN	-	$< 10^{-6}$	$< 10^{-4}$

TABLE 3.1: **Gate errors for different noise sources** Hyphens indicate non-existent or negligible errors.

We conclude that quasi-static E_z noise dephasing and charge-phonon relaxation T_1 are the main sources of error and the most deleterious ones for flip-flop qubits. Therefore our analysis is sufficient to provide a reliable estimate of dephasing and gate errors. Indeed, low-frequency noise was found to be the most deleterious one in a hybrid donor-dot qubit in a silicon MOS device [83]. Finally, note that we do not assume any type of dynamical noise correction or cancellation to be applied, and therefore our calculations are a worst-case scenario. Table 3.1 summarizes these results.

3.8 Dipole-dipole coupling

To couple two flip-flop qubits, we exploit the electric dipole that naturally arises when a donor-electron wavefunction is biased to the ionization point, due to the fact that a negative charge has been partly displaced away from the positive ^{31}P nucleus. The electric field produced by this induced dipole in turn, modifies the energy of a nearby donor which is also biased at the ionization point, resulting in a long-range coupling between the two dipoles (Fig. 3.18).

The interaction energy between two distant dipoles, μ_1 and μ_2, oriented perpendicularly to their separation r is

$$V_{\mathrm{dip}} = \mu_1\mu_2/(4\pi\varepsilon_r\varepsilon_0 r^3), \tag{3.55}$$

where ε_0 is the vacuum permittivity and ε_r the material's dielectric constant ($\varepsilon_r = 11.7$ in silicon) [107]. The electric dipole of each donor-interface state is

$$\mu_i^c = ed_i(1+\sigma_{z,i})/2, \tag{3.56}$$

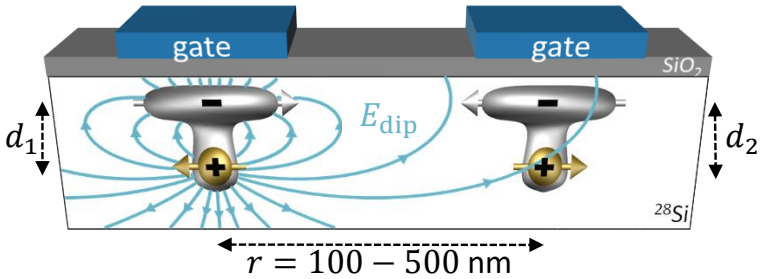

FIGURE 3.18: **Electric dipole-dipole interaction between two distant flip-flop qubits.** Device schematic for coupling flip-flop qubits, showing dipole field lines, $\boldsymbol{E}_{\text{dip}}$, produced by the dipole with dipole length d_1 on the left. The distance r between two qubits can be up to 500 nm.

which yield an interaction energy of

$$V_{\text{dip}} = \frac{1}{16\pi\varepsilon_0\varepsilon_r}\frac{e^2 d_1 d_2}{r^3}, \tag{3.57}$$

which implies that the dipole-dipole interaction Hamiltonian between two such dipoles is:

$$\mathcal{H}_{\text{dip}} = V_{\text{dip}}\left(\sigma_{z,1}\sigma_{z,2} + \sigma_{z,1} + \sigma_{z,2}\right). \tag{3.58}$$

This electric dipole-dipole interaction is therefore equivalent to a small shift in the equilibrium orbital position of both electrons plus a coupling term between the charge qubits (blue dashed rectangle in Fig. 3.20a) equal to:

$$\begin{aligned} g_{\text{dd}} &= \langle g_2 e_1 | \mathcal{H}_{\text{dip}} | g_1 e_2 \rangle \\ &= V_{\text{dip}} \langle e_1 | \sigma_{z,1} | g_1 \rangle \langle g_2 | \sigma_{z,2} | e_2 \rangle \\ &= V_{\text{dd}} \frac{V_{t,1} V_{t,2}}{\epsilon_{\text{o},1}\epsilon_{\text{o},2}}. \end{aligned} \tag{3.59}$$

The strength of this dipole interaction is influenced by screening effects due to the dielectric/metal surface above it.

3.8.1 Dipole Screening

Our device topology consists of a SiO_2 layer sandwiched between a metal gate and a silicon substrate, with the donor embedded in the substrate. In such a topology, the image charges of the donor electron and nucleus will be located above the donor, thereby creating an additional vertical dipole. The magnitude and polarity of the image charges depend on the details of the nanostructure, such as the donor depth and thickness of the oxide.

We first analyse two extreme scenarios, considering image charges at (i) silicon-metal and (ii) silicon-oxide interfaces. For a source donor electron (or nuclear) charge $\mathcal{D}_{\text{e(n)}}$, in silicon, the image charge $\mathcal{I}_{\text{e(n)}}$ in the interface material is given by [79]

$$\mathcal{I}_{\text{e(n)}} = Q\,\mathcal{D}_{\text{e(n)}}, \tag{3.60}$$

where

$$Q = \frac{\epsilon_{\text{Si}} - \epsilon_{\text{I}}}{\epsilon_{\text{Si}} + \epsilon_{\text{I}}}, \tag{3.61}$$

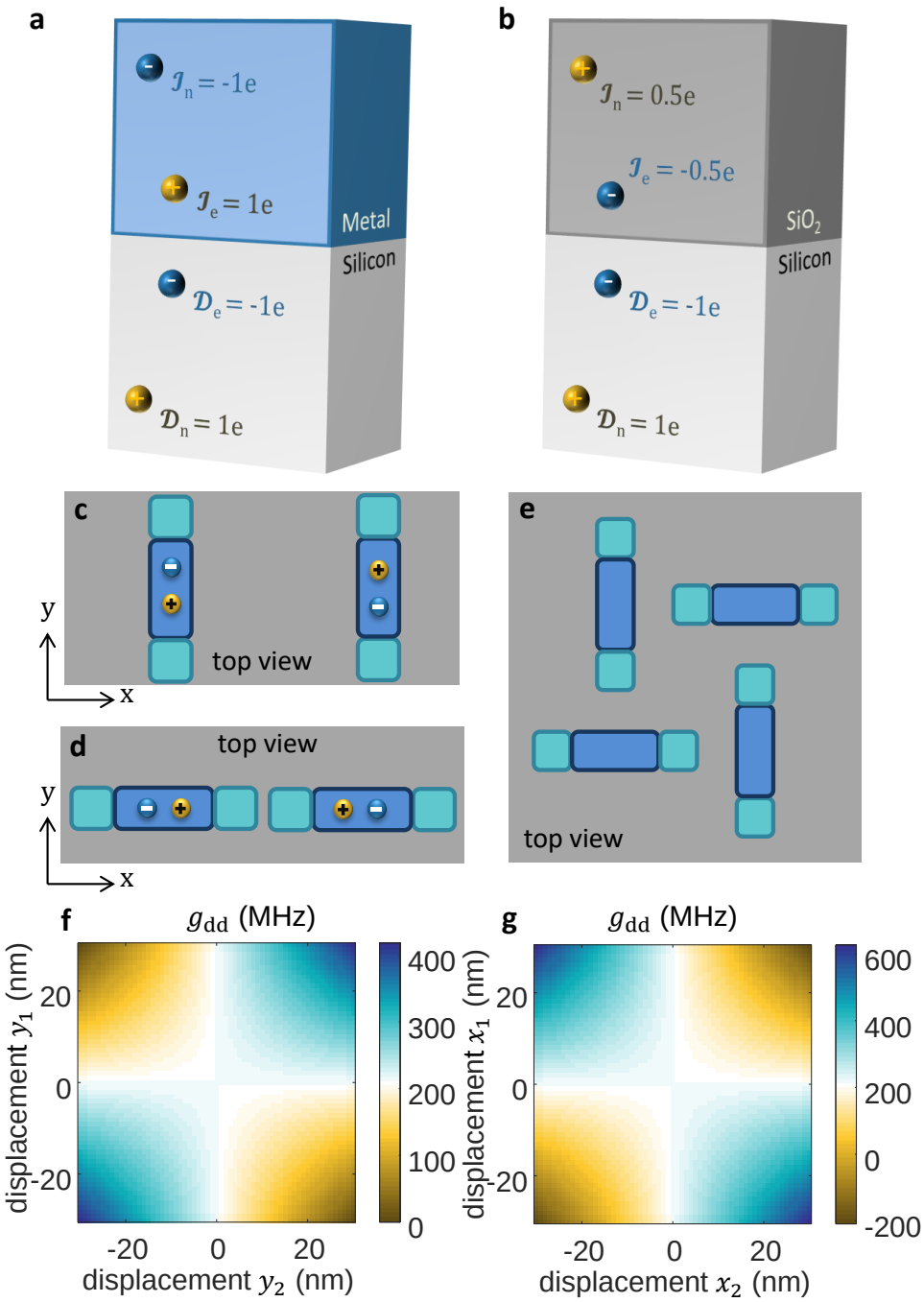

FIGURE 3.19: **Screening and image charges.** Image ($\mathcal{I}_e$ and $\mathcal{I}_n$) charges of the donor electron ($\mathcal{D}_e$) and nucleus ($\mathcal{D}_n$) for silicon-metal (**a**) and silicon-oxide (**b**) interfaces. The magnitude and polarity of the image charges are given by Eq. 3.60. Schematic top view of two interacting dipoles when the negative charges (blue spheres) are displaced in perpendicular (**c**) and parallel (**d**) direction to the inter-dipole separation. **e** Top view of a gate stack that tunes each qubit's V_t by displacing their interface states perpendicularly to their nearest neighbour displacement, leaving g_{dd} unchanged. Inter-dipole coupling g_{dd}, as predicted by Eq. (3.59) using Eq. (3.63), for the orientation shown in **c** (**f**) and **d** (**g**), for $r = 200$ nm, $d_1 = d_2 = 10$ nm and $Q = -0.5$.

defines the strength and polarity of the image charge according to the difference between the dielectric constant of silicon $\epsilon_{\mathrm{Si}} = 11.7$ and the SiO_2 interface $\epsilon_{\mathrm{I}} = 3.9$ or the metal interface $\epsilon_{\mathrm{I}} = \infty$ respectively[6]. Figs. 3.19a,b show the magnitude and polarity of the image charges for both types of interfaces. For simplicity, we assume in Fig. 3.19 and Eq. 3.60 that the donor electron as well as its image are point charges. Given that the separation between the two donors is at least 180 nm (more than hundred times the Bohr radius of the donor electron), the above assumption is valid when calculating their dipolar interaction.

Vertical dipole We first consider the electric dipole to be vertical. For the silicon-metal interface (Fig. 3.19a) we find $Q = -1$. Therefore the image charges have the opposite sign and same magnitude as the source charges. As a result, the total electric field E_{dip} from each donor will be enhanced by a factor of 2. This improves the electric dipole coupling g_{dd} between the two donors by a factor of 4. On the contrary, for the silicon-oxide interface (Fig. 3.19b), the image charges have the same sign and reduced magnitude ($Q = 0.5$) as the source charges, which decreases E_{dip} by half and therefore g_{dd} to a quarter of its bare value.

For a real device, which typically contains a few metal gates on top of a ~ 8 nm thick SiO_2, it is difficult to make a precise estimate of the extra electric field from image charges. Rahman *et. al.* [79] assumed that a combination of metallic and oxide screening effects yields $Q = -0.5$, corresponding to an improvement in the magnitude of the electric dipole by $\approx 50\%$, which yields an improvement in g_{dd} by 125%. This means that, while building a real device, one would have to aim for slightly larger inter-donor separations than the ones presented here.

Including a lateral dipole component Since the donor-interface tunnel coupling V_t has to be tuned to a precise value, the dipole will also have lateral components (insets of Fig. 3.10). These components will also be affected by image charges. In the case of a metallic interface (Fig. 3.19a), the lateral image dipole has opposite direction as the original one. Hence, in the far field, the two horizontal dipoles cancel each other out, leaving only an electric quadrupole which produces an electric field that decays like r^5. On the other hand, for the Si/SiO_2 interface (Fig. 3.19b), the lateral component of the dipole will be enhanced by 50%. Finally, for our assumed real structure ($Q = -0.5$), the lateral dipole will decrease to half its original value.

In total, the dipole size and orientation, including screening, will be:

$$\mathbf{D}_i = \mathbf{d}_i + Q \times (d_{i,x}, d_{i,y}, -d_{i,z}), \tag{3.62}$$

where $\mathbf{d}_i$ refers to the bare dipole, with x, y and z components $d_{i,x}$, $d_{i,y}$ and $d_{i,z}$, respectively.

As the image charges decrease a lateral dipole in a real device, the uncertainty in the total electric dipole of a donor-interface state is minimal, even when displacing the interface wavefunction laterally to tune up V_t. At $V_t \approx 10$ GHz, the vertical total dipole size (Fig. 3.2, $d_z = 11$ nm) is $(1 + 0.5)d_z = 16.5$ nm, while the total dipole size with a laterally displaced wavefunction (Fig. 3.10, $d_z = 5$ nm, $d_x = 25$ nm) is $\sqrt{[(1 + 0.5)d_z]^2 + [(1 - 0.5)d_x]^2} = 14.6$ nm. This is important for qubit reproducibility over a large scale processor.

[6]The dielectric constant describes how much the electric field due to the Coulomb force between two point charges in a material is reduced relative to vacuum. In a conductor, no electric field can exist. Hence, the dielectric constant is infinite.

To include images charges and angular dependencies, the dipole-dipole interaction term V_{dip} (Eq. 3.57), has to be modified to [107]:

$$V_{\text{dip}} = \frac{e^2}{16\pi\varepsilon_0\varepsilon_r h}\frac{\mathbf{D}_1\cdot\mathbf{D}_2 - 3(\mathbf{D}_1\cdot\mathbf{r})(\mathbf{D}_2\cdot\mathbf{r})/r^2}{r^3}, \tag{3.63}$$

Note, that we neglect the interaction of a dipole with its own charge since it does not produce inter-donor coupling.

Lateral displacement influence on the dipole-dipole coupling strength Laterally displacing the interface charge is also alters the total electric dipole direction and can therefore affect the dipole-dipole coupling g_{dd} between neighbouring qubits.

We first consider the case in which the displacements are perpendicular to the separation between dipoles (Fig. 3.19c). The g_{dd} dependence on y_1 and y_2 is plotted in Fig. 3.19f, for maximum displacements of 30 nm (enough to tune V_t by two orders of magnitude - see Fig 3.10b). It shows that, provided that the interface states are displaced along the same direction, g_{dd} only varies by a factor of two.

For completeness, we also analyze the case in which the interface states are displaced in the same direction as the inter-donor separation (Fig. 3.19d). Here, g_{dd} varies by a factor of three if the interface states are displaced in opposite directions.

Finally, the variation in g_{dd} can be reduced even further by fabricating the gate stack in such a way that the charges in neighbouring qubits are displaced in perpendicular directions (Fig. 3.19e). In this way, from Eq. (3.63), the only dipole terms contributing to the coupling are the vertical ones, and therefore g_{dd} is unchanged (to first order) while tuning V_t.

3.8.2 Two-qubit coupling

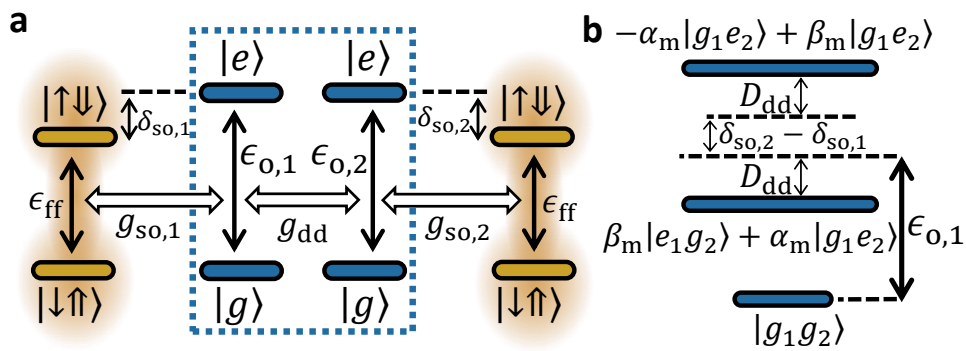

FIGURE 3.20: **Level diagrams two qubits coupled via electric dipole-dipole interactions.** **a** Two flip-flop qubits are coupling second-order by the dipole-interaction between their charge qubits. **b** Lowest molecular eigenstates for the two charge qubits inside dashed rectangle in **a**.

The electric dipole-dipole interaction provides a natural way to couple two distant flip-flop qubits since each flip-flop qubit is coupled to their electron position (Eq. 3.8, Fig. 3.20a). The two qubit system is described by the Hamiltonian

$$\mathcal{H}_{2q}^{\text{ff}} = \mathcal{H}_{\text{ff}}^1 + \mathcal{H}_{\text{ff}}^2 + \mathcal{H}_{\text{dip}}. \tag{3.64}$$

We compute the 2-qubit coupling strength between the singlet ground state and excited triplet state

$$|S\rangle = \frac{1}{\sqrt{2}}\left(|g_1 \uparrow_1 \Downarrow_1, g_2 \downarrow_2 \Uparrow_2\rangle - |g_1 \downarrow_1 \Uparrow_1, g_2 \uparrow_2 \Downarrow_2\rangle\right), \tag{3.65a}$$

$$|T\rangle = \frac{1}{\sqrt{2}}\left(|g_1 \uparrow_1 \Downarrow_1, g_2 \downarrow_2 \Uparrow_2\rangle + |g_1 \downarrow_1 \Uparrow_1, g_2 \uparrow_2 \Downarrow_2\rangle\right) \tag{3.65b}$$

from $\mathcal{H}_{2q}^{ff}$ as half of the corresponding eigenenergy difference. Fig. 3.21a shows the results at the ionization point

$$E_z^{0,2q} = E_z^0 - \frac{g_{dd}}{ed_i}, \tag{3.66}$$

which is shifted by the presence of the second qubit i, for a range of qubit distances r. The coupling rate exceeds 10 MHz around two narrow regions.

We also analyse the coupling as a function of electric field at a fixed inter-qubit distance of $r = 180\,\text{nm}$ (Fig. 3.21b) which also yields two regions with high coupling rates.

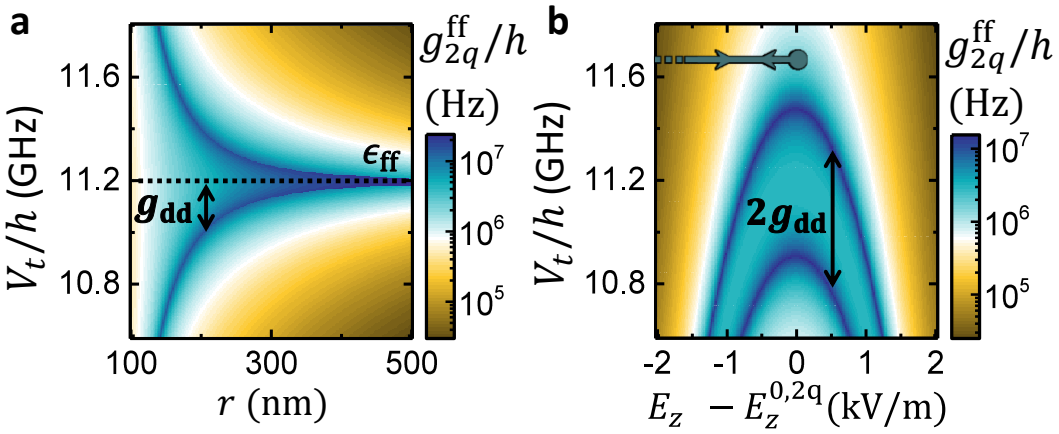

FIGURE 3.21: **Coupling rate between two flip-flop qubits.** Effective coupling between two flip-flop qubits as a function of $V_{t,1} = V_{t,2} = V_t$, inter-qubit distance r (**a**) and electric field $E_{z,1} = E_{z,2} = E_z$ (**b**). The arrows in **b** represent the adiabatic path followed for 2-qubit gates.

In these regions of high coupling the flip flop qubit is, while detuned from each individual charge qubit, in resonance with a molecular charge state. This molecular state is formed when the dipole coupling g_{dd} between the two charge qubits hybridizes the charge qubit states (Fig. 3.20b) such that the eigenstates are

$$\tilde{g} = |gg\rangle, \tag{3.67a}$$

$$\tilde{e}_1 = \beta_m |e_1 g_2\rangle + \alpha_m |g_1 e_2\rangle, \tag{3.67b}$$

$$\tilde{e}_2 = -\alpha_m |e_1 g_2\rangle + \beta_m |g_1 e_2\rangle, \tag{3.67c}$$

with (see App. A)

$$\alpha_m = \frac{1}{\sqrt{1+\Phi^2}} \tag{3.68a}$$

$$\beta_m = \frac{\Phi}{\sqrt{\Phi^2+1}}, \tag{3.68b}$$

where

$$\Phi = \frac{\delta_{\mathrm{so},2} - \delta_{\mathrm{so},1} + \sqrt{(\delta_{\mathrm{so},2} - \delta_{\mathrm{so},1})^2 + 4g_{\mathrm{dd}}^2}}{2g_{\mathrm{dd}}}. \tag{3.69}$$

While the coupling rates are high in this resonant regime, the charge qubits are also resonantly excited which induces relaxation errors. Therefore, it is best to detune the flip-flop qubits from the molecular states, while still keeping a substantial inter-qubit coupling rate, via a second-order process. The coupling rate between the flip-flop qubits in the dispersive regime is given by

$$g_{2\mathrm{q}}^{\mathrm{ff}} = g_{\mathrm{so},1} g_{\mathrm{so},2} \alpha_{\mathrm{m}} \beta_{\mathrm{m}} \left(\frac{1}{D_{\mathrm{dd}} - \delta_{\mathrm{so},1}} + \frac{1}{D_{\mathrm{dd}} + \delta_{\mathrm{so},2}} \right) \tag{3.70}$$

where

$$D_{\mathrm{dd}} = \frac{\delta_{\mathrm{so},2} - \delta_{\mathrm{so},1}}{2} \left(\sqrt{1 + \frac{4g_{\mathrm{dd}}^2}{(\delta_{\mathrm{so},2} - \delta_{\mathrm{so},1})^2}} - 1 \right) \tag{3.71}$$

the dispersive shift of the charge qubit eigenenergies due to the coupling between the two qubits (compare Sec. 3.2.3).

3.8.3 Two-qubit gates with optimized adiabatic pulse shapes

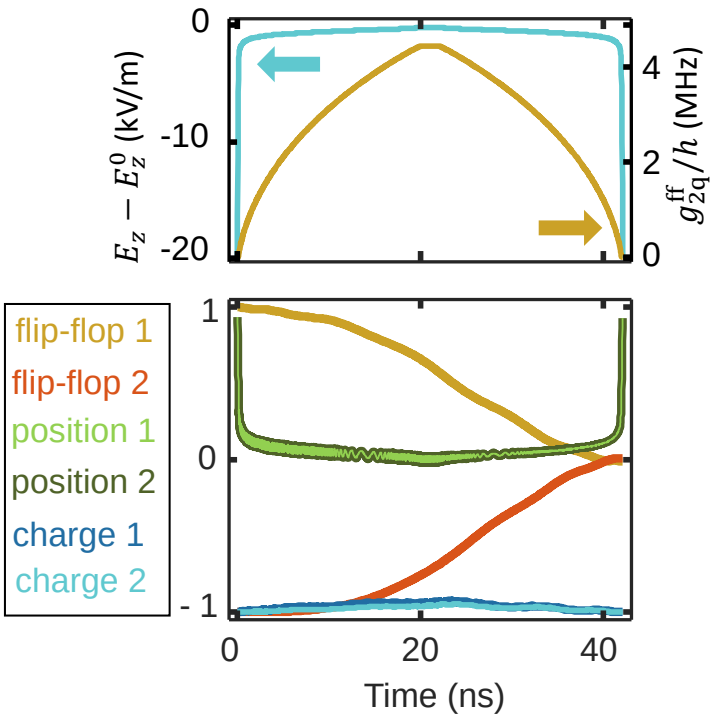

FIGURE 3.22: **Dynamics during an adiabatic $\sqrt{i\mathrm{SWAP}}$ gate between two distant flip-flop qubits.** Time evolution of an adiabatic $\sqrt{i\mathrm{SWAP}}$ gate, for $K = 30$, $r = 180$ nm, $B_0 = 0.4$ T and $V_t/h = 11.58$ GHz.

To perform high-fidelity two-qubit gates, we again use optimised adiabatic pulse shapes. We start with both electrons at the interface, where qubits are decoupled since the electric dipoles and the hyperfine interactions are first-order insensitive to vertical electric fields. Indeed, from Eq. (3.70), $g_{2\mathrm{q}}^{\mathrm{ff}}$ is negligible since g_{so} vanishes

and δ_{so} diverges. The electrons are then simultaneously and adiabatically displaced to the ionization point for a time necessary for an $\sqrt{i\text{SWAP}}$ gate, before returning to the interface (Fig. 3.22, with an adiabatic factor $K = 30$, trajectory indicated by arrows in Fig. 3.21b). Similarly to 1-qubit z gates (compare Sec. 3.5), the electron is first displaced on a fast time scale ($\sim$ 0.3 ns) set by the charge qubit parameters (ϵ_o and V_t), followed by a slower sweep ($\sim$ 19 ns) set by the spin-charge coupling parameters (δ_{so} and g_{so}), until it reaches the ionization point. The electron remains at the ionization point for a short time before the whole process is then reversed. In the end a $\sqrt{i\text{SWAP}}$ gate is performed. While some amount of charge is excited during the process, it goes back to its ground state, $|gg\rangle$, with an adiabatic error around 10^{-3}.

Overall, we find that the a two-qubit gate is best achieved by adiabatically bringing both qubits into resonance, in a similar fashion to the single qubit adiabatic z-gates.

Adiabatic 2-qubit gate errors

We quantify the 2-qubit gate fidelity in presence of the most deleterious noise types for our qubits, namely quasi-static E_z noise and charge-phonon relaxation. For this, we observe that the optimal gate fidelities are achieved when $E_z(\tau_{\sqrt{i\text{SWAP}}}/2) \approx E_z^0$. Similarly to 1-qubit x-gates, this happens because $\sqrt{i\text{SWAP}}$ gates are sensitive to gate time jitter, and therefore errors are minimized at the charge qubit clock transition where g_{2q}^{ff} is robust against E_z noise to first order (Fig. 3.21b and Eq. 3.70).

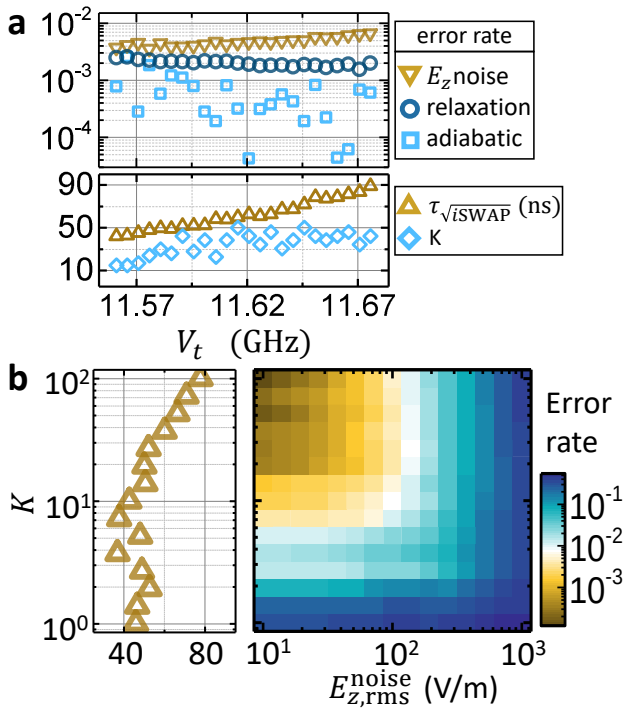

FIGURE 3.23: **Error rates for adiabatic $\sqrt{i\text{SWAP}}$ gates between two distant flip-flop qubits.** **a**, Optimized $\sqrt{i\text{SWAP}}$ gate error, gate time and adiabatic factor K for $r = 180$ nm and $B_0 = 0.4$ T. **b** Optimized error rate arising from quasi-static E_z-noise, for different noise amplitudes and adiabatic factor K (which sets the gate time) at $V_t/h = 11.58$ GHz.

We find the best adiabaticity K that minimizes errors due to E_z noise for each value of $V_{t,1} = V_{t,2} = V_t$ (Fig. 3.23a). Smaller detunings δ_{so} (small V_t) result in shorter

gate times, which in turn reduces errors from quasi-static noise. However, this also implies a larger admixture of charge in the qubit eigenstates, which slightly increases relaxation errors. The lowest error rates, $\sim 3 \times 10^{-3}$ are found at small detunings, $V_t - \epsilon_{\mathrm{ff}} - D_{\mathrm{dd}} \approx 100$ MHz ($V_t/h \approx 11.59$ GHz). At even smaller detunings, the 2-qubit coupling rate becomes too fast, requiring faster adiabatic sweeps to avoid over-rotation (lower K, Fig. 3.23a) and generating more leakage errors. The gate errors remain within $10^{-3} - 10^{-2}$ for a wide range of V_t.

Finally, we estimate how noise errors depend on the noise amplitude and adiabatic factor K, which sets the gate time (Fig. 3.23b). We find that a slower sweep (larger K) leads to less errors for low noise levels, same as for the 1-qubit gates (Fig. 3.17b).

Robustness against donor misplacement

Our proposed 2-qubit gates are not only well protected against noise, but also robust against donor misplacement. Variations in r, d_1 and d_2 mainly cause variations in the charge qubits' coupling g_{dd}, therefore simply changing the energy separation between molecular charge states (Fig. 3.20b). However, the coupling $g_{2\mathrm{q}}^{\mathrm{ff}}$ between the flip-flop qubits can be kept essentially constant by simply readjusting V_t (Sec. 3.4). Fig. 3.21a shows that one can keep a constant value of, for example, $g_{2\mathrm{q}}^{\mathrm{ff}} = 1$ MHz for any inter-donor spacing between 180 nm and 500 nm, by adjusting V_t/h between 11.3 GHz and 11.8 GHz.

In other words, since the flip-flop qubit coupling is mediated by a tunable interaction with their respective charge qubits, the inter-qubit interaction does not need to decay with r^3, as one would otherwise get when the dipole interaction couples the qubits directly [72], [77], but can stay constant over several hundred nanometers. Therefore, two-qubit operations can be turned on between pairs of qubits separated by many sites in a 2-dimensional array. This tunable long-range connectivity can be exploited to great advantage in large-scale quantum processors [108]. The large tolerance in g_{dd} also accommodates very well the donor depth uncertainties inherent to ion implantation [88], given the linear dependence of $g_{2\mathrm{q}}^{\mathrm{ff}}$ on d_i (Eqs. 3.57 and 3.59).

We conclude that our scheme provides a dramatic reduction in the fabrication complexity, especially compared to schemes that require placing a gate between a pair of tightly-spaced donors, such as the Kane's proposal [22], which requires $r \approx 15$ nm separation between two ^{31}P nuclear spins.

Note that, by relocating the problem of valley oscillations from the exchange interaction [22] to the tunnel coupling, we have effectively provided a way in which the delicate parameter can now be tuned using a much simpler gate geometry.

3.9 Scaling up using cQED

In order to reach the long-term goal of a large-scale quantum processor, wiring up the control and read-out lines for each individual qubit is not trivial, given the high density in typical spin qubit architectures [109]. Recent solutions include cross-wiring using multilayer lithography [72] or floating gate electrodes inspired by dynamic random access memory (DRAM) systems [110]. In both cases, using flip-flop qubits with long-distance interactions would result in widely spaced donors and loose fabrication tolerances. In addition, since flip-flop qubits are coupled via electric fields, they could be spaced further apart by using electrical mediators. These

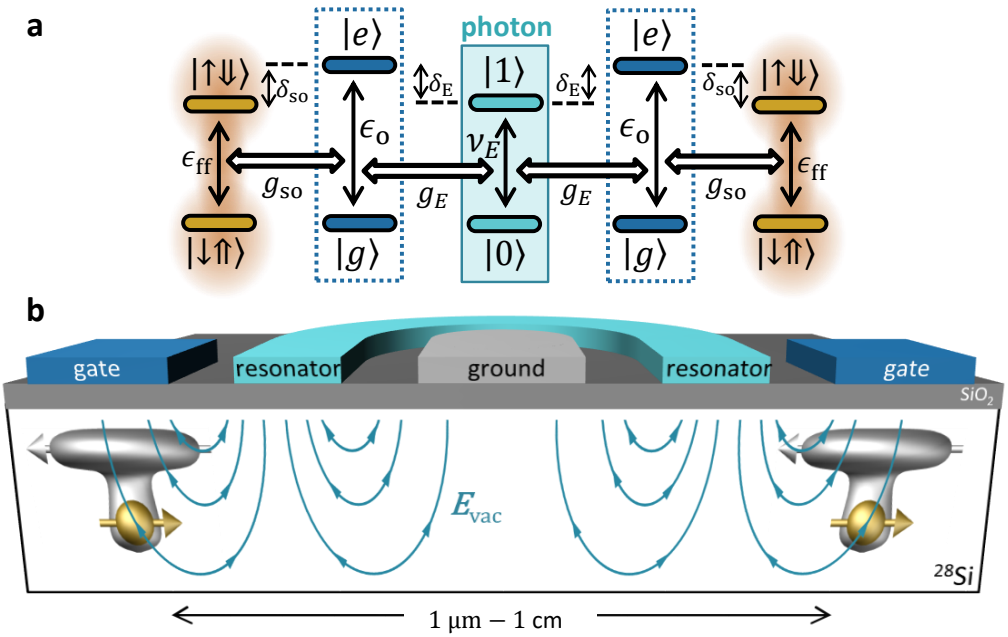

FIGURE 3.24: **Coupling to a single photon in a superconducting resonator.** **a** Level diagram for distant flip-flop qubit coupling via a photon in a microwave resonator, showing photon number states and off-resonant charge states. **b** Device schematic for coupling qubits via a photonic link. Distant donors, placed next to the resonator center line and biased to their ionization point, are subject to the vacuum electric field $\boldsymbol{E}_{\text{vac}}$ of a shared microwave resonator.

include floating metal gates [76] or even microwave resonators. Indeed, the use of electric dipole transitions allows a natural integration of donor-based spin qubits into a cQED architecture [54], [111]–[113] (see Fig. 3.24b for a possible device layout).

A photon of the resonator electric vacuum field couples to the charge qubit with coupling rate g_{E} (Eq. 3.35), with ν_E now representing the resonator fundamental mode frequency and E_{ac} the amplitude of the resonator vacuum field E_{vac}. More rigorously, we can determine the coupling rate g_{E} of the charge qubit to the resonator through analysis of their Jaynes-Cummings Hamiltonian

$$H_{\text{JC,orb}} = \frac{V_t}{2}\sigma_x - \frac{e\Delta V d}{2hs}\sigma_z, \tag{3.72}$$

where

$$\Delta V = \sqrt{\frac{\hbar\omega_{\text{r}}}{2C}}\left(\boldsymbol{a}^{\dagger} + \boldsymbol{a}\right) \tag{3.73}$$

is the voltage across the resonator (Eq. 2.46) and s the distance between the resonator ground plane and the central conductor (see. Fig. 6.4). This results in a coupling of

$$g_{\text{JC,E}} = \frac{ed}{2hs}\sqrt{\frac{\hbar\omega_{\text{r}}}{2C}} \tag{3.74}$$

close to the ionization point.

Again, it is best to have the charge excited state detuned from the flip-flop transition and resonator photon (Fig. 3.24a), therefore minimizing charge excitation while retaining a second-order flip-flop-photon coupling g_{E}^{ff} (Eq. 3.36). Assuming

z-gates		x(y)-gates			2-qubit $\sqrt{i\text{SWAP}}$ gates			Photonic link
τ_π	Error	$\tau_{\pi/2}$	Power	Error	Distance	$\tau_{\sqrt{i\text{SWAP}}}$	Error	Coupling
70 ns	10^{-4}	30 ns	< 1 pW	10^{-3}	100 - 500 nm	40 ns	10^{-2} - 10^{-3}	$g_E^{\text{ff}}/\text{h} = 3$ MHz

FIGURE 3.25: **Gate performance summary**. Figures of merit summarizing the speed and error rates of different gate schemes presented in this chapter, assuming realistic noise sources.

$\delta_{\text{so}} \approx \delta_E \approx 10 g_{\text{so}} \approx 10 g_E$, a $z_d = 15$ nm deep ^{31}P flip-flop qubit would be coupled to photons at a $g_E^{\text{ff}}/h \approx 3$ MHz rate.

This coupling rate is three orders of magnitude faster than the electron-spin coupling rate to a resonator via its magnetic vacuum field [114], [115], and comparable to the coupling strength obtained by using strong magnetic field gradients [116], [117], but without the need to integrate magnetic materials within a superconducting circuit. This assumes a vacuum field amplitude $E_{\text{vac}} \approx 30$ V/m, which can be obtained by using tapered coplanar waveguide or high-impedance resonators [118].

The possibility of coupling the qubits to microwave photons provides a path for dispersive qubit readout, as well as for photonic interconnects. Near-quantum limited amplifiers have recently become available to obtain excellent readout speed and fidelities [119].

The resonator can also be used as a quantum bus to couple two spin qubits separated by as far as 1 cm (Fig. 3.24b), a distance given by the mode wavelength, at a coupling rate of [54]

$$g_{2\text{q}}^{\text{ff}} \approx (g_{\text{E}}^{\text{ff}})^2/\delta_{\text{E}}^{\text{ff}}, \tag{3.75}$$

where $\delta_E^{\text{ff}} = \nu_E - \epsilon_{\text{ff}}$ is the detuning between the resonator and the qubit. To avoid losses from photon decay, the qubits should be detuned from the resonator (Fig. 3.24a) by an amount much greater than the qubit-photon coupling rates. Assuming $\delta_E^{\text{ff}} = 10 g_E^{\text{ff}}$, the effective 2-qubit coupling $g_{2\text{q}}^{\text{ff}}/h \approx 0.3$ MHz yields a $\sqrt{i\text{SWAP}}$ gate that takes only 0.4 μs.

Thus, microwave resonators could be also used to interface donors with superconducting qubits [120], [121], for the long-term goal of a hybrid quantum processor that benefits from the many advantages of each individual architecture [112].

3.10 Conclusion

In conclusion, we have presented a way to encode quantum information in the electron-nuclear spin states of implanted ^{31}P donors in silicon which enables fast, high-fidelity, electrically-driven universal quantum gates.

The key figures of merit of our flip-flop qubits coupled by electric dipole interactions are summarized in Fig. 3.25. Fast 1-qubit x-gates are attainable with low electric drive power and error rates $\sim 10^{-3}$. 2-qubit $\sqrt{i\text{SWAP}}$ gates are fast and with error rates approaching 10^{-3}. At the end of all operations, the phase of each qubit can be corrected, via adiabatic z-gates, in fast time scales and low error rates $\sim 10^{-4}$. These values are based on current experimentally known values of charge noise in silicon devices [98], and are possibly amenable to improvement through better control of the fabrication parameters. More advanced control pulse schemes could allow for faster gates with less leakage [122]–[124], and active noise cancellation techniques, *e.g.* pulses for gate time jitter [125] or decoherence [126] suppression, could further improve gate fidelities.

Consequently, our proposal provides a credible pathway to the construction of a large-scale quantum processor as it not only features qubits with low error rates, compatible with fault-tolerant quantum error correction but also enables large qubit spacing, not requiring atomic-scale precision in the qubit placement.

Chapter 4

The nuclear spin qubit with an electric dipole transition

"I've yet to see any problem, however complicated, which when you looked at it the right way didn't become still more complicated."
–Poul Anderson, *Call Me Joe*

The nuclear spin state of a phosphorus donor in isotopically enriched ^{28}Si is an excellent host to store quantum information in the solid state. The spin's insensitivity to electric fields yields a solid-state qubit with record coherence times but also renders coupling to other quantum systems very challenging. In this chapter, we describe how to generate a strong electric dipole ($>$ 100 D) at microwave frequencies for the nuclear spin. This is achieved by applying a magnetic drive to the electrically driven flip-flop qubit. The dipole then allows for coupling to microwave resonators, with a vacuum Rabi splitting of the order of 1 MHz. This work brings the ^{31}P nuclear qubit into the realm of hybrid quantum systems and opens up new avenues in quantum information processing.

The work presented in this chapter has been published in:
G. Tosi, F. A. Mohiyaddin, **S. Tenberg**, A. Laucht, A. Morello. "Robust electric dipole transition at microwave frequencies for nuclear spin qubits in silicon", *Physical Review B* Vol. 98, 075313 (2018).

The author acknowledges G. Tosi for the conception of the idea and large parts of the simulation work and F. A. Mohiyaddin for tight-binding simulations and electric modelling. The author helped develop the project, interpret the results, assisted with simulations and constructed parts of the theoretical framework.

4.1 Introduction

The nuclear spin of a phosphorus donor in silicon has long been the subject of much study in the context of solid-state quantum information processing, either as a qubit cell for large-scale quantum processors [22], [72], [77], or a memory for long-lived quantum information storage [127], [128]. Whether in ensemble form [60] or as individual qubit [30], the ^{31}P nuclear spin has record-long coherence times, thanks to its insensitivity to charge noise and the possibility to drastically reduce magnetic environmental noise by hosting it in isotopically pure ^{28}Si [65]. However, as it is well isolated, it cannot trivially be coupled to other quantum systems, and therefore all quantum computing proposals so far impose short interaction distances and slow quantum gate operations [22], [72], [77].

In the hybrid approach to quantum information processing [112], different quantum systems interact in a large architecture that benefits from the best properties of each system, which are often coupled together via microwave resonators. In order to couple to individual spin qubits, the resonator vacuum field can be enhanced by shrinking its dimensions in the vicinity of the spin qubit, thereby enhancing the spin-photon coupling rate [114], [115], [129], [130]. However, having a Zeeman splitting in the radio-frequency range and a null electric dipole, phosphorus nuclear-spins do not interact naturally with microwave resonators.

The artificial creation of electric dipole transitions has been proposed for different spin systems [114], [131]–[134], as a way to facilitate scalability. The challenge is how to make the spin drivable by electric fields without making it too susceptible to electrical noise, which is significant in nanoscale electronic devices. In this chapter, we show how to engineer a strong electric dipole transition at microwave frequencies for the nuclear spin, based on the flip-flop qubit and our findings from Chap. 3, by applying an oscillating magnetic field to the nucleus while the electron is shared between the donor and a quantum dot defined at the Si/SiO_2 interface [25], [80], [83], [114]. While the admixture of spin and charge states can potentially make the system very sensitive to electric noise, we show that the nuclear spin precession frequency and electric dipole strength can be rendered highly immune to electrical noise by a specific choice of spin-charge hybridization, same than for the flip-flop qubit. By providing a robust coupling between the nuclear spin and electric fields, our scheme opens up new avenues to couple ^{31}P qubits to other quantum systems, including microwave resonators, superconducting qubits, or simply other nuclear spins but at distances and with rates that had not been anticipated so far.

4.2 Second-order Raman drive of a ^{31}P nuclear spin

Usually, the phosphorus nuclear (electron) spin is coherently driven by conventional magnetic resonance using an oscillating magnetic field at radio (microwave) frequencies [41] (Chap. 2.3.2). In particular, the nuclear spin transition frequency when the electron spin is $|\downarrow\rangle$ (i.e. the $|\downarrow\Uparrow\rangle \leftrightarrow |\downarrow\Downarrow\rangle$ transition) is:

$$\epsilon_{\mathrm{ns}}(A) = \gamma_n h B_0 + hA/2. \tag{4.1}$$

Now however, to create an electric dipole transition, we drive the nuclear spin via a Raman transition, such that it is coupled via a second-order process to the flip-flop qubit.

Driving a Raman transition requires a three-level Λ system (Fig. 4.1), where two stable states $|0\rangle, |1\rangle$ are coupled via a higher radiative virtual state $|2\mathrm{v}\rangle$, which is

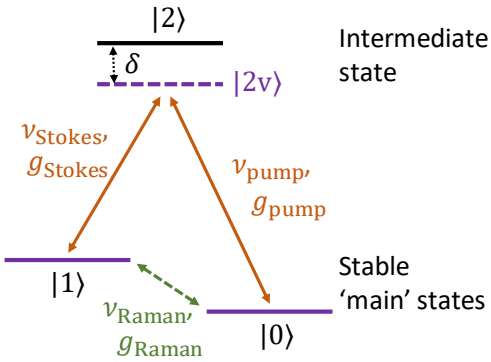

FIGURE 4.1: **Raman Λ transition.** A three-level system with stable states $|0\rangle, |1\rangle$ and intermediate state $|2\rangle$ enables a Raman drive. The Raman transition $|0\rangle \leftrightarrow |1\rangle$ is driven via the virtual level $|2v\rangle$ with driving fields of frequency ν_{pump} and ν_{Stokes}. The detuning δ between $|2\rangle$ and $|2\text{v}\rangle$ is large in comparison with the couplings g_{Stokes} and g_{pump} of the driving fields.

detuned by δ from an intermediate state $|2\rangle$. Two fields with frequency ν_{Stokes} and ν_{pump} couple the states $\{|1\rangle, |2\rangle\}$ with strength g_{Stokes} and $\{|0\rangle, |2\rangle\}$ with strength g_{pump} respectively[1]. In a Stokes Raman process the energy $h\nu_{\text{pump}} - h\nu_{\text{Stokes}}$ is absorbed to drive the Raman transition ν_{Raman} with strength [135], [136]

$$g_{\text{Raman}} = \frac{g_{\text{pump}} g_{\text{Stokes}}}{\delta}. \tag{4.2}$$

In the electron-nuclear spin system, the stable states are the flip-flop state $|\downarrow\Uparrow\rangle$ and the "nuclear" state $|\downarrow\Downarrow\rangle$, while the intermediate state is the flip-flop state $|\uparrow\Downarrow\rangle$ (Fig. 4.2b). The flip-flop transition is driven with a microwave electric field (the pump field) with coupling strength g_{E}^{ff} (Eq. 3.36). The electron transition $|\downarrow\Downarrow\rangle \leftrightarrow |\uparrow\Downarrow\rangle$ is driven via a magnetic microwave drive $B_{\text{ac}}\cos(2\pi\nu_B t)$ (ESR, Stokes field), perpendicular to the static B_0 (Fig 4.2a), with a Hamiltonian

$$\mathcal{H}_{\text{ESR}} = hB_{\text{ac}}\cos(2\pi\nu_B t)\left(\gamma_e \boldsymbol{S_x} - \gamma_n \boldsymbol{I_x}\right) \tag{4.3}$$

and coupling strength

$$g_B = \langle\downarrow| \mathcal{H}_{\text{ESR}} |\uparrow\rangle = \gamma_e h B_{\text{ac}}/4. \tag{4.4}$$

Consequently, the Hamiltonian describing this system is

$$\mathcal{H}_{\text{ns}} = \mathcal{H}_{\text{ff}} + \mathcal{H}_{\text{E}} + \mathcal{H}_{\text{ESR}}. \tag{4.5}$$

With the electron in the ground spin state $|\downarrow\rangle$, the AC electric and magnetic fields drive the nuclear-spin "up", $|\downarrow\Uparrow\rangle$, and "down", $|\downarrow\Downarrow\rangle$, states, respectively, to a virtual level detuned from the $|\uparrow\Downarrow\rangle$ state by $\delta \gg g_B, g_E^{\text{ff}}$. As a result, the nuclear spin is driven via a second order Raman process, with minimal excitation of the electron spin, at a rate (Eq. 4.2)

$$g_E^{\text{ns}} = \frac{g_B g_E^{\text{ff}}}{\delta}. \tag{4.6}$$

This Raman process provides a way of controlling the nuclear spin state without any radiofrequency field, by using instead two microwave-frequency excitations,

[1]The coupling g corresponds to half the Rabi frequency.

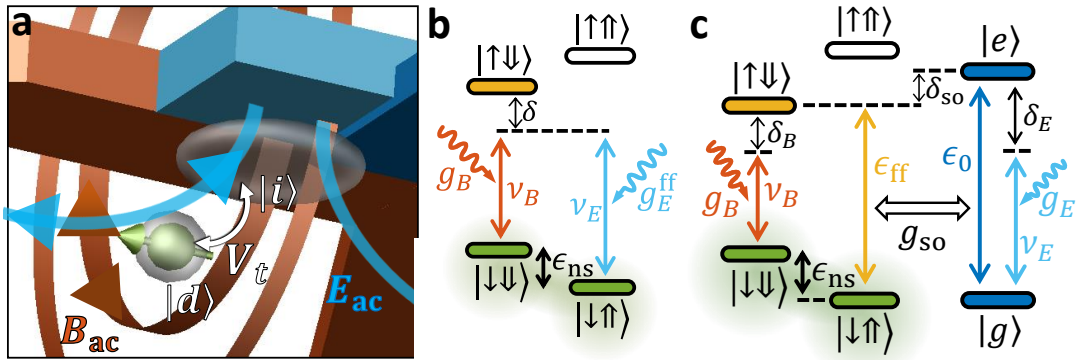

FIGURE 4.2: **Nuclear Raman transition.** **a** Components of a Raman-enabled Si:P nuclear electric dipole transition. The electron spatial wavefunction (transparent gray) is shared between an interface-dot, $|i\rangle$, and a donor-bound state, $|d\rangle$, coupled by a tunnel rate V_t, such that a charge qubit is formed. Metallic gates (blue) on top of SiO_2 dielectric (not shown) control the charge qubit via a static vertical field E_{dc}, and can introduce an oscillating electric field E_{ac}, controlling the flip-flop states. In a cQED setup, the electrostatic gate can be replaced by the inner conductor of a microwave resonator, and E_{ac} by the vacuum field of such resonator. A nearby broadband antenna [68] (orange) provides the magnetic drive B_{ac}. **b** Energy level diagram for Raman-drive of the Si:P nuclear-spin qubit, with energy splitting ϵ_{ns}. The second-order Raman drive is obtained by combining the microwave electric flip-flop drive and a magnetic ESR drive, having frequencies ν_B and ν_E, and coupling rates g_B and g_E^{ff}, respectively. The drive is detuned by a frequency δ from the $|\uparrow\Downarrow\rangle$ state. **c** Expanded energy diagram including the charge states, that enable the electric flip-flop drive.

one of which is the local electric flip-flop drive (Fig. 4.2a). This has important advantages over magnetic-only schemes [127], [128], since it allows coupling a nucleus to the vacuum electric field of a microwave cavity, or to another nucleus similarly equipped with an electric dipole, as we will show below.

The nuclear Raman transition can be interpreted such that the microwave magnetic drive B_{ac} creates an electric dipole transition for the nuclear spin mediated by the flip-flop qubit, with strength:

$$p_E^{ns} = \frac{4g_E^{ns}}{E_{ac}} = \frac{4g_B g_E^{ff}}{E_{ac}\delta}. \tag{4.7}$$

The coupling g_E^{ff} between the flip-flop qubit and the AC electric field corresponds to a strong electric-dipole flip-flop transition ($\sim$ 80 Debye, assuming $\delta_{so} = 10g_{so}$). Combining the strong flip-flop drive with the magnetic drive at rate g_B (Eq. 4.6) results in a strong electric dipole transition for the nuclear spin ($\sim$ 8 Debye, assuming $\delta = 10g_B$).

However, since the nuclear transition frequency depends linearly on A (Eq. 4.1), and A is a very sensitive function of electric field near the donor ionization point (Fig. 3.4), electrical noise in the device will cause fast dephasing of the nuclear precession.

4.3 Robust electric dipole transition of a Si:P nuclear spin

4.3.1 Electron, nuclear and charge hybridization

We now show that, by adopting a specific choice of device tuning, the nuclear spin can be made largely insensitive to electrical noise, while having its electric dipole

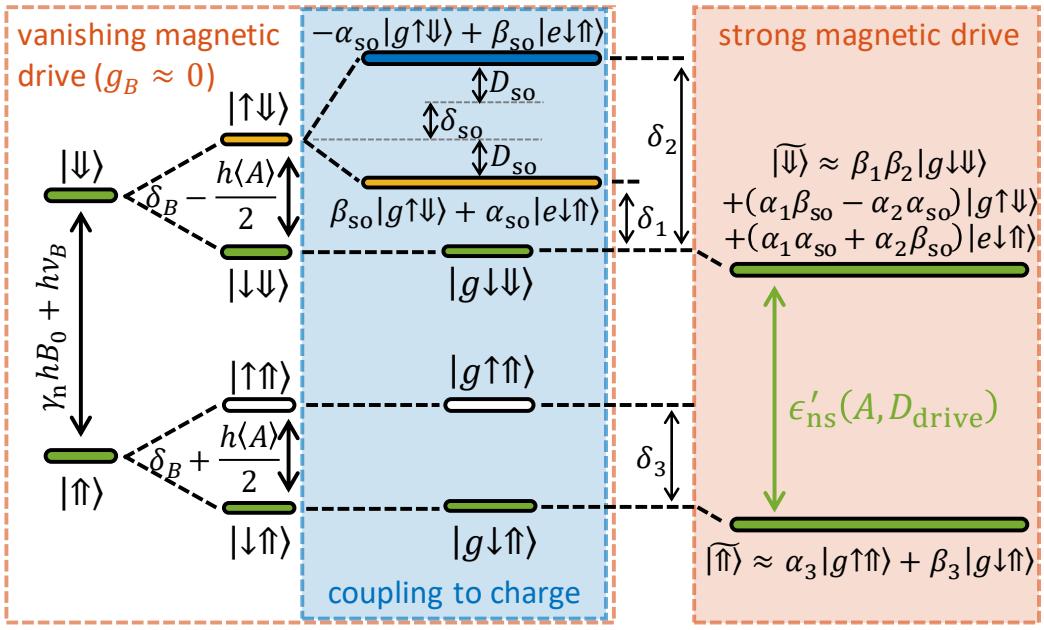

FIGURE 4.3: **Nuclear spin level diagram with a strong magnetic drive in the rotating frame.** Nuclear spin levels in the rotating frame of the magnetic drive B_{ac} at frequency ν_B. From left to right, the system eigenstates are shown while adding the electron spin state, then the charge state, then increasing the strength of the magnetic drive. See main text for a detailed description.

transition increased even further. This is achieved by tuning all qubit levels in resonance: the charge qubit is in resonance with the flip-flop qubit ($\epsilon_o \approx \epsilon_{ff}$, i.e. $\delta_{so} \approx 0$), the magnetic drive is in resonance with the electron spin ($\delta_B = \gamma_e hB_0 - h\langle A\rangle/2 - h\nu_B \approx 0$), and the electric drive is in resonance with the flip-flop (and charge) qubit ($\delta_E \approx 0$). In this strongly hybridized regime, second-order perturbation theory can not be directly applied. We therefore analyse the nuclear spin Hamiltonian H_{ns} by expressing it in the rotating frame of the magnetic drive by using the transformation:

$$\mathcal{H}' = \boldsymbol{U}^\dagger \mathcal{H}_{ns} \boldsymbol{U} - i\hbar \boldsymbol{U}\dot{\boldsymbol{U}}^\dagger, \tag{4.8a}$$

$$\boldsymbol{U} = e^{i2\pi\nu_B t(S_z + I_z)}. \tag{4.8b}$$

We get

$$i\hbar \boldsymbol{U}\dot{\boldsymbol{U}}^\dagger = h\nu_B\left(\boldsymbol{S_z} - \boldsymbol{I_z}\right) \tag{4.9}$$

and with $\cos(2\pi\nu_B t) = \frac{1}{2}\left(e^{i2\pi\nu_B t} + e^{-i2\pi\nu_B t}\right)$ follows

$$\boldsymbol{U}\mathcal{H}_{ESR}\boldsymbol{U}^\dagger = \frac{hB_{ac}}{2}\left[\gamma_e \begin{pmatrix} 0 & e^{2\cdot i2\pi\nu_B t} + 1 \\ e^{-2\cdot i2\pi\nu_B t} + 1 & 0 \end{pmatrix} - \gamma_n \begin{pmatrix} 0 & e^{2\cdot i2\pi\nu_B t} + 1 \\ e^{-2\cdot i2\pi\nu_B t} + 1 & 0 \end{pmatrix}\right]. \tag{4.10}$$

We neglect the counter-rotating terms, according to the rotating wave approximation and arrive at the transformed Hamiltonian

$$\mathcal{H}' = \underbrace{(\gamma_e hB_0 - h\nu_B)}_{\delta_B}\boldsymbol{S_z} - (\gamma_n hB_0 + h\nu_B)\boldsymbol{I_z} + \frac{hB_{ac}}{2}\left(\gamma_e \boldsymbol{S_x} - \gamma_n \boldsymbol{I_x}\right) + \mathcal{H}_{orb} + \mathcal{H}_A^{orb} + \mathcal{H}_E, \tag{4.11}$$

where the magnetic drive is time-independent.

The dominant energy scale in the above Hamiltonian is given by the term $-(\gamma_n h B_0 + \nu_B h)\boldsymbol{I_z}$, which represents the energy splitting of the nuclear spin states, but shifted to microwave frequencies by the transformation to the rotating frame of the magnetic drive. The corresponding energy levels are shown as $|\Uparrow\rangle, |\Downarrow\rangle$ at the left-most end of Fig. 4.3. These levels are further split due to the electron spin states, by $(\delta_B + h\langle A\rangle I_z)\, S_z + 2g_B S_x$, where the expectation value of the hyperfine coupling $\langle A\rangle$ depends on the electron charge state, yielding the electron-nuclear spin levels shown in Fig. 4.3, depicted in the limit of vanishing B_{ac} (and therefore g_B) (compare Fig. 3.6). In this case, the nuclear-spin transition frequency, in the rotating frame, with the electron in the ground state, is:

$$\epsilon'_{\mathrm{ns}}(A) = \gamma_n h B_0 + h\nu_B + h\langle A\rangle/2. \tag{4.12}$$

In Fig. 4.4a we plot $\epsilon'_{\mathrm{ns}}(A)$ (dashed line) by including the dependence of $\langle A\rangle$ on vertical electric field E_{dc} (Eq. 3.9). This is valid when the electron charge states are far detuned from the spin levels ($\delta_{\mathrm{so}} \gg g_{\mathrm{so}}$). The plot highlights the strong dependence of ϵ'_{ns} on electric fields under such conditions.

However, the nuclear spin dispersion changes dramatically when δ_{so} approaches zero. In that case, $\mathcal{H}_A^{\mathrm{orb}}$ hybridizes the flip-flop and charge states, as shown in the blue panel within Fig. 4.3. The overall ground state is $|g\downarrow\Uparrow\rangle$, but the excited flip-flop state splits into two hybridized states $\beta_{\mathrm{so}}|g\uparrow\Downarrow\rangle + \alpha_{\mathrm{so}}|e\downarrow\Uparrow\rangle$ and $-\alpha_{\mathrm{so}}|g\uparrow\Downarrow\rangle + \beta_{\mathrm{so}}|e\downarrow\Uparrow\rangle$, with (compare Sec. 3.2.3, Eq. 3.15)

$$\alpha_{\mathrm{so}} = \frac{1}{\sqrt{\phi_{\mathrm{so}}^2+1}}, \quad \beta_{\mathrm{so}} = \frac{\phi_{\mathrm{so}}}{\sqrt{\phi_{\mathrm{so}}^2+1}}, \quad \text{where} \quad \phi_{\mathrm{so}} = \frac{\delta_{\mathrm{so}} + \sqrt{{\delta_{\mathrm{so}}}^2 + 4{g_{\mathrm{so}}}^2}}{2g_{\mathrm{so}}}, \tag{4.13}$$

so that $\alpha_{\mathrm{so}} = \beta_{\mathrm{so}} = 1/\sqrt{2}$ for $\delta_{\mathrm{so}} = 0$.

As a final step, by increasing the magnetic drive amplitude B_{ac}, the Hamiltonian term $2g_B S_x$ couples the electron spin $|\uparrow\rangle$ and $|\downarrow\rangle$ states, further hybridizing the system eigenstates $|g\downarrow\Downarrow\rangle$ with the hybridized flip-flop states as well as $|g\uparrow\Uparrow\rangle$. Two of those eigenstates, which we call $\widetilde{|\Downarrow\rangle}$ and $\widetilde{|\Uparrow\rangle}$ (Fig. 4.3, orange box), are chiefly composed of the tensor product of the nuclear $|\Downarrow\rangle$, $|\Uparrow\rangle$ states with the ground charge state $|g\rangle$ and the ground $|\downarrow\rangle$ electron spin state. They are obtained as:

$$\widetilde{|\Downarrow\rangle} \approx \beta_1\beta_2|g\downarrow\Downarrow\rangle + (\alpha_1\beta_{\mathrm{so}} - \alpha_2\alpha_{\mathrm{so}})|g\uparrow\Downarrow\rangle + (\alpha_1\alpha_{\mathrm{so}} + \alpha_2\beta_{\mathrm{so}})|e\downarrow\Uparrow\rangle, \tag{4.14}$$

$$\widetilde{|\Uparrow\rangle} \approx \alpha_3|g\uparrow\Uparrow\rangle + \beta_3|g\downarrow\Uparrow\rangle, \tag{4.15}$$

with coefficients α_i, β_i ($i = 1,2,3$) given by (analogous to Eq. (3.15), App. A):

$$\alpha_1 = \frac{1}{\sqrt{{\phi_1}^2+1}}, \quad \beta_1 = \frac{\phi_1}{\sqrt{{\phi_1}^2+1}}, \quad \phi_1 = \frac{\delta_1 + \sqrt{{\delta_1}^2 + (2\beta_{\mathrm{so}}g_B)^2}}{2\beta_{\mathrm{so}}g_B}, \tag{4.16a}$$

$$\alpha_2 = \frac{1}{\sqrt{{\phi_2}^2+1}}, \quad \beta_2 = \frac{\phi_2}{\sqrt{{\phi_2}^2+1}}, \quad \phi_2 = \frac{\delta_2 - \sqrt{{\delta_2}^2 + (2\alpha_{\mathrm{so}}g_B)^2}}{2\alpha_{\mathrm{so}}g_B}, \tag{4.16b}$$

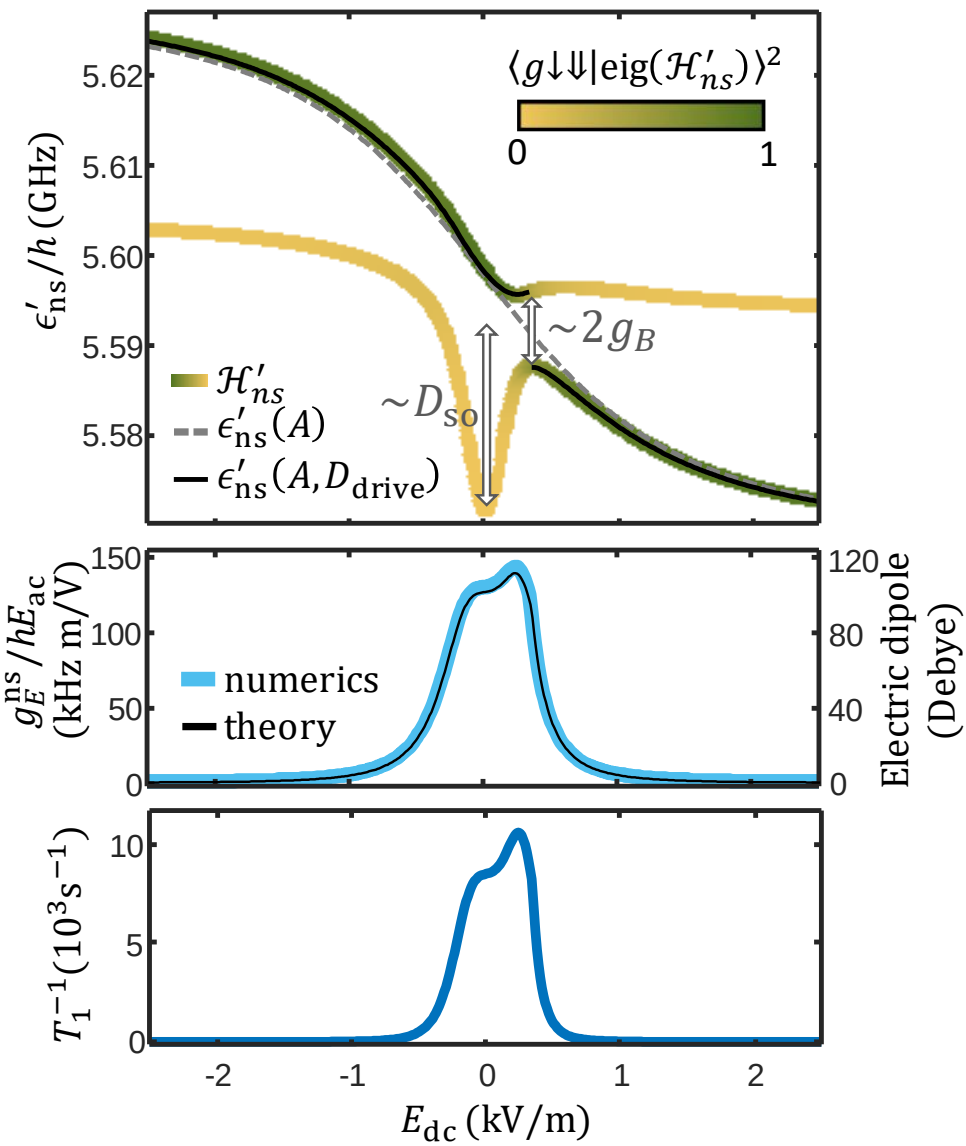

FIGURE 4.4: **Nuclear qubit dispersion, dipole strength and relaxation. a** Nuclear spin transition frequency ϵ'_{ns} in the rotating frame of the magnetic drive B_{ac}, as a function of the static vertical electric field E_{dc} across the donor-dot system, for vanishing magnetic drive ($\epsilon'_{\mathrm{ns}}(A)$ – Eq. 4.12, grey dashed line) and strong magnetic drive ($\epsilon'_{\mathrm{ns}}(A, D_{\mathrm{drive}})$ – Eq. 4.17, black solid line). We have assumed $B_0 = 0.2$ T, $B_{\mathrm{ac}} = 0.6$ mT, $d = 15$ nm, $V_t \approx \epsilon_{\mathrm{ff}}$ and $\nu_B \approx \gamma_e B_0 - A/4$ (since $\langle A\rangle = A/2$ at the ionization point). Green/yellow lines show transition frequencies calculated numerically from the Hamiltonian in Eq. 4.11. The color indicates the degree of admixture of the bare $|g\downarrow\Downarrow\rangle$ state into the higher $\mathcal{H}'_{ns}$ eigenstate corresponding to each transition. The nuclear spin transition (predominantly $|g\downarrow\Uparrow\rangle \leftrightarrow |g\downarrow\Downarrow\rangle$, green) anticrosses a flip-flop transition (predominantly $|g\downarrow\Uparrow\rangle \leftrightarrow |g\uparrow\Downarrow\rangle$, yellow) at $E_{\mathrm{dc}} = 350$ V/m, with a splitting $\sim 2g_B$ set by the strength of the magnetic drive. The flip-flop transition is strongly shifted by D_{so}, due to its coupling to the charge qubit states around $E_{\mathrm{dc}} = 0$. At $E_{\mathrm{dc}} = 250$ V/m, the nuclear-spin excited eigenstate has $\sim 75\%$ of $|g\downarrow\Downarrow\rangle$ and is robust against electrical noise ($\partial\epsilon'_{\mathrm{ns}}/\partial E_{\mathrm{dc}} = 0$). **b** Nuclear electric dipole strength $p_E^{\mathrm{ns}} = \partial g_E^{\mathrm{ns}}/\partial E_{\mathrm{ac}}$ obtained from Eqs. 4.19 (theory, black line), or for numerical diagonalization of the full Hamiltonian $\mathcal{H}'$ under E_{ac} drive (numerics, light blue line). For the choice of parameters used in this figure, p_E^{ns} peaks where $E_{\mathrm{dc}} = 250$ V/m. **c** Nuclear spin relaxation rate $1/T_{1,\mathrm{ns}}$ in the presence of the magnetic drive B_{ac} and the effect of coupling to phonons via charge states, Eq. 4.20.

$$\alpha_3 = \frac{1}{\sqrt{{\phi_3}^2+1}}, \quad \beta_3 = \frac{\phi_3}{\sqrt{{\phi_3}^2+1}}, \quad \theta_3 = \frac{\delta_3 - \sqrt{{\delta_3}^2 + 4{g_B}^2}}{2g_B}. \tag{4.16c}$$

The energy splitting between $|\widetilde{\Downarrow}\rangle$ and $|\widetilde{\Uparrow}\rangle$, ϵ'_{ns}, equals the bare nuclear-spin transition, $\epsilon'_{\text{ns}}(A)$ (Eq. 4.12), plus an amount that dependents on E_{dc}:

$$\epsilon'_{\text{ns}}(A, D_{\text{drive}}) = \epsilon'_{\text{ns}}(A) - D_{\text{drive}}(E_{\text{dc}}), \tag{4.17}$$

where D_{drive} is a dispersive shift given by perturbation theory to (analogous to Eqs. 3.18, 3.71):

$$D_{\text{drive}}(E_{\text{dc}}) = \sum_{i=1,2,3} \frac{\delta_i}{2} \left(\sqrt{1 + \left(\frac{2g_i}{\delta_i}\right)^2} - 1 \right), \tag{4.18a}$$

$$g_1 = \beta_{\text{so}} g_B, \quad g_2 = -\alpha_{\text{so}} g_B, \quad g_3 = g_B. \tag{4.18b}$$

This equation agrees with numerical simulations of the full Hamiltonian in the rotating frame of Eq. (4.11) (Fig. 4.4a). Around the ionization point, the flip-flop transition (itself strongly affected by the hybridization with the charge state) anti-crosses the nuclear spin transition (in the rotating frame), creating a region where $\partial\epsilon'_{\text{ns}}/\partial E_{\text{dc}} = 0$, i.e. a first-order 'clock transition' [90], [137] where ϵ'_{ns} is insensitive to electric noise to first order. Further adjustment of the parameters allows for $\partial^2\epsilon'_{\text{ns}}/\partial {E_{\text{dc}}}^2 = 0$ (second-order clock transition), improving noise insensitivity even further.

In a key result of our proposal, the small admixture of the excited charge state, $|e\rangle$, into $|\widetilde{\Downarrow}\rangle$ creates an electric-dipole transition for the nuclear spin. Indeed, the $|\widetilde{\Downarrow}\rangle \leftrightarrow |\widetilde{\Uparrow}\rangle$ transition can be electrically-driven at a rate given by the charge admixture coefficients in Eq. 4.16:

$$g_E^{\text{ns}} = g_E \beta_3 \left(\alpha_1 \alpha_{\text{so}} + \alpha_2 \beta_{\text{so}}\right). \tag{4.19}$$

This electric dipole transition, at microwave frequencies, can reach > 100 Debye around $E_{\text{dc}} = 0$ (Fig. 4.4b). This means that even an extremely weak AC electric field, $E_{\text{ac}} \approx 3\,\text{V/m}$, can drive a nuclear spin transition at a megahertz Rabi frequency. This is two orders of magnitude faster than the typical Rabi frequencies obtained with standard (NMR) magnetic drive at radiofrequency [41], and an order of magnitude faster than obtained (at very high electric drive amplitudes) in a recent experiment where electrically-driven NMR was achieved by modulating the quantization axis of the electron spin [138].

4.3.2 Resilience against charge noise

The issue of charge noise is of paramount importance in semiconductor spin qubits. It is known, experimentally and theoretically, that charge fluctuators yield a $1/f$ frequency dependence of the noise spectral density [95]. These models capture the averaged collective effect of many charge fluctuators on the qubit operation. In this case, charge noise results in a slow drift of the qubit electrostatic environment. Indeed, since individual qubit operations take less than a microsecond, the qubit environment is usually static within a single operations, but fluctuates in between operations. On the basis of typical experimental values of charge noise found in literature [98], we estimate a 1.7 μeV r.m.s. noise amplitude in our system, which, given the

distance between donor and interface $d \approx 15$ nm, corresponds to an r.m.s. noise on the amplitude of the vertical electric field of order 100 V/m (refer to Sec. 3.7 for a detailed noise discussion). Inserting this noise magnitude into our model of the qubit dephasing rate (Eq. 3.20) yields a predicted nuclear spin dephasing rate of order $1 - 10 \times 10^3\,\mathrm{s}^{-1}$. Note that, similarly to dressed states [105], [139], [140], the addition of the strong magnetic drive has the effect of extending the coherence of our qubit. However, here the suppressed noise is of electrical nature (despite the drive being magnetic), given the particular hybridization with charge states.

We thus derived the striking result that the nuclear spin has a strong electric dipole despite being robust against electrical noise. This is because, while the qubit precession frequency is insensitive to noise, its effective transverse matrix element is strongly dependent on electric fields. Importantly, the electric dipole is induced on the nuclear spin only around the flip-flop transition frequency, which is at several gigahertz. Since the charge and gate noise in nanoscale devices mainly has a $1/f$ spectrum, the power spectral density of the noise at the frequency that would affect the nuclear qubit is expected to be very weak. Moreover, at the same bias point where the clock transition ($\partial\epsilon'_{\mathrm{ns}}/\partial E_{\mathrm{dc}} = 0$) for the nuclear energy takes place, the nuclear electric dipole itself is also first-order insensitive to electrical noise, since $\partial g_E^{\mathrm{ns}}/\partial E_{\mathrm{dc}} = 0$ (Fig. 4.4b). A realistic 1.5 μeV charge detuning noise [98] would make g_E^{ns} fluctuate by only $\sim 2\%$. In other words, in this system both the free precession frequency and the Rabi frequency can be made first-order insensitive to charge noise.

As a final note, although we assumed $\delta_{\mathrm{so}} \to 0$, the electric and magnetic driving fields are still off-resonance with the eigenstates of the full Hamiltonian $\mathcal{H}_{\mathrm{ns}}$ due to the hybridized charge-flip-flop states, ensuring minimal excitation of the $|\uparrow\rangle$ and $|e\rangle$ states.

4.3.3 Coupling to microwave cavity photons

This strong electric dipole at microwave frequencies provides a pathway for strongly coupling ^{31}P nuclear spins to microwave resonators [54], where a vacuum field E_{vac} of a few V/m can result in vacuum Rabi splittings around 1 MHz. This could be achieved *e.g.* by connecting the top blue gate on Fig. 4.2a to the center pin of a superconducting coplanar waveguide resonator. Our proposal thus provides a solution to the fact that the standard (NMR) nuclear-spin transition does not naturally couple to microwave resonators. Similarly to other proposals [111], [141]–[143], here it is a classical drive (B_{ac}) that enables coupling to a quantum field (E_{vac}).

4.3.4 Nuclear spin relaxation

The engineered nuclear electric dipole also opens up a new pathway for nuclear spin relaxation: $|\widetilde{\Downarrow}\rangle$ can decay into $|\widetilde{\Uparrow}\rangle$ through a peculiar effect, where a photon from the driving field is combined with the nuclear spin energy (which is at radiofrequency) to emit a phonon at microwave frequency. The rate for this process can be roughly estimated as the admixture of the $|e\rangle$ charge excited state into the $|\widetilde{\Downarrow}\rangle$ eigenstate times the charge relaxation rate $1/T_{1,\mathrm{c}}$ (Eq. 3.21):

$$\frac{1}{T_{1,\mathrm{ns}}} = \frac{|\langle\widetilde{\Downarrow}|e\rangle|^2}{T_{1,\mathrm{c}}} \approx \frac{|\alpha_1\alpha_{\mathrm{so}} + \alpha_2\beta_{\mathrm{so}}|^2}{T_{1,\mathrm{c}}}. \tag{4.20}$$

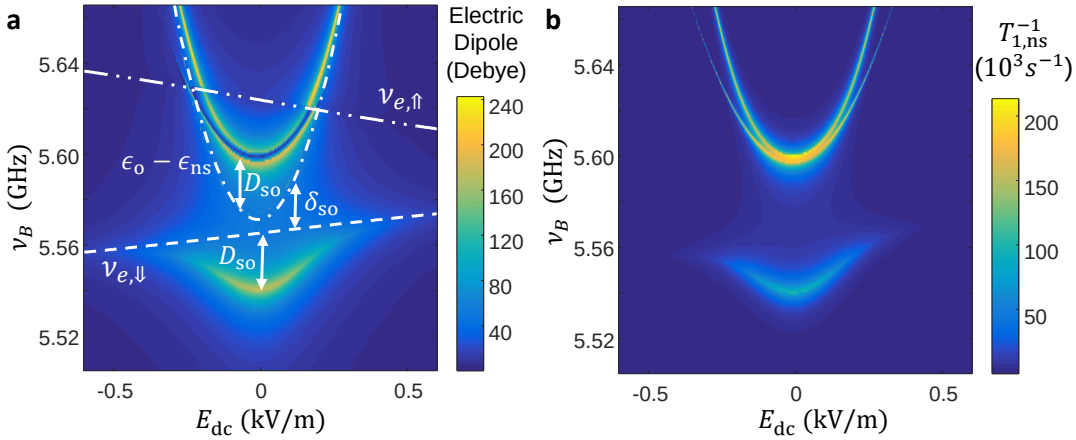

FIGURE 4.5: **Nuclear electric dipole strength and relaxation as a function of electric field.** **a** Nuclear electric dipole strength p_E^{ns} and **b** nuclear spin relaxation rate $1/T_{1,\mathrm{ns}}$, as a function of the donor-dot electric field detuning, E_{dc}, and the magnetic drive frequency, ν_B. $E_{\mathrm{dc}} = 0$ is the ionization point. In **a**, the dashed line shows the ESR frequency $\nu_{e,\Downarrow}$ when the nuclear spin is in the $|\Downarrow\rangle$ state, the dot-dashed line shows the charge qubit frequency minus the nuclear spin frequency, $\epsilon_{\mathrm{o}}/h - \epsilon_{\mathrm{ns}}/h$, and the dot-dot-dashed line the electron spin resonance frequency $\nu_{e,\Uparrow}$ when the nuclear spin is in the $|\Uparrow\rangle$ state. The charge and flip-flop states are detuned by δ_{so}, which is close to zero at $E_{\mathrm{dc}} = 0$. Charge and flip-flop states then hybridize, shifting the system eigenenergies by an AC-Stark shift D_{so}. The plots in Figs. 4.4b,c correspond to specific line cuts of the graphs shown here, for $\nu_B = \nu_{e,\Downarrow}$ at $E_{\mathrm{dc}} = 0$, *i.e.* $\nu_B = 5.565$ GHz.

As Fig. 4.4c shows, $1/T_{1,\mathrm{ns}}$ peaks, around the ionization point, at a value that is still two orders of magnitude slower than e.g. the spin's coupling rate to a microwave resonator, therefore allowing the strong coupling regime to be well within reach.

4.3.5 Dependence of electric dipole strength and spin relaxation rate on frequency and field detuning

In Fig. 4.4 we have shown an operation point ($E_{\mathrm{dc}} = 250$ V/m, $B_0 = 0.2$ T and $\nu_B = 5.565$ GHz) where the proposed nuclear spin electric dipole transition is robust against noise, i.e. both its precession frequency, ϵ'_{ns}, and electric dipole strength, $p_{\mathrm{ns}}^E = g_E^{\mathrm{ns}}/E_{\mathrm{ac}}$, are to first order insensitive to small perturbations of the static electric field. To understand how the system behaves when slightly detuned from the optimal working point, we calculate the dependence of the nuclear spin electric dipole strength p_{ns}^E and relaxation rate $1/T_{1,\mathrm{ns}}$ on the magnetic drive frequency, ν_B, and on the static electric field, E_{dc} (Fig. 4.5). Both plots show two branches (bright yellow) where both dipole moment and relaxation rate are enhanced. To understand these branches, we refer to the level diagrams in Figs. 4.2b,c. First, note that ν_B unequivocally sets the electric dipole transition frequency ν_E (in the simplest case, $\nu_E = \nu_B + \epsilon_{\mathrm{ns}}/h$). The two bright branches in Fig. 4.5 correspond to ν_E being in resonance with either of the two charge-flip-flop hybridized states (yellow and blue states inside the light blue rectangle in Fig. 4.3). If the charge and flip-flop states were uncoupled or off-resonance, then the lower branch would simply correspond to the flip-flop dipole transition, $\nu_E = \nu_{e,\Downarrow} + \epsilon_{\mathrm{ns}}/h$ (where $\nu_{e,\Downarrow}$ is the electron spin resonance frequency when the nuclear spin is in the 'down' state), which means that the magnetic drive frequency simply coincides with the electron spin resonance $\nu_B = \nu_{e,\Downarrow}$. This would represent a simple, on-resonance Raman transition, i.e. as in the sketch

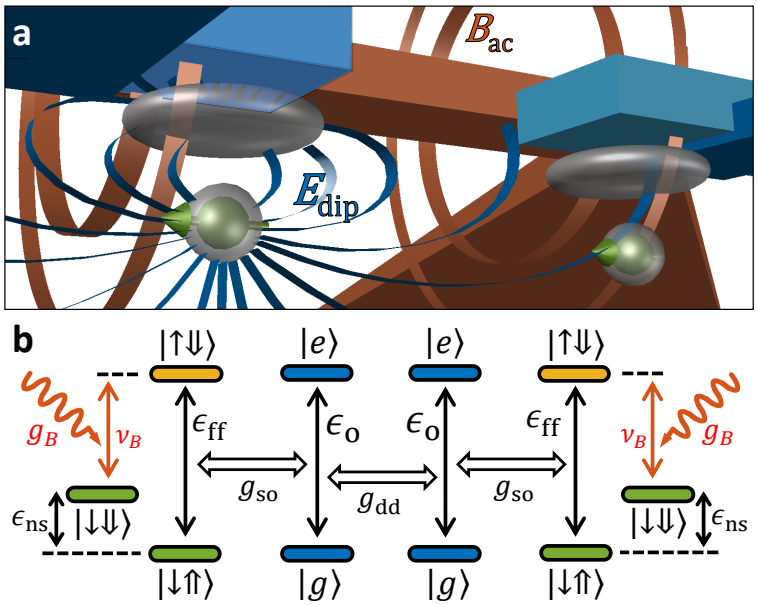

FIGURE 4.6: **Long distance coupling of two nuclear qubits.** **a** Components and **b** level diagram for long-distance coupling of two ^{31}P nuclear spins via electric dipole-dipole interactions. Each displaced electron produces an electric dipole field E_{dip} (shown only for one electron). The charge dipoles induced by displacing the electron wavefunction partly towards the interface dot interact with a strength g_{dd} (Eq. 3.59), and the charge qubits interact with the flip-flop states with strength g_{so} (Eq. 3.10). Adding the (global) magnetic drive of strength g_B and tuning the system to the fully-hybridized regime described in Sec. 4.3 results in a nuclear-nuclear coupling strength $g_{2\text{q}}^{\text{ns}} \approx 0.55$ MHz at a 400 nm distance (Eq. 4.21).

in Fig. 4.2b but where $\delta = 0$. Then, the upper branches in Fig. 4.5 would correspond to the pure charge transition, $\nu_E = \epsilon_o/h$, or equivalently $\nu_B = \epsilon_o/h - \epsilon_{\text{ns}}/h$. However, since the charge and flip-flop states are coupled, they hybridize and further split the two branches by an amount equal to D_{so}.

Upon closer inspection, the upper branch shows an extra subtle feature. This branch corresponds to excitation conditions that put the magnetic drive frequency close to the electron spin resonance frequency when the nuclear spin is in the $|\Uparrow\rangle$ state, $\nu_{e,\Uparrow}$. This, in turn, creates a pair of dressed electron spin states that further split the upper branch into two, separated by the ESR (magnetic) Rabi frequency of the $\nu_{e,\Uparrow}$ resonance.

4.4 Long-distance coupling of nuclear spin qubits

We have shown in the previous section that a robust electric dipole at microwave frequencies is induced on the nuclear spin by the magnetic drive B_{ac}, combined with the spin-charge hybridization that is obtained by displacing the electron from the donor towards an interface quantum dot. A natural and important extension of this effect is to exploit the induced electric dipole to achieve a long-distance coupling of the nuclear spins, mediated by long-range electric dipole interaction, similar to coupling two distant the flip flop qubits (Sec. 3.8, Fig. 4.6a). This dipole interaction between two charge qubits results in a coupling of g_{dd} (Eq. 3.59).

Two distant nuclear spin qubits can then be coupled when both electrons are around their ionization point, and an AC magnetic drive B_{ac} is applied (Fig. 4.6a,b) to each of them, resulting in the electric dipole p_E^{ns} at microwave frequencies. For

the operation parameters used in Fig. 4.4, $\epsilon_o \approx \epsilon_{ff} \approx h\nu_B + \epsilon_{ns}$ and $g_B \ll g_{so}$, the two-qubit coupling rate is obtained as:

$$g_{2q}^{ns} = \left(\frac{g_B}{g_{so}}\right)^2 g_{dd}, \tag{4.21}$$

which is valid if $g_B \ll (g_{so})^2/g_{dd}$. For two nuclear spins $r = 400$ nm apart, $g_{2q}^{ns} = 0.55$ MHz, yielding a $\sqrt{i\text{SWAP}}$ gate time of ~ 230 ns. To put this in perspective, the Kane's proposal [22] described a system of two ^{31}P nuclear spins placed $r = 15$ nm apart, where a $\sqrt{i\text{SWAP}}$ gate mediated by the electron spin exchange interaction requires 3 μs - an order magnitude slower, for over an order of magnitude tighter spacing. A recent proposal by Hill et al. [72] describes a CNOT gate between nuclear spins mediated by the electron magnetic dipole interaction, wherein the 2-qubit gate time requires 300 μs for donors spaced 30 nm apart - three orders of magnitude slower than the electric-dipole mediated gate we have introduced here.

This method of coupling nuclear spin qubits at long distances via their induced electric dipole can be switched off completely - $p_E^{ns} \approx 0$ when the electron charge is moved back to the donor - thus offering great flexibility in how multi-qubit operations are undertaken in a large array of qubits. The magnetic drive B_{ac} necessary to induce the dipole can be a global, always-on field, acting on every donor in the array. This can be optimally achieved by placing the device in a three-dimensional microwave cavity with good B_{ac} homogeneity [144]. Alternatively, B_{ac} could be delivered locally using a grid of microwave striplines [108]. The "robust" mode of operation described in Sec. 4.3 requires $\delta_B \approx 0$, i.e. B_{ac} in resonance with the electron spin transition. However, this resonance condition must be met while the donor is at the ionization point, where the hyperfine coupling is approximately half the value it has while the electron is fully at the donor ($\langle A \rangle \approx A/2$), thus $\nu_B \approx \gamma_e B_0 - A/4$. Therefore, idle qubits with the electron resting at the donor will be left unaffected by the global magnetic drive, and completely decoupled from both electric and magnetic AC-fields.

4.5 Conclusion

The exceptional quantum coherence of ^{31}P nuclear spins in isotopically enriched ^{28}Si is experimentally well established [30], [60]. However, it has been widely accepted that using the ^{31}P nuclear spin as the physical qubit in a quantum computer architecture requires dealing with the very small nuclear magnetic dipole, which renders operation and multi-qubit coupling slow and cumbersome [22], [72], [77], even with inter-donor spacings ~ 10 nm. Indeed, most of the recent focus on ^{31}P nuclei for quantum information has been on using them as long-lived quantum memories [127], [128] rather than data qubits.

By engineering an electric dipole transition, we have shown here that the ^{31}P qubit can also be driven at microwave frequencies, and coupled to other nuclei or to microwave cavities via electric dipole interactions, thus making it also a convenient system as a data qubit. The effects of electrical noise can be strongly suppressed by operating around clock transitions, which allow the ^{31}P system to retain dephasing times in the $0.1 - 1$ ms range. The nuclear spin, equipped with an artificial electric dipole, can then be incorporated into large hybrid quantum architectures [112] where - in analogy to flip-flop qubits - large arrays of nuclear qubits couple either by electric dipole-dipole coupling or via cavity microwave photons (see Chap. 5). In

such architectures, the spacing between qubits can be several hundreds of nanometers, leaving ample space for classical interconnects [145], [146] and readout devices, fabricated using conventional silicon nanoelectronics fabrication methods.

Chapter 5

Building a quantum processor

"Think big. Think fast. Think ahead. Ideas are no ones monopoly."
–Dhirubhai Ambani

The ultimate aim of quantum computing - a high stakes competition - is a fault-tolerant large scale quantum computer, that is capable of solving relevant, complex problems. In this chapter we present our bet at it, employing the advances the flip-flop and nuclear qubit bring. We present ideas ranging from an immediately achievable small quantum processor to a large scale architecture.

Parts of the work presented in this chapter have been published in:
G. Tosi, F. A. Mohiyaddin, V. Schmitt, **S. Tenberg**, R. Rahman, G. Klimeck, A. Morello. "Silicon quantum processor with robust long-distance qubit couplings." *Nature communications* vol. 8, 450 (2017).
G. Tosi, F. A. Mohiyaddin, **S. Tenberg**, A. Laucht, A. Morello. "Robust electric dipole transition at microwave frequencies for nuclear spin qubits in silicon." *Physical Review B* vol. 98, 075313 (2018).

The author acknowledges G. Tosi for the conception of the idea and J. O'Gorman for discussions about fault-tolerant quantum computation.

5.1 Quantum Error Correction

Efficient quantum algorithms use large arrays of entangled qubits, whose quantum states are fragile. Any interference from the environment and imprecisions in the operations lead to a loss of the quantum information and induce errors into the algorithm. Hence, large scale quantum computation is all but impossible unless all errors are accounted for.

To make qubits robust against errors, logical qubits are encoded in multiple physical qubits, similar to classical error correction. However, the principles, which make quantum information fundamentally different from classical information, have to be considered while implementing quantum error correction [147]. Most importantly, quantum information cannot be cloned, which means that it cannot be copied as in classical systems. Moreover, the number of error processes is infinite as qubits are coupled to a continuum of environmental states, and any measurement of a qubit state destroys the quantum information it contains. The principles of quantum error correction are explained briefly in this section. More detailed information and a generous overview is given in Refs. [147], [148].

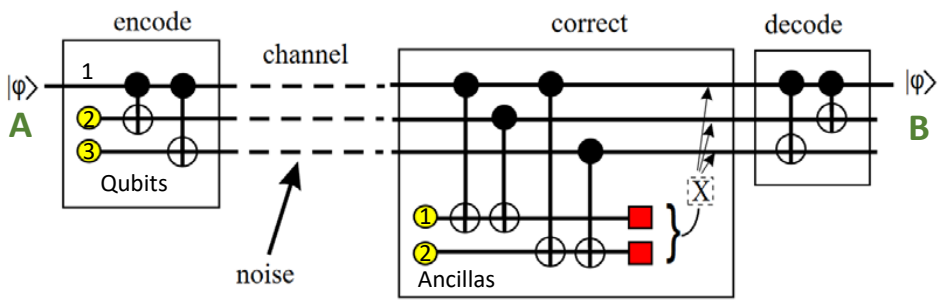

FIGURE 5.1: **Simple example of quantum error correction**. The information $|\varphi\rangle$ is transferred from A to B, encoded in three qubits with controlled-NOT operations. Errors are detected by two ancilla qubits through two controlled-NOT operations each. The error syndrome, acquired by the readout of the ancillas, gives the information to correct the errors. Finally the information is recovered at B, after decoding. The figure is adapted from Ref. [149].

A simple quantum error correction scheme is presented in Fig. 5.1, where the information $|\varphi\rangle = a\,|0\rangle + b\,|1\rangle$ is transferred from A to B. We initialize two additional qubits in state $|0\rangle$ to detect and correct errors caused by noise. Thus, the total initial state is

$$|\varphi\rangle = a\,|000\rangle + b\,|100\rangle\,. \tag{5.1}$$

Now, we encode the information in all three qubits, forming a logical qubit. Therefore we perform an entangling controlled-NOT gate between the first and second and the first and third qubit sequentially. A controlled-NOT gate inverts the state of the second qubit when the first qubit is in state 1. Hence, the encoded state reads

$$|\varphi'\rangle = a\,|000\rangle + b\,|111\rangle \tag{5.2}$$

and is sent out towards B. During the information transfer, noise may have changed the qubits' states and introduced errors. To gather information about the noise, we add another pair of qubits, called ancillas, prepared in state $|00\rangle$. We perform controlled-NOT gates from the first and second received qubits to the first ancilla

Error syndrome	Error type	Action
00	no error	nothing
01	bit-flip on qubit 3	σ_x to qubit 3
10	bit-flip on qubit 2	σ_x to qubit 2
11	bit-flip on qubit 1	σ_x to qubit 1

TABLE 5.1: **Quantum error correction with three qubits and two ancillas.** The measurement of the ancillas yields the error syndrome which contains the information which error occurred and where. Thus, the error can be corrected.

and then from the first and third received qubits to the second ancilla. Now we measure both ancilla qubits to gain information about their state, called error syndrome. The error syndrome contains information if an error occurred and where, such that the error can be corrected (Tab. 5.1).

Describing error correction codes in form of the encoded states' vector representation, as has been done here, is inconvenient as it will differ between different codes. A general method for error correction, with which most error correction codes can be described, is the stabilizer formalism [150]. It describes quantum states in terms of operators in the Heisenberg picture. If a state $|\psi\rangle$ is in the positive eigenstate of an operator K

$$K|\psi\rangle = |\psi\rangle\,, \tag{5.3}$$

it is stabilized by K. For a single qubit, $K \in \mathcal{P}$, where

$$\mathcal{P} = \{\pm\mathbb{1}, \pm i\mathbb{1}, \pm\sigma_x, \pm i\sigma_x, \pm\sigma_y, \pm i\sigma_y, \pm\sigma_z, \pm i\sigma_z\} \tag{5.4}$$

is the Pauli group. For N qubits the group can be extended by taking the N-fold tensor product of all elements of $\mathcal{P}$. Some well known stabilizer states are the two-qubit Bell states, Greenberger-Horne-Zeilinger (GHZ) states [151] and Cluster states [152]. Error detection in a stabiliser code is achieved by measuring all stabilizers K to acquire the error syndrome.

To accomplish fault-tolerant quantum computing, "a single error will cause at most one error in the output for each logical qubit block" [148]. This leads to the threshold theorem, which implies that for a finite error rate p per physical qubit, the logical qubit error can be made arbitrarily small by concatenating many encoding levels which correct errors. The threshold for the physical error rate is determined by $p_{\text{th}} < 1/c$, where c is given by the probability of two errors or more occurring at the physical qubit level while an error correction cycle is running.

Most efficient quantum error correction codes with low error thresholds of $10^{-3} - 10^{-2}$ like the Bacon-Shor code [153], [154] and the surface code [56], [57], require a 2D qubit architecture with nearest-neighbour interactions, where error-detection measurements can be performed at several locations simultaneously. Otherwise, errors cannot be as quickly detected as they are generated. While in 1D architectures error correction can still be performed to form a logical qubit [155], [156], an extension to many logical qubits is not possible.

In the following section we will present ideas, how a logical qubit can be implemented with donors in silicon, as well as how a large scalable quantum processor could be build.

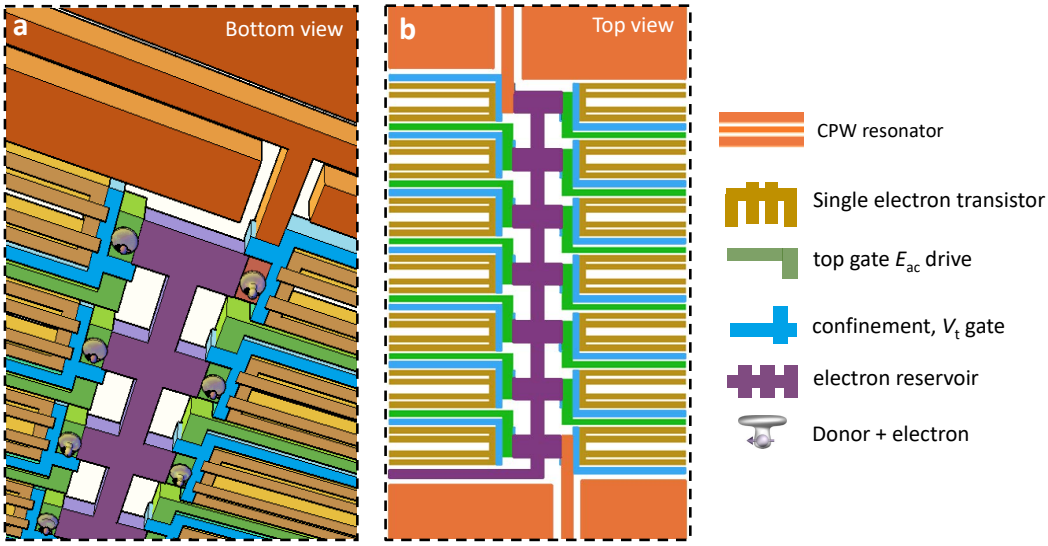

FIGURE 5.2: **Qubit cell out of 14 flip-flop qubits**. Bottom (**a**) and top (**b**) view of schematic of a small-scale qubit array which is feasible to build with current fabrication standards in our laboratory. 14 flip-flop qubits are coupled via dipole-dipole interaction to their nearest-neighbours and next-nearest neighbours. Electrons can be loaded via a central reservoir (purple) and each qubit is read-out via a SET (yellow). Long range connections to other 14-qubit cells are also possible by coupling one qubit to a CPW resonator.

5.2 Quantum processor architectures

The flip-flop and the nuclear qubit, presented in Chaps. 3 and 4, are excellent building blocks for a large scale quantum processor due to their long range couplings and low error rates.

Firstly however, we present a small-scale qubit array, that only uses current standar university fabrication techniques (Chap. 6.2) and can be fabricated in our laboratory. The array consists out of 14 flip-flop qubits that are connected via dipole-dipole interaction to their nearest-neighbours and next-nearest neighbours. The electrons can be loaded onto the donor via a central reservoir (purple). Readout is performed via a SET (yellow) for each individual qubit. This architecture is basically a linear array, although it does allow for cross-coupling between qubits and consequently offers more flexibility. In such an array, we can encode one logical qubit robust against errors [155]–[158] and implement Shor's 9 qubit code, where the remaining 5 qubits are needed for error detection [159]. Long range connections to other 14-qubit cells can be added by coupling one qubit to a CPW resonator to extend the computing capabilities.

In the long run, we need a large-scale quantum processor of millions of qubits to outperform classical computers [160]. Fig. 5.3 shows a design aimed to accommodate many qubits. We incorporate large 2D arrays of dipolar coupled flip-flop qubits with CPW resonators. Here, the size of the 2D flip-flop arrays is limited by the space required by read-out and control lines. In this case advanced error-correction codes may be implemented [55], [58], [59], [161]. The limitation of this design is given by the size of the 2D array and the capability of operating many stabilizer measurements simultaneously. This type of 2D arrays already requires 3D CMOS fabrication as the control and read-out lines need to be connected from above or below to achieve reasonable large flip-flop arrays. The CPW resonators can also be used to couple the silicon qubits to another type of qubit, e.g. Transmon qubits [120], [121].

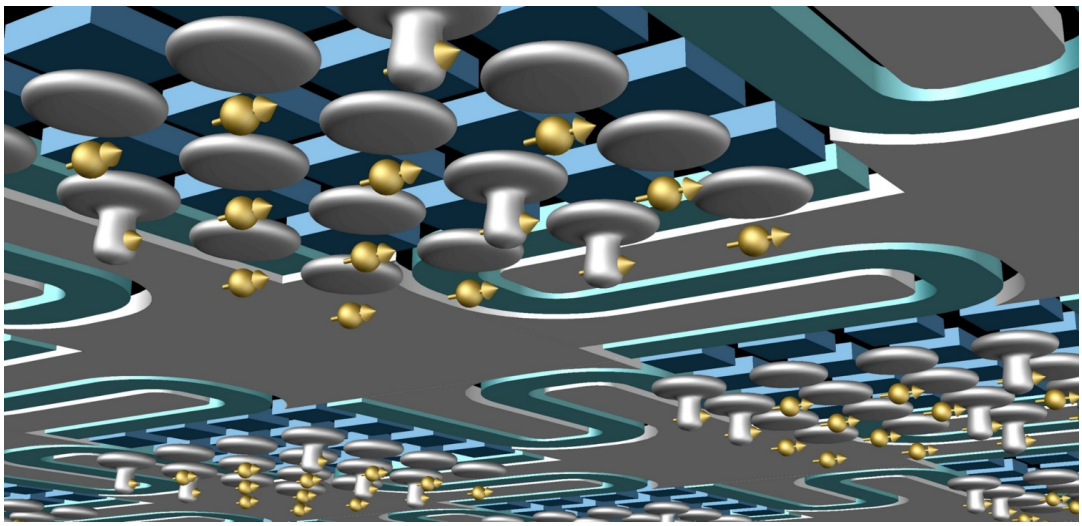

FIGURE 5.3: **Large-scale hybrid quantum processor**. Schematic of a large-scale quantum processor where 2D arrays of 16 dipolar coupled flip-flop qubits are connected via CPW resonators. The drawing is not to scale, control lines and readout devices are not shown.

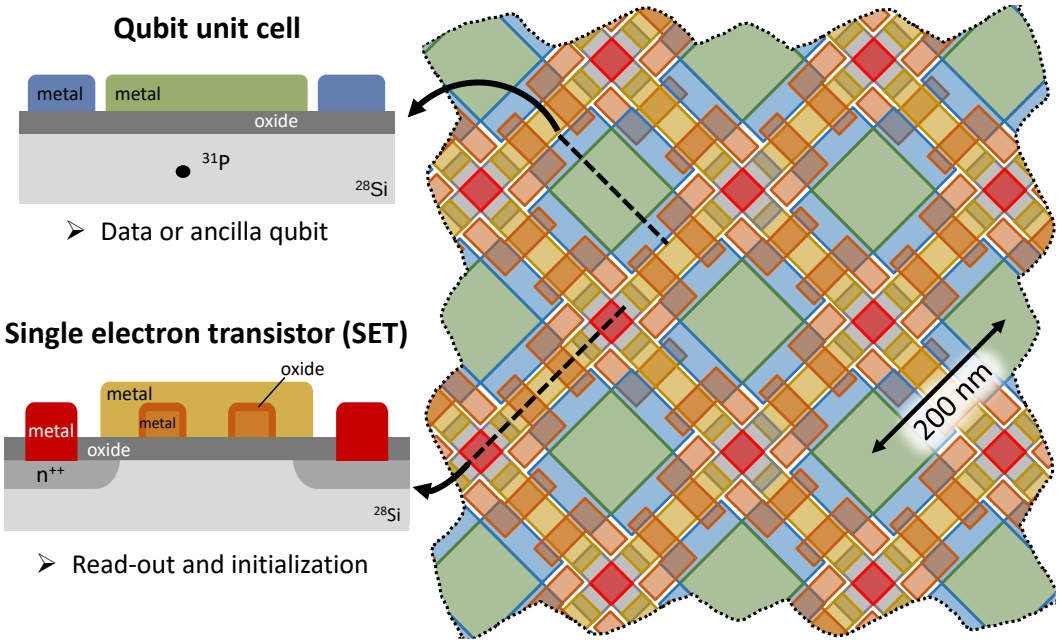

FIGURE 5.4: **Large-scale qubit array**. Schematic of a large-scale quantum processor that is compatible with the quantum error correction. Qubit unit cells consisting out of donors with a gate stack for tunnel coupling control are coupled via the dipole-dipole interaction. Readout and initialization is performed via a SET.

Ultimately, one wants to achieve a full 2D array of only dipolar coupled flip-flop qubits (Fig. 5.4), compatible with industry CMOS standards. This architecture not only allows quantum error correction but can also accommodate many qubits within a small spacing. All mutual qubit couplings are tunable and gateable, resulting in full in-situ control.

5.3 Operation principles of an electrically controlled donor quantum processor

The fundamental operation principle for a quantum processor consisting out of flip-flop qubits remains the same for all suggested implementations.

To initialize the qubit, we load an electron onto the donor either from the SET island when in Coulomb blockade, or from a designated reservoir. Idle qubits have electrons either at the interface or the donor, leaving them completely uncoupled to other qubits. The electrons are then adiabatically shifted towards the donor ionization point for quantum operations (Secs. 3.5, 3.6). Qubit read-out can be obtained by spin-dependent tunnelling into a cold charge reservoir, detected by a SET (Sec. 2.3.3). Read-out times can be $\sim 1\ \mu$s with cryogenic amplifiers [162], which is comparable to the time necessary to perform, for example, ~ 20 individual gates lasting ~ 50 ns each, in a surface code error correction protocol [56].

Instead of flip-flop qubits, nuclear qubits can also be used in the quantum processor. These have the advantage of having record coherence times $T_2 \gtrsim 30$ s [30] when the donor is ionized (the electron is at the interface). The magnetic drive can be a global, always-on field, e.g. supplied by a 3D microwave cavity. Quantum information can be swapped between the nuclear and the flip-flop qubit by simply applying a local ESR π-pulse that excites the $|\downarrow\Downarrow\rangle$ state to $|\uparrow\Downarrow\rangle$.

Chapter 6

Device fabrication and experimental methods

"They say the definition of madness is doing the same thing and expecting a different result...That's right!"
–The Hives, *Try It Again*

In this chapter we present the device design of the flip-flop qubit, the device fabrication techniques and the experimental set-ups developed to carry out the experiments.

The author acknowledges the following facilities and its staff that enabled the work in this thesis: Most fabrication has taken place in the Australian National Fabrication Facility at the University of New South Wales. Donor implantation was carried out by the group of Prof. David Jamieson at the University of Melbourne. Experiments were performed at the low-temperature facilities at the Centre for Quantum Computation and Communication Technology at the University of New South Wales and the Fundamental Quantum Technologies laboratory. The isotopically-purified silicon wafers were provided by K. Itoh of Keio University.

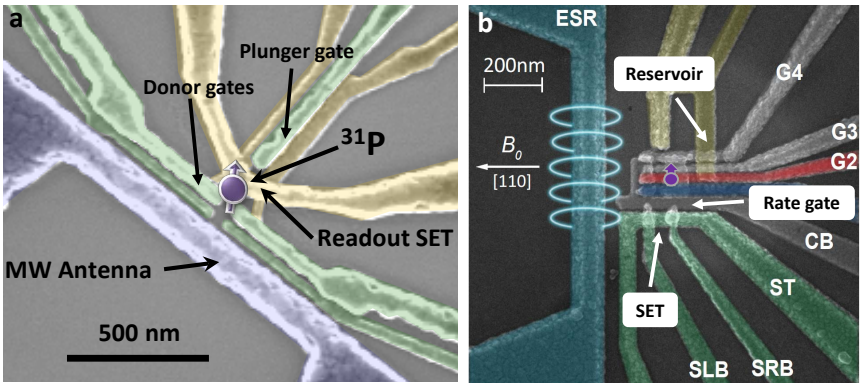

FIGURE 6.1: **Silicon donor and quantum dot qubit designs. a** Scanning electron micrograph of a typical phosphorus donor device in silicon. Both the electron and the nucleus can be operated as a qubit in this device structure. **b** Scanning micrograph of a typical CMOS quantum dot device in silicon which can be operated as a single or double quantum dot qubit. Fig. **b** is adapted from Ref. [26].

6.1 Device design

To propel the flip-flop qubit from theory to reality, we are using nanofabrication techniques to build the qubit, starting from a blank silicon wafer. We invent device designs for both the direct dipole-dipole coupling approach (Sec. 3.8) and coupling to a superconducting resonator (Sec. 3.9). These designs need to fulfil all requirements necessary to operate the flip-flop qubit while complying with the fabrication tool abilities available to us.

The flip-flop qubit requirements entail the following: We need to be able to readout the electron spin state, control the tunnel coupling between the Si/SiO_2 interface and the donor, confine the electron at the interface and most importantly electrically control the donor electron both with DC voltages and fast electric pulses. Additionally we would like a microwave antenna to be able to perform ESR and NMR on the electron and nuclear spin states separately from any flip-flop control, just like in a standard donor qubit device. The following section describes how these requirements can be implemented for direct dipole-dipole coupling while Sec. 6.1.2 discusses the resonator approach.

6.1.1 Coupling two flip-flop qubits via dipole-dipole interaction

We base our flip-flop qubit device design on existing donor and quantum dot structures, nanometric multi-layer aluminium devices (Fig. 6.1), that have made our research teams at UNSW very successful over the last decade [25], [30]. The flip-flop qubit is a donor qubit that exhibits quantum dot features when we confine the electron at the Si/SiO_2 interface. Hence, the flip-flop qubit gate layout will be a hybrid of the donor design (Fig. 6.1a) and the quantum dot design (Fig. 6.1b). The first generation of the flip-flop qubit is shown in Fig. 6.2a with a color-coded gate layout on the left and a scanning electron micrograph image on the right.

The key elements prominent in both donor and dot devices are also prominent in the flip-flop qubit: We use a SET for electron spin readout (yellow), consisting out of two barriers ("right barrier" - RB, "left barrier" - LB) and a top gate (TG) which overlaps with two degenerately doped (n+) regions ("source" - S and "drain" - D). Moreover, we employ a coplanar microwave antenna (MW, grey) to supply microwave and radio frequency magnetic fields to control the qubit spin states.

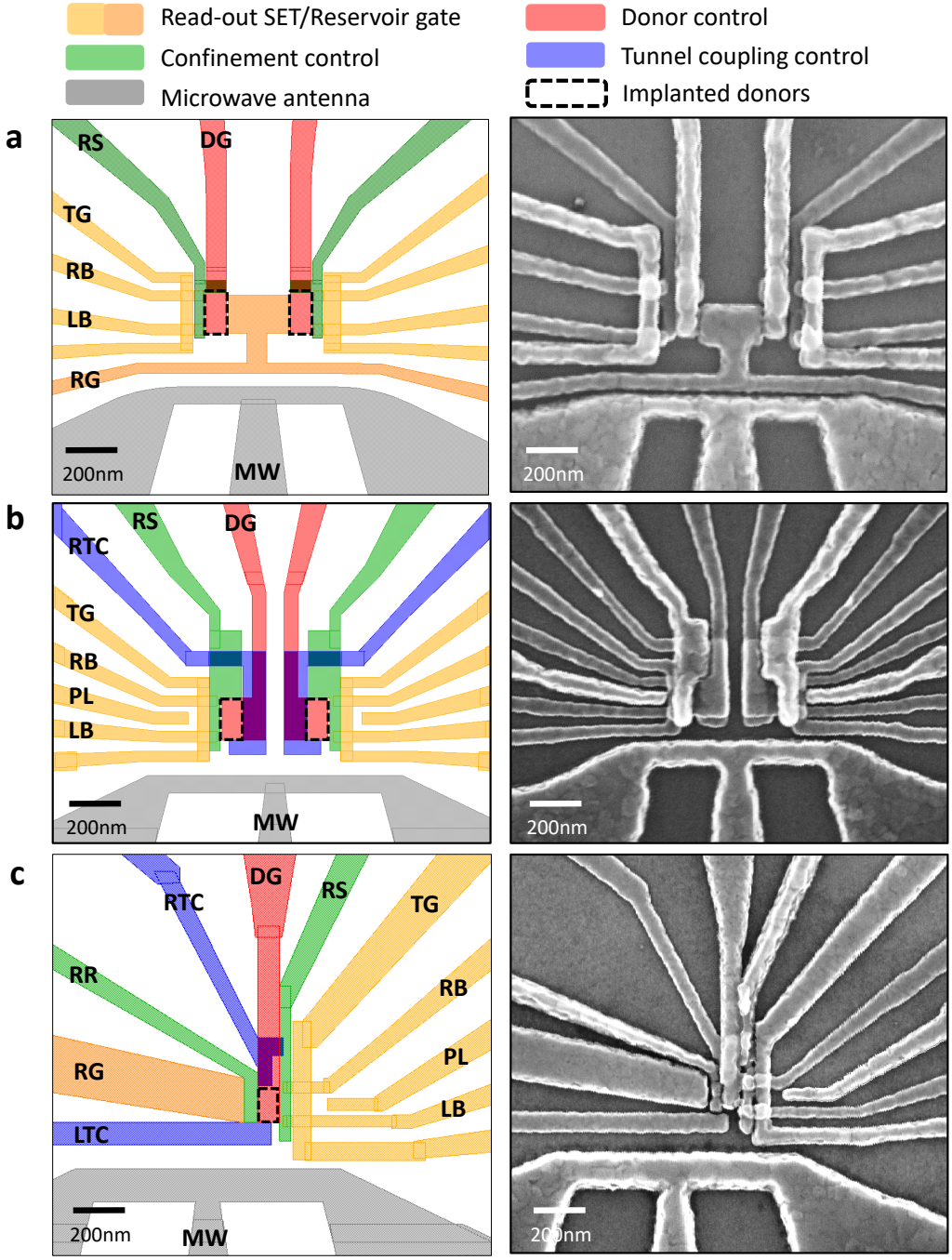

FIGURE 6.2: **Flip-flop qubit designs for direct dipole-dipole coupling.** The left column shows the flip-flop qubit design color-coded with gate purpose and gate labels while the right column shows the corresponding scanning electron micrograph of the finished devices. **a** Two-qubit flip-flop design featuring a donor gate (DG, red), a SET (TG, RB, LB, yellow), a microwave antenna (MW, grey), electron confinement control (RS, green) and a second reservoir (RG, orange). The confinement gate RS can also be used to modify the tunnel coupling within the voltage range set by the readout constrains. **b** Two-qubit flip-flop design with extended tunnel coupling control (RTC, blue). A plunger gate (PL, yellow) was added for increased adjustability of the SET. However the second reservoir was removed. **c** Single flip-flop qubit device with full tunnel coupling control (RTC, LTC, blue) and readout adjustability (RR, RS, green and RG, orange).

We position a gate between the donor and the SET ("rate gate SET" - RS, green), like in the quantum dot devices, to control the tunnel rate of the electron to the SET and prevent escape of the quantum dot interface state. Within the voltage range that yields good readout, this gate can also be used to shift the electron wavefunction laterally and thus decrease the tunnel coupling of the donor to the interface.

Most importantly we add a gate on top of the donor ("donor gate" - DG, red) to control the donor orbital state and send fast electric pulses. This gate is an impedance matched coplanar waveguide, until only the central conductor remains on the last 50 μm before the donor.

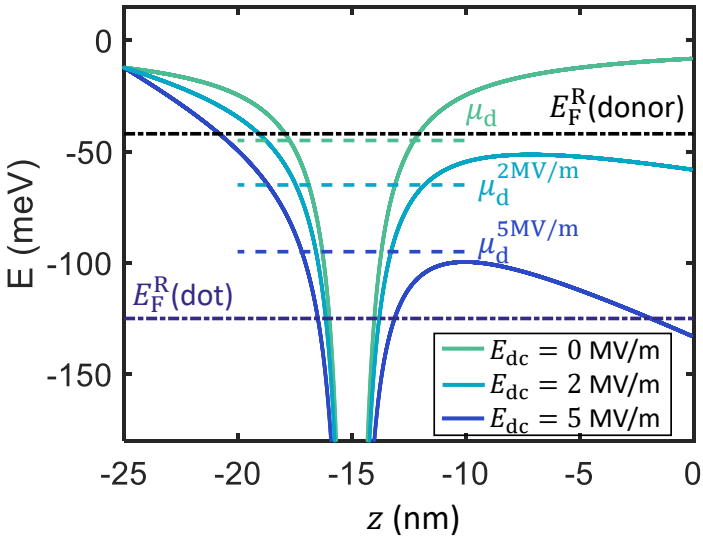

FIGURE 6.3: **Flip-flop qubit readout energy diagram.** Coulomb energy of the donor without and with an electric field of $E_{dc} = 2\,\mathrm{MV/m}$ (light blue) and $E_{dc} = 5\,\mathrm{MV/m}$ (dark blue) applied. The D_0 donor ionization energy is 45.6 mV. The Si/SiO_2 interface is positioned at $z = 0\,\mathrm{nm}$. The dotted lines show the reservoir Fermi energy E_F^R adjusted for donor readout (black, E_F^R(donor)) and dot readout (blue, E_F^R(dot)). μ_d ($\mu_d^{2MV/m}$, $\mu_d^{5MV/m}$) is the donor electrochemical potential (with $E_{dc} = 2\,\mathrm{MV/m}$, $E_{dc} = 5\,\mathrm{MV/m}$ applied).

One difficulty we encounter is that to tune the tunnel coupling significantly we need to pull the electron horizontally by up to 30 nm. Thus we choose an implantation window size of 60×120 nm, where donors will be randomly implanted, which is positioned next to the SET rate gate. Consequently the distance of the donor to the SET reservoir can potentially be over 100 nm - too far to achieve significant electron tunnelling rates to the SET reservoir for readout. To account for this difficulty, we add a second reservoir ("reservoir gate" - RG, orange, "reservoir source" - R). This brings two distinct advantages: Firstly, any donor close to either the SET island or the second reservoir can be read out directly from the donor as the SET will sense the change of the donor charge state regardless of where the electron tunnels to. A similar approach has been successful for silicon quantum dots [25]. Hence we significantly increase the likelihood of finding a donor in a position that allows its readout. Secondly, if the electron cannot be read out from the donor, we can read out the interface quantum dot state instead. The dot's wavefunction is more spread out and we can even move the wavefunction laterally with the confinement and tunnel coupling control gates. This increases the tunnel rate between the electron and the reservoir such that readout becomes possible. To transfer the electron from the donor to the interface dot, we bias the donor with large positive gate voltages until the dot state becomes favourable (Fig. 6.3). However, to perform spin-dependent readout of the

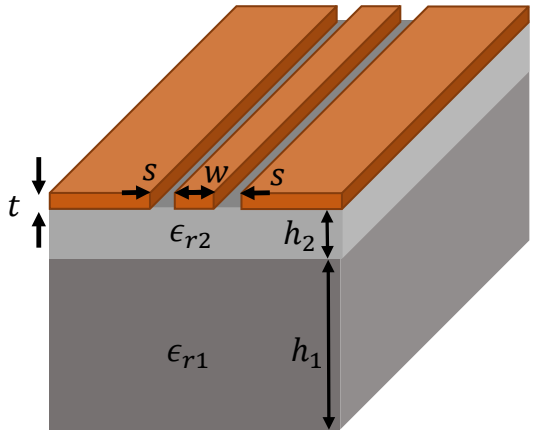

FIGURE 6.4: **Coplanar waveguide resonator geometry**. Geometric dimensions determining the impedance of a coplanar waveguide resonator consisting out of a superconducting film (orange) on top of two dielectric layers (grey).

electron from the quantum dot, we need to adjust the Fermi level of the reservoir E_F^R such that $\mu_{QD,\uparrow} > E_F^R > \mu_{QD,\downarrow}$, where $\mu_{QD,\uparrow}$ ($\mu_{QD,\downarrow}$) is the electrochemical potential of the quantum dot with the electron in state $|\uparrow\rangle$ ($|\downarrow\rangle$). During this process, the SET Fermi level E_F stays constant to provide charge sensing.

To achieve a two-qubit device, we mirror this one-qubit structure at a distance of 200 nm.

One drawback of this basic flip-flop design is that it only has a very limited lateral control of the electron wave function. Hence in the second generation of the devices (Fig. 6.2b) we added an additional tunnel gate ("right tunnel coupling gate" - RTC, blue). Furthermore, we also inserted a plunger gate (PL, yellow) for increased SET adjustment. However, in this device structure the second reservoir gate was removed due to space restrictions.

Generation three (Fig. 6.2c) incorporates both high tunnel coupling control with another additional tunnel coupling control gate ("left tunnel coupling gate" - LTC, blue) and a highly tunable read out with a plunger gate, a second reservoir (RG) and two rate gates ("rate gate reservoir" - RR and RS, green). In this layout, we decide to concentrate on developing a single, highly tunable flip-flop qubit instead of attempting to fabricate a two-qubit device. A few additional small design changes are to be noted. The SET rate gate as well as the plunger gate have been moved slightly further away from the SET top gate to reduce the effect of strain on the 2DEG below the SET as this can prevent turn-on. Furthermore, short-circuit termination of the microwave antenna has been increased in both width and thickness to make it less susceptible to electrostatic discharge (ESD).

6.1.2 Coupling a flip-flop qubit to a coplanar waveguide resonator

Resonator design

To couple our flip-flop qubit to a single photon, we use a standard coplanar waveguide resonator (CPWR). This geometry consists of a central conductor with a ground plane on either side (Fig. 6.4). The waveguide width and gap size are chosen for an impedance of $Z_0 = 50\,\Omega$ to $w = 20\,\mu$m and $s = 12\,\mu$m ($s/w = 0.6$). The relevant parameters are $\epsilon_1 = 11.7$, $h_1 = 500\,\mu$m for the silicon wafer, $\epsilon_2 = 3.78$, $h_2 = 8$ nm for

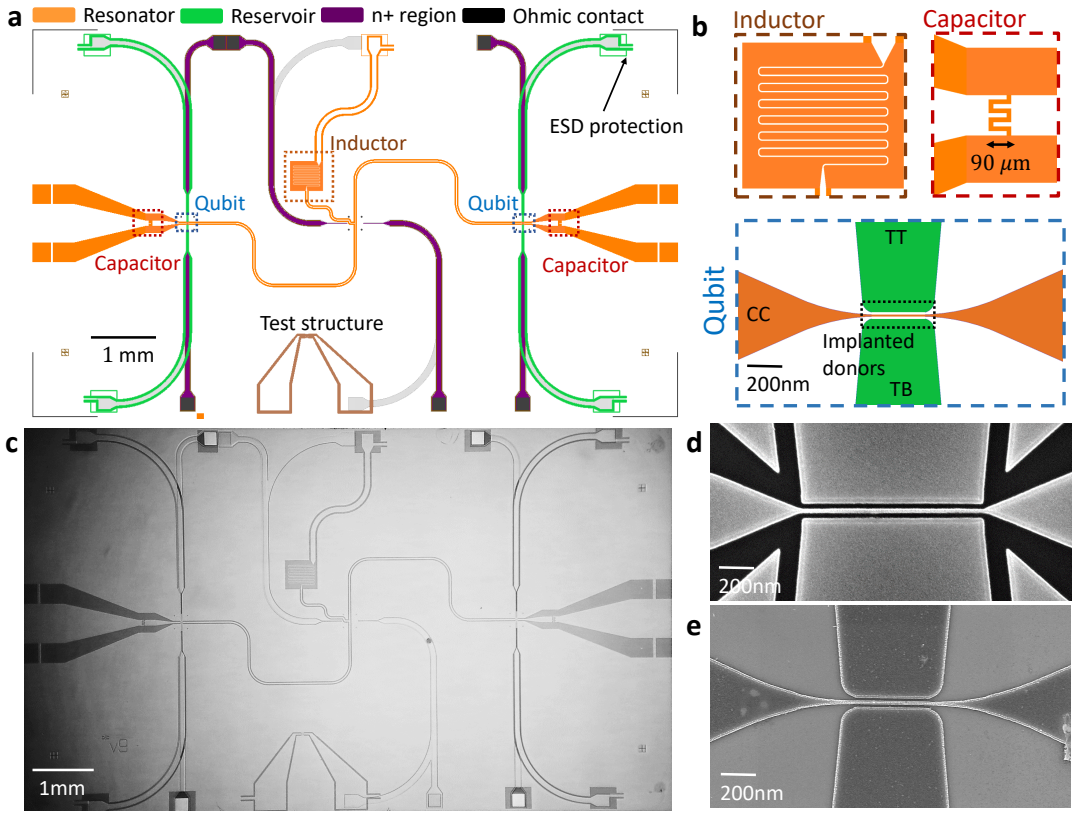

FIGURE 6.5: **CPWR qubit design. a** Overview of the CPWR design, color-coded with feature purpose. The sample is covered in a superconducting film with etched regions indicated in orange and green. Purple shows the $n+$ regions with their respective Ohmic contacts in black. The qubit region, the capacitors and the inductor are shown in detail in **b** with gate labels. **c** Scanning micrograph of the CPWR. **d, e** Scanning micrograph of the qubit region for two different designs. To avoid ESD in the devices, we have removed the ground plane tips which can channel a voltage (**d**) in an improved design (**e**). Additionally, all gates are connected to the large ground planes by leaving small strips of metal unetched (**a,c**).

the silicon oxide layer and $t = 50\,\text{nm}$ for the superconducting film thickness [163], [164].

We like to operate the resonator at a frequency $f_r \gg k_B T/h \approx 250\,\text{MHz}$ to reduce thermal population, choosing $f_r \approx 6\,\text{GHz}$ to keep component costs low. We operate the fundamental mode of a $\lambda/2$ resonator which determines the resonator length to $l = \frac{c_0}{2\sqrt{\epsilon_{\text{eff}}}}/f_r = 9.95\,\text{mm}$. ϵ_{eff} is the effective permittivity of the wave guide which can be estimated to $\epsilon_{\text{eff}} = (1+\epsilon_1)/2 = 6.3$ [164], [165]. The resulting resonator is shown in Fig. 6.5a (orange).

The coupling of the resonator to the feedlines is determined by the size of the capacitor at each end of the resonator, acting as a semi-reflecting mirror, introducing a strong impedance mismatch (Sec. 2.4.2). We are aiming for the over-coupled regime where the coupling exceeds the internal losses ($\kappa_L \ll \kappa_c$). We simulate the capacitor size in a finite-elements computer simulation theory microwave studio® (CST MWS). Ultimately however, we rely on testing different designs. Fig.6.5b shows an example capacitor design. As we are working in transmission mode, we place one capacitor at each end of the resonator, connecting it to two transmission lines.

Now we integrate our spin qubit into the resonator design by placing several phosphorus donors directly beneath the resonator central conductor (CC). However, we require a vacuum electric field amplitude of $E_{\text{vac}} \approx 30\,\text{V/m}$ to achieve high

qubit-resonator coupling rates (Sec. 2.4.3, 3.9). These electric field amplitudes can be reached by narrowing the central conductor in the qubit region to 100 nm or less (Fig. 6.5b, d, e) [118]. In order to load electrons to the donors, we bring a 2DEG close to the qubit. Therefore, we add two n+ regions, Ohmic contacts ("source" - S and "drain" - D) and reservoir top gates ("top top gate" - TT and "bottom top gate" - TB, green) for each qubit region.

Finally, we need to apply a bias to the qubit to control the donor electron orbital. Thus we have to bias the centre conductor. Therefore, we add a DC feed line at the electric field node at the centre of the resonator. High frequency signals are filtered with an on-chip inductor (Fig. 6.5a,b).

Due to the large metallic ground planes involved in this design, ESD can be a serious problem with charges accumulating on the metal during fabrication and chip handling. Consequently, we removed the tips of the ground plane which can channel a voltage (Fig. 6.5d, improved design in Fig. 6.5e) and grounded all gates to the large ground planes by leaving small strips of metal unetched. After a device has been mounted to an enclosure (Sec. 6.3) and all gates are grounded, these strips can be disconnected by scratching with a diamond-tip pen or scriber.

Advanced resonator qubit design

While the design presented in the previous section is proficient to operate a flip-flop qubit in its most basic functionality with a bit of luck in the donor placement (Sec. 7.3.3), its qubit control capability is very limited. The reservoir gates allow biasing, however they are far away from the qubit due to fabrication limitations (Sec. 6.2.3) and thus wavefunction control will be very limited if not impossible. Furthermore, many electrons can be loaded under the central conductor during qubit loading. To mitigate these issues, we are developing a design that is both more robust against implantation uncertainties as well as allowing higher qubit control, inspired by designs of other groups that achieved strong coupling in silicon [113], [166].

The main difference between the new advanced design (Fig. 6.6) and the current design is that we use a two-layer aluminium structure in the qubit region (Fig. 6.6c), allowing for a much smaller feature size and a more complex gate layout. Furthermore we operate the resonator in reflection. We have only one qubit region but fit two qubits inside it. Both have a separate reservoir ("reservoir gate" - RG, yellow) as well as two gates to confine the electron and control the tunnel coupling ("tunnel coupling gate" - TC and "confinement gate" - CG, green). Each of these gates has its own on-chip inductor to allow for loss-less DC biasing. We also incorporate a microwave antenna into our design to allow for individual electron and nuclear spin control.

6.2 Device fabrication

In this section the device fabrication techniques for our qubit devices are presented.

6.2.1 Silicon wafer

All devices start off as a bare silicon wafer. For testing, high resistivity, uncompensated, intrinsic natural silicon wafers are used, while highly precise qubit experiments are performed on wafers with an 800 nm epitaxial layer of isotopically purified ^{28}Si on top of 500 μm thick natural silicon, provided by Prof. K. Itoh. The ^{28}Si has a residual concentration of 730 ppm of ^{29}Si and 30 ppm ^{30}Si.

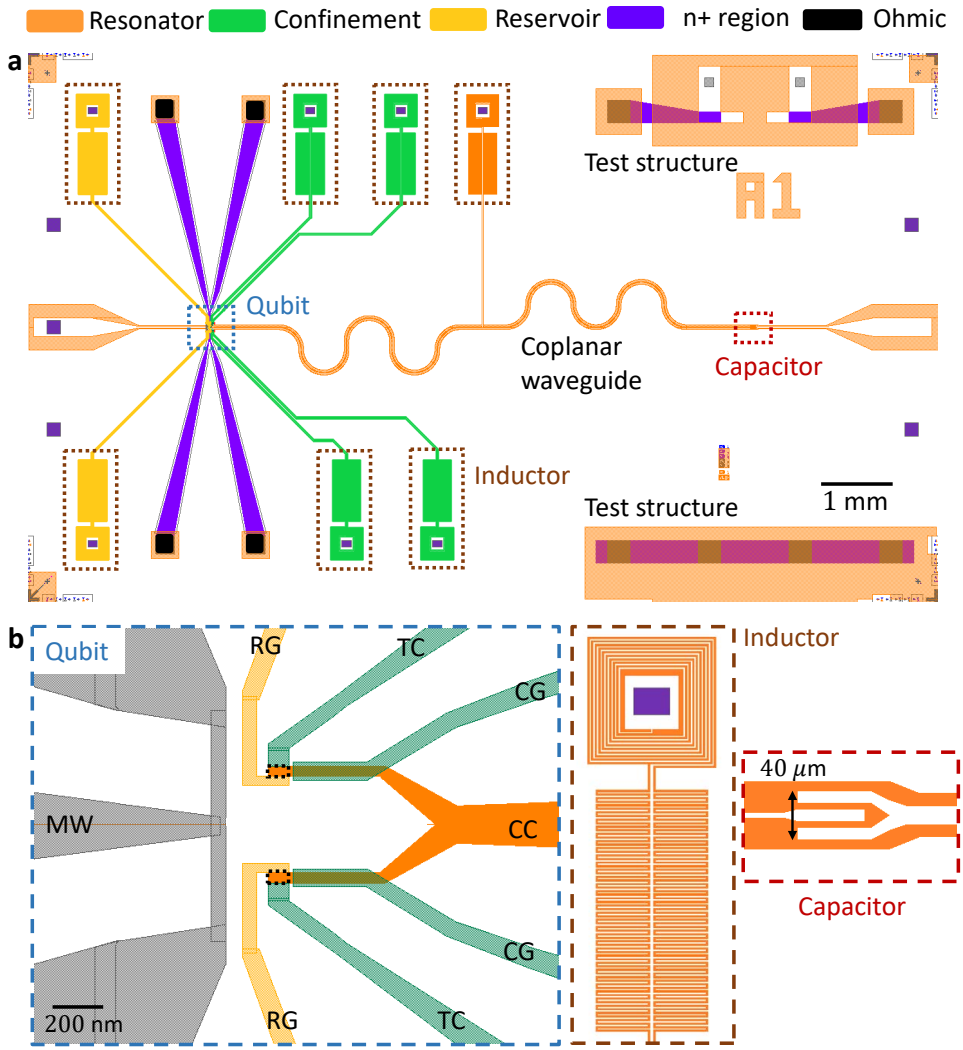

FIGURE 6.6: **Advanced CPWR qubit design. a** Overview of an advanced resonator flip-flop qubit structure, color-coded with feature purpose. The design includes several control gates and the resonator is operated in reflection. **b** Detailed view of the qubit region with gate labels, the inductor and an example capacitor.

We have two different wafer designs for multi-layer aluminium devices (direct dipole-dipole coupled flip-flop qubit, electron and nuclear qubit) and resonator devices (Fig. 6.7). However, the wafers are processed in the same way with the following steps:

1. A thorough clean to remove oils and organic residues is performed.
2. Optical alignment marks are etched into the silicon.
3. The wafers are weakly doped with Boron to create $p+$ regions. These positively charged regions block any conducting channels that are formed when positive charges trapped in the thick field SiO_2 induce an unintentional leakage path.
4. Phosphorus is diffused to create $n+$ regions to form the source and drain contacts.
5. 200 nm of field oxide are grown in a wet thermal oxidation furnace.

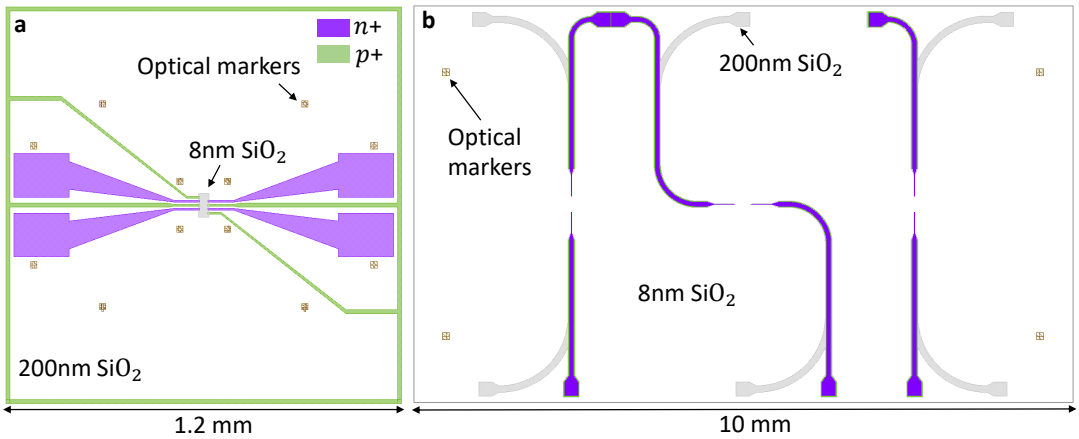

FIGURE 6.7: **Silicon wafer layout.** Layout of the features patterned on the silicon wafer during wafer preparation for the standard aluminium devices (**a**) and the resonator devices (**b**). Doped $n+$ and $p+$ regions are created and optical markers are added.

6. The field oxide is removed in the active qubit region to be replaced by 8 nm of high quality gate oxide, grown in an ultra-dry furnace.

7. Micrometer sized markers formed out of platinum on top of titanium (TiPt markers) are patterned for coarse alignment with electron beam lithography (EBL).

The one noticeable difference between the two wafer designs is that for the resonator structures most of the wafer is considered the active region and thus a thick field oxide is grown only where the top gates are intended.

Once the silicon wafers have been processed in this way, they are ready for device fabrication and are called "stock".

6.2.2 Nano-fabrication process - multi-layer aluminium devices

Once the silicon wafers have been prepared, they are diced into smaller chips for different projects. While all silicon donor multi-layer aluminium devices use inherently a very similar fabrication process, small differences occur due to individual preferences and cleanroom superstitions. In the following the process specific to the flip-flop qubit used by the author of this thesis is presented.

Cleaning To remove any residue of resist or other contaminants the chips are cleaned by soaking them first in acetone and subsequently in isopropyl alcohol (IPA) for each 10 min while applying ultrasound. The cleaning process is finished with 10 min of oxygen plasma ashing at a power of 50 W.

TiPt markers The first processing step is the formation of the nanometric markers in each device cell which allow alignment of different layers during EBL. These markers need to withstand temperatures of 1000 °C during subsequent processing steps. Therefore we use 65 nm of platinum which not only has a very high melting point of 1763 °C but also has a high atomic number resulting in good contrast under the electron beam microscope. For adhesion to the silicon oxide surface, we add a thin 15 nm layer of titanium with a melting point of 1668 °C. Regardless of these high melting points, large TiPt structures would nonetheless slightly deform during the

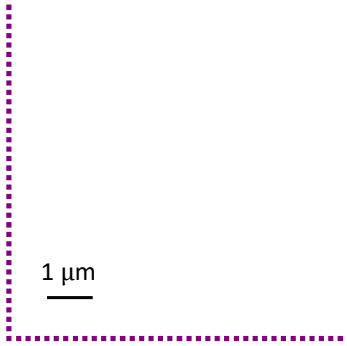

FIGURE 6.8: **TiPt marker design.** Nanometric TiPt markers used for EBL alignment of the different layers. The individual square design is robust against melting during RTA.

high-temperature rapid thermal anneal (RTA). Therefore we use instead a pattern of many small 100×100 nm squares (Fig. 6.8). Even if the individual squares were to deform at high temperature, the overall location of the pattern would remain very accurate. We create these markers with EBL, applying the following steps.

Standard EBL process:

1. EBL resist is applied. Therefore, we bake the chip at 180 °C for 10 min and then spin polymethyl methacrylate (PMMA) A4 resist with 4000 rpm for 40 s which includes 10 s of 8000 rpm at the end. This gives a resist thickness of 200 nm. The resist is then baked for 90 s at 180 °C.

2. Droplets of colloidal gold solution can be placed on the corners of the chip as focus markers.

3. The pattern is written with a RAITH150-Two EBL system with an acceleration voltage of 30 keV and a dose of around 500 μC/cm^2, depending on aperture, feature size and geometry.

4. After exposure, the resist is developed for 40 s in a 1:3 solution of methyl-sobutyl-ketone (MIBK) and IPA and for 20 s in IPA with a 5 s ultrasound finish.

After EBL, 15 nm of Titanium and 65 nm of Platinum are evaporated by electron beam physical vapour deposition (EBPVD). Then the chip is placed in N-methyl-2-pyrollidone (NMP) at 80 °C for 5 min to perform lift off.

Donor implantation The next step is the implantation of the phosphorus donors. Therefore a PMMA mask of dimensions 120 nm$\times$60 nm is patterned with EBL in each device cell ("implantation window"). We require a donor depth of around $10 - 15$ nm below the silicon oxide. As the tunnel coupling between the donor and dot can be reduced but not increased we aim for 10 nm. An acceleration voltage of 12 keV of phosphorus ions complies with this requirement as the simulated ion depth distribution in Fig. 6.9 shows. We aim for around 10 donors in our implantation window which corresponds to a fluence of 2×10^{11}/cm^2 and an average donor distance of 25 nm. The implantation is performed by the group of Prof. David Jamieson at the University of Melbourne.

After the implantation is completed the resist is removed and the chip undergoes RTA for 5 s at 1000 °C. This activates the donors and repairs the damage caused in the silicon lattice by the ion implantation [167].

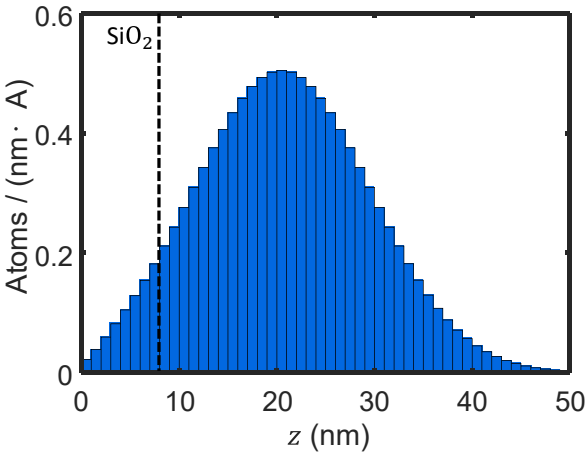

FIGURE 6.9: **Ion distribution for phosphorus implantation.** Distribution of phosphorus ions as a function of depth z for an acceleration voltage of 12 keV with a fluence of $2 \times 10^{11}/\text{cm}^2$ and an implantation window of area $A = 60\,\text{nm} \times 120\,\text{nm}$.

Ohmic contacts Then aluminium Ohmic contacts to the diffused $n+$ regions are formed and activated with a forming gas anneal (FGA, N_2 95%, H_2 5%) at 400 °C for 15 min in the clean anneal furnace. Afterwards, the chip is diced into pieces with 4×4 device cells for individual processing.

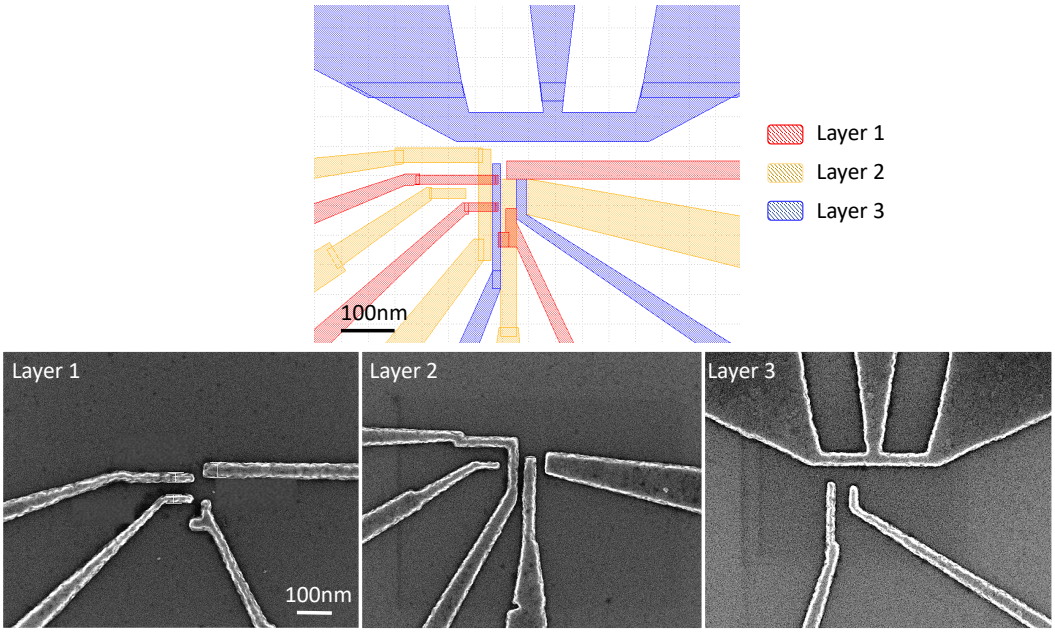

FIGURE 6.10: **Aluminium layer arrangement of the dipole flip-flop qubit.** Qubit gate layout color-coded for the three aluminium layers, and corresponding scanning electron micrograph images for each layer.

Multi-layer aluminium nanostructures On each 4×4 piece, three layers of aluminium gates on top and around the implantation window are added (Fig. 6.10). For each layer the piece undergoes the following steps.

1. The wafer piece is cleaned (see paragraph **Cleaning** 6.2.2).

2. EBL resist is applied, exposed and developed (see paragraph *Standard EBL process* 6.2.2).

3. Aluminium is evaporated either in a thermal or an EBPVD evaporator. Tests have been performed and we find that the evaporation rate and its stability directly influences the aluminium grain size. Thermal evaporation can be unstable due to a fluctuating current and is restricted to rates below 3 Å/s. Thus it regularly leads to a larger grains than EBPVD where evaporation rates of 10 Å/s can be achieved - see figure 6.11. With EBPVD, we evaporate 25 nm, 45 nm and 80 nm subsequently for the different layers

4. The aluminium is lifted off in hot NMP for 1.5 − 3 h.

5. The outer 2 − 3 nm of each aluminium layer are oxidized to form an electrically insulating layer by oxygen plasma ashing and baking.

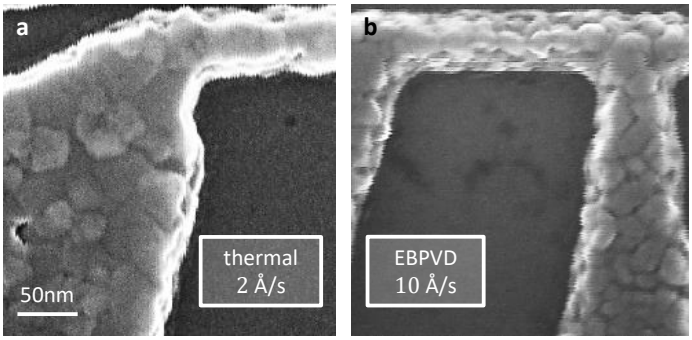

FIGURE 6.11: **Aluminium grain size for thermal evaporation and EBPVD. a** Aluminium structure evaporated at a rate of 2 Å/s in a thermal evaporator. The grains are 30 − 50 nm large. **b** Aluminium structure evaporated at a rate of 10 Å/s with EBPVD. The grains are 10 − 30 nm large.

Finish After the last layer has been completed, the piece is cleaned one more time and FGA is performed for 15 min to passivate any charge traps at the Si/SiO_2 interface [168].

6.2.3 Nano-fabrication process - resonator devices

As our research group had not fabricated any form of superconducting devices before, we started building up a new process which is still undergoing development. This section describes the fabrication performed for the measurements presented in this thesis, using the simple resonator design and niobium for the superconducting film. An outlook for the new, advanced resonator devices will also be given.

Cleaning Starting from the resonator specific stock, first the wafer is cleaned in the same way as for the aluminium devices. However, once the niobium layer has been deposited, oxygen ashing oxidises the niobium - the film can even become insulating. Thus, no plasma ashing will be performed on the niobium films.

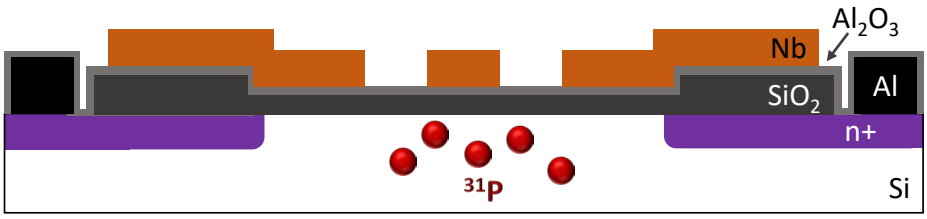

FIGURE 6.12: **Cross-section of a Nb resonator device.** A 50 nm layer of niobium is sputtered on top of the silicon stock which is covered with 3 nm of Al_2O_3. The resonator gap is then etched such that the central conductor constriction is on top of the donors. Ohmic contacts to $n+$ regions allow to bring a 2DEG close to the donors. Distances are not to scale.

Donor implantation The next step is the implantation of the phosphorus donors, performed at the university of Melbourne. Therefore a photo mask of dimensions $44 \times 24\,\mu$m is patterned with photo-lithography in each pixel ("implantation window"). We implant phosphorus ions with an acceleration voltage of 11 keV and a fluence of $1 \times 10^{11}/\text{cm}^2$ which corresponds to an average donor distance of 38 nm. After the implantation is completed the resist is removed and the wafer undergoes RTA. Finally, aluminium Ohmic contacts to the diffused $n+$ regions are formed and activated with FGA for 15 min.

Sputtering First, we apply a thin layer of Al_2O_3 that serves as an etch stopper. Using atomic layer deposition (ALD) we run 30 cycles at 250 °C which gives 3 nm. Then the wafer is sent to CSIRO at Lindfield where 50 nm of niobium are sputtered. However, the effective film thickness fluctuates between $30 - 50$ nm which is determined with a stylus profilometre. Using a 4-point measurement we find these films to have a resistivity of 38 nΩ·m at room temperature.

Resonator structures To create the resonator devices (cross section in Fig. 6.12) we employ the following steps.

1. We pattern the resonator design with EBL (see paragraph *Standard EBL process* 6.2.2). In contrast to the aluminium style devices, we will etch the niobium wherever the resist has been exposed. Moreover, the resonators are larger than one EBL write field. To create a smooth coplanar waveguide we employ the fixed beam moving stage (FBMS) technique that moves the stage below the beam for the entirety of the device, thus preventing stitching issues.

2. We perform hollow cathode reactive ion etching (HC RIE) with a gas mixture of 20 sccm CF_4 and 10 sccm Ar at a pressure of 5 Pa with 50 W power to remove the niobium not protected by our PMMA mask. This process needs to be carefully calibrated so that after the etch duration the niobium is fully removed but the PMMA mask is still protecting the remaining niobium surface, otherwise the niobium quality will be compromised (Fig. 6.13). For this purpose we always add test samples to the process. The usual etch time is 10 min. The Al_2O_3 layer acts as an etch stopper once the niobium has been fully etched.

3. The sample is cleaned with acetone and IPA (including USB) and ready for packaging.

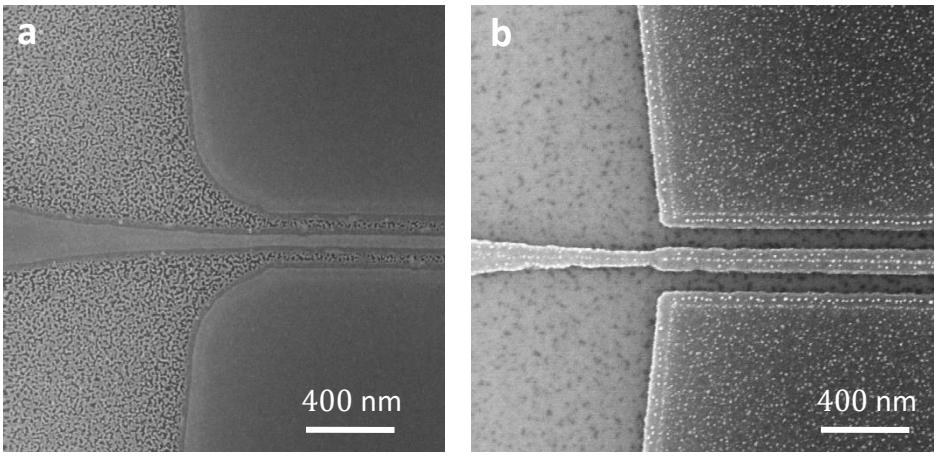

FIGURE 6.13: **Niobium resonators, under- and over-etched. a** A niobium resonator which has not been etched enough. Niobium particles remain in the gaps. This can create losses and even shorten the resonator. **b** A niobium resonator which has been etched too long, such that the PMMA mask was destroyed and the niobium of the resonator has been etched slightly. This leads to a high surface roughness which can compromise the conductivity. The dark spots in the gaps are PMMA residue, supporting the need for a thorough clean after etching.

Outlook for advanced resonator devices The advanced resonator design fabrication deviates in a few important steps. Firstly, we will use NbTiN instead of niobium, which has a higher critical field. This makes the resonator more resilient to field misalignment - it can withstand a higher perpendicular field component until its superconductivity is destroyed. Additionally, NbTiN allows for plasma ashing, as no oxide is formed. Secondly, the resonator will be patterned with optical lithography using the mask shown in Fig. 6.6a. After etching, we then fabricate the qubit nanostructures like the aluminium devices described in Sec. 6.2.2.

6.3 Device packaging

To connect our samples to electronics, we use a printed circuit board (PCB) inside a copper enclosure as shown in Fig. 6.14. These PCBs have been carefully designed with impedance matched lines for all high frequency ports and spare ports to accommodate design changes. The dipole PCB (Fig. 6.14a) holds two devices which makes chip handling slightly easier as the device cell size is only 1.2 mm×1.2 mm. It features two SMA lines ($<$ 18 GHz), one K-type line ($<$ 40 GHz) and 22 MMCX lines (DC). The CPWR PCB (Fig. 6.14b) holds one device and has two SMA and 12 MMCX lines.

The device is mounted in the PCB opening with PMMA and subsequently connected to the PCB lines with an aluminium wedge wire bonder. Fast frequency lines are bonded as matched as possible by using many short bonds. The CPW requires many additional bonds (from PCB ground to sample ground and across the different ground sections on the sample) to properly secure the ground plane over the entire chip. During the bonding process all lines remain grounded to avoid ESD damage.

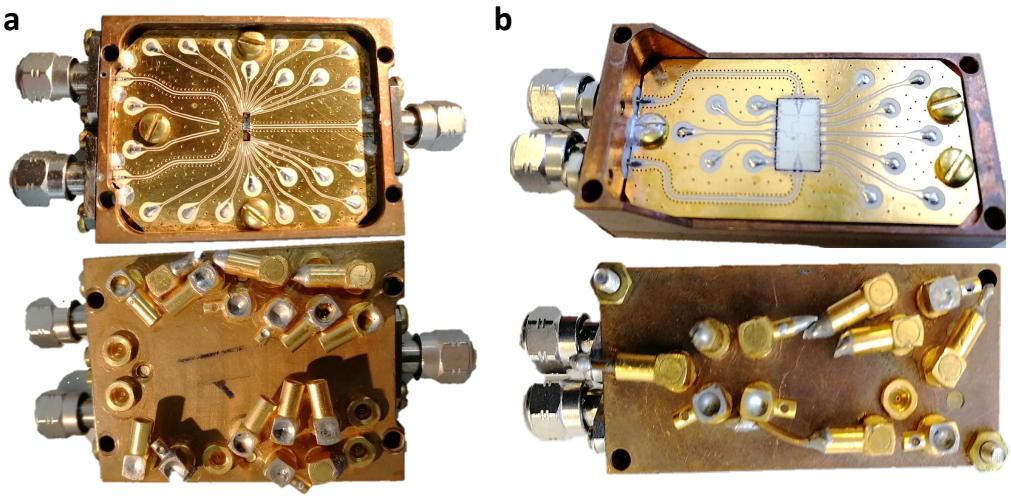

FIGURE 6.14: **Flip-flop qubit enclosures.** Enclosure with PCB for the dipole-coupled flip-flop qubit (**a**) and the resonator qubit (**b**).

6.4 Experimental setup

Our experiments are performed at low temperatures ($\sim$ 11 mK) to prevent spurious thermal excitation as much as possible. Cryogen-free dilution refrigerators (BlueFors LD400) can achieve these temperatures by exploiting the enthalpy of mixing of ^{4}He and ^{3}He [169]. The coldest part of the fridge is where the gases mix and is fittingly called the mixing chamber. There we attach the sample enclosures with our qubits to a cold finger. The fridge is fitted with a superconducting magnet. The qubit sits in the centre of this magnet and thus experiences a homogeneous magnetic field of up to 5 T.

In this thesis, three different types of qubits are discussed: the standard electron qubit (Chaps. 2, 8), the flip-flop qubit implemented with direct dipole-dipole coupling and resonator coupling (Chap. 3 and 7). These different qubits have different demands on the measurement setup which will be explained in the following sections.

6.4.1 Electron and nuclear qubit

Cables and filtering

The qubit has three distinct types of connections to the room temperature world outside of the dilution refrigerator: DC, AC (80 MHz) and high frequency ($\lesssim$ 40 GHz). Each type of connection aims to allow a sufficient amount of power down to the qubit while simultaneously minimizing any thermal noise. Any resistor R at temperature T emits thermal white noise, called Johnson-Nyquist noise [170], [171] with a spectral density of $v_n^2 = 4k_BTR$. For each line this noise is transmitted through the line to the device at low temperatures. However, it can be reduced either by attenuation or filtering. We choose our approach according to the bandwidth of line. Fig. 6.15 shows the schematic of the line attenuation, filtering and instrument control used for the electron and nuclear qubit.

The DC lines require a fixed voltage bias and consist of the left (LB) and right (RB) SET barrier, the SET top gate (TG), and two donor gates (DS1, DS2). To minimize the Johnson-Nyquist noise as much as possible we filter these lines with a home-built

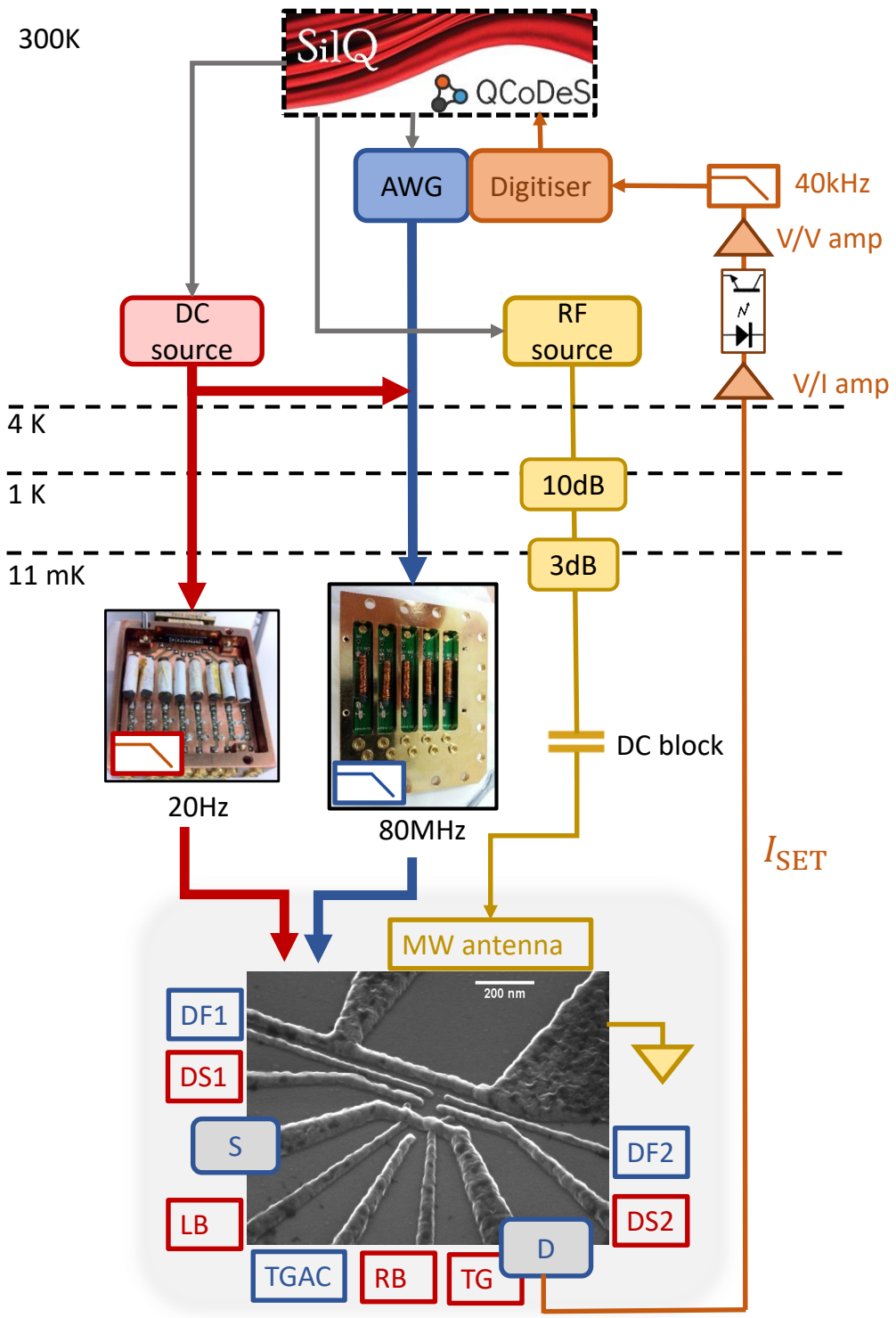

FIGURE 6.15: **Electron qubit setup**. Schematic of the experimental setup for the electron qubit. Detailed description in the main text.

filter box that acts as a low pass filter and attenuates any signal above 20 Hz. It consists of two passive first-order RC filters in series, with thin-film nichrome resistors of 20 kΩ and 470 nF and 1 pF ceramic capacitors, resulting in cut-off frequencies of 20 Hz and 8 MHz respectively. The lines running from room temperature to the filter box are copper-nickel twisted-pair wires that are thermalized at every temperature stage (11 mK, 1 K, 4 K, 64 K).

The AC lines - two fast donor gates (DF1, DF2), source (S), drain (D) and the plunger gate (TGAC) - require a fixed voltage bias, but also pulsing on the order of megahertz. Thus we use copper semi-rigid (EZ47) coaxial lines and a filter box with a cut-off frequency of 80 MHz, consisting of seventh-order integrated LC filters (Mini-Circuits LFCN-80).

In addition to the passive filters, both filter boxes contain an anti-inductive wound coil with an ECCOSORB®core in series to reduce high-frequency noise. Connections from both filter boxes to the enclosure are made with copper semi-rigid coaxial cables with diameter 0.047", terminated by MMCX connectors.

The high frequency line needs to transmit pulses of up to 40 GHz, thus cannot be low-pass filtered. Consequently we use attenuators at different temperature stages to create a good thermal contact between the coaxial signal line of the copper-nickel cable, with silver-plated inner conductor (EZ86), and the ground shield which in turn is thermalized to the fridge using copper anchors. The attenuation depends on the required power at the sample and the cooling power at the respective temperature stage. We place 10 dB of attenuation at 1 K and 3 dB at 11 mK, which results in a noise temperature of 15.5 K [1]. Additionally we add an Aeroflex 8141A DC block at mK to remove any DC current noise.

Instrument control

All instruments are controlled with our home-built measurement software SilQ [172] which is a python environment built on top of the open-source quantum measurement package QCoDes [173]. DC voltages are applied with the National instruments PXIe4322 voltage source card in the PIXe rack, directly controlled with SilQ. AC voltages are also supplied by the PXI, however for TGAC, DF1 and DF2 the DC voltage is combined by a resistive combiner with a pulse from a Signadyne M3300A arbitrary waveform generator (AWG). ESR pulses are generated by the Agilent E8267D Vector Source. The measurement signal of the device consists of the SET current, usually of magnitude of $I \sim 1\,\mathrm{nA}$. We amplify the current using a FEMTO DLPCA-200 transimpedance amplifier set at 10^7 V/A. Afterwards the voltage is further amplified by a SIM910 voltage amplifier with a gain of 10 V/V, which also acts as a ground decoupling point, by choosing the "float" setting of the input connector. This prevents a large ground loop through the fridge between source and drain. Finally the signal is filtered by a SIM965 analogue filter module set to a low-pass fourth order Bessel filter with a cut-off frequency of 40 kHz before it is acquired with the a Signadyne M3300A digitizer card. SilQ controls the data acquisition and transmission from the Signadyne temporary storage to the data hard drive.

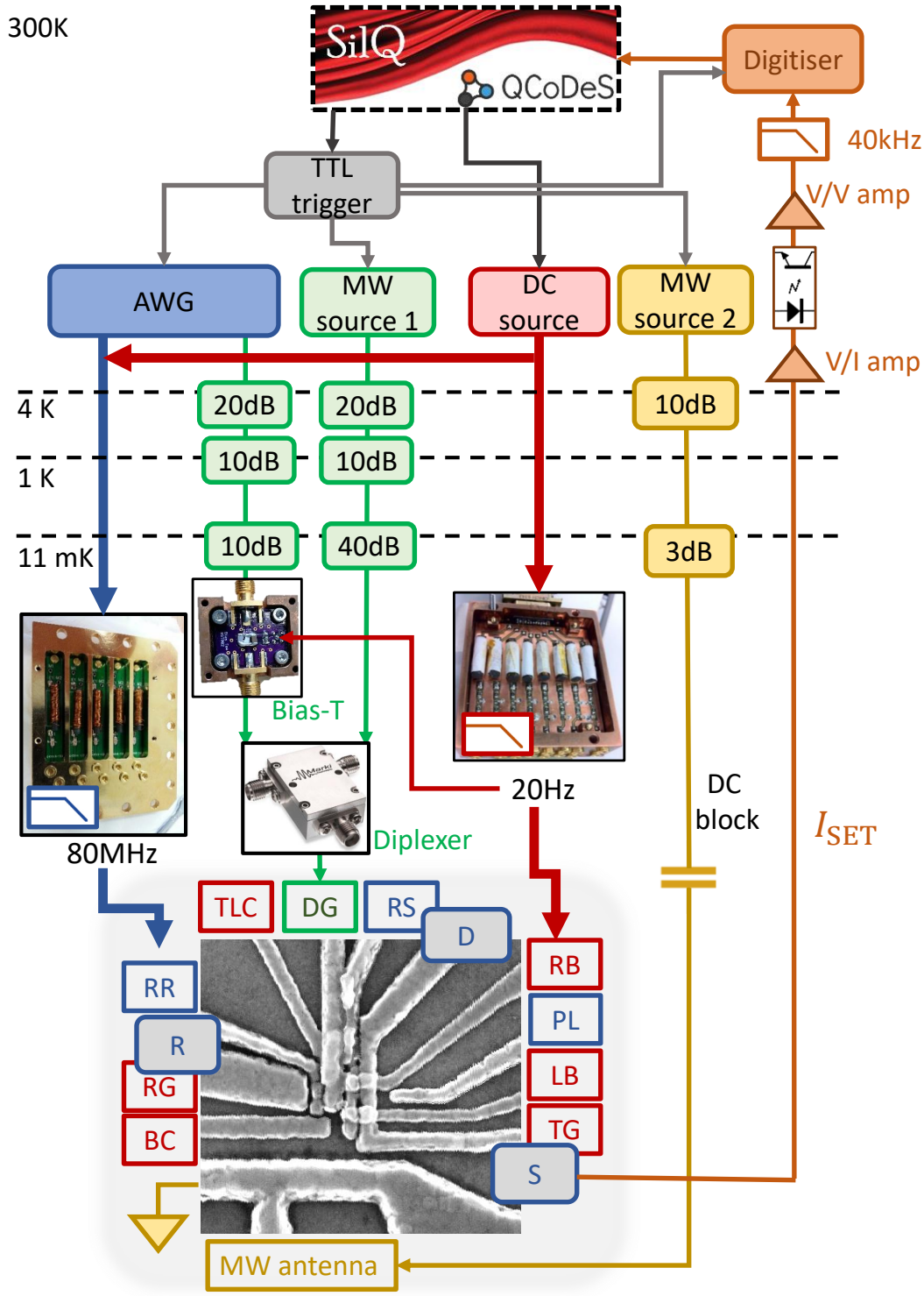

FIGURE 6.16: **Flip-flop qubit setup**. Schematic of the experimental setup for the dipole-coupled flip-flop qubit. Detailed description in the main text.

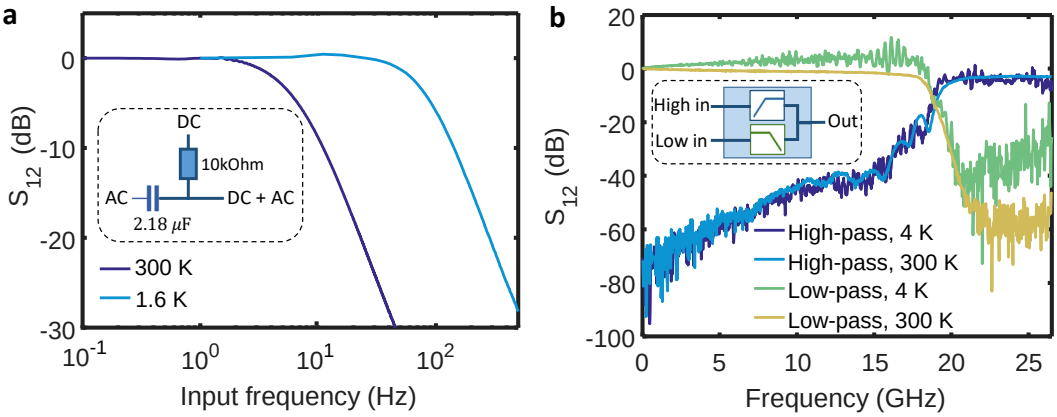

FIGURE 6.17: **Bias-T and diplexer transmission measurements. a** Home-build bias-T transmission from AC to combined port (schematic in top corner) at 1.6 K and 300 K. The -3 dB point shifts from 5 Hz at room temperature to 70 Hz at 1.6 K. **b** Transmission of a Marki microwave DPX-1721 diplexer for the low-pass and the high-pass port at 4 K and 300 K. The cut-off frequency is at 18 GHz. Note, that the transmission of > 0 dB for the cryogenic low-pass measurement (green) is not physical and arises from calibration inaccuracies of the cabling with the VNA.

6.4.2 Flip-flop qubit

The setup for the dipole coupled flip-flop qubit (Fig. 6.16) is very similar to the standard electron qubit setup. The qubit has 6 DC lines (RB, LB, TG, TLC, BC and RG), 6 AC lines (S, D, PL, RS, RR, and R) and the high-frequency microwave line. All these lines are wired and operated in the same fashion as for the electron qubit. The distinct difference to that standard setup is that the donor gate (DG) requires both fast pulsing (40 GHz) as well as a DC voltage and AC (1 GHz) pulsing. To combine these three different frequency lines we use a home-built bias-T and a Marki Microwave DPX-1721 diplexer at the mixing chamber.

The bias-T consists of a 10 kOhm thin-film nichrome resistor and a 2.18 μF ceramic capacitor (inset Fig. 6.17a) resulting in a cut-off frequency of 5 Hz at room temperature which shifts to 70 Hz at 1.6 K (Fig. 6.17a). We use this bias-T to combine the DC bias from the DC sources, filtered by the 20 Hz filter box, with an attenuated AC pulse from the AWG of up to 1 GHz. We choose attenuators of 20 dB at 4 K, 10 dB at 1 K and 10 dB at 11 mK, giving a noise temperature of 170 mK at base [2].

The diplexer passively combines high-frequency and low-frequency signals by frequency-domain multiplexing with a cut-off at 18 GHz (Fig. 6.17b). We connect the low-frequency port to the output of the bias-T and the high-frequency port to a microwave source with attenuators of 20 dB at 4 K, 10 dB at 1 K and 40 dB at 11 mK, resulting in a noise temperature of 15 mK at base.

In this setup, we are using Stanford Research Systems (SRS) SIM928 Isolated Voltage Source modules in a SIM900 mainframe, a TTL pulse generator (SpinCore PulseBlasterESR-PRO) for triggering, the Lecroy ArbStudio AWG and a AlazarTech ATS9440 PCI digitizer card instead of the PXI and Signadyne cards.

[1] 300 K room temperature noise gets reduced by a factor 10 (10 dB) at 1 K, leading to 30 K additional noise. 31 K thermal noise at 1 K gets reduced by a factor 2 (3 dB) at 11 mK, leading to thermal noise of temperature 15.5 K at the sample.

[2] Assuming an applied voltage of 5 mV at the sample with a 50 Ω impedance, we create 500 nW power dissipation at sample and 5 μW at 11 mK which can be handled by our dilution refrigerator which has a cooling power of 20 μW at 20 mK [169].

6.4.3 Resonator flip-flop qubit

When coupling the flip-flop qubit to a superconducting resonator, the setup (Fig. 6.18) changes significantly from the electron qubit setup. The four gates (TT, TB, S, D) and the inductor of the central conductor (CC) are connected via the 80 MHz filter box to the Stanford Research Systems (SRS) SIM928 Isolated Voltage Source modules in a SIM900 main frame. These lines are thermalized at every temperature stage.

Readout is performed by analysing the transmitted signal through the resonator. We operate in transmission mode. We use a Keysight N5231A vector network analyser (VNA), a machine that sends a microwave signal and detects the amplitude and phase of the transmitted or reflected signal. The input signal is attenuated by 20 dB at 4 K and 11 mK and by 10 dB at 1 K (noise temperature of 180 mK) . The output signal is routed through two PAM TECH 55387 circulators (with a 50 Ω termination on the unused port) to reduce any thermal noise coming down the line and a Micro-Tronics BPC50403 $4-8$ GHz bandpass filter to reduce any noise before amplification. The signal then passes a cryogenic low noise amplifier (LNF-LNC1-12A s/n 265B) with 38 dB gain and a room temperature low noise amplifier (LNF-LNR1-15A) with 37 dB gain before entering the VNA. SilQ controls the SIM modules and the VNA.

Advanced resonator design

The setup for the advanced resonator (Fig. 6.19) design is more complex as we now not only have several additional gates and a microwave antenna but also are operating the resonator in reflection. It is basically a hybrid between the more simple resonator design and the dipole flip-flop design with some additional components for good reflective resonator operation.

The microwave antenna and the AC gates (S, RT, TLT and CB) are connected as for the dipole-coupled flip-flop qubit in Sec. 6.4.2, with the difference that each gate has its own on-chip inductor. The central conductor is biased through an on-chip inductor where the DC signal from a SIM module is combined via the home-made bias-T with a signal from an AWG which is attenuated with 20 dB at 4 K, 10 dB at 1 K and 10 dB at 11 mK. This is the same setup as for the donor gate AC line of the dipole-coupled flip-flop qubit donor gate.

The resonator is operated in reflection where the readout is performed by analysing the reflected signal at one port of the resonator. The signal is generated by the VNA, attenuated by 20 dB at 4 K, 1 K and 11 mK, passes through a PAM TECH 55387 circulator and reaches the resonator. Then the signal is reflected, travels up the same line and enters the circulator where it is separated from the input signal. It is then fed into a Pulsar (CS10-56-436/20) directional coupler where the signal is combined with a pump tone from a second microwave source of a frequency and power calibrated to the signal. This tone is required at the next stage, the Josephson travelling-wave parametric amplifier (TWPA), confined in a lead box, which amplifies the signal up to 20 dB over a 3 GHz bandwidth [174]. Following is the same readout setup as for the previous resonator design.

We add Aeroflex 8143A double-DC blocks on all high-frequency lines to prohibit ground loops.

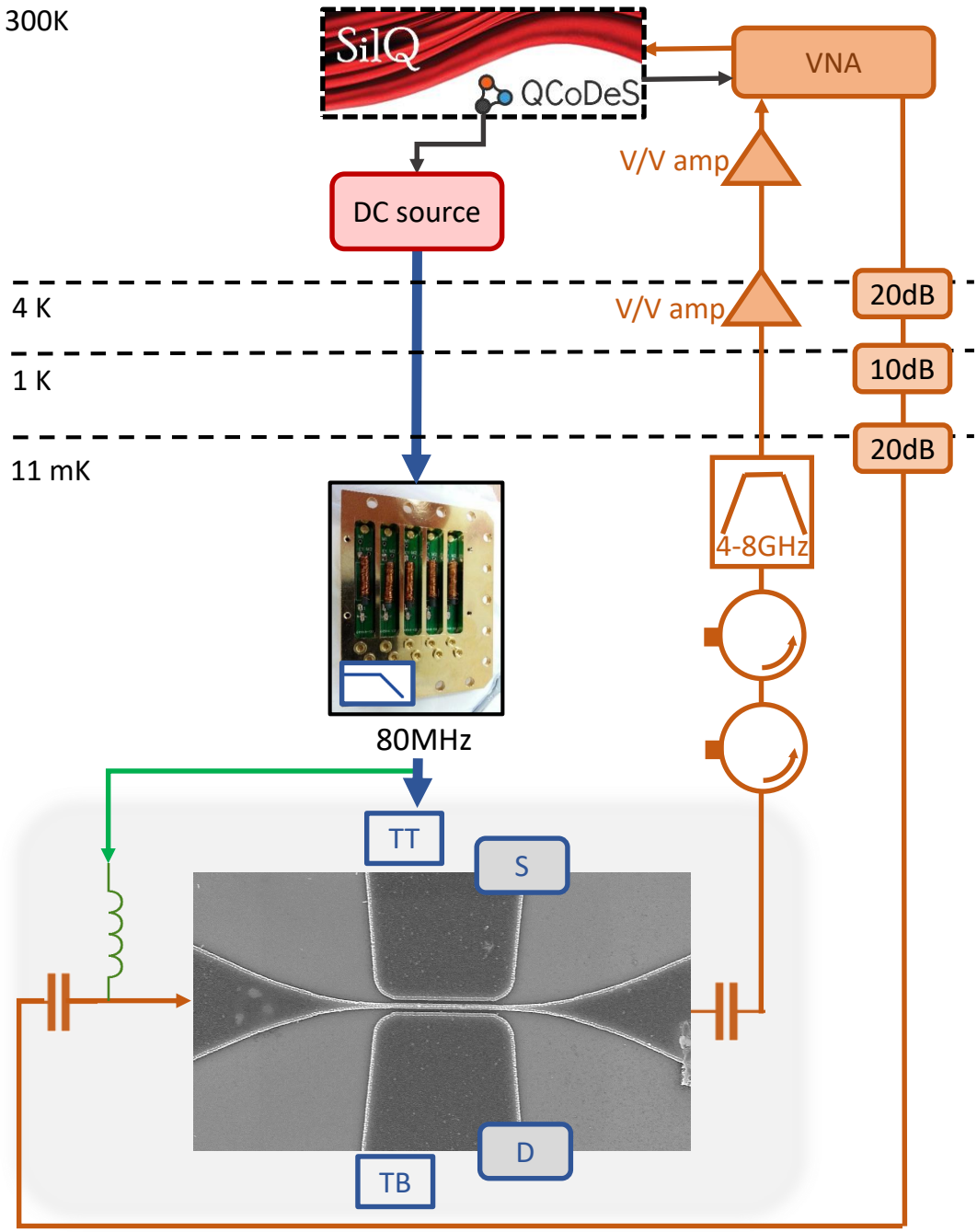

FIGURE 6.18: **Flip-flop resonator qubit setup**. Schematic of the experimental setup for the flip-flop qubit coupled to a superconducting resonator. Detailed description in the main text.

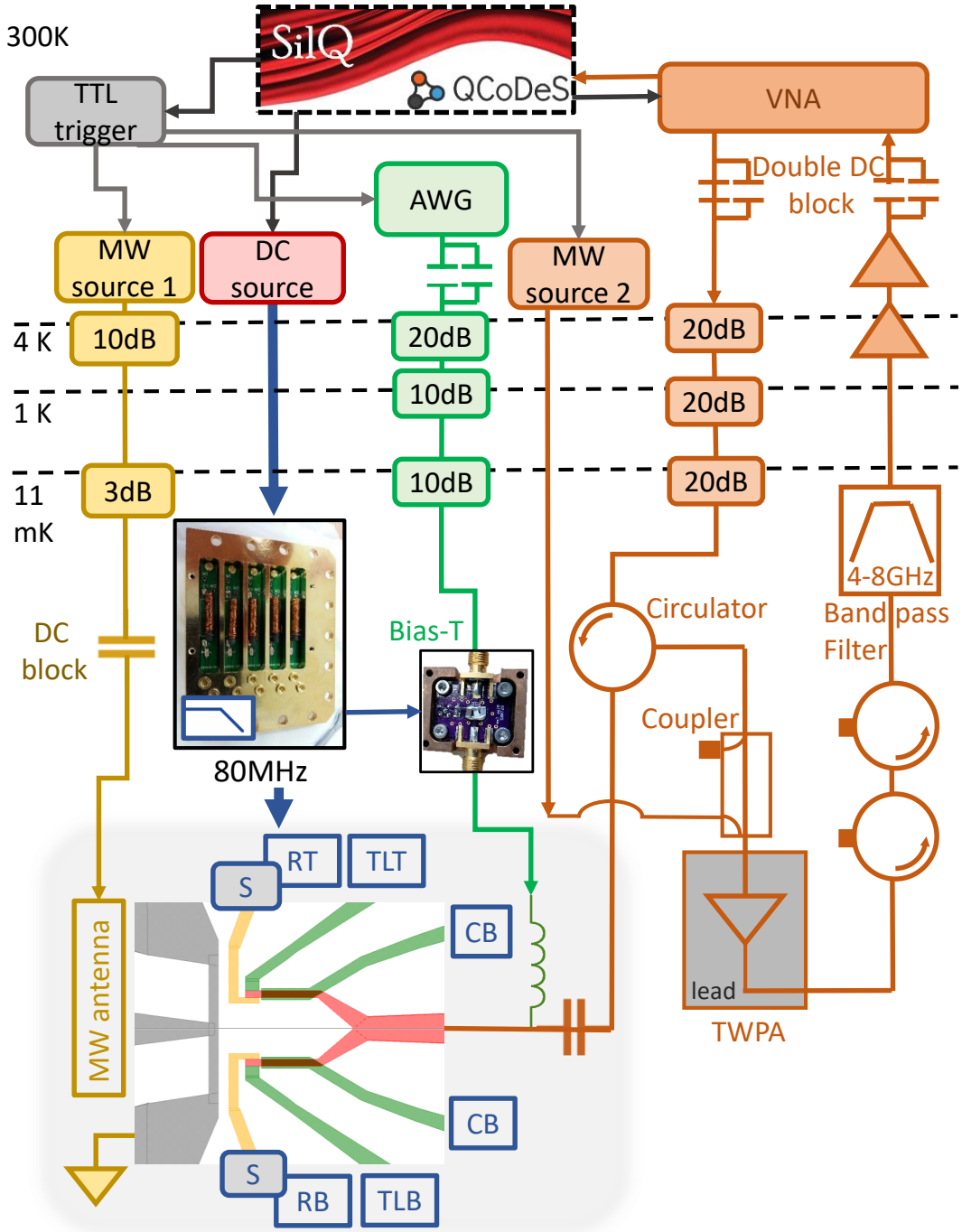

FIGURE 6.19: **Advanced flip-flop resonator qubit setup**. Schematic of the experimental setup for the flip-flop qubit coupled to a superconducting resonator with the advanced design. Detailed description in the main text.

Chapter 7

Flip-flop qubit measurements

"Beginnings are always messy."
– John Galsworthy

Many flip-flop devices, for both dipole-dipole and resonator coupling, were fabricated and tested by the author during the duration of her PhD. This chapter presents the most representative and successful measurements, showing preliminary results about flip-flop qubit operation.

The author acknowledges assistance of A. Laucht with the measurements in Fig. 7.2, G. Tosi with resonator fabrication and V. Schmitt with resonator measurements.

7.1 Proof of principle flip-flop measurement

7.1.1 Driving the flip-flop transition on an electron qubit device

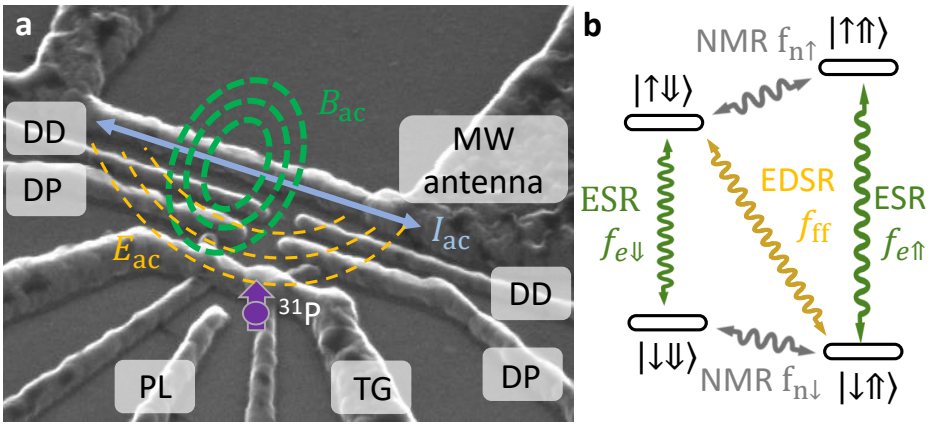

FIGURE 7.1: **Driving the flip-flop transition on an electron qubit device.** **a** Scanning electron micrograph of a device similar to the one used in the experiment. A SET charge sensor is used for electron readout. Two sets of donor gates (DD, DP) as well as a plunger gate (PL) tune the potential and electric field at the donor location. A positive applied voltage attracts the electron towards the Si/SiO_2 interface. A microwave antenna emits predominantly an AC magnetic field, but also emits a spurious AC electric field. **b** Level diagram of the phosphorus donor with one electron. ESR, NMR and flip-flop transition (EDSR) are indicated.

While we were developing dedicated flip-flop qubit devices, we measured the flip-flop transition on an electron and nuclear qubit device (Sec. 6.4.1, Fig. 7.1a). This device contains a SET for readout, a plunger gate (PL), two sets of donor gates (DD, DP) and a microwave antenna. In this design we do not have proper control of the electron orbital degree of freedom, as the electron cannot be confined at the interface. Moreover, the device lacks a gate designated for electrical driving. However, we can harness the imperfections in the device to drive the flip-flop resonance nevertheless.

Firstly, the hyperfine coupling between the electron and phosphorus nucleus was measured to $A \approx 98.5\,\text{MHz}$, deviating strongly from the bulk value of 117.6 MHz. For phosphorus donors, the hyperfine interaction is strongly dominated by the Fermi contact interaction. Consequently, the deviation of the hyperfine coupling shows a distortion of the electron wave function. This can be caused by external electric fields applied to the donor gates and by strain in the sample due to the different thermal expansion coefficients of aluminium and silicon. The measured device is expected to exhibit strain of 0.05 % in-plane with B_0 and -0.1 % perpendicular to B_0 (Supplementary of Ref. [175]), which statically distorts the electron wave function by separating the electron slightly from the nucleus. An applied oscillating electric field can then by used to modulate the hyperfine interaction and drive flip-flop rotations. The device shows a hyperfine tunability of $\Delta A = 0.4\,\text{MHz}$ for an applied voltage of $V_{DG} = 250\,\text{mV}$ on the donor gates (Supplementary of Ref. [175]). As the cut-off frequency for these gates is around 1 MHz, they cannot be used to drive the flip-flop transition. However, the microwave antenna supports gigahertz driving.

The coplanar waveguide microwave antenna is usually used to supply the magnetic drive to perform ESR on the electron and NMR on the nucleus. It is designed

to maximize the magnetic field and minimize the electric field at the short tip. Nevertheless, imperfections result in the emission of a spurious electric field at high frequencies $> 20\,\mathrm{GHz}$ [176]. Here, we deliberately exploit such imperfections and seek specific frequencies where the antenna appears to emit the strongest electric field. We estimate the emitted electric field by measuring the response of the SET current to a microwave pulse repeatedly, when the SET is tuned in Coulomb blockade (Fig. 7.2c). At a frequency of $43.38 \pm 0.04\,\mathrm{GHz}$ we observe a significant increase of the SET current which indicates a shift of the SET tuning induced by a large electric field emitted by the antenna (Fig. 7.2c). The repetitions show that the current spikes are a real effect due to the microwave and not random noise. Once the frequency yielding maximum electric field has been found, we adapt the magnetic field B_0 to provide the flip-flop resonance at the desired frequency. In this, we apply an external magnetic field of $B_0 = 1.55\,\mathrm{T}$ such that the flip-flop transition appears at (Eq. 3.19)

$$f_{\mathrm{ff}} = \sqrt{(\gamma_e + \gamma_n)^2 B_0^2 + A^2} = 43.38\,\mathrm{GHz}, \tag{7.1}$$

neglecting any change in γ_e and orbital shift D_{orb} due to the small shift of the electron.

7.1.2 Measuring the flip-flop transition

To measure the flip-flop transition, we determine whether the nuclear spin has flipped after an adiabatic EDSR pulse has been applied. Therefore we use the following pulse sequence (Fig. 7.2a). First, we perform a nuclear readout. To this end, we load an electron in state $|\downarrow\rangle$, apply an electron π-pulse with frequency $f_{\mathrm{e}\Downarrow}$ and readout the electron. If the electron is in state $|\uparrow\rangle$, the nuclear spin is in state $|\Downarrow\rangle$ and if the electron is in state $|\downarrow\rangle$, the nuclear spin is in state $|\Uparrow\rangle$. Now, that we know the initial nuclear state, we perform the flip-flop EDSR rotation. Therefore, we load $|\downarrow\rangle$. If the nucleus is $|\Downarrow\rangle$, we are outside of the flip-flop space and need to apply another electron π-pulse with frequency $f_{\mathrm{e}\Downarrow}$ to reach $|\uparrow\Downarrow\rangle$. This pulse will have no effect on a $|\downarrow\Uparrow\rangle$ state. Once we initialized in the flip-flop subspace $|\downarrow\Uparrow\rangle, |\uparrow\Downarrow\rangle$, we perform an adiabatic inversion (50 kHz sweep in 10 ms) at frequency f_{EDSR} with a power of 18 dBm at room temperature. If the flip-flop transition is successfully driven, both the electron and the nuclear spin will flip. To determine whether such a flip has occurred, we measure the nuclear spin state again. Is the nuclear state different than at the start of the pulse sequence, we know that we have successfully driven the flip-flop transition[1]. We repeat this pulse sequence many times to find the nuclear spin flip probability for each frequency f_{EDSR}.

Additional, we measure the electron spin flip probability for the two ESR transitions with a drive power of 18 dBm at room temperature.

7.1.3 Analysis of the flip-flop drive

We find a clear peak in the nuclear spin flip probability for the flip-flop drive (Fig. 7.2c,d) at $f_{\mathrm{ff}}^{\mathrm{meas}} = 43.3782\,\mathrm{GHz}$ (Gaussian fit with width 50 kHz, corresponding to adiabatic sweep depth). To compare this value to the expectation, we determine the ESR transition frequencies $f_{\mathrm{e},\Downarrow}, f_{\mathrm{e},\Uparrow}$. As these transitions were measured with very high power, the resonance lines exhibit oscillations that indicate coherent Rabi drive of the spin (Fig. 7.2c). To determine the respective resonance frequencies, we fit the

[1] As the nuclear spin relaxation time is on the order of hours, we assume that no non-driven flips occur.

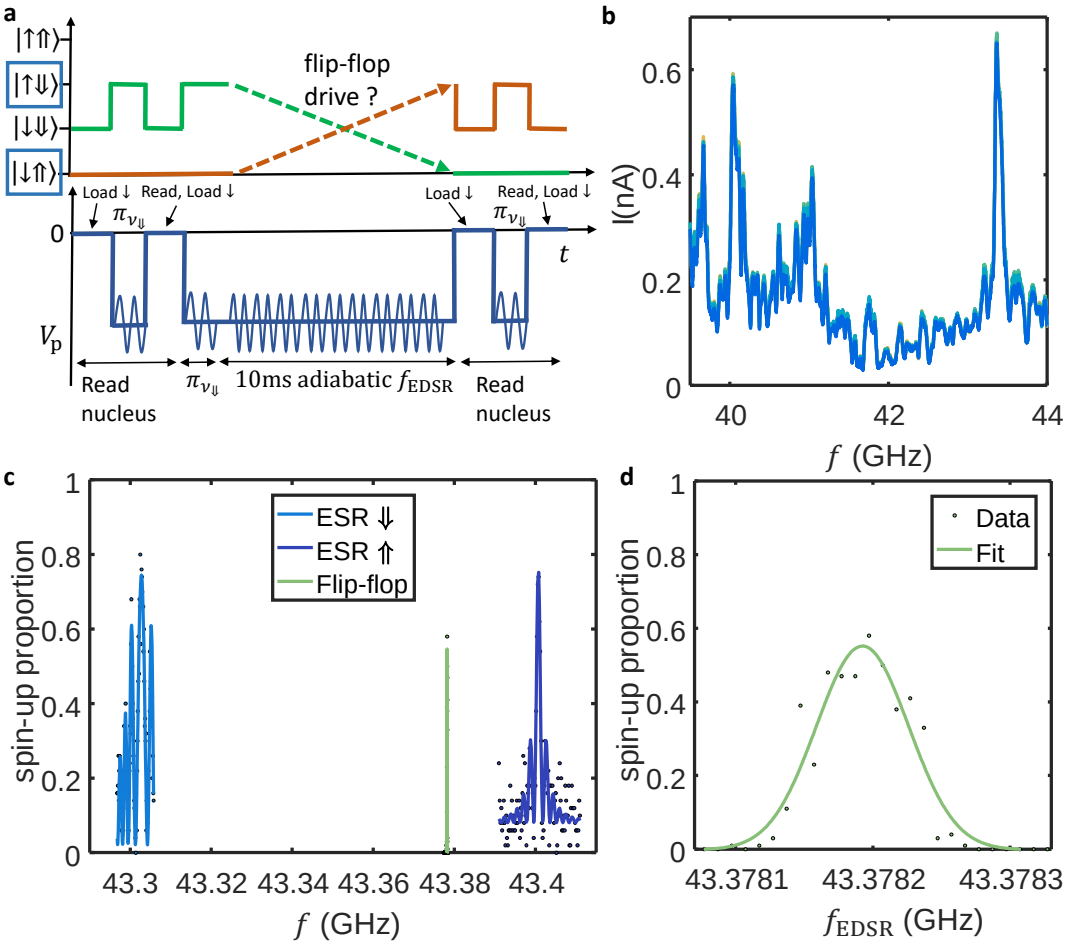

FIGURE 7.2: **Flip-flop qubit resonance.** **a** Pulsing scheme to drive the flip-flop resonance. The top panel shows the state of the qubit during the pulse sequence, when the nuclear spin is initially $|\Uparrow\rangle$ (orange) or $|\Downarrow\rangle$ (green). The bottom panel shows the pulse sequence. First a nuclear readout is performed. Than $|\downarrow\rangle$ is loaded and a π-pulse at $f_{e\Downarrow} = 43.302415\,\text{GHz}$ is performed to bring an initial state of $|\downarrow\Downarrow\rangle$ into the flip-flop space $|\downarrow\Uparrow\rangle, |\uparrow\Downarrow\rangle$. Subsequently an adiabatic inversion (50 kHz sweep in 10 ms) at f_{EDSR} with a power of 18 dBm at room temperature is performed. Finally the nuclear spin is read out again. **b** Multiple SET current traces measured, while tuned in Coulomb blockade and applying a microwave pulse with the ESR line. **c** Spectrum with ESR and flip-flop transitions. Fitting the Rabi formula to the ESR transitions gives $f_{e\Downarrow} = 43.3028\,\text{GHz}$ with a pulse length of $t_p = 911\,\text{ns}$ and a Rabi frequency of $f_R = 2.9\,\text{MHz}$ for $|\Downarrow\rangle$ and $f_{e\Uparrow} = 43.4007\,\text{GHz}$ with a pulse length of $t_p = 653\,\text{ns}$ and a Rabi frequency of $f_R = 1.1\,\text{MHz}$ for $|\Uparrow\rangle$. Fitting a Gaussian to the EDSR flip-flop transition gives $f_{ff}^{meas} = 43.3782\,\text{GHz}$.

transitions with the Rabi formula

$$P_{\uparrow}(f) = \frac{f_R^2}{f_R^2 + (f_0 - f)^2} \sin\left(2\pi\sqrt{f_R^2 + (f_0 - f)^2}/2 \cdot t_p\right)^2 + \text{offset}, \tag{7.2}$$

where f_R is the Rabi frequency, t_p the Rabi pulse length and f_0 the resonance frequency. This gives $f_{e\Downarrow} = 43.3028\,\text{GHz}$ with a pulse length of $t_p = 911\,\text{ns}$ and a Rabi frequency of $f_R = 2.9\,\text{MHz}$ for $|\Downarrow\rangle$ and $f_{e\Uparrow} = 43.4007\,\text{GHz}$ with a pulse length of $t_p = 653\,\text{ns}$ and a Rabi frequency of $f_R = 1.1\,\text{MHz}$ for $|\Uparrow\rangle$.

We calculate the expected flip-flop frequency from these measurements to

$$f_{ff}^{exp} = f_{e\Downarrow} + A/2 + \gamma_n B_0 = 43.3784\,\text{GHz}. \tag{7.3}$$

The difference between the directly measured flip-flop transition f_{ff}^{meas} and the expectation f_{ff}^{exp} is 0.2 MHz. This small deviation can be attributed to changes in the hyperfine coupling of up to 200 kHz depending on the exact device tuning [175].

Consequently, we confirm with this measurement that we can drive the flip-flop transition electrically. However, the small range of hyperfine coupling tunability and the small electric drive through the magnetic antenna, prevented us from coherent control.

7.2 Dipole-dipole coupling devices

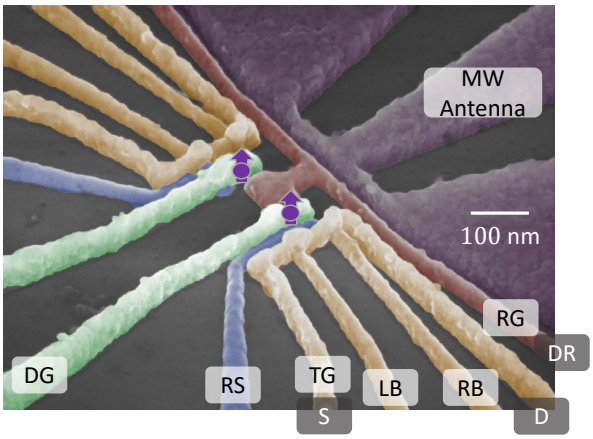

FIGURE 7.3: **Device layout of the flip-flop qubit.** Scanning electron micrograph of a device similar to the one used in the experiment. A SET charge sensor is used for electron readout (TG, LB, RB, yellow). A donor gate (DG, green) tunes the potential and electric field at the donor location and emits electric fields at microwave frequencies. A confinement gate (RS, blue) controls the electron tunnel rate to the SET and tunes the electron wavefunction laterally. An additional reservoir (RG, red) allows for more electron readout options and a microwave antenna (MW, purple) emits an AC magnetic field to drive ESR and NMR transitions.

Many two qubit flip-flop devices designated for direct dipole-dipole coupling were measured. The results shown in this section were measured on a device as depicted in Fig. 7.3 at 12 mK and are representative for other measured devices (see Sec. 6.1.1 for device designs). In this section, we will walk the reader through the measurements performed on any new donor or quantum dot qubit device to establish its basic functionality. Therefore, we firstly form a SET and then establish

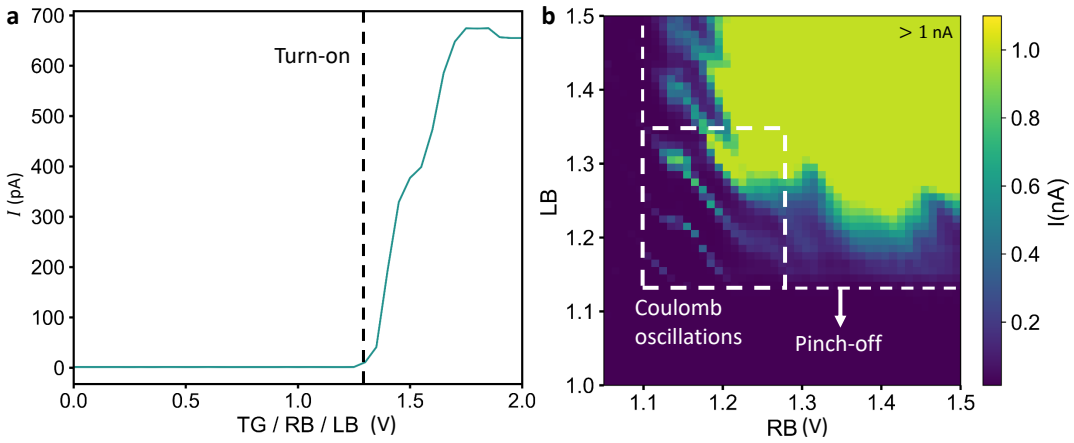

FIGURE 7.4: **SET turn-on and pinch-off.** **a** Current characteristic when increasing the SET gates, TG, RB and LB, simultaneously. At 1.3 V the channel between S and D becomes conducting - the transistor "turns-on". **b** Current measured when the SET barriers LB and RB are decreased individually until the conducting channel is "pinched-off" and no current flows at 1.15 V and 1.1 V respectively. Just above pinch-off we observe Coulomb oscillations when a quantum dot is formed between the barriers (region in dashed square).

electron readout (compare Sec. 2.3.3 for a detailed description of the concepts), as will be described in the following sections.

7.2.1 SET characterization

When a new qubit device is tested, the first step is to test all gates for leakage currents. As all gates are open circuits, no current flow is expected. However, imperfections in the device can create current pathways (more details will be discussed in Sec. 7.2.3).

If all gates are well isolated, the next step is to form a SET. Therefore, the current between source S and drain D is measured while increasing the voltage on the SET top-gate TG and the two barriers RB and LB simultaneously, with a small bias voltage of 250 μV applied to S while D is grounded (Fig. 7.4a). We observe that the channel between S and D becomes conducting above the threshold voltage of 1.3 V when a 2DEG is induced under the gates - this is called the transistor "turn-on". The current increases until it saturates, mostly because the resistance of the channel becomes negligible compared to the resistance of the Ohmics. By increasing the S-D voltage difference, the transistor current can be increased if desired.

Next, we test if the SET barriers are working. We set the top gate TG above turn-on at 1.8 V and decrease the voltage of both barriers LB and RG independently until the current flow has stopped - the conducting channel is "pinched-off" (Fig. 7.4b). Just before the current flow is completely restricted, electrons are still trapped on the SET island in between the barriers and a many-electron quantum dot is formed. When both barriers are near "pinch-off", we observe Coulomb oscillations of the current when the electron occupancy of the island changes by one (highlighted region in Fig. 7.4b). Decreasing the barrier voltage increases the barrier height and opaqueness. Electrons are forced out one-by-one until any current is suppressed when the barriers become fully opaque and no electron can come through.

We aim to form a large quantum dot, the SET island, that only allows for single electron transport. Therefore we tune the barriers just above pinch-off such that the

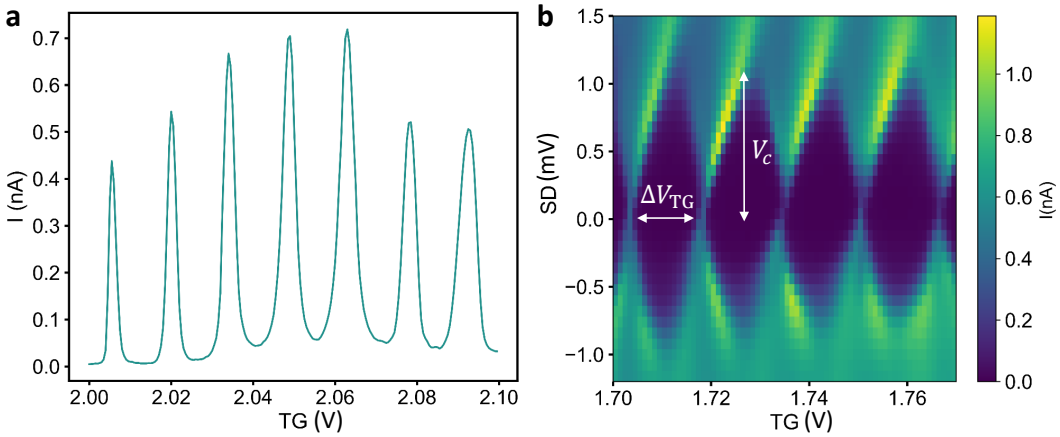

FIGURE 7.5: **Coulomb oscillations and Coulomb diamonds.** **a** Coulomb oscillations of the SET current showing the single electron transport through the SET with the barriers just above pinch-off (LB= 1.25 V, RB= 1.2 V). **b** Coulomb diamonds of the SET current when TG and the S-D bias are varied. The parameters $\Delta V_{\mathrm{TG}} = 15.8\,\mathrm{mV}$ and $V_{\mathrm{c}} = 1.2\,\mathrm{mV}$ relate to the lever arm of TG to μ_{SET} and the charging energy of the SET island respectively.

Coulomb oscillations are sharp and have maximum contrast: the current is maximum during an electron tunnel event and zero otherwise, when the island is in Coulomb blockade (Fig. 7.5a). When increasing the TG voltage, we sequentially load electrons one-by-one. The plunger gate PL can also be used to fine-tune the SET.

Finally, we measure the so-called "Coulomb diamonds" by sweeping both the TG voltage and the S-D bias (Fig. 7.5b). We observe periodic regions, where the conduction is blocked, which are the Coulomb diamonds. From the height V_{c} and width ΔV_{TG} of the diamonds, we can extract the charging energy of the SET island to

$$E_c = V_{\mathrm{c}} \cdot e = 1.2\,\mathrm{meV} \tag{7.4}$$

and the lever arm α_{TG} of the gate TG to the shift in μ_{SET} to

$$\alpha_{TG} = \frac{V_{\mathrm{c}}}{\Delta V_{TG}} = \frac{C_{\mathrm{TG}}}{C} = 0.038, \tag{7.5}$$

where C_{TG} is the capacitance between TG and the SET island and C is the total capacitance of the island.

7.2.2 Donor and quantum dot formation and readout

Now that we characterized our SET, we are looking for donors in our device. Therefore, we sweep TG and the donor gate DG over a vast range of bias voltages while measuring the SET current and monitoring the Coulomb peaks. This results in a 2D map, the "charge stability diagram". Donors are revealed by discontinuities in the Coulomb peaks when the donor charge state changes, the "charge transition"[2]. These transitions indicate the boundary between donor ionization and neutralization. Fig. 7.6a shows such a charge stability diagram with four donor charge transitions visible.

[2]Note, that any charge transition, e.g. a charge trap being loaded, will appear in the charge stability diagram. While the charge transfer signal (size of the break of the Coulomb peaks, see Sec. 2.3.3) can give an indication whether it is a donor, only an ESR measurement at finite B_0 can confirm this.

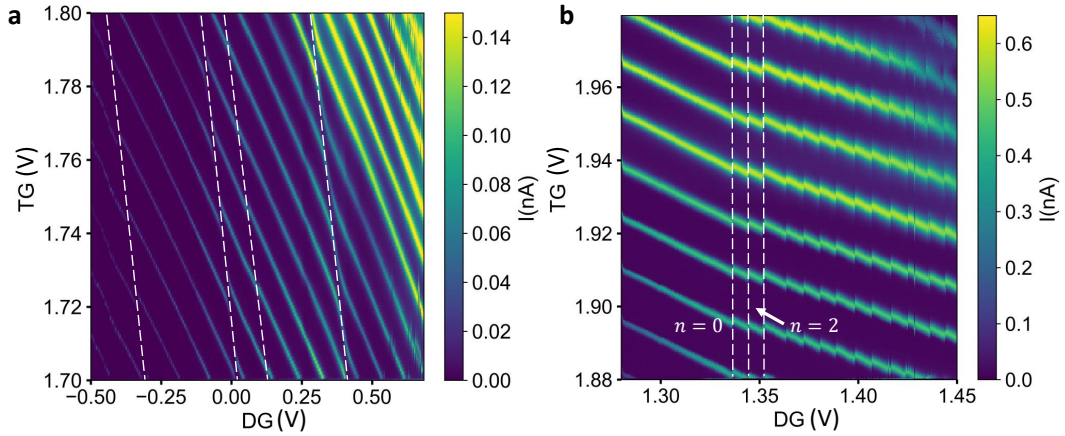

FIGURE 7.6: **Flip-flop qubit charge stability diagrams.** Map of the SET Coulomb peaks with SET top gate TG and donor gate DG voltage bias, showing several donor transitions (**a**) and the transitions of a quantum dot that is filled with electrons one-by-one (**b**, n is the number of electrons in the dot) (indicated with white dashed lines).

It is important to note that donor charge transitions can appear over a wide range of voltages and their visibility strongly depends on the device tuning. Depending on the exact location of the donor, each gate has a different effect on the donor due to a different capacitive coupling. Thus, varying all available gate voltages in a systematic way while searching for donors is necessary. Determining the capacitive coupling of each gate to a specific donor also allows for an estimate of the donor location by triangulation [175].

The flip-flop device design also allows for the formation of a quantum dot at the interface. Fig. 7.6b shows the charge stability diagram with many charge transitions of such a quantum dot. Each transition indicates the loading of one more electron onto the dot and the transitions are spaced by $\Delta V_{\mathrm{DG}} = E_{\mathrm{C}}^{\mathrm{QD}}/e\beta$, where β is the lever arm between the donor gate and the quantum dot electrochemical potential and $E_{\mathrm{C}}^{\mathrm{QD}}$ is the charging energy of the quantum dot.

Once donor and dot charge transitions have been identified, we need to establish spin-readout. Therefore we choose a donor (or dot) transition and tune to a voltage such that we observe a high current when the donor is ionised and zero current when the donor is neutral (red dot in Fig. 7.7a). When tuned exactly at the boundary between ionization and neutralization, we measure at $B_0 = 0\,\mathrm{T}$ a random telegraph signal of short current peaks ("blips", inset in Fig. 7.7a) caused when the electron tunnels on and off the donor randomly. Once we observe blips we can apply an external magnetic field and use the pulse sequence empty-load-read (Fig. 7.7b) to determine the tuning spot where we observe high current while emptying, zero current while loading and blips at the start of the read-phase. This is the indicator that we are tuned such that $\mu_{\uparrow} - E_{\mathrm{Z}}/2 = \mu_{\mathrm{SET}} = \mu_{\downarrow} + E_{\mathrm{Z}}/2$ and only $|\uparrow\rangle$ electrons escape the donor. When $|\uparrow\rangle$ escapes, it will eventually be replaced by $|\downarrow\rangle$, which stays confined and no more blips are observed. Consequently, we can distinguish between the two electron spin states. Measuring this pulse sequence repeatedly gives the contrast between between $|\uparrow\rangle$ and $|\downarrow\rangle$, which shows how well we can distinguish the two. If a contrast well above 50 % can be achieved, the donor or dot is deemed operational. Unfortunately, we could not find any spin readout in this device.

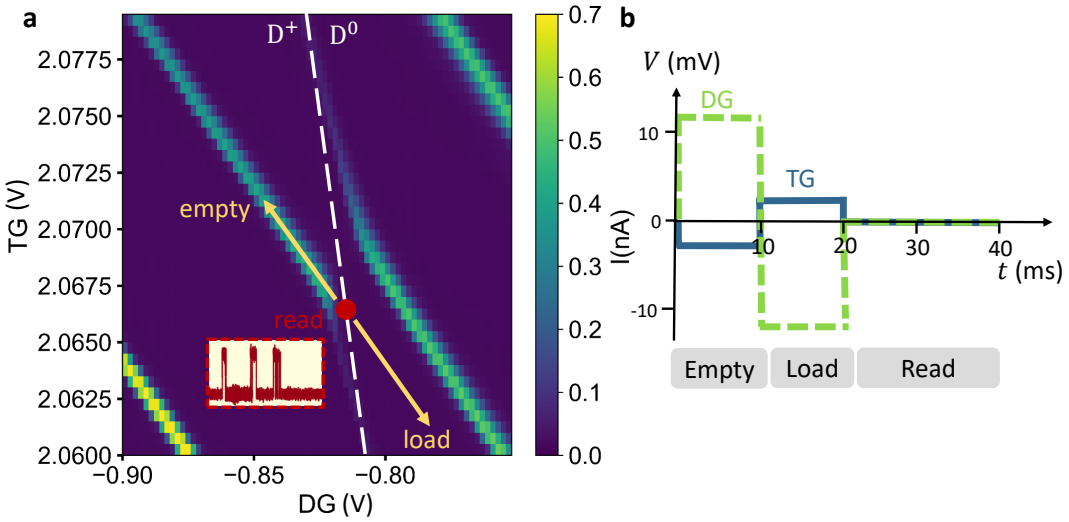

FIGURE 7.7: **Qubit spin readout.** **a** Charge stability diagram with donor transition (white dashed line). The red dot marks the readout position where we measure a random telegraph signal at $B = 0$ (inset) and should achieve spin readout for $B_0 \gg k_B T$. To empty the dot we move into the ionized regime and to load into the neutral regime, while keeping the SET electrochemical potential constant. **b** Pulse sequence of the TG and DG voltages for an empty-load-read sequence.

7.2.3 Failure modes of devices

Nanometric devices, as were fabricated and measured in this thesis, are very fragile. Different failure modes can cause a device to not function properly.

One major failure mode concerns the conduction between source and drain. At temperatures $T < 50\,\mathrm{K}$ in intrinsic silicon, the thermally-induced charge carriers freeze out, resulting (theoretically) in zero current between S and D, unless an electron channel is formed by applying a voltage above turn-on to the top gate. Nevertheless, we encountered many devices where the S-D channel was conducting several nA without any applied voltage. In this case the SET cannot be operated, as the transistor can never be turned-off. This failure mode arises from the fact, that positive charges trapped in the thick SiO_2, grown by wet oxidation, attract electrons and induce a 2DEG along random paths. If a continuous path between S and D is created in this way, we observe a leakage current and have to discard the device. This problem is currently being addressed in two ways. Firstly, we introduced $p+$ doped regions which block the conducting pathways between S and D. Secondly, we are refining the stock fabrication such that a cleaner SiO_2 is used which contains fewer trapped positive charges.

Another common failure mode, related to the previous issue, are leakage currents from the gates to ground or S/D. Small holes in the SiO_2 in combination with the randomly induced conductive channels allow for a current flow from a gate to the substrate and then to ground or S/D. These issue is also being addressed by a refined stock fabrication.

Another problem are small holes in the Al_2O_3, separating overlapping gates, which lead to leakage between those gates. Moreover, lift-off issues, where parts of the gates have either been removed or wrongly connected, can cause individual gates to not function. With proper oxidation and careful device processing however, these problems occur rarely.

A further issue is electro static discharge (ESD) which can destroy the whole device. Even with careful grounding during mounting and bonding, severe ESD can sometimes occur during fabrication. Thus, recently we have started to connect all gates to ground with small aluminium connections during the whole fabrication process which are later removed once the device has been bonded and grounded.

Finally, we have to find an appropriate donor which can be readout with the SET and that has a tunnel coupling to the interface dot roughly of the right order of magnitude.

Engineering of the stock, the device fabrication, device layout and donor implantation is still ongoing to improve device yield.

7.3 Resonator qubit devices

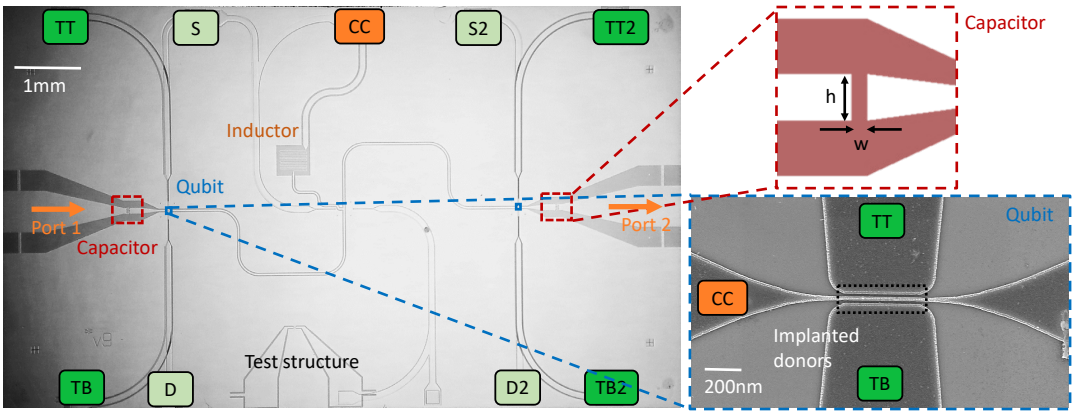

FIGURE 7.8: **Charge qubit resonator design.** Scanning micrograph of the resonator with the qubit region and the capacitor shown in detail. The resonator is operated in transmission with the input at port 1 and the output at port 2. The central conductor (CC) can be biased through an on-chip inductor. A 2DEG can be induced under the top gates TT and TB (and TT2, TB2). The capacitor dimensions are $h = 90\,\mu$m and $w = 30\,\mu$m. The constriction of the central conductor, where the donors are implanted, is 80 nm.

The results presented in this section were measured on a resonator device as shown in Fig. 7.8 and are representative for all other measured devices (see Sec. 6.1.2 for device designs). For a detailed description of the concepts see Sec. 2.4.

7.3.1 Resonator characterization

We operate the resonator in transmission and characterize it by finding its resonance frequency, the coupling strength to the transmission lines described by the quality-factor $Q_c \propto \sqrt{C}$ (C is the coupling capacitance on both ports) and internal losses described by the internal quality-factor $Q_{\text{int}} \propto 1/R$ (R is the resistance that describes the internal losses). In transmission mode the transmitted amplitude $|S_{21}(f)|^2$ and phase $\angle S_{21}(f)$ can be expressed from Eq. (2.57) as

$$|S_{21}(f)|^2 = \left(\frac{Q_{\text{tot}}}{Q_c}\right)^2 \frac{1}{1 + 4Q_{\text{tot}}^2 \left(\frac{f - f_r}{f_r}\right)^2} \tag{7.6}$$

$$\angle S_{21}(f) = -\arctan\left(2Q_{\text{tot}} \frac{f - f_r}{f_r}\right) \tag{7.7}$$

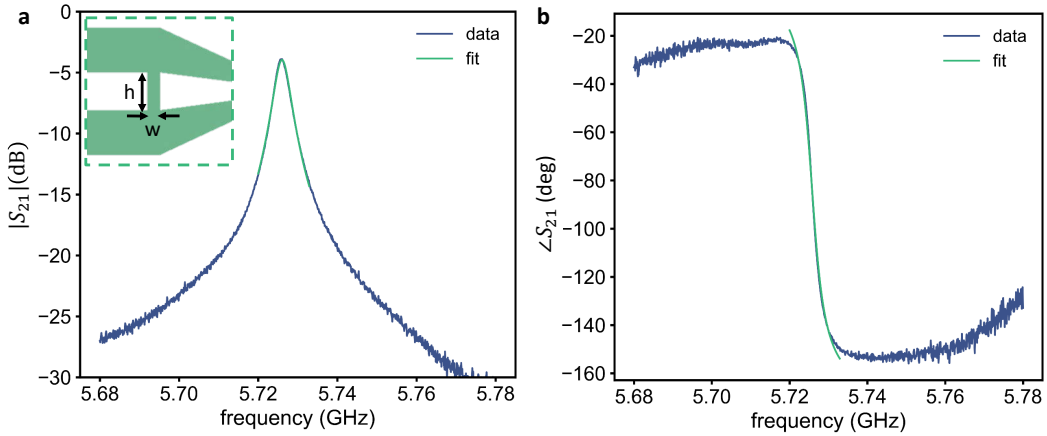

FIGURE 7.9: **Resonator transmission amplitude $|S_{21}|$ (a) and phase $\angle S_{21}$ (b).** The input power is -35 dBm at room temperature. The fit uses Eqs. (7.6) and (7.7) and gives $f_r = 5.7260$ GHz, $Q_{\text{tot}} = 1307$ and $Q_c = 2062$ for the amplitude and $f_r = 5.7259$ GHz and $Q_{\text{tot}} = 1114$ for the phase. The capacitor design that leads to this coupling strength is shown in the inset, with dimensions $h = 90\,\mu$m and $w = 30\,\mu$m.

where

$$\frac{1}{Q_{\text{tot}}} = \frac{1}{Q_c} + \frac{1}{Q_{\text{int}}} \tag{7.8}$$

is the total quality factor and f_r the resonance frequency. Thus, by fitting these expressions to the measured resonance curves, we can extract the required knowledge about our resonator.

Fig. 7.9 shows the amplitude and phase measurement of the resonators resonance including a fit of Eq. (7.6) and (7.7). We extract

$$\begin{aligned} f_r &= 5.726 \pm 0.002\,\text{GHz}, \\ Q_{\text{tot}} &= 1210 \pm 136, \\ Q_c &= 2062. \end{aligned}$$

The values of Q_c and Q_{tot} lead to $Q_{\text{int}} = 2928$. Consequently, our resonator is overcoupled, as intended. However, this also means that the internal losses cannot be properly determined and Q_{tot} and Q_{int} are to be considered with care. The insert in Fig. 7.9a shows the capacitor design that results in the measured Q_c with dimensions $h = 90\,\mu$m and $w = 30\,\mu$m.

To achieve a good understanding of our resonators, we observe their behaviour under temperature and external magnetic field change. These characteristics will not only give insight into the internal losses of the resonator but also help with understanding the resonators behaviour at different measurement conditions.

Only at zero frequency are superconductors truly lossless, otherwise they dissipate power [177]. Bardeen–Cooper–Schrieffer (BCS) theory predicts losses through the acceleration of quasi-particles which depend on the quasi-particle density which in turn diminishes with temperature. Additionally dissipation can be caused by radiation or dielectric losses [165]. Moreover, the conductivity of a superconductor is predicted to change, leading to a change in the resonance frequency.

When studying the effect of temperature on the resonator frequency f_r and the internal quality factor Q_{int}, we indeed observe a shift of f_r and an increase of Q_{int} upon lowering the temperature (Fig. 7.10). The former saturates below 2.5 K, while

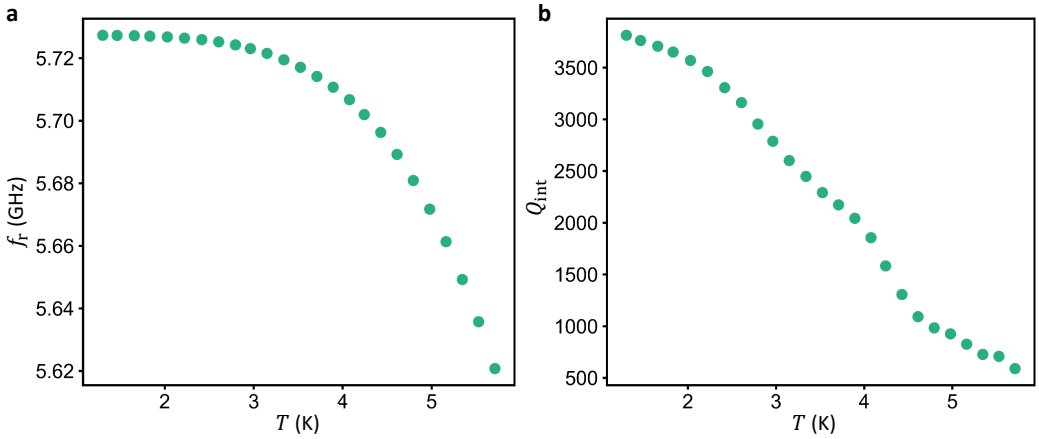

FIGURE 7.10: **Resonance temperature dependence.** **a** Resonance frequency f_r shift with temperature. **b** Internal quality-factor Q_{int} change with temperature.

the latter continues to increase until the lowest temperature in the range allowed by our variable-temperature insert (VTI) system, $T = 1.3\,\mathrm{K}$. As we aim to operate over-coupled resonators the internal losses of the resonator do not concern us as long as they are lower than Q_c. For $Q_c \approx 2000$, internal losses are negligible for $T \lesssim 3.8\,\mathrm{K}$. It is important to note that this temperature lies below the temperature of 4.2 K of liquid helium. Consequently, any studies of these resonators at 4.2 K will be limited by the internal losses.

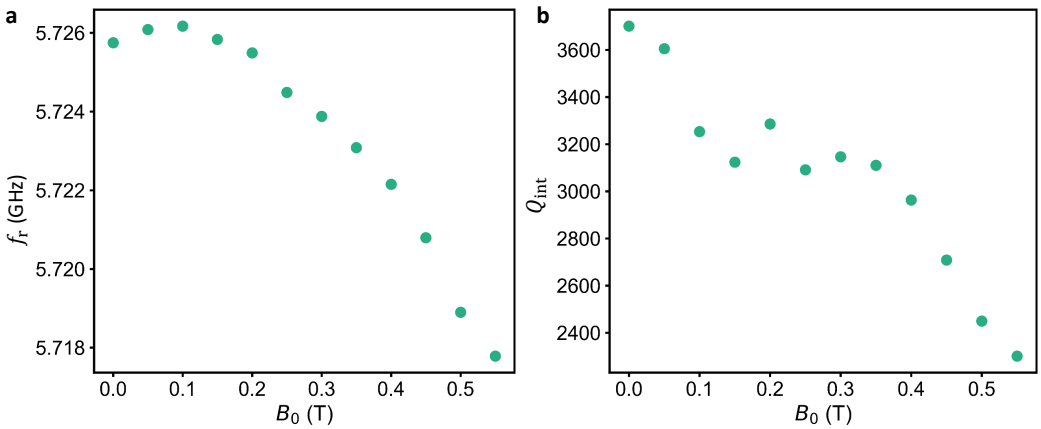

FIGURE 7.11: **Resonance magnetic field dependence.** **a** Resonance frequency f_r shift with external magnetic field. **b** Internal quality-factor Q_{int} change with external magnetic field B_0.

When analysing the dependence of the resonance frequency and the internal quality factor with applied external magnetic field B_0, applied in-plane with the niobium film, we observe a shift in resonance frequency and an increase in Q_{int} towards lower magnetic fields (Fig. 7.11), as for the temperature dependence. Although, here the dependence is much less significant. The resonance shift is most likely caused by a change in the kinetic inductance of the resonator which increases with greater magnetic field. The internal losses are enhanced when vortices are induced and the critical magnetic field is approached. However, we are planning to operate at magnetic fields of $200 - 400\,\mathrm{mT}$ where the induced losses are still small. Note that, small perpendicular field components, resulting from a misalignment between B_0

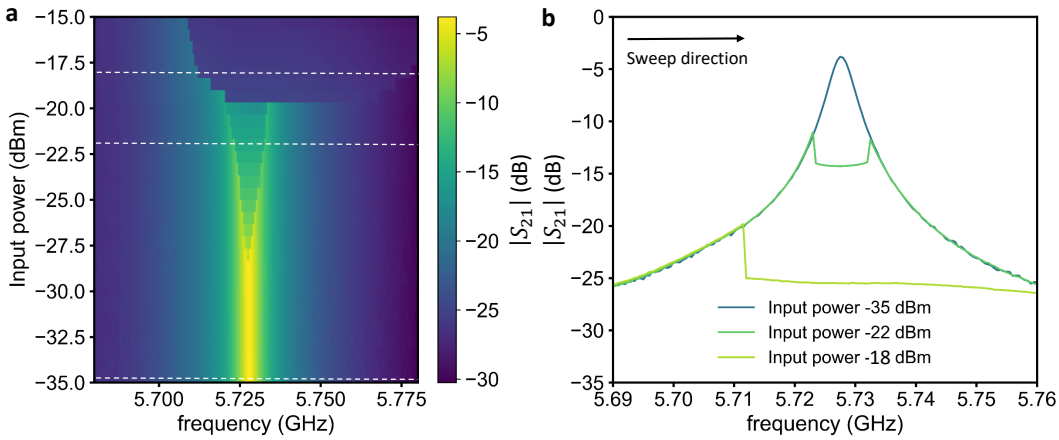

FIGURE 7.12: **Resonance dependence on excitation power.** **a** Resonance amplitude $|S_{21}|$ with input power. **b** Line traces from (**a**, white dashed lines) at three different powers, showing the different regimes of the resonator operation. The frequency sweep direction is from left to right, indicated by the arrow.

and the chip, reduce the critical magnetic field and introduce additional losses due to trapped vortices.

Finally, we characterize the resonator performance with input power (Fig. 7.12). The power indicated here, is the output power of the VNA at room temperature. At cold temperatures attenuation of in total -60 dB is added in from of attenuators, on top of any line attenuation (see Fig. 6.18). When increasing the input power, we increase the photon number in the resonator. A high photon number leads to non-linear effects and the destruction of the resonance when the superconductivity breaks down. The large powers cause heating of the metal, creating hot spots and ultimately the metal transitions from superconducting to normal [178]. While performing qubit measurements, we aim to operate the resonator in the single-photon regime (corresponding to -64 dBm at room temperature), way below any non-linear effects.

7.3.2 2DEG influence

After characterizing the resonator, we test the qubit functionalities. To load an electron onto the donor, we need to activate a 2DEG below the reservoir top gates TT and TB and load the electron from the reservoir onto the donors by biasing the central conductor CC. To determine whether we are inducing a 2DEG, we measure the current from source S to drain D through the central conductor, passing through the gap (see inset in Fig. 7.13a). However, this induces a 2DEG below the entire central conductor. We measure a turn-on at 1.45 V (Fig. 7.13a) and achieve a pinch-off of the current by controlling the bias voltage on both TB, TT and the central conductor CC (Fig. 7.13b).

Now that we have confirmed that we can indeed induce a 2DEG and bias the central conductor, we study the influence of a 2DEG beneath the resonator (Fig. 7.14). When inducing a 2DEG beneath the central conductor, we measure an increase of internal losses (corresponding to a reduction of Q_{int}, Fig. 7.14d) until the resonance ultimately breaks down at $CC = 2.5$ V. We relate these losses to the excitation of the mobile charge carriers below the resonator which resonate with the resonator. The more carriers are induced, the stronger the effect becomes until a critical number of charge carriers is reached. The movement of this many charges can also lead to

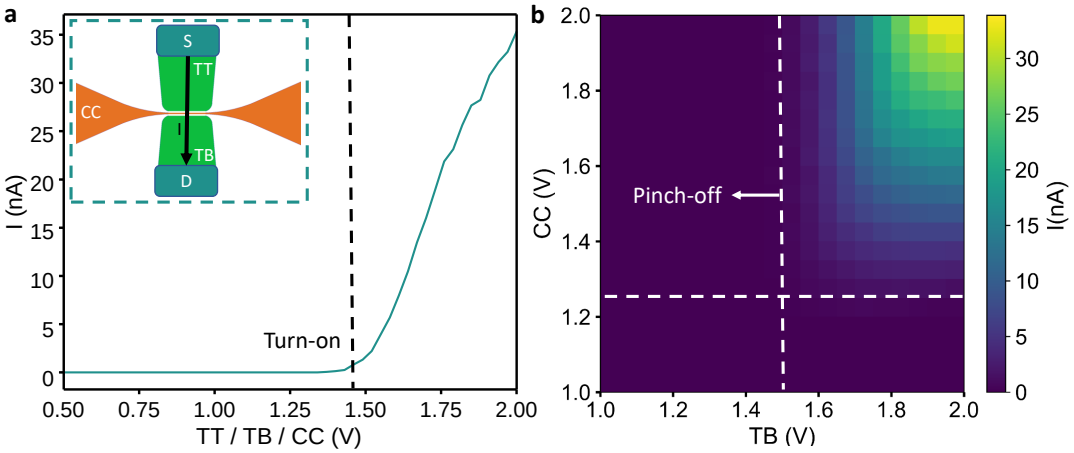

FIGURE 7.13: **Resonator turn-on and pinch-off. a** Measured current flow from source S to drain D along the gates TT, CC and TB as shown in the inset, when increasing their bias voltages simultaneously. At 1.45 V the channel between source and drain becomes conducting and the transistor turns-on. **b** Current measured when the bias voltages of the reservoir top gate TB and the central conductor CC are decreased individually until the conducting channel is pinched-off and no current flows at 1.5 V and 1.25 V respectively, while TT is biased above turn-on at 1.6 V.

heating of the device and cause a breakdown of superconductivity as was observed for high input powers. We also observe a shift in resonance frequency (Fig. 7.14c) which indicates an increase in the kinetic inductance of the resonator by the charge carriers.

7.3.3 Charge qubit

After establishing and analysing the basic functionalities of our resonator qubit device, we search for the charge qubit at $B_0 = 0\,\mathrm{T}$ while operating the resonator in the single photon regime.

The charge qubit frequency is given by Eq. (3.3)

$$f_\mathrm{c} = \sqrt{(V_t/h)^2 + [e(E_z - E_z^0)d/h]^2}.$$

Here the vertical electric field E_z is applied through the resonator central conductor CC with $E_z = \alpha_E V(\mathrm{CC})$, where $\alpha_E = \partial E_z/\partial V$ is the conversion factor between the bias voltage on the central conductor and the resulting electric field at the donor, specific to this device.

f_c is controlled by the tunnel coupling V_t between the donor and the interface dot state. Thus, when coupling the charge qubit to the resonator, we can operate in three different regimes, depending on V_t: the dispersive regime with $V_t/h \gg f_\mathrm{r}$ (Fig. 7.15a), the resonant regime with $V_t/h = f_\mathrm{r}$ (Fig. 7.15b), and $V_t/h \ll f_\mathrm{r}$ (Fig. 7.15c).

The coupling between the charge qubit and the resonator is given by Eq. (3.35)

$$g_\mathrm{E} = \frac{eE_\mathrm{ac}d}{4h}\frac{V_t}{\epsilon_\mathrm{o}}.$$

Assuming a dipole length of $d = 11\,\mathrm{nm}$ and an AC electric field of the resonator at the qubit of maximally $E_\mathrm{ac} = 30\,\mathrm{V/m}$, the coupling is expected to be at most $g_\mathrm{E} \simeq 79\,\mathrm{MHz}$. As V_t is determined by the ion implantation and thus uncertain by several orders of magnitude, we will most likely find $V_t/h \neq f_\mathrm{r}$. The coupling between the

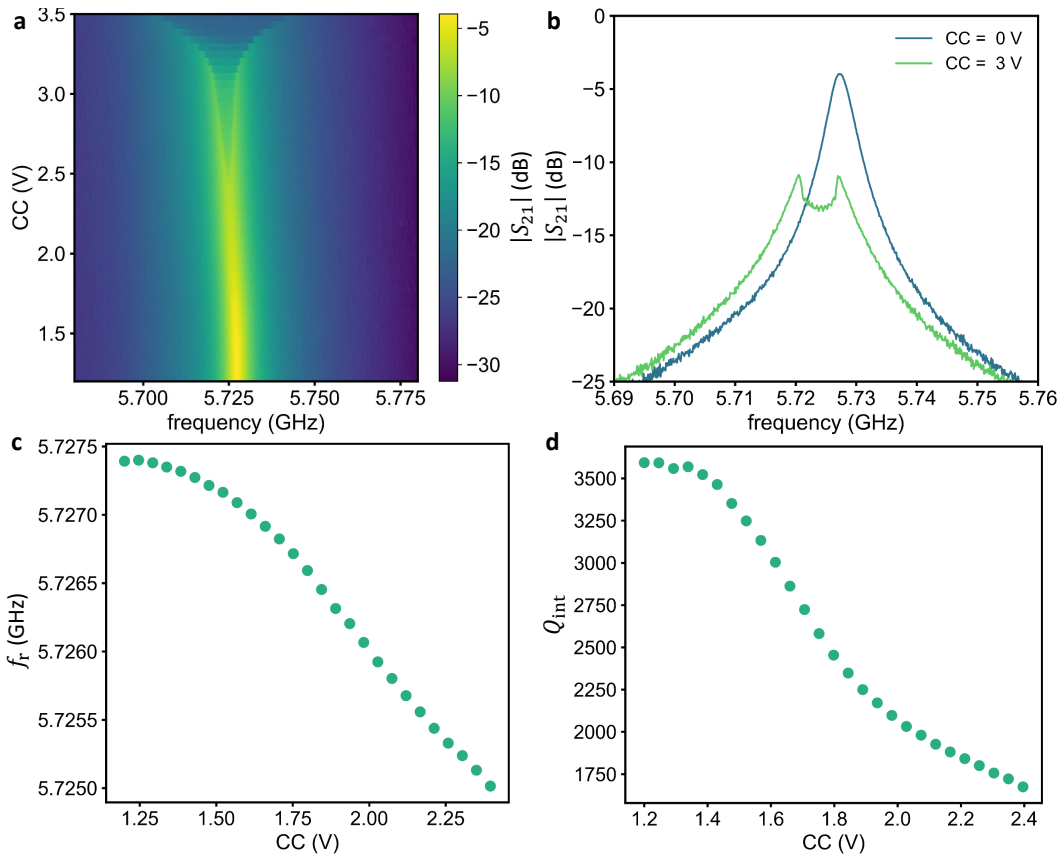

FIGURE 7.14: **Resonance dependence on 2DEG induction.** **a** Resonance amplitude $|S_{21}|$ with central conductor bias voltage CC while TT and TB are biased at 1.6 V. At 1.25 V a 2DEG is induced beneath the central conductor which changes the resonance. **b** Resonance amplitude traces at two different voltages, one with a strong 2DEG induced ($CC = 3\,\mathrm{V}$) and one without ($CC = 0\,\mathrm{V}$). **c** Resonance frequency f_r shift and internal quality-factor Q_{int} change (**d**) with applied bias voltage on the central conductor.

qubit and the resonator photon will cause a dispersive shift of g_E^2/Δ with $\Delta = f_r - f_c$ for $V_t/h \gg f_r$. When $V_t/h \ll f_r$, we will observe the anti-crossing between the charge qubit excited state $|e\rangle$ and the single photon resonator state $|1\rangle$.

To observe the resonator-charge qubit coupling, we are applying the following measurement procedure. First, we are loading any potential donors by biasing TT and TB above turn-on to induce a 2DEG and increasing CC to 1 V, below turn-on to avoid flooding the central conductor with charge carriers. Then we are turning-off TT and TB again so that the electrons remain trapped at the donors. Once the loading phase is completed, we measure the amplitude and phase response of the resonator at f_r in the single photon regime (excitation power of $P < -124\,\mathrm{dBm}$ at 12 mK) while sweeping CC. The bias will separate the electron from the donor and a charge qubit is formed. The qubit then couples to the resonator photon and induces a dispersive shift. Once a shift has been detected, we measure the amplitude and phase response of the resonator for frequencies and bias voltages in the vicinity (Fig. 7.16).

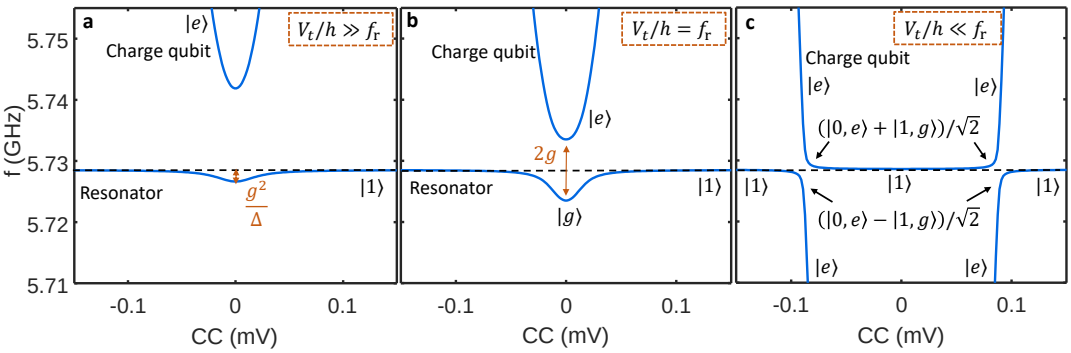

FIGURE 7.15: **Resonator-charge qubit interaction Jaynes-Cummings Hamiltonian calculations.** Eigenenergies E_{JC} of the Jaynes-Cummings Hamiltonian (Eq. 7.9) describing the resonator-charge qubit system for three different values of V_t, calculated with $g = 5\,\mathrm{MHz}$ and $f_{\mathrm{r}} = 5.7285\,\mathrm{GHz}$. **a** Dispersive regime with $V_t/h = 5.74\,\mathrm{GHz}$ ($\Delta = 12\,\mathrm{MHz}$), where the resonator resonance is shifted by the qubit. **b** Resonant regime where we can observe strong coupling. **c** For $V_t/h = 5.5\,\mathrm{GHz} < f_{\mathrm{r}}$, the qubit and the resonator anti-cross. The dominantly populated eigenstate is indicated in each sub-figure.

We fit the Jaynes-Cummings Hamiltonian of the charge-qubit resonator system

$$\begin{aligned}\mathcal{H} &= \mathcal{H}_{\mathrm{orb}} + \mathcal{H}_{\mathrm{r}} + \mathcal{H}_{\mathrm{int}} \\ &= \frac{V_t}{2}\sigma_x + \frac{e\alpha_E V(\mathrm{CC})d}{2}\sigma_z + f_{\mathrm{r}}h\left(\boldsymbol{a}^\dagger\boldsymbol{a} + \frac{1}{2}\right) + g_{\mathrm{E}}h\left(\sigma_+\boldsymbol{a} + \sigma_-\boldsymbol{a}^\dagger\right)\end{aligned} \tag{7.9}$$

to the measured amplitude and phase (dashed lines). The fit gives an estimation of $V_t/h = 5.695 \pm 0.005\,\mathrm{GHz}$, $E_z^0 = 0.1753 \pm 0.0001\,\mathrm{MV/m}$ (which corresponds to $38.975 \pm 0.002\,\mathrm{mV}$), $\alpha_E = 1.6 \pm 0.3\,\mathrm{MV/m/V}$ and $g_{\mathrm{E}} = 2 \pm 1\,\mathrm{MHz}$.

Electrical simulations with Synopsis® TCAD found $\alpha_E = 2 - 10\,\mathrm{MV/m/V}$ (Chap. 3, 8, Supp. Ref. [175]) and tight-binding simulations yield $V_t/h = 9.3\,\mathrm{GHz}$ and $E_z^0 = 4.085\mathrm{MV/m}$ for $d = 11\,\mathrm{nm}$ (Sec. 3.2.2). These simulations strongly depend on the donor depth and the corresponding dipole strength. However, due to the implantation uncertainty, we do not know these parameters for the resonator device. Consequently, we consider the simulated values as a guide only. Nevertheless, the simulations and the fit values agree well, supporting the conclusion that a donor charge qubit was measured. However, without characterizing the donor spin by, for instance, spin resonance or spin relaxation, the charge transition cannot with certainty be distinguished from a MOS interface defect.

Unfortunately, the device was very unstable and the ionization point voltage varied between each measurement by up to 1 mV. Thus, no further measurements were performed. The reason for the charge fluctuations can be many, for instance a high donor implantation density, trapped electrons under the resonator after turn-on or simply a low SiO_2 or Al_2O_3 quality.

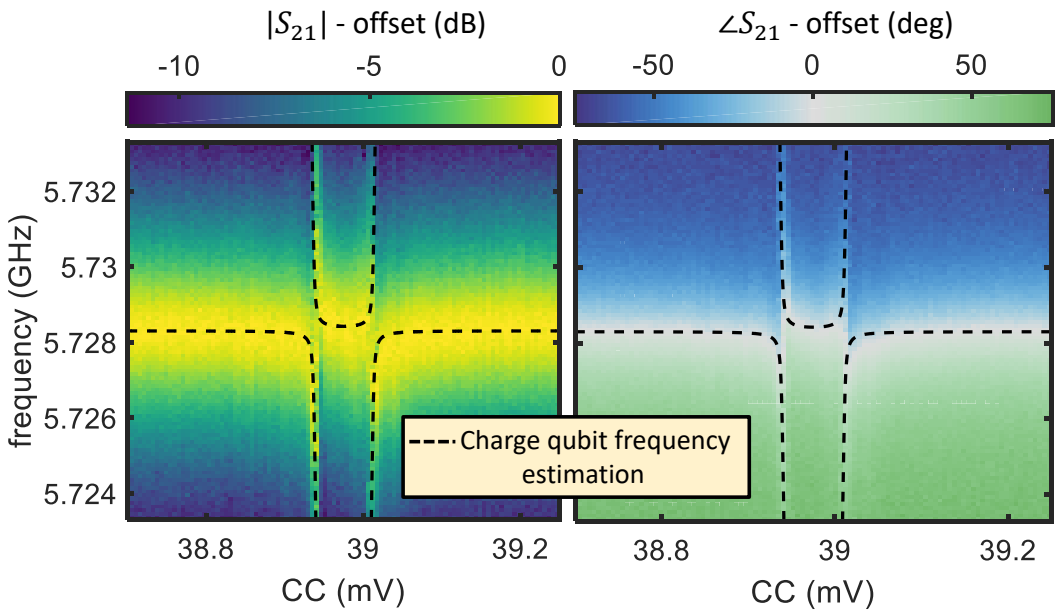

FIGURE 7.16: **Charge qubit coupling to the resonator.** Resonance amplitude $|S_{21}|$ (**a**) and phase $\angle S_{21}$ (**b**) when sweeping the central conductor bias voltage CC. The shift in both frequency and phase is consistent with the coupling of a charge qubit to the resonator photon. The dashed line indicates a fit of the resonator and charge qubit frequencies resulting from the Jaynes-Cummings Hamiltonian of the coupled qubit-resonator system (Eq. 7.9), giving $V_t/h = 5.695 \pm 0.005\,\mathrm{GHz}$, $E_z^0 = 0.1753 \pm 0.0001\,\mathrm{MV/m}$ (which corresponds to $38.975 \pm 0.002\,\mathrm{mV}$), $\alpha_E = 1.6 \pm 0.3\,\mathrm{MV/m}$ and $g_\mathrm{E} = 2 \pm 1\,\mathrm{MHz}$.

Chapter 8

Electron spin relaxation of single phosphorus donors in metal-oxide-semiconductor nanoscale devices

"In physics, you don't have to go around making trouble for yourself - nature does it for you."
–Frank Wilczek

Understanding our qubits fully is of utmost importance for large scale quantum computing. In this chapter we analyse the electron spin relaxation the donor electron qubit with external magnetic field and donor confinement depth. We observe interesting effects such as evanescent wave Johnson noise, strain and tunnelling that all influence the relaxation time. These results give precious insights into the microscopic phenomena that affect spin relaxation in MOS nanoscale devices, and provide strategies for engineering spin qubits with improved spin lifetimes.

The work presented in this chapter has been submitted for publication:
S. Tenberg, S. Asaad, M. Madzik, M.A.I. Johnson, B. Jöcker, A. Laucht, F.E. Hudson, D.N. Jamieson, J.C. McCallum, A.S. Dzurak, R. Joynt, A. Morello. "Electron spin relaxation of single phosphorus donors in metal-oxide-semiconductor nanoscale devices." arXiv:1812.06644 (2018).

The author acknowledges S. Asaad for performing the measurements in Fig. 8.8 in conjunction with the author and for general assistance with measurements, M. Madzik for providing the T_1 measurement of device 2018A in Fig. 8.3, B. Jöcker for the electrical simulations in Fig. 8.6 and R. Joynt for the EWJN theory.

8.1 Introduction

Electrons bound to shallow donors in silicon became a centerpoint of solid-state physics in the 1950s, when the study of their spin and orbital states was used as a benchmark for the then emerging theories of band structure, effective mass and impurity states in solids [36]. In particular, the detailed analysis of the donor electron spin-lattice relaxation time T_1 provided key insights into the multi-valley band structure of silicon, and the way it influences spin-phonon coupling [179].

Fast-forward half a century, donor spins have become the subject of intense research for their potential use in quantum computing [22], [72], [78], [114]. In this context, the old results on the electron spin T_1 seemed to provide ample reassurance that spin lifetime would not constitute a limitation to the encoding and protection of quantum information. The donor electron T_1 in bulk samples exceeds an hour at cryogenic temperatures and moderate magnetic fields [84], whereas the spin decoherence time T_2 is limited to a few hundred microseconds [40], [180], due to the coupling of the electron spin to the bath of spin-1/2 ^{29}Si nuclei present with 4.7% abundance in natural silicon. However, the adoption of isotopically enriched ^{28}Si samples, where the conentration of ^{29}Si nuclei is reduced below 0.1% [65], has allowed extending T_2 close to [30] or beyond [181] one second. This comes within an order of magnitude of the T_1 time observed in nanoscale single-donor qubit devices [24] at the magnetic fields $\gtrsim$ 1 T typically used for control and readout of the electron spin [40], and calls for an effort to understand in detail all spurious channels of spin relaxation.

In this chapter, we provide an extensive collection of experimental results and theoretical models on the electron spin relaxation time T_1 of single ^{31}P donors in silicon metal-oxide-semiconductor (MOS) nanoelectronics devices, with the aim of elucidating how the environment of the donors influences the spin lifetime. Earlier measurements of T_1 on single donors in nanoscale devices [24], [33], [182], [183] had already shown evidence of deviation from bulk-like behavior. Here, by analyzing data on 7 different devices, we uncover several microscopic mechanisms that affect the spin relaxation time. In particular, we provide evidence for relaxation induced by evanescent-wave Johnson noise (EWJN), by electron tunneling to a nearby reservoir, and modifications of the spin-phonon relaxation rate caused by strain.

8.2 Background on electron spin relaxation in donors

We describe a single ^{31}P donor in silicon, subjected to an external magnetic field $B_0 \parallel \hat{z}$, with the following spin Hamiltonian:

$$\mathcal{H}_{\mathrm{P}} = g_z \mu_{\mathrm{B}} B_0 S_z - h\gamma_n B_0 I_z + hA\mathbf{S}\cdot\mathbf{I}, \tag{8.1}$$

where h is the Planck constant, g_z is the component the electron Landè g-tensor along the field direction, μ_{B} is the Bohr magneton, $\gamma_n = 17.25$ MHz/T is the nuclear gyromagnetic ratio, A is the electron-nuclear hyperfine coupling, $\mathbf{S}$ and $\mathbf{I}$ are spin-1/2 vector Pauli matrices describing the electron and the ^{31}P nuclear spins, respectively, and S_z, I_z are the operators representing the electron and nuclear spin projections along the $\hat{z}$-axis. For ^{31}P donors in bulk silicon, the parameters in Eq. 8.1 take the values $g_z = 1.9985$ (corresponding to $g_z\mu_{\mathrm{B}}/h = 27.971$ GHz) and $A = 117.53$ MHz, but the distortion of the wavefunction caused by electric fields, strain or local confinement can result in small shifts of such values [175].

In this chapter we focus on the physics of the electron spin alone. Earlier experiments on the ^{31}P nucleus [41] have shown that it retains its state for extremely long times (typically many days, or even months). Moreover, we work in the regime where the electron Zeeman energy $g\mu_B B_0$ greatly exceeds the hyperfine coupling A, and the electron-nuclear eigenstates are simply the tensor products of the electron ($|\downarrow\rangle, |\uparrow\rangle$) and nuclear ($|\Downarrow\rangle, |\Uparrow\rangle$) basis states. Therefore, choosing for example the nuclear $|\Uparrow\rangle$ state, the donor Hamiltonian can be truncated to an electron-only operator:

$$\mathcal{H} = g_z \mu_B B_0 S_z - hA/2. \tag{8.2}$$

The constant energy offset $-hA/2$ is inconsequential for the discussion of electron spin relaxation, and will be ignored from here onward.

Electron spin relaxation consists of transitions between the $|\uparrow\rangle$ and $|\downarrow\rangle$ basis states leading to thermal equilibrium with a bath at temperature T, and is mathematically described by the presence of off-diagonal matrix elements in the Hamiltonian, coupling the spin to some operators of the bath. In a simplified picture, we can describe the bath as a noise source that introduces a perturbation to the Hamiltonian described by:

$$\mathcal{H}'[\lambda(t)] = \boldsymbol{\Delta}_\perp[\lambda(t)]\boldsymbol{S}. \tag{8.3}$$

Here $\boldsymbol{\Delta}_\perp[\lambda(t)]$ is an operator that does not commute with $\mathcal{H}$, and depends on the parameter $\lambda(t)$ which describes the noise acting on the electron spin. The electron relaxation rate is the sum of the decay ($W_{\uparrow\downarrow}$) and excitation ($W_{\downarrow\uparrow}$) rates:

$$T_1^{-1}(\lambda) = W_{\uparrow\downarrow} + W_{\downarrow\uparrow}. \tag{8.4}$$

Thermal equilibrium is obtained by imposing that decay and excitation rates obey the detailed balance condition:

$$\frac{W_{\downarrow\uparrow}}{W_{\uparrow\downarrow}} = \exp\left(-\frac{g_z \mu_B B_0}{k_B T}\right). \tag{8.5}$$

In the experiments presented here, conducted at $B_0 > 0.5$ T and $T \approx 200$ mK, $g_z \mu_B B_0 \gg k_B T$ and we can approximate $T_1^{-1}(\lambda) \approx W_{\uparrow\downarrow}$, with:

$$W_{\uparrow\downarrow} = \frac{2\pi}{\hbar} \left|\langle\downarrow| \mathcal{H}'[\lambda(t)] |\uparrow\rangle\right|^2 \rho_f. \tag{8.6}$$

This expression is an application of Fermi's golden rule, where ρ_f is the density of available final states for emission of energy from the spin into the bath. Introducing the transition operator of the noise perturbation

$$\boldsymbol{D}_{\perp,\lambda} = \frac{\partial \mathcal{H}'[\lambda(t)]}{\partial \lambda} \tag{8.7}$$

and the noise power spectral density

$$S_\lambda(\omega) = \int_{-\infty}^{+\infty} d\tau \langle \lambda(0)\lambda(\tau)\rangle \exp(-i\omega\tau), \tag{8.8}$$

we can express the total relaxation rate as [184], [185]

$$T_1^{-1} = \sum_\lambda \frac{|\langle\uparrow| \boldsymbol{D}_{\lambda,\perp} |\downarrow\rangle|^2}{\hbar^2} S_\lambda(\omega_0). \tag{8.9}$$

8.2.1 Phonon-induced relaxation

In bulk silicon, the dominant mechanism that creates a transverse operator $\mathbf{\Delta}_\perp[\lambda(t)]$ acting on the donor electron spin is the modification of the g-tensor caused by elastic distortions of the crystal lattice (phonons).

The band structure of silicon contains six degenerate conduction band minima along directions $\pm x, \pm y, \pm z$ (labeled below by the index $j = 1, 2, \ldots, 6$) at finite crystal momentum k_0, called valleys. A bound electron state in silicon must be constructed from linear combinations of the 6 valleys, whose index effectively constitutes an additional quantum number, in addition to the usual hydrogen-like principal, orbital and magnetic quantum numbers. The spherical symmetry of the Coulomb potential produced by the donor nucleus is broken by the cubic crystal field potential, creating a valley-orbit coupling. As a result, the ground 1s orbital state is further split into six valley-orbit states: a singlet with A_1 symmetry (ground state), a triplet with T_2 symmetry and a doublet with E symmetry, with wave functions $\Psi_i = \sum_{j=1}^{6} \alpha_i^{(j)} \psi^{(j)}$ (Eq. 2.9), where $\psi^{(j)}$ are envelope-modulated Bloch functions of the 1s orbital and [36], [37]

$$\alpha_{A_1}^{(j)} = \frac{1}{\sqrt{6}}(1,1,1,1,1,1), \tag{8.10a}$$

$$\alpha_{T_2^x}^{(j)} = \frac{1}{\sqrt{2}}(1,-1,0,0,0,0), \tag{8.10b}$$

$$\alpha_{T_2^y}^{(j)} = \frac{1}{\sqrt{2}}(0,0,1,-1,0,0), \tag{8.10c}$$

$$\alpha_{T_2^z}^{(j)} = \frac{1}{\sqrt{2}}(0,0,0,0,1,-1), \tag{8.10d}$$

$$\alpha_{E^{xy}}^{(j)} = \frac{1}{2}(1,1,-1,-1,0,0), \tag{8.10e}$$

$$\alpha_{E^z}^{(j)} = \frac{1}{2}(1,1,0,0,-1,-1). \tag{8.10f}$$

When a phonon with wave vector $\mathbf{q}$ travels through the crystal, it creates a local strain $\vec{U}$ that inhomogeneously deforms the lattice by the displacement

$$\mathbf{Q}(\mathbf{r}) = \sum_{q,t} \left[\mathbf{e}_t(\mathbf{q}) a_{\mathbf{q},t} e^{i\mathbf{q}\cdot\mathbf{r}} + \mathbf{e}_t^*(\mathbf{q}) a_{\mathbf{q},t}^* e^{-i\mathbf{q}\cdot\mathbf{r}} \right], \tag{8.11}$$

where $\mathbf{e}(\mathbf{q}) = \mathbf{e}^*(-\mathbf{q})$ is the polarization vector, $a_{\mathbf{q},t}$ the displacement amplitude and $t = x, y, z$. The deformation alters the crystal symmetry such that the jth valley is shifted by an energy

$$\epsilon^{(j)} = \sum_{t,t'} U_{t,t'} \left(\Xi_d \delta_{t,t'} + \Xi_u G_t^{(j)} G_{t'}^{(j)} \right), \tag{8.12}$$

where $U_{t,t'}$ is the component of the strain tensor $\vec{U}$, $\mathbf{G}^{(j)}$ is the unit vector pointing from the origin to the bottom of the jth valley in the first Brillouin zone, and Ξ_d and Ξ_u are the Herring deformation-potential which describe the shift in the band edge energy caused by isotropic dilations and uniaxial strain, respectively [186], [187]. If unperturbed, the ground state A_1 (Eq. 8.10) has an equal population of all valleys. As a consequence of the energy shifts $\epsilon^{(j)}$ caused by the lattice phonon, the relative valley populations become unequal, causing the mixing of some excited states with

the ground state. This effect is called "valley-repopulation" and causes a change in the electron g-factor.

The g-factor of each valley depends on the spin-orbit interaction, which differs whether the electron moves in or out of plane with respect to the external magnetic field, resulting in an anisotropic value given by [179]:

$$g^2 = g_{||}^2 \cos^2\theta + g_{\perp}^2 \sin^2\theta, \tag{8.13}$$

where θ is the angle between B_0 and the valley axis and $g_{||}$ and $g_{\perp}$ are the g values with B_0 pointing parallel and perpendicular to the valley axes, respectively. In the unperturbed case, once averaged over all valley states according to their population, the g-factor actually becomes isotropic for the A_1 ground state due to the even valley population:

$$g_0 = \frac{1}{3} g_{||} + \frac{2}{3} g_{\perp}. \tag{8.14}$$

However, in the strained case, the valley population is unequal which leads to an anisotropic g which depends on the amount of strain. For instance, for stress along the [100] direction, the g-factor becomes [179]:

$$g - g_0 = \frac{1}{6}\left(g_{||} - g_{\perp}\right)\left(1 - \frac{3}{2}\sin^2\theta\right) \times \left[1 - (1 + 3x/2)\sqrt{1 + x/3 + x^2/4}\right], \tag{8.15}$$

with $x = \Xi_u'/E_{12}$, where Ξ_u' is the deformation potential adjusted for stress and E_{12} is the valley-orbit splitting between the ground state A_1 and the doublet state E. This g-factor anisotropy effectively couples the electron spin $\mathbf{S}$ to the lattice phonon $\mathbf{q}$ via the Hamiltonian [187]:

$$\mathcal{H}'_{\text{ph}} = \frac{2g'\mu_B B_0 \Xi_u}{-3E_{12}} f(q) q \left(a_{\mathbf{q},t} \sum_r D_r^{(t)} D_r^{(t')} + c.c.\right) S_{t'} \tag{8.16}$$

where $g' = \frac{1}{3}(g_{||} - g_{\perp})$, $f(q) = 1/\left[1 + \frac{1}{4}a_0^{*2}q^2\right]^2$, a_0^* is the effective Bohr radius, and

$$D_r = 3\sum_j \alpha^{(j)} \alpha_r^{(j)} \mathbf{U}^{(j)} \tag{8.17}$$

is a tensor that describes the geometrical structure of the conduction band edge, with r labeling the valley-orbit excited states and $\mathbf{U}^{(j)}$ the tensor that selects the direction of the j-th valley.

The spin-phonon interaction described by Eq. (8.16) represents one example of off-diagonal perturbation $\mathcal{H}'$ as in the general formalism of Eq. (8.6). From this, Hasegawa [187] calculated the donor spin-lattice relaxation rate as:

$$\begin{aligned} T_{1,\text{rp}}^{-1} &= \frac{1}{90\pi}\left(\frac{g_{||} - g_{\perp}}{g_0}\right)\left(\frac{\Xi_u}{E_{12}}\right)^2 \left(\frac{1}{\rho v_t^5} + \frac{2}{3\rho v_l^5}\right) \\ &\times \left(\frac{g\mu_B B_0}{\hbar}\right)^4 f_{\text{rp}}(\theta) \cdot k_B T \\ &= K_4^{\text{rp}} B_0^4 T, \end{aligned} \tag{8.18}$$

where $v_t = 5860$ m/s and $v_l = 8480$ m/s are the transverse and longitudinal sound

velocities in silicon, respectively, $\rho = 2330\ \mathrm{kg/m^3}$ is the density of silicon and $f_{\mathrm{rp}}(\theta) = \sin^2\theta(1+3\cos^2\theta)$ is a geometric factor where θ is the angle between B_0 and the [100] crystal axis [179], [187].

Even if the electron wave function were entirely confined in one valley, strain can cause a change in g-factor by shifting the nearby energy bands that determine g [179], [188]. This "one-valley" mechanism yields a spin-lattice relaxation rate of the form:

$$\begin{aligned} T_{1,\mathrm{ov}}^{-1} &= \frac{1}{20\pi}\left(\frac{M}{g_0}\right)^2\left(\frac{\Xi_u}{E_{12}}\right)^2\left(\frac{1}{\rho\bar{v}_t^5}+\frac{2}{3\rho\bar{v}_l^5}\right) \\ &\times\left(\frac{g\mu_{\mathrm{B}}B_0}{\hbar}\right)^4 f_{\mathrm{ov}}(\theta)\cdot k_{\mathrm{B}}T \\ &= K_4^{\mathrm{ov}}B^4T, \end{aligned} \tag{8.19}$$

where $M = 0.44$ is the matrix element of the one-valley g-factor shift and $f_{\mathrm{ov}}(\theta) = \cos^4\theta(1+1/2\sin^4\theta)$ [188]. Since the magnetic field in our experiment is aligned along the [110] direction, $\theta = 45°$, both the "valley repopulation" and the "one-valley" mechanisms provide a channel for spin relaxation.

The spin relaxation rates in Eq. (8.18) and (8.19) were derived in the high-temperature limit, $k_{\mathrm{B}}T \gg g\mu_{\mathrm{B}}B_0$, where both spontaneous and stimulated phonon emission take place. These are described by including a factor $(1+n_{\mathrm{ph}})$ in the rate calculation, where $n_{\mathrm{ph}} = 1/[\exp(g\mu_{\mathrm{B}}B_0/k_{\mathrm{B}}T)-1]$ is the Bose occupation factor for phonons of energy matching the electron Zeeman energy. The factor $k_{\mathrm{B}}T$ in Eqs. (8.18), (8.19) appears because $(1+n_{\mathrm{ph}}) \approx k_{\mathrm{B}}T/g\mu_{\mathrm{B}}B_0$ in the high-T limit.

The low-temperature limit of the spin relaxation rates, of relevance to experiments we present here, is obtained by replacing $k_{\mathrm{B}}T/g\mu_{\mathrm{B}}B_0$ with 1 in Eqs. (8.18), (8.19), which results in the well-known $T_1^{-1} \propto B^5$ dependence [17], [24]:

$$T_1^{-1}|_{\mathrm{low-T}} = K_4\frac{g\mu_B}{k_B}B_0^5 = K_5B_0^5. \tag{8.20}$$

8.2.2 Evanescent-wave Johnson noise

Another mechanism inducing electron spin relaxation is magnetic noise leaking from the aluminum gates in the vicinity of the electron. Quantum and thermal fluctuations of the electrical currents in the metal create electromagnetic fluctuations known as Johnson noise [170], [171], [189]. The Johnson noise leaks out of the metal into the insulator in form of evanescent waves when the photon modes in the metal are totally reflected at the metal-insulator interface (Fig. 8.4a) [190]. This effect is called evanescent-wave Johnson noise [100], [101], [191] and is particularly strong near a metal interface. EWJN can cause spin relaxation at low temperatures because the evanescent waves constitute an electromagnetic reservoir that can absorb energy (Eq. 8.6).

In the nanoscale MOS devices studied here, the main sources of EWJN are the metallic control gates (see Fig. 8.1a). At $\boldsymbol{r}$, the position of the donor, this noise is characterized by the power spectrum

$$\begin{aligned} S_{ii}(\omega) &= \int_{-\infty}^{\infty} e^{i\omega t}\left\langle B_i(\mathbf{r},t)\,B_i(\mathbf{r},0)\right\rangle\,dt \\ &= \left\langle B_i(\mathbf{r})\,B_i(\boldsymbol{r})\right\rangle_\omega. \end{aligned} \tag{8.21}$$

Here $i = x, y, z$ is a Cartesian index and B the magnetic component of the EWJN field. The angle brackets denote a thermal average over the quantum states of the system. The power spectrum determines T_1 according to the formula

$$\frac{1}{T_1} = \left(\frac{\mu_B}{\hbar}\right)^2 \left[S_{xx}(\omega_0) + S_{yy}(\omega_0)\right], \tag{8.22}$$

for $\mathbf{B}_0$ in the z direction.

As will be shown below, the conditions of our experiment are such that firstly we can approximate the electromagnetic fields as quasi-static, since the vacuum photon wavelength is on the order of cm and exceeds the device dimensions. Secondly, we anticipate a local relation between the electric field and the electric displacement since the devices satisfy the inequalities $\ell \ll a \ll \delta$, where a is any linear dimension of the metal pieces,

$$\ell = v_{\mathrm{F}} \frac{m_e}{ne^2} \sigma \tag{8.23}$$

is the mean free path with v_{F} as the electron Fermi velocity, m_e the electron mass, n the electron density, and

$$\delta = \sqrt{2/\mu_0 \mu_R \sigma \omega_0} \tag{8.24}$$

is the skin depth with μ_0 as the magnetic permeability constant and μ_R as the relative permeability. $\mu_R = 1$ for our device.

For this situation, it has been shown that [191]

$$\frac{1}{T_1} = \frac{1}{\mathcal{L}} \frac{\mu_B^2 \mu_0^2 \sigma \omega_0}{4\pi\hbar}, \tag{8.25}$$

where $\mathcal{L}$ is a length that depends only on the geometry of the metallic elements of the device and the position of the qubit. Its calculation can be rather involved and we will give estimates for our device in Sec. 8.4.1.

8.2.3 Charge noise

Charge noise does not directly couple to the spin of the qubit. However, when combined with spin-orbit coupling, it creates a fluctuating effective magnetic field that will contribute to T_1 [192]. According to Ref. [192], if the frequency dependence of the charge noise power spectrum is proportional to $1/f^a$, then the field dependence of $1/T_1$ is B_0^{2-a}. For $1/f$ noise ($a = 1$) this would give $1/T_1 \sim B_0$. While a $1/f$ charge noise spectrum has been observed between 10^{-2} and 3×10^5 Hz in Si-based devices [61], it is exceedingly unlikely that it would hold up to the $> 10^{10}$ Hz frequency range that is relevant for $1/T_1$. Indeed, a recent re-analysis of the data in Ref. [61] suggests that the noise spectrum changes from $1/f$ to $1/f^2$ for $f > 2 \times 10^5$ Hz [193].

In the MOS donors-based devices discussed in this work, the noise spectrum became white for $f \geq 10$ kHz [30]. This would give $1/T_1 \sim B_0^2$ if extended up to the electron Larmor frequency.

8.3 The qubit system and measurement methods

8.3.1 Qubit setup

Our qubit system consists of a single electron spin confined by a phosphorus ^{31}P donor, implanted in either natural silicon ^{nat}Si or isotopically-enriched ^{28}Si with 800 ppm residual ^{29}Si nuclei (Fig. 8.1a) [65]. With the ion implantation parameters

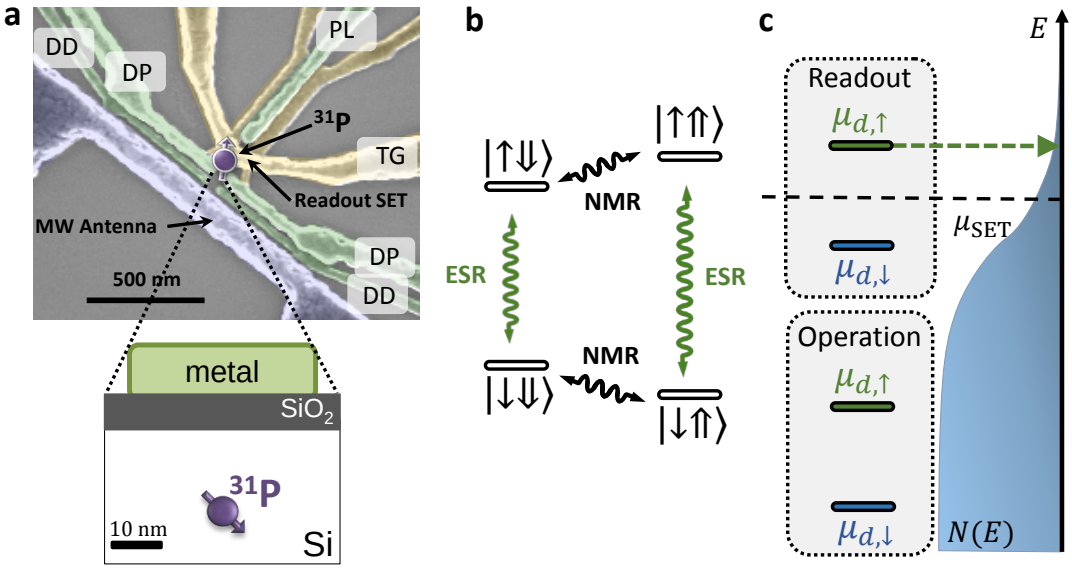

FIGURE 8.1: **Phosphorus donor qubit system.** **a** Schematic of a phosphorus donor implanted in silicon with a false-colored scanning electron micrograph of a device similar to the ones measured. Two independent gates control the donor potential (DD and DP, green) while a single-electron transistor (SET, yellow) determines the donor charge state, which is correlated to the electron spin state via a spin-dependent tunneling process. A plunger gate (PL, green) controls the electrochemical potential of the SET (and of a donor, if one is present in its vicinity). A broadband microwave antenna (purple) provides a magnetic drive for both the electron and the nuclear spins. **b** Energy level diagram of the electron-nuclear spin system, with electron spin resonance (ESR) and nuclear magnetic resonance (NMR) transitions indicated. **c** Schematic of the (electron-spin dependent) donor electrochemical potentials $\mu_{d,\uparrow}, \mu_{d,\downarrow}$ during readout and operation. The nuclear state is irrelevant in the readout process. For readout, the donor is tuned such that $\mu_{d,\uparrow} - E_Z/2 = \mu_{SET} = \mu_{d,\downarrow} + E_Z/2$ and $|\uparrow\rangle$ can tunnel out, leaving the donor ionized. The resulting positive donor charge shifts the SET tuning to a high-conductance point. In contrast, $|\downarrow\rangle$ stays confined, keeping the SET in Coulomb blockade. For operation, both spin states are well confined below the SET electrochemical potential with $\mu_{d,\downarrow}, \mu_{d,\uparrow} \ll \mu_{SET}$, so the electron cannot escape. This is the bias point for the device during the wait time for spin relaxation measurements. $N(E)$ is the density of states in the SET island.

used for the devices described in the present work, each device contains typically $10 - 20$ donors in a 100×100 nm^2 window[1].

Aluminum gates, defined by electron beam lithography, control the electrostatic environment and allow selecting a specific donor for the measurements. Here, spin readout is obtained via spin-dependent tunneling into the island of a single-electron transistor (SET) [24] kept at a low electron temperature ($T \approx 100$ mK). It is always possible to tune the gate voltages in such a way that one and only one donor has its electrochemical potential aligned with that of the SET island, while all other donors are either already ionized, or are kept far below the Fermi level (Fig. 8.1c).

A DC-only (DD) and a pulsed (DP) gate above the donor control the donor potential. Additionally a plunger gate (PL) is used to manipulate the donor potential and the SET electrochemical potential μ_{SET}. In all devices from 2013 onward, a broadband microwave antenna [176] is used for microwave and radio frequency pulses,

[1]For details on the fabrication techniques see Sec. 6.2.2, as the electron qubit devices measured here follow a very similar fabrication as the dipole-dipole coupled flip-flop devices.

allowing for full control over the electron [40] and nuclear [41] spins (Fig. 8.1b, Sec. 6.4.1).

8.3.2 Measurement procedures

Donor control via a virtual gate. The spin readout process depends on the relative alignment of the (spin-dependent) donor electrochemical potentials $\mu_{d,\uparrow}, \mu_{d,\downarrow}$ with respect to the SET electrochemical potential μ_{SET} [24], [43]. To simplify the analysis we define a virtual pulsed gate voltage V_{DV} by combining the effects of the voltage pulses on the SET plunger, V_{PL}^{ac}, and on the donor pulsed gates, V_{DP}^{ac}:

$$V_{DV} = \sqrt{(\beta V_{PL}^{ac})^2 + \left(V_{DP}^{ac}\right)^2}. \tag{8.26}$$

These pulsed voltages are applied in addition to the DC voltages V_{PL} and V_{DP} chosen to select a specific donor to be near the readout condition.

The factor β determines the way in which we choose to shift μ_d and μ_{SET}. We typically choose "compensated pulses", i.e. keep μ_{SET} fixed while moving μ_d by using V_{PL} to compensate for the effect of V_{DP} on μ_{SET}. We thus call β_c the slope of the Coulomb peaks in the charge stability diagram of the donor and plunger gates (Fig. 8.2a), determined by the ratio of capacitive couplings of gates PL and DP to the SET island:

$$\begin{aligned} \beta_c &= \Delta V_{PL}/\Delta V_{DP} \\ &= C_{SET-PL}/C_{SET-DP}. \end{aligned} \tag{8.27}$$

Any other value of β corresponds to an uncompensated operation (β_{uc}), i.e. one where μ_{SET} varies during the pulsing.

We also define the donor plunge voltage V_p^c (V_p^{uc}) as the effective voltage that determines how far below μ_{SET} the donor electrochemical potential μ_d is plunged when operating compensated (uncompensated):

$$V_p^{c/uc} = V_{DV}(\beta_{c/uc}) \sin\theta, \tag{8.28}$$

where $\theta = \angle[V_{DV}(\beta_{c/uc}), \mu_{SET}]$. Note that, for V_p^{uc}, the shift of μ_{SET} caused by the uncompensated pulsing can result in a change in the electron number in the SET island.

Electron spin read out. The current through the SET, I_{SET}, is used to determine the charge state of the donor which, in turn, correlates to the electron spin state in the presence of spin-dependent tunneling [19], [24], [43], [194] (see Sec. 2.3.3 for general concepts). The SET is biased in Coulomb blockade ($I_{SET} \approx 0$) when the donor is in the neutral charge state. For spin readout, the donor and SET electrochemical potentials are tuned such that $\mu_{d,\uparrow} - E_Z/2 = \mu_{SET} = \mu_{d,\downarrow} + E_Z/2$. This ensures that the electron can only leave the donor and tunnel onto the SET if in state $|\uparrow\rangle$, leaving behind a positively charged donor which shifts the SET bias point and brings it to a high-conductance state ($I_{SET} \approx 1$ nA). Coulomb blockade is restored when a $|\downarrow\rangle$ electron tunnels back onto the donor. Thus we observe a current spike whenever the electron was in state $|\uparrow\rangle$, while the current stays low if in state $|\downarrow\rangle$ (Fig. 8.1c). This donor tuning is called"read level" and, in our definition, corresponds to $V_p = V_{DV} = 0$ V (Fig. 8.2a).

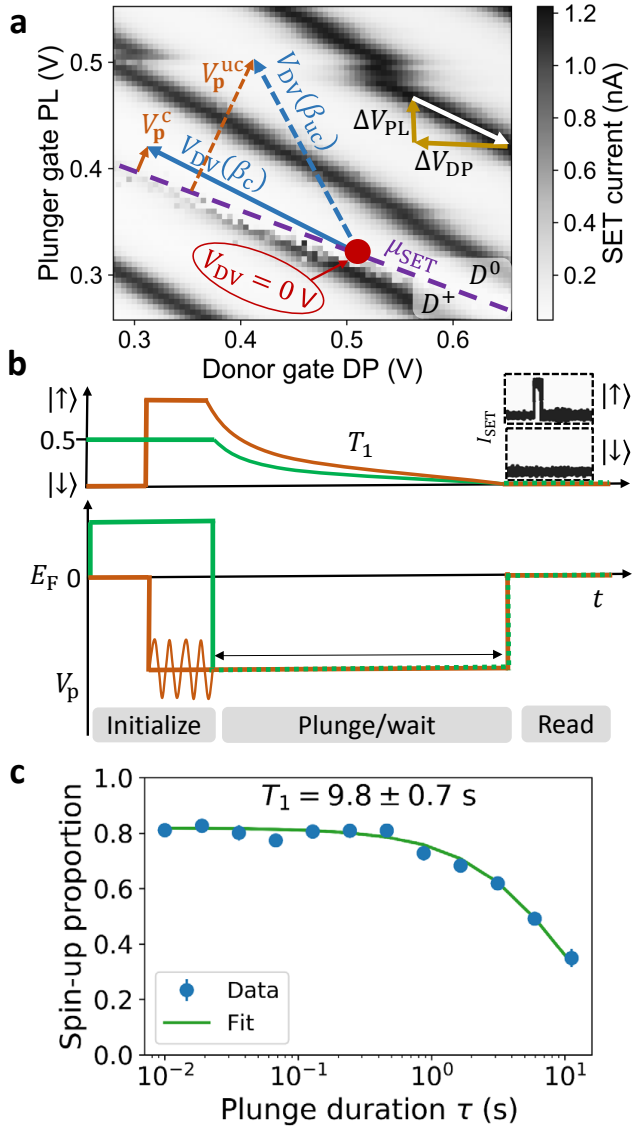

FIGURE 8.2: **Relaxation rate measurement. a** Charge stability diagram of plunger gate (PL) and donor gate (DP). We observe the donor transition from ionized (D^+) to neutral (D^0) when $\mu_d = \mu_{SET}$, indicated by the dashed purple line. The virtual gate voltage $V_{DV}(\beta_c = -0.51)$ is indicated (blue arrow), determined by ΔV_{PL} and ΔV_{DP} (Eq. 8.27). $V_p^{c/uc}$ is the effective plunge voltage. **b** Schematic of the T_1 pulse sequence and corresponding spin-up proportion. For fields $B_0 \leq 1.5$ T (orange line), $|\downarrow\rangle$ is initialized and then inverted with an adiabatic ESR pulse while for $B_0 > 1.5$ T (green line) an electron with a random spin state is loaded. Then the donor is plunged for time τ until the spin state is determined by spin-dependent tunnelling with the SET. **c** Example of a T_1 measurement at $B_0 = 1$ T. The relaxation time $T_1 = 9.8 \pm 0.7$ s is extracted using a least-square exponential fit (Eq. 8.29), with $C_{offset} = 0.10$ determined in a separate experiment.

Electron spin initialization For $B_0 \leq 1.5$ T we prepare a $|\uparrow\rangle$ state in two steps. First we use the read level, $V_p = 0$ V, to initialize $|\downarrow\rangle$. After a waiting time suitably longer than the electron tunnel-out time, a $|\uparrow\rangle$ will have escaped the donor and be replaced by a $|\downarrow\rangle$, while $|\downarrow\rangle$ will remain in place. Second, we invert the spin from $|\downarrow\rangle$ to $|\uparrow\rangle$ using an oscillating magnetic field B_1 whose frequency is adiabatically swept through the resonance [195].

For $B_0 > 1.5$ T the above method would require ESR frequencies higher than those available with our microwave source. We thus resort to a random electron initialization, obtained by loading the electron when $\mu_{d,\downarrow}, \mu_{d,\uparrow} \ll \mu_{SET}$. In this case both the $|\uparrow\rangle$ and $|\downarrow\rangle$ states are accessible and electron spin is prepared with roughly equal probability of the two.

Spin relaxation measurement. The electron spin relaxation time T_1 is obtained by measuring the probability of finding the spin in the $|\uparrow\rangle$ state after a wait time τ has elapsed. To this end, we apply the pulse sequence illustrated in Fig. 8.2b to the virtual gate DV.

For $B_0 \leq 1.5$ T we prepare a $|\uparrow\rangle$ state while for $B_0 > 1.5$ T a random electron is initialized with roughly equal probability of $|\uparrow\rangle$ and $|\downarrow\rangle$ (see paragraph *Electron spin initialization*).

Next, we plunge the donor electrochemical potential far below μ_{SET} with a voltage pulse of amplitude V_p and duration τ. This ensures that the previously initialized electron spin cannot escape the donor (see, however, Sect. 8.5). Finally, a single shot-spin readout is performed at $V_p = 0$ V.

We repeat this sequence 30 times to determine the spin-up fraction $P_\uparrow$ after each wait time τ. The measurement of $P_\uparrow(\tau)$ is repeated multiple times to check for consistency, which can be occasionally disrupted by drifts and jumps in the electrostatic environment.

T_1 is extracted by performing a least-square fit to $P_\uparrow(\tau)$ with the exponential decay:

$$P_\uparrow(\tau) = C_{init} e^{-\tau/T_1} + C_{offset}, \tag{8.29}$$

where C_{init} is the initial spin-up proportion and C_{offset} the offset at $\tau \to \infty$ created by erroneous spin-up counts, caused e.g. by tunnel-out events of $|\downarrow\rangle$ spins into states made available in the electron reservoir by thermal excitations, or by noise spikes counted as $|\uparrow\rangle$ spins. C_{init} and T_1 are free fitting parameters, whereas C_{offset} is determined separately by measuring the spin-up proportion after $|\downarrow\rangle$ has been initialized, and is fixed at that value in the fit.

As an example, Fig. 8.2c shows set of $P_\uparrow(\tau)$ that, fitted to Eq. (8.29), yielded the longest measured relaxation time at $B_0 = 1$T, $T_1 = 9.8 \pm 0.7$ s.

8.4 Relaxation time dependence on external magnetic field

The dependence of the electron relaxation rate T_1^{-1} on the strength of the external magnetic field B_0 gives insight into the mechanisms that lead to the relaxation itself. Fig. 8.3 (a) shows sets of relaxation rates as a function of B_0 for seven different donor qubit devices, fabricated and measured in our laboratory between 2010 and 2018. Devices 2010A, 2010B (described in Ref. [24]) and 2011A were fabricated on ^{nat}Si. Devices 2013A, 2013B, 2017A (described in Ref. [30]), 2018A were fabricated on enriched ^{28}Si. We fit the relaxation rate of devices 2010A, 2010B, 2017A and 2018A

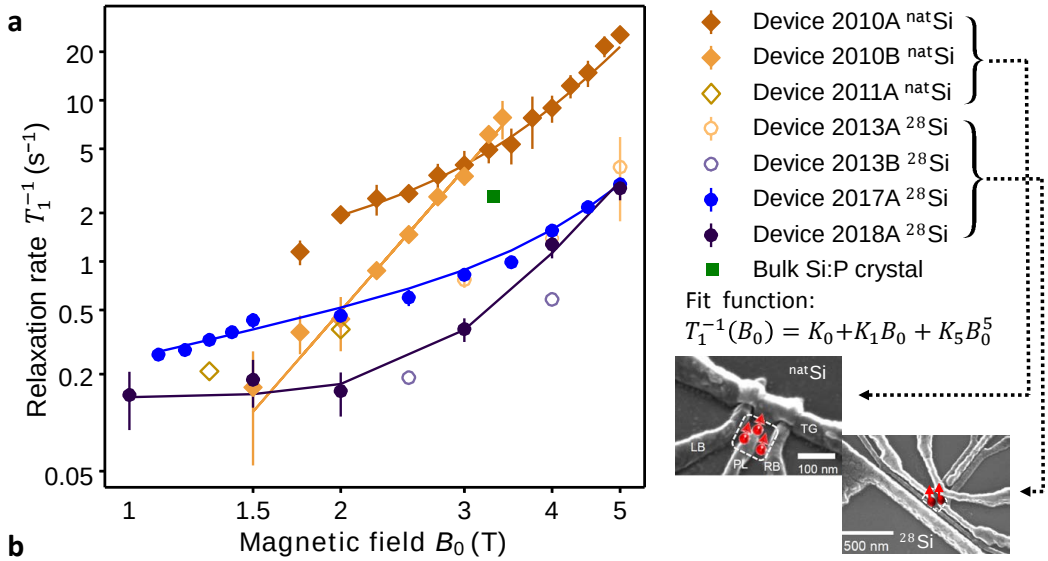

b

	K_0(s^{-1})	K_1(s^{-1}T^{-1})	K_5 (s^{-1}T^{-5})
2010 A	-	0.88 ± 0.02	$(5.5 \pm 0.5) \times 10^{-3}$
2010 B	-	-	$(1.54 \pm 0.05) \times 10^{-2}$
2017 A	-	0.250 ± 0.004	$(5.6 \pm 0.7) \times 10^{-4}$
2018 A	0.14 ± 0.02	-	$(10 \pm 1) \times 10^{-4}$

FIGURE 8.3: **Relaxation rate as a function of external magnetic field. a** Measurements of the electron relaxation time T_1 as a function of external magnetic field B_0 for different samples. Devices 2010A and 2010B are republished from Ref. [24] and fabricated on ^{nat}Si, same as device 2011A (diamonds). Devices 2013A, 2013B, 2017A and 2018A have been fabricated on Si^{28} (dots). For reference, a data point measured on a bulk Si:P crystal at $T < 5$ K is shown (green square, J. J. L. Morton, personal communication). For devices 2010A, 2010B, 2017A and 2018A polynomials of form $T_1^{-1}(B_0) = K_0 + K_1 B_0 + K_5 B_0^5$ have been fitted to the relaxation rate. The insets show the respective device designs. **b** Fit results of the different samples. A dash indicates that the parameter was fixed at $K_i = 0$.

with a polynomial function of the form:

$$T_1^{-1}(B_0) = K_0 + K_1 B_0 + K_5 B_0^5, \tag{8.30}$$

with the results displayed in Tab. 8.3b (a dash indicates that the parameter was fixed at $K_n = 0$).

The prefactor K_5 describing the phonon-induced relaxation rate $\propto B_0^5$ at high magnetic fields varies significantly between the different devices (see Sec. 8.4.2). Furthermore, all fitted devices show a deviation from $T_1^{-1} \propto B_0^5$ at magnetic fields $B_0 \lesssim 3$ T, except for device 2010B: devices 2010A and 2017A follow $T_1^{-1} \propto B_0$, while device 2018A shows a $T_1^{-1} \sim$ const. behavior at low field.

These deviations from bulk-like relaxation behaviors unveil details of the interaction betwen the donor electron spin and its environment in the MOS nanostructures under study.

8.4.1 Evanescent wave Johnson noise induced relaxation

In our metal-oxide-semiconductor devices, the electrostatic gates, SET, and microwave antennas are all potential sources of EWJN (Fig. 8.4a).

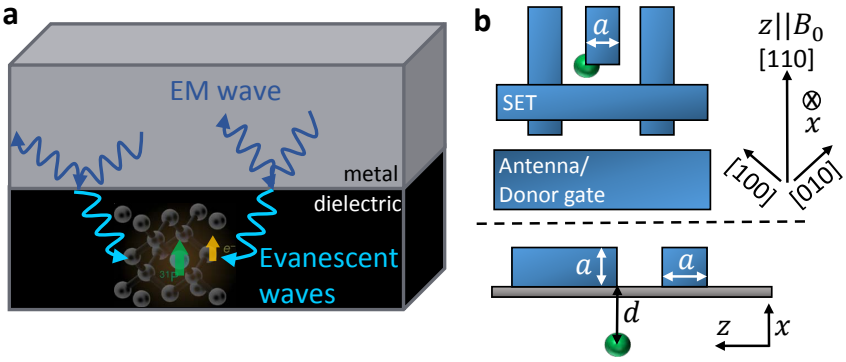

c d (nm)	$T_{1,x}^{-1}(s^{-1})$ theory	$T_{1,y}^{-1}(s^{-1})$ theory	$T_{1,z}^{-1}(s^{-1})$ theory	$T_{1,z}^{-1}(s^{-1})$ measured
20	2.4	3.9	3.8	1.32 ± 0.03 (2010A) 0.375 ± 0.006 (2017A)
50	0.4	2.1	1.5	

FIGURE 8.4: **Evanescent wave Johnson noise. a** Schematic of the origin of EWJN in our qubit devices. **b** Device layout showing the donor position, the external magnetic field and the crystal orientation. a is the metallic gate dimension, d is the distance between the donor and the metal gates. **c** Relaxation rates predicted by the EWJN theory using $\sigma = 1.6 \times 10^7$ S/m, $B_0 = 1.5$ T, $a = 50$ nm and $d = 20$ or 50 nm, compared to two measured values.

Replacing the qubit Larmor frequency with $\omega_0 = g\mu_B B_0/\hbar$ in Eq. (8.25) yields:

$$\begin{aligned} T_1^{-1} &= \frac{\mu_B^2 \mu_0^2 \sigma g B_0}{4\pi\hbar^2} \frac{1}{\mathcal{L}} \\ &= K_1 B_0. \end{aligned} \tag{8.31}$$

The most important point about this formula is that no other plausible spin relaxation mechanism gives a rate proportional to B_0. Linearity of T_1^{-1} in B_0 is thus a convincing signature of EWJN.

For the validity of the analysis that follows, the value of the electrical conductance σ of the aluminum structures is very important. σ determines the characteristic length scales ℓ (mean free path) and δ (skin depth) and the resulting magnitude of the relaxation. We extracted σ from 4-point measurements on Hall bar structures (Fig. 8.5a) with feature sizes varying from 300 nm to 30 nm. We tested aluminum layers formed both via thermal evaporation and electron beam physical vapour deposition (EBPVD), but all devices on which spin relaxation was measured and reported in Fig. 8.3 were fabricated using thermal evaporation.

We find that the conductivity drops with reduced feature size but only up to a factor of 2 (Tab. 8.5b), which is consistent with a grain size of approximately 20 nm, i.e. comparable but still smaller than the width and thickness of the fabricated gates. We base the calculations below on the value $\sigma = 1.6 \times 10^7$ S/m obtained for the 30 nm feature size, which corresponds to the smallest gate dimensions used in donor devices studied in this paper. This conductance results in a skin depth $\delta(B_0 = 1\,\mathrm{T}) = 752$ nm (Eq. 8.24) and a mean free path $\ell = 6.3$ nm (Eq. 8.23) with $\mu_R = 1$, $n = 18 \times 10^{28}\,\mathrm{m}^{-3}$ and $v_F = 2 \times 10^2$ m/s [197]. This shows that ℓ is always smaller than even the smallest feature sizes in our devices, placing the conduction electrons in the aluminum gates in the diffusive regime.

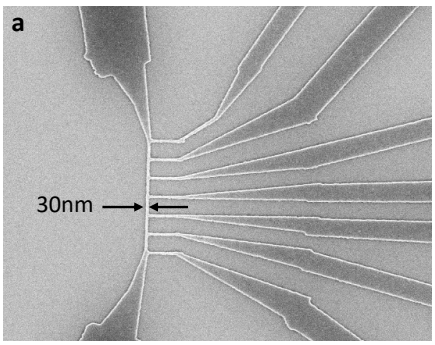

b	σ (S/m)
Room temperature bulk	$3.8 \cdot 10^7$
300nm width, thermal, 4 K	$3.9 \cdot 10^7$
100nm width, thermal, 4 K	$3.4 \cdot 10^7$
30nm width, thermal, 4 K	$\mathbf{1.6 \cdot 10^7}$
300nm width, EBPVD, 4 K	$6.9 \cdot 10^7$
100nm width, EBPVD, 4 K	$4.2 \cdot 10^7$

FIGURE 8.5: **Aluminium conductivity measurements. a** Scanning electron micrograph of a Hall bar structure to measure the conductivity σ of the Al gates. The width is $w = 30$ nm in the depicted device. **b** Conductance of 50 nm thick Al metal, measured at temperature $T = 4$ K with Hall bar structures as in (**a**), for different feature width w, formed either by thermal evaporation or electron-beam physical vapour deposition (EBPVD). Room-temperature bulk value for comparison [196].

EWJN depends on the gate geometry through the geometric factor $\mathcal{L}$ (Eq. 8.31). $\mathcal{L}$ can be calculated analytically for different cases: half spaces and spheres. The electron spin effectively sees a metallic half space when its distance to the gates d is much smaller than the gate lateral dimensions a. When the spin is further away from a finger gate or an antenna ($d \gg a$, Fig. 8.4b), it sees approximately a conducting cylinder. Since our devices have $d \approx 10 - 20$ nm and $a \approx 30 - 80$ nm, we employ an interpolation between both cases in form of

$$1/T_{1i} = 1/\left[T_{1i}(\mathcal{L}_{\text{hs}}) + T_{1i}(\mathcal{L}_{\text{cyl}})\right], \tag{8.32}$$

where i indicates the direction x, y or z of the applied field B_0. We model an antenna or finger gate as a string of spherical beads. The final relaxation rate follows as

$$T_{1,x}^{-1} = \frac{\mu_B^2 \mu_0^2 \sigma \omega_0}{32\pi\hbar d}\left(1 + \frac{256 d^4}{15\pi a^4}\right)^{-1}, \tag{8.33a}$$

$$T_{1,y}^{-1} = \frac{3\mu_B^2 \mu_0^2 \sigma \omega_0}{64\pi\hbar d}\left(1 + \frac{256 d^4}{91\pi a^4}\right)^{-1}, \tag{8.33b}$$

$$T_{1,z}^{-1} = \frac{3\mu_B^2 \mu_0^2 \sigma \omega_0}{64\pi\hbar d}\left(1 + \frac{256 d^4}{47\pi a^4}\right)^{-1}. \tag{8.33c}$$

Using the measured conductivity (Tab. 8.5b), the predicted relaxation rate due to EWJN for $B_0 = 1.5$ T applied in the z-direction (in the plane of the device) is $T_{1z}^{-1} \approx 4\,\text{s}^{-1}$, for a donor depth $d = 20$ nm and aluminum gates of width $a = 50$ nm (Tab. 8.4c). This prediction is close to the measured value of $T_1^{-1} = 1.3\,\text{s}^{-1}$ in device 2010A, while it overestimates T_1^{-1} by around one order of magnitude for device 2017A. Neither device 2010B nor device 2018A exhibit a $T_1^{-1} \propto B_0$ behaviour within the measured range of magnetic fields.

This order of magnitude agreement between theory and experiment can be considered satisfactory, in light of the many experimental parameters that are only approximately known, such as the donor depth d, as well as the lateral position of the donor with respect to the gates (the devices that show no evidence of $1/T_1 \propto B_0$ could have the donor underneath the gaps between the gates, for example).

Tab. 8.4c shows the predicted anisotropy of $1/T_1$ as a function of the direction of B_0. In the future, such anisotropy of the EWJN contribution could provide a further test of the theory, if $1/T_1$ were measured as a function of field direction using a 3D vector magnet.

8.4.2 Phonon-induced relaxation: effects of lattice strain

The phonon-induced electron spin relaxation strongly depends on the crystalline environment of the donor. We observed nearly two orders of magnitude variation in the prefactor K_5 of the term $T_1^{-1} \sim B_0^5$ (Fig. 8.3). We tentatively attribute this variability to the variation of local strain in the devices. Strain in MOS devices arises due to the different thermal expansion coefficients of aluminum and silicon [198]. The donors are quite close to the Al gates, and the presence of strain has been documented in several experiments, especially for its impact on the hyperfine coupling A [175], [199], [200].

As shown in Eq. (8.12), the valley energies shift with strain. This leads to a lowering in energy of the E excited states [Eq. (8.10)e,f], i.e. to a reduction of the valley-orbit splitting E_{12} [179], [201], which would suggest that the spin relaxation becomes faster with strain [see Eqs. (8.18),(8.19)]. However, for large compressive strain in the z-direction the lowest-energy valley-orbit states become symmetric and antisymmetric combinations of the $\pm z$ valleys. This causes the overlap matrix element D_r [Eq. (8.17)] to become vanishingly small [201]. The decrease of D_r caused by the change in valley composition greatly outweighs the increase of $1/E_{12}$, resulting in an overall reduction T_1^{-1}, according to Eq. (8.16).

Device 2017A was also the subject of the experiments by Laucht *et. al.* [175]. In that work, the analysis of the hyperfine shift yielded $s_{xy} \approx -0.1\%$ in-plane compressive strain. This device exhibits the slowest phonon-induced relaxation (lowest K_5) among all tested and, significantly, the strongest deviation from the bulk value of the hyperfine coupling ($A \approx 97$ MHz).

In Device 2018A we measured $A \approx 115$ MHz from which, using the atomistic tight binding simulations from Fig. S6 in Ref. [175], we estimate a strain $s_{xy} \approx -0.05\%$. This lower value of the strain is consistent with the faster spin-phonon relaxation observed in this device ($K_5 \approx 10 \times 10^{-4}$ s^{-1}T^{-5}, compared to $K_5 \approx 5 \times 10^{-4}$ s^{-1}T^{-5} in Device 2017A).

The highest value of $K_5 \approx 1.5 \times 10^{-2}$ was found in Device 2010B. That device did not have a microwave antenna, so the hyperfine coupling could not be measured. Interestingly, $1/T_1$ in Device 2010B coincides with the relaxation rate measured in an all-epitaxial single-donor device fabricated via STM hydrogen lithography [183]. The STM device is likely to exhibit very little strain, since the donor is deeply embedded in the silicon crystal and no metal gates are present in its vicinity. This findings suggest that device 2010B contained a donor implanted deeper than usual, far away from the aluminium gates, and therefore subjected to a reduced amount of strain. The deep location of the donor would also explain the absence of EWJN-induced relaxation in this device, which followed $1/T_1 \propto B_0^5$ down to the lowest field.

8.4.3 Other relaxation processes

One device, 2018A, exhibits a field-independent relaxation rate for $B_0 < 2$ T. In Ref. [24], the relaxation rate of Device 2010A was also interpreted as a combination of $1/T_1 \propto B_0^5$ and $1/T_1 = const.$ (the data point at $B_0 = 1.75$ T was thought to be an outlier), and a quantitative model was developed to justify the constant contribution.

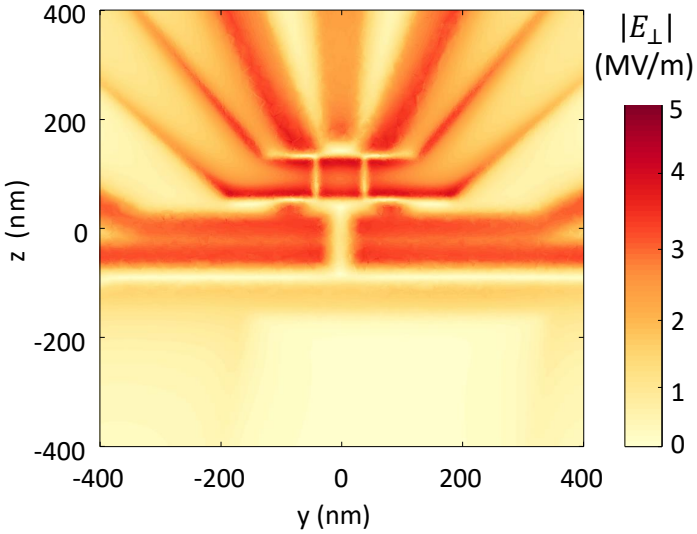

FIGURE 8.6: **Perpendicular electric field at the typical donor depth.** Absolute value of the electric field component $|E_\perp|$ perpendicular to the magnetic field applied along the z-axis, calculated using the COMSOL finite-elements electrostatic package. We show values 10 nm under the Si/SiO_2 interface, a typical implantation depth. The model consists of a $2\,\mu m \times 2\,\mu m \times 2\,\mu m$ silicon substrate grounded at the bottom. On top of a 8 nm SiO_2 layer, we define the aluminum gates, which are coated by 2 nm of Al_2O_3. We assume typical voltages, i.e. 0.4 V to the barrier, plunger and donor gates, 2 V to the top gate, and we set the potential of the microwave antenna at ground. To model the 2DEG under the top gate, we ground the Si/SiO_2 interface in the relevant regions.

Since our devices contain on average $10 - 20$ donors in a 100×100 nm^2 region, we analyzed the rate at which a spin excitation on the donor under measurement can diffuse to nearby donors by means of magnetic dipole-dipole interactions. The flip-flop rate Γ_{ff} between a pair of donors can be expressed as [24]:

$$\Gamma_{ff} \approx \frac{\pi}{2\langle \Delta\omega_I \rangle} M_{ff}(\theta, d), \tag{8.34}$$

where $\langle \Delta\omega_I \rangle$ is the half-width of each electron spin resonance as caused by the Overhauser field from the ^{29}Si nuclei, and M_{ff} is the flip-flop matrix element in the magnetic dipolar coupling Hamiltonian, which depends on the angle θ and the distance d between the spins. This model yields $\Gamma_{ff} \approx 2$ s^{-1} using $d = 24$ nm and taking $\langle \Delta\omega_I \rangle / \hbar \approx 3.5$ MHz [40] as the typical value of Overhauser field broadening in ^{nat}Si.

It is immediately clear from Eq. (8.34) that this model would yield implausible results when applied to the ^{28}Si enriched samples, where $\langle \Delta\omega_I \rangle / \hbar \approx 1$ kHz is three orders of magnitude smaller than in ^{nat}Si [30]. This is because Eq. (8.34) assumes that the donors have the same hyperfine coupling A and the same g-factor, and their resonance frequencies are detuned solely by Overhauser fields. We now know that this assumption is, in general, unlikely to hold: we have observed hyperfine couplings ranging from 97 to 116 MHz in various devices, with the spread arising from different local electric fields and strain [175]. Including the effect of locally different A and g for different donors within the same device would result in a near-complete suppression of the (energy-conserving) flip-flop processes. Therefore, we do not believe that this mechanism can be responsible for the field-independent relaxation rate observed in Device 2018A.

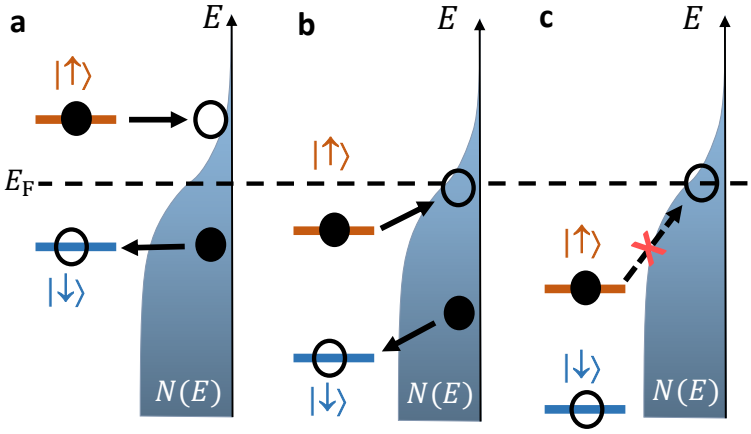

FIGURE 8.7: **Spin relaxation through quantum tunnelling.** **a** Spin relaxation via direct tunneling of $|\uparrow\rangle$ from the donor into the SET reservoir as long as $\mu_{d,\uparrow} \gtrsim \mu_{SET}$. $|\uparrow\rangle$ is then replaced by $|\downarrow\rangle$. **b** Spin relaxation via co-tunneling of $|\uparrow\rangle$ into a virtual free state in the SET while $|\downarrow\rangle$ tunnels onto the donor. **c** For $\mu_d \ll \mu_{SET}$ all tunnel processes are suppressed.

Another relaxation mechanism, recently discovered in STM-fabricated donor devices [33], is a spin-orbit coupling (SOC) induced by the presence of an electric field $E_\perp$ perpendicular to the external magnetic field B_0. In our devices, the direction and strength of the electric field at the donor can vary significantly, depending on where exactly the donor is located with respect to the gates (Fig. 8.6). An electric field component $E_\perp$ perpendicular to B_0 should, in general, be expected. This mechanism would mediate an additional spin-phonon relaxation channel on top of the bulk-like valley repopulation and one-valley relaxation, resulting in values of K_5 higher than in the bulk. Instead, in all devices except 2010A and 2010B, we found K_5 to be lower than the bulk value. This does not mean that this SOC mechanism does not exist in our devices, but it indicates that, in almost all cases, its contribution is less significant than the suppression of the relaxation rate caused by local strain.

8.5 Tunnelling effects

The experiments described in this work rely upon switching between a "plunge/wait" phase, during which the electron remains bound to the donor while its spin is allowed to relax, and a "read" phase, during which electron tunneling between the donor and the SET island is used to measure the spin state (Fig. 8.1c). Here we discuss the impact on the measurement results of the possibility that the electron tunnels out of the donor during the plunge/wait phase.

To describe the rate of first-order tunneling between donor and SET island, we first define α_p as the lever arm of the gate voltages to the donor, which determines the shift in μ_d induced by the effective donor plunge V_p [see Eq. (8.28)]:

$$\Delta\mu_d = -e\alpha_p V_p \tag{8.35a}$$

$$\alpha_p = \frac{\beta_c C_{d-PL} + C_{d-DP}}{C_\Sigma} \tag{8.35b}$$

where C_{d-PL} and C_{d-DP} are the capacitances between the donor and the plunger gate PL and the donor and the donor gate DP, respectively, and C_Σ is the total capacitance of all gates to the donor. In the presence of a magnetic field we define the donor

electrochemical potential as the average of the $|\downarrow\rangle$ and $|\uparrow\rangle$:

$$\mu_{\mathrm{d}} = \frac{\mu_{\mathrm{d},\downarrow} + \mu_{\mathrm{d},\uparrow}}{2}. \tag{8.36}$$

With this definition, the direct (first-order) tunnel-out rate of the $|\uparrow\rangle$ electron at electrochemical potential $\mu_{\mathrm{d},\uparrow}$ can be written as [202], [203]:

$$\Gamma_{\mathrm{DT}} \approx \Gamma_0 \cdot [1 - f(V_{\mathrm{p}}, T_e)], \tag{8.37}$$

where

$$f(V_{\mathrm{p}}, T_e) = \frac{1}{\left(1 + \exp \frac{-e\alpha_{\mathrm{p}} V_{\mathrm{p}} + E_Z/2}{k_B T_e}\right)} \tag{8.38}$$

is the Fermi function, T_e is the electron temperature of the SET island and the term $-e\alpha_{\mathrm{p}} V_{\mathrm{p}} + E_Z/2 = \mu_{\mathrm{d},\uparrow} - \mu_{\mathrm{SET}}$ describes the energy detuning between the $|\uparrow\rangle$ state and the SET electrochemical potential at a plunge voltage V_{p}. Since $k_B T_e \ll E_Z$ in our experiments, Γ_0 effectively represents the bare $|\uparrow\rangle$ tunnel-out rate at the "read" position. For simplicity, we assumed that Γ_0 remains independent of V_{p} within the small voltage range used in the experiment.

This direct tunnel process results in an apparent electron spin relaxation, when $|\uparrow\rangle$ tunnels from donor to SET and is replaced by a different electron in state $|\downarrow\rangle$ (Fig. 8.7a). The spin relaxation rate is therefore similar (although not identical [204]) to the charge tunneling rate. In this work, we have used the first-order tunneling process to deliberately initialize the spin in the $|\downarrow\rangle$ state for the experiments at $B_0 \leq 1.5$ T. Direct tunneling is exponentially suppressed with the energy difference between μ_{d} and μ_{SET} and is only expected as long as $|\uparrow\rangle$ is aligned with available free states in the SET island, above or just below μ_{SET}.

Even if no free states are available for first-order tunneling, the $|\uparrow\rangle$ electron can relax via a second-order tunneling process. If an empty state at energy $E > \mu_{\mathrm{d},\uparrow}$ is available in the electron reservoir, the $|\uparrow\rangle$ donor electron can virtually occupy such state for a time $t_{\mathrm{H}} \sim \hbar/(E - \mu_{\mathrm{d},\uparrow})$ given by the Heisenberg uncertainty principle. During this time, another electron coming from the reservoir can occupy the donor state. This process can be elastic if the original $|\uparrow\rangle$ electron is replaced by a $|\downarrow\rangle$ electron from the reservoir (Fig. 8.7b). This process is then called spin-flip co-tunneling, and leads to a spin relaxation rate described by [204]–[206]

$$\Gamma_{\mathrm{CT}} = \frac{E_z}{\pi\hbar} \cdot \left(\frac{\hbar\Gamma_0}{e\alpha V_{\mathrm{p}}}\right)^2. \tag{8.39}$$

Eq. (8.39) shows that the co-tunnelling rate is suppressed only quadratically (instead of exponentially) with plunge voltage, so it can in principle remain significant for $\mu_{\mathrm{d},\uparrow} \lesssim \mu_{\mathrm{SET}}$. Eventually, when $\mu_{\mathrm{d}} \ll \mu_{\mathrm{SET}}$ all tunnel process should be suppressed (Fig. 8.7c).

However, Γ_{CT} also depends quadratically (instead of linearly) on the bare tunnel rate Γ_0. Experiments showing co-tunneling effects have been ones where the electron under study was strongly tunnel-coupled to the charge reservoir, typically in a quantum transport setup [206], [207], which requires $\Gamma_0 \gtrsim 1 \times 10^9$ s^{-1}. Here we have instead $\Gamma_0 \lesssim 1 \times 10^3$ s^{-1}, making the co-tunneling process extremely weak.

In Fig. 8.8 we present the measurements of the spin relaxation rate $1/T_1$ as a function of plunge voltage V_{p}. Fig. 8.8a shows the measured plunge voltage points with respect to μ_{SET} (dashed purple line) in the charge stability diagram. We both

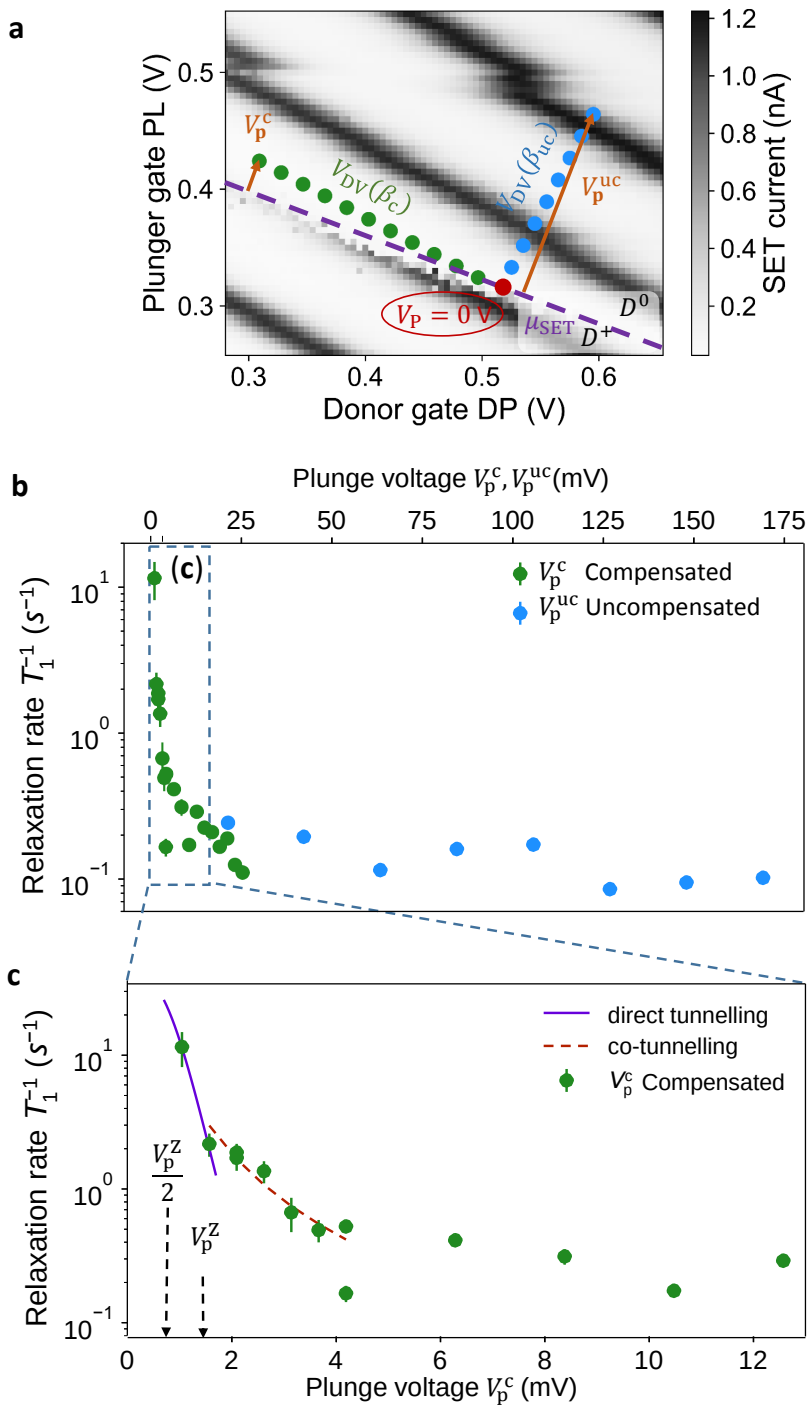

FIGURE 8.8: **Relaxation rate as a function of plunge voltage. a** Charge stability diagram of plunger gate (PL) and donor gate (DP). The donor transition from ionized (D^+) to neutral (D^0) when $\mu_d = \mu_{SET}$ is indicated by the dashed purple line. Virtual gate voltage $V_{DV}(\beta_c = -0.51)$ (compensated plunging, green) and $V_{DV}(\beta_{uc} = 1.81)$ (uncompensated plunging, blue) are indicated. The corresponding effective plunge voltage is $V_p^{c/uc}$ (orange arrows). **b** Relaxation rates as a function of $V_p^{c/uc}$. The dotted region indicates the position we show in greater detail in (**c**). **c** Zoomed-in plot for low plunge voltages with voltage V_p^Z ($V_p^Z/2$) corresponding to the Zeeman energy E_Z ($E_Z/2$) marked. The direct tunnelling process is described by Eq. (8.37) (purple line). The red dotted line indicates a potential co-tunnelling process.

move μ_d while keeping $\mu_{SET} = const.$, using $\beta_c = -0.51$ (compensated plunging, green points, V_p^c), as well as perpendicular, using $\beta_{uc} = 1.82$ (uncompensated, blue points, V_p^{uc}). The latter allows for much higher V_p but also shifts μ_{SET} and even leads to a change in SET electron number N when a Coulomb peak is crossed.

As expected, the relaxation rate strongly decreases the deeper the donor is plunged below μ_{SET} (Fig. 8.8b), until it stabilises at around $T_1^{-1} = 9^{-1}\,s^{-1}$. Clearly we identify two regimes: On the one hand, at high plunge voltages ($V_p^{c/uc} \gtrsim 10\,mV$) the relaxation rate shows no dependence on $V_p^{c/uc}$ which implies that the relaxation rate is not limited by any type of tunnel process. On the other hand, at low $V_p^{c/uc}$, the relaxation strongly depends on $V_p^{c/uc}$. Fig. 8.8c shows the region $V_p^c \in (0, 13)\,mV$ in greater detail.

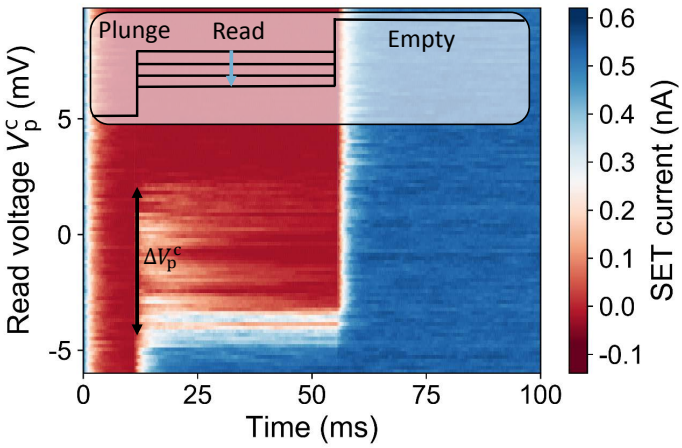

FIGURE 8.9: **Spin tail measurement.** SET current as a function of the read level voltage V_p^c, resulting is a spin tail of $\Delta V_p^{c/uc} = 7.2\,mV$ at $B_0 = 5\,T$. Inset shows the applied pulse sequence.

To relate V_p^c to energy, we determine α_p by measuring the Zeeman energy through spin-dependent tunnelling (Fig. 8.9). Therefore, we tune the read level and measure at which voltages $|\uparrow\rangle$ and $|\downarrow\rangle$ tunnel out of the donor. We relate

$$\Delta\mu_d = \mu_{d,\uparrow} - \mu_{d,\downarrow} = E_Z. \tag{8.40}$$

To perform this measurement, we apply the following pulse sequence (inset Fig. 8.9). We load an electron with a random spin state, bias the donor at the read level with voltage V_p^c and finally empty it. During the whole pulse sequence, the SET current is measured. Then we repeat the pulse sequence while varying V_p^c from $\mu_{d,\downarrow} > \mu_{SET}$, causing a high current by lifting Coulomb blockade regardless of the spin state, to $\mu_{d,\uparrow} < \mu_{SET}$, blocking conduction fully. In the intermediate regime where $\mu_{d,\downarrow} \leq \mu_{SET} \leq \mu_{d,\uparrow}$, $|\uparrow\rangle$ tunnels to the SET, creating a current spike, and is replaced by $|\downarrow\rangle$ - we observe a spin tail [24]. The voltage range of this tail $\Delta V_p^c = 7.2\,mV$ corresponds to the Zeeman energy at the external magnetic field of $B_0 = 5\,T$. We calculate the lever arm to

$$\alpha_p = \frac{E_Z}{\Delta\mu_d} = \frac{g\mu_B B_0}{e\Delta V_p^c} = 0.08. \tag{8.41}$$

The voltage corresponding to the Zeeman energy at 1 T is $V_p^Z = 1.4\,mV$ which is marked in Fig. 8.8c. We also mark half the Zeeman energy as this is the plunge voltage where $\mu_{d,\uparrow} \geq \mu_{SET}$.

Within the detailed region in 8.8c, we can again identify two regimes: For $V_p \lesssim 2\,\text{mV}$, we observe a strong dependence of the relaxation rate on V_p^c which we attribute to direct tunnelling from $|\uparrow\rangle$ to the SET reservoir enhancing the relaxation process. The purple line shows Eq. (8.37) with the realistic experimental parameters $\Gamma_0 = 50\ \text{s}^{-1}$, $T_e = 250\,\text{mK}$, and $V_p^Z = 1.4\,\text{mV}$, $\alpha_p = 0.08$, as determined by the spin tail measurement.

For $V_p^c \in (2, 4)\,\text{mV}$ we observe a slower decrease of the relaxation rate. Due to the slow direct tunnelling rate $\Gamma_0 = 50\ \text{s}^{-1}$, Eq. (8.39) predicts an extremely slow co-tunnelling rate $\Gamma_{CT}(V_p^c = 2\,\text{mV}) = 3 \times 10^{-9}\ \text{s}^{-1}$. This rules out co-tunnelling for this relaxation process and leaves us searching for an explanation. Note, however, that a co-tunnelling process with $\Gamma = 1.4 \times 10^6\ \text{s}^{-1}$ would fit the data (see dotted red guideline in Fig. 8.8c).

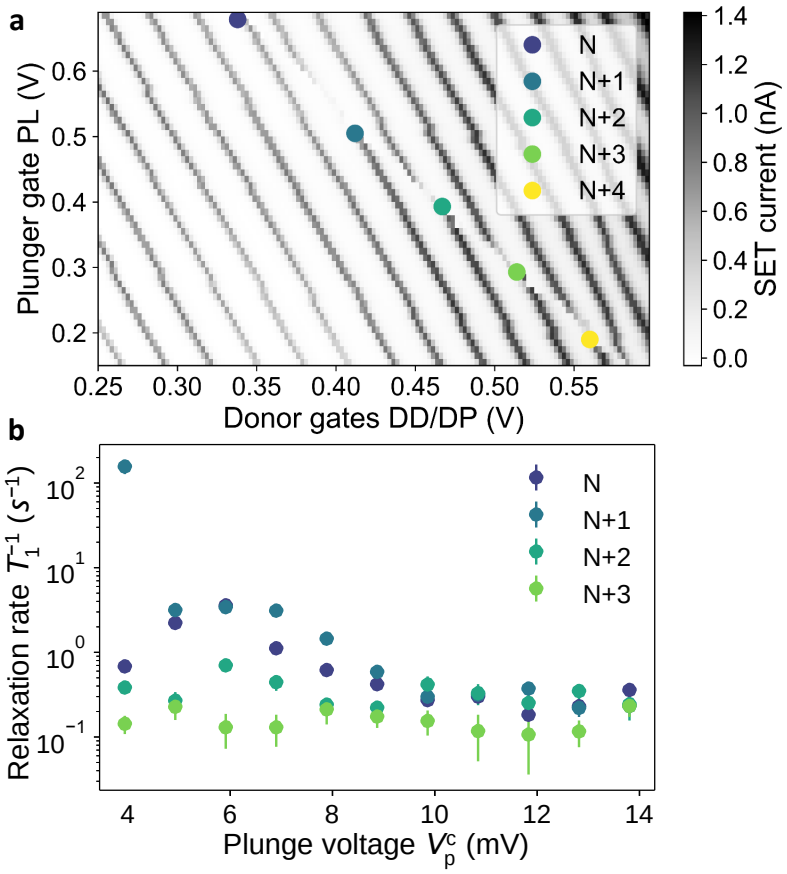

FIGURE 8.10: **Relaxation rate as a function of electron number. a** Charge stability diagram of plunger gate (PL) and donor gates (DD, DP) with bias points corresponding to different SET island electron numbers N indicated. **b** Relaxation rates with plunge voltage for different N. Only compensated plunging is performed.

We also study the relaxation time for several different Coulomb peaks, corresponding to a different electron number N on the SET island. (Fig. 8.10). A thermal cycle of the measured device was performed which results in a different device tuning as in Fig. 8.8. We find a strong variation in relaxation behaviour between different electron numbers for $V_p^c \lesssim 10\,\text{mV}$, when tunnelling processes are relevant. For any tunnelling process the density of free states of the SET island is paramount. We estimate our SET with around 100 electrons, in the transition regime where the SET island does not yet behave like a proper metallic electron reservoir with a continuous density of states but shows some remaining many-electron quantum-dot behaviour

[44]. As a consequence the density of states is modulated by quantum effects arising from the Hund's rule when consecutively filling the electron orbitals. Different orbitals have different wave functions which can lead to different tunnel rates between the SET island and the donor. The same effect occurs for a shift of the wave function due to a different voltage bias. Consequently, the direct tunnel rate Γ_0 and in turn the relaxation rate can vary strongly with voltage bias when tuned to a voltage where the electron sees a non-uniform SET density of states. We also observe this effect in the spin tail measurement (Fig. 8.8c) as the tail is non-uniform. Changing the SET electron number has the same effect, as μ_{SET} is shifted. Nevertheless, for deep plunge voltages, tunnel effects are suppressed and these differences disappear.

8.6 Conclusion

In summary, we find that EWJN is a likely candidate for the increase of the relaxation rate at low magnetic fields if the qubit is close to a strongly conducting surface, like aluminium gates. Moreover, we discover that strain at the donor site decreases the relaxation rate. This can lead to very long T_1 times of up to 9 s at $B = 1\,\mathrm{T}$. Furthermore, tunnel effects influence the relaxation, esp. at low plunge voltages. This has to be taken into consideration for any qubit experiments of long duration - deep plunging is required.

Overall, we believe that this work expands the scope of fundamental research on donor qubits in silicon. We highlight several effects that influence qubit performance and need to be taken into consideration during high precision experiments. Even though (or especially because!) the origin of some of our observations are still not fully understood, we hope to inspire more theoretical and experimental research in this area to not only keep improving a promising qubit, but also understand more about donors in semiconductors.

Chapter 9

Conclusion

"Climb the mountain not to plant your flag, but to embrace the challenge, enjoy the air and behold the view. Climb it so you can see the world, not so the world can see you."
– David McCullough Jr.

Since the first realization of a donor spin qubit in 2012 by J. Pla *et al.* [40], these qubits have advanced significantly. Single Clifford gate fidelities of 99.94 % [42] and 99.99 % [30] have been achieved for the electron and the nuclear qubit, with coherence times of $T_2 = 980\,\mathrm{ms}$ [46] and $T_2 = 35.6\,\mathrm{s}$ [30] respectively. Exquisite single qubits need to be augmented with a clear pathway to multi-qubit operations and device scalability. This thesis has provided several contributions to the quest of building a large-scale donor-based quantum computer.

9.1 Understanding dopants in silicon: electron spin relaxation

One important issue is to gain full understanding of our qubit system. When engineering reproducible, high quality qubits with low decoherence and high fidelites, accurate knowledge of the fundamental physics of donors in silicon is of key importance.

The electron spin relaxation time T_1 gives insight into the mechanisms that couple the electron spin to its environment. While for many years most research efforts were focussed on extending T_2 when qubits were limited by dephasing, recently the interest in T_1 has been revived when the limit $1/T_2 \leq 1/2\,T_1$ was approached. This occurred, in donor spin qubits, because T_2 was extended significantly through the application of purified silicon ^{28}Si and clever pulse sequences [46], [208], [209].

Previous research has mainly focussed on spin-orbit induced relaxation in SiGe quantum dots [31], [32] and donors [33]. This thesis concentrates on relaxation due spin-orbit coupling of deformation potential phonons, evanescent wave Johnson noise and tunnelling effects (Chap. 8).

We have measured T_1 as a function of external magnetic field and observed phonon-induced relaxation at high magnetic fields of $B_0 \gtrsim 3\,\mathrm{T}$. We found that the strength of this phonon-induced relaxation varied by up to two orders of magnitude between different devices and relate this variation to different amounts of strain in the devices. Strain arises due to the difference in thermal expansion coefficients of the device materials aluminium and silicon. As such, it can differ for different devices and donor positions. The presence of strain shifts the valleys and reduces the relaxation rate. Hence, one can engineer qubits with longer relaxation times by purposefully introducing strain to the sample. However, the strain magnitude needs to be carefully adjusted to not lower the excited valley states too strongly. To expand our knowledge of the phonon-induced relaxation, it would be interesting to measure T_1 as a function of the angle θ between the crystal axis and B_0. Phonons cause electron spin relaxation both through repopulation of different valley states and energy shifts within one valley. These two effects have different dependences on θ. Thus their individual strength could be evaluated.

Furthermore, we found that at low magnetic fields $B_0 \lesssim 3\,\mathrm{T}$ the relaxation rate is dominated by EWJN, which results in magnetic noise emitted from the aluminium gates. The strength of this effect depends on the aluminium conductivity, the gate geometry and the distance between the donor and the gates. Measuring T_1 as a function of θ would also give further insight into the anisotropy of this effect.

We also analysed T_1 as a function of plunge voltage, which determines the difference between the electrochemical potential of the donor and the SET. The measurements show that direct tunnelling of the electron between the donor and the SET limits the relaxation times for low plunge voltages. This effect can be mitigated by deeply plunging the donor below the SET electrochemical potential such that any

tunnel process is suppressed. Employing this strategy, we have measured a very long relaxation time of a single donor electron spin to $T_1 = 9.8 \pm 0.7\,\mathrm{s}$.

9.2 Robust two-qubit coupling

Another outstanding challenge concerning donor qubits, maybe the most important one, is coupling two donor qubits with high fidelity while having some tolerance on the donor placement precision.

While the exchange interaction is the most natural way to couple two donor spins, it demands very precise donor placement, on the order of one lattice site. Even though this requirement can be slightly relaxed when using a hyperfine-controlled exchange interaction between electron spin qubits [71], scaling up this approach to many qubits will be very challenging. Other proposals include a slow magnetic dipole-dipole coupling effective at $\sim$ 30 nm distances [72], donor chains [73], [74], charge-coupled devices [75], ferromagnets [76], probe spins [77] or quantum dots [78]. These approaches either only provide slow gates or demand a complex device architecture due to the use of intermediate couplers.

In this thesis, we have addressed this problem by proposing a new type of donor qubit, the flip-flop qubit, consisting of the combined electron-nuclear states $\{|\uparrow\Downarrow\rangle, |\downarrow\Uparrow\rangle\}$ (Chap. 3).

We separate the electron from the donor to form a vertical charge qubit where the electron can be at the donor or at the Si/SiO_2 interface. This introduces an artificial spin-orbit coupling through the change in hyperfine interaction, when the electron wavefunction is manipulated, and makes the qubit electrically accessible. Single qubit gates can be performed by applying a microwave electric drive, and the predicted error rates are below 10^{-3}, assuming an r.m.s. charge noise of 1.5 μeV.

The charge qubit is associated with a large artificial electric dipole. Two distant $(200 - 500\,\mathrm{nm})$ flip-flop qubits can then be coupled via second-order dipole-dipole interaction at strength exceeding 1 MHz with gate errors below 10^{-2}. The two-qubit coupling is robust again donor misplacement since the electric dipole interaction scales very gently with inter-donor distance. In this scheme, the exponentially sensitive parameter is the tunnel coupling between the donor and the interface dot, which can be tuned in-situ by laterally displacing the dot wave function using surface gates. The flip-flop qubit can also be coupled to the electric field of a superconducting resonator, opening the pathway for hybrid quantum computers and long distance coupling.

The concept of creating an artificial spin-orbit coupling and a large dipole by separating the electron charge from the donor can be extended to couple two nuclear spins robustly over hundreds of nanometers (Chap. 4). For that purpose, we apply a magnetic microwave drive simultaneously with the electric flip-flop drive. This results in a second-order Raman process between the "nuclear qubit" states $\{|\downarrow\Uparrow\rangle, |\downarrow\Downarrow\rangle\}$. The magnetic drive effectively creates an electric dipole transition for the nuclear spin. The dipole moment can reach $> 100\,\mathrm{D}$ such that the nuclear spin can be driven at 1 MHz with a dephasing rate of $1 - 10 \times 10^3\,\mathrm{s}^{-1}$. This also allows us to couple the nuclear spin to a superconducting resonator with a coupling of 1 MHz and to couple two nuclear spins at long distances. For a separation of 400 nm, a two qubit coupling of 0.55 MHz can be achieved.

Both the flip-flop and the nuclear qubit can be implemented with current fabrication techniques, based on the successful donor and quantum dot MOS structures. We followed two approaches: coupling two flip-flop qubits directly via dipole-dipole

interaction and coupling a flip-flop qubit to a superconducting resonator. In this thesis, the device design, the device fabrication and the measurement setup have been developed (Chap. 6). Many tests were performed to evolve the qubit fabrication.

The experimental demonstration of electric dipole coupling has been hindered by fabrication issues such as leakage between the gates and the Ohmic contacts and ESD. The former issue is being addressed by improving the initial processing of the silicon wafer. The quality of the SiO_2 has to be improved to prevent the appearance of holes in the oxide which create leakage. The ESD is puzzling as it appears even when all gates are connected. More testing on how often, where and when exactly it happens, needs to be done.

Once the device fabrication issues have been resolved, the first measurements will include full control of the electron wave function with the donor top gate, separating the electron from the donor and measuring the hyperfine interaction with ESR. Next, we will implement gate control of the donor-dot tunnel coupling, and fine-tune the flip-flop qubit Hamiltonian parameters to enter the ideal regime where the spin is dispersively coupled to the charge. Finally, we will seek to observe and characterize the second-order clock transition for the flip-flop qubit frequency, as predicted by our theory.

For the cQED approach, we have tested the resonator design and found a total quality factor of $Q_{\text{tot}} \approx 1200$, which is dominated by the external coupling. We can induce a 2DEG beneath the qubit gates and bias the central conductor. On such a resonator device we observed coupling of the charge qubit to the resonator with $g_{\text{E}} \approx 2\,\text{MHz}$ (Chap. 7). However, due to strong charge fluctuations in the device, no spin control or strong coupling was achieved. The design of this device was very limited in terms of qubit control due to the small number of gates, imposed by the single layer etching technique. Thus, for future measurements we developed an aluminium-niobium hybrid device where the flip-flop Hamiltonian parameters can be optimized to achieve strong coupling between a spin in silicon and a photon [113], [166]. In this design, we can accommodate many gates in a two- or three-layer aluminium process, analogous to the direct flip-flop devices. These structures are currently under test.

9.3 Large scale silicon quantum computing

Ultimately, we need a large quantum computer with many interconnected qubits which performs quantum error correction. In this thesis, we have envisioned a clear pathway towards such a quantum computer using donor qubits in silicon (Chap. 5). Both the flip-flop and the nuclear qubit can be coupled in large arrays and be interconnected with superconducting resonators. While ours is a competitive approach to large scale quantum computing, alternative proposals using donors [72], [77], [78], silicon MOS quantum dots [110] and SiGe quantum dots [108] have been made.

While academic researchers work in the laboratory to build well-functioning, cleverly designed qubits, the silicon industry is preparing already for large scale qubit fabrication. Currently silicon wafers specifically for quantum computing are being developed by Intel [210], CEA-leti and IMEC. With competitive companies investing in silicon quantum computing and strongly cooperating with researchers, we can hope to see many more advances in large scale silicon fabrication geared towards quantum computing. Electronics companies are also developing compact

and capable control apparatuses such as AWGs and cold amplifiers to cater to the ever-growing quantum community.

Overall, both advances at the small scale for one- and two-qubit devices as well as new large scale technologies will improve qubit performance and interconnectability. In the end, it may be one specific idea that triggers a breakthrough and decides which qubit platform will be most successful. It is important to note though, that most technologies and discoveries made in the "quantum race" can be transferred between different platforms, especially within the family of silicon qubits. Hence, combining our efforts is the most likely pathway to success.

9.4 A personal viewpoint

While quantum computing in general, and silicon quantum computing specifically, has made large strides in the recent years, it is still uncertain when (and maybe even *if*) we will achieve to build a quantum computer. How it will be build is even more uncertain. Although at this point in time, it seems most likely that the first proof of quantum supremacy over classical computing will be accomplished with superconducting qubits - both IBM and Google are working on qubit processors with 50 [211] and 72 [15] qubits respectively which should be capable to outperform a classical computer [212]. Nevertheless, a million qubit quantum computer might be based on silicon as typical qubit unit cells are much smaller for spin qubits than superconducting qubits.

Overall, this research field still has no certainties, but that is one of the reasons it remains so exciting. Every year new interesting quantum effects are observed. The amount of control we exhibit over quantum properties on nanometric scales is staggering. New control technologies and fabrication techniques allow for ever cleaner, smaller devices and more precision. Even if a quantum computer never came to be, we will have learned physics of immeasurable value and advanced technology for many applications. However, I am a believer.

"Remember tonight... for it is the beginning of always."

Dante Alighieri

Appendix A

Hamiltonian calculations

A.1 Eigenvectors

For a general Hamiltonian of

$$H = \begin{pmatrix} -C & D \\ D & C \end{pmatrix} \tag{A.1}$$

we aim to find the eigenvectors

$$|e\rangle = \alpha_1 |1\rangle + \beta_1 |0\rangle = \begin{pmatrix} \alpha_1 \\ \beta_1 \end{pmatrix}, \tag{A.2a}$$

$$|g\rangle = \alpha_2 |1\rangle + \beta_2 |0\rangle = \begin{pmatrix} \alpha_2 \\ \beta_2 \end{pmatrix} \tag{A.2b}$$

in the basis of $|0\rangle = \begin{pmatrix} 0 \\ 1 \end{pmatrix}$ and $|1\rangle = \begin{pmatrix} 1 \\ 0 \end{pmatrix}$.

The eigenvectors are calculated by

$$\begin{pmatrix} -C - \lambda_{1,2} & D \\ D & C - \lambda_{1,2} \end{pmatrix} \cdot \begin{pmatrix} \alpha_{1,2} \\ \beta_{1,2} \end{pmatrix} = \begin{pmatrix} 0 \\ 0 \end{pmatrix}, \tag{A.3}$$

where $\lambda_{1,2}$ are the corresponding eigenvalues. We arrive at the set of linear equations

$$(-C - \lambda_{1,2})\, \alpha_{1,2} + D\beta_{1,2} = 0, \tag{A.4a}$$

$$\alpha_{1,2} D + (C - \lambda_{1,2})\, \beta_{1,2} = 0. \tag{A.4b}$$

Furthermore, the eigenstates need to be normalized which gives the normalization condition

$$\beta_{1,2} = \sqrt{1 - \alpha_{1,2}^2}. \tag{A.5}$$

We insert equation (A.5) into (A.4a), (A.4b) and get

$$\alpha_{1,2} = \frac{1}{\sqrt{1 + \frac{(C+\lambda_{1,2})^2}{D^2}}}, \tag{A.6}$$

$$\beta_{1,2} = \sqrt{1 - \frac{1}{1 + \frac{(C+\lambda_{1,2})^2}{D^2}}}. \tag{A.7}$$

With

$$\lambda_{1,2} = \pm\sqrt{C^2 + D^2} \tag{A.8}$$

follows

$$\begin{aligned}
\alpha_1 &= \frac{1}{\sqrt{\Phi^2+1}} = \beta_2 \equiv \beta, \\
\beta_1 &= \frac{\Phi}{\sqrt{1+\Phi^2}} \equiv \alpha, \\
\alpha_2 &= \frac{1}{\sqrt{1+\Theta^2}} = -\beta_1 = -\alpha, \\
\beta_2 &= \frac{\Theta}{\sqrt{1+\Theta^2}} = \beta,
\end{aligned} \tag{A.9}$$

where

$$\begin{aligned}
\Phi &= \frac{C+\sqrt{C^2+D^2}}{D}, \\
\Theta &= \frac{C-\sqrt{C^2+D^2}}{D}.
\end{aligned} \tag{A.10}$$

Thus, we find the eigenstates

$$|e\rangle = \beta\,|1\rangle + \alpha\,|0\rangle\,, \tag{A.11a}$$

$$|g\rangle = -\alpha\,|1\rangle + \beta\,|0\rangle\,. \tag{A.11b}$$

With $\cos(\arctan(x)) = \frac{1}{\sqrt{1+x^2}}$ and $\sin(\arctan(x)) = \frac{x}{\sqrt{1+x^2}}$ we can also express the eigenstates as

$$|e\rangle = \cos\eta\,|1\rangle + \sin\eta\,|0\rangle\,, \tag{A.12a}$$

$$|g\rangle = -\sin\eta\,|1\rangle + \cos\eta\,|0\rangle\,. \tag{A.12b}$$

with $\tan\eta = \Phi$.

Bibliography

[1] G. Ifrah, *The Universal History of Computing: From the Abacus to the Quantum Computer*. Wiley, 2002.

[2] G. E. Moore, "Cramming more components onto integrated circuits", *IEEE Solid-State Circuits Society Newsletter*, vol. 11, no. 3, pp. 33–35, 2006, Reprinted from Electronics, volume 38, number 8, April 19, 1965, pp.114 ff.

[3] B.-K. Kim, *Internationalizing the internet: The Co-evolution of influence and technology*. Edward Elgar Pub, 2005.

[4] J. Preskill, "Quantum computing and the entanglement frontier", 2012. arXiv: 1203.5813.

[5] F. Jensen, *Introduction to Computational Chemistry*. 2007.

[6] A. Aspuru-Guzik, A. D. Dutoi, P. J. Love, and M. Head-Gordon, "Simulated quantum computation of molecular energies", *Science*, vol. 309, no. 5741, pp. 1704–1707, 2005.

[7] R. P. Feynman, "Simulating physics with computers", *International Journal of Theoretical Physics*, vol. 21, pp. 467–488, 1982.

[8] C. Cohen-Tannoudji, B. Diu, and F. Laloe, *Quantum Mechanics*. Wiley, 1991.

[9] S. Lloyd, "Universal quantum simulators", *Science*, vol. 273, no. 5278, pp. 1073–1078, 1996.

[10] C. Hempel, C. Maier, J. Romero, J. McClean, T. Monz, H. Shen, P. Jurcevic, B. P. Lanyon, P. Love, R. Babbush, A. Aspuru-Guzik, R. Blatt, and C. F. Roos, "Quantum chemistry calculations on a trapped-ion quantum simulator", *Phys. Rev. X*, vol. 8, p. 031 022, 2018.

[11] I. M. Georgescu, S. Ashhab, and F. Nori, "Quantum simulation", *Rev. Mod. Phys.*, vol. 86, pp. 153–185, 2014.

[12] P. J. Coles, S. Eidenbenz, S. Pakin, A. Adedoyin, J. Ambrosiano, P. Anisimov, G. Chennupati, C. Coffrin, H. Djidjev, D. Gunter, S. Karra, N. Lemons, A. Lokhov, A. Malyzhenkov, D. Mascarenas, S. Mniszewski, B. Nadiga, O Malley, D. Oyen, L. Prasad, R. Roberts, P. Romero, N. Santhi, P. Swart, M. Vuffray, J. Wendelberger, B. Yoon, R. Zamora, and W. Zhu, "Quantum Algorithm Implementations for Beginners", 2018. arXiv: 1804.03719v1.

[13] T. D. Ladd, F. Jelezko, R. Laflamme, Y. Nakamura, C. Monroe, and J. L. O'Brien, "Quantum computers", *Nature*, vol. 464, pp. 45–53, 2010.

[14] J. Zhang, G. Pagano, P. W. Hess, A. Kyprianidis, P. Becker, H. Kaplan, A. V. Gorshkov, Z. X. Gong, and C. Monroe, "Observation of a many-body dynamical phase transition with a 53-qubit quantum simulator", *Nature*, vol. 551, no. 7682, pp. 601–604, 2017.

[15] J. Kelly, "A Preview of Bristlecone, Google's New Quantum Processor", 2018.

[16] J. M. Gambetta, J. M. Chow, and M. Steffen, "Building logical qubits in a superconducting quantum computing system", *npj Quantum Information*, vol. 3, no. 2, 2017.

[17] F. A. Zwanenburg, A. S. Dzurak, A. Morello, M. Y. Simmons, L. C. L. Hollenberg, G. Klimeck, S. Rogge, S. N. Coppersmith, and M. A. Eriksson, "Silicon quantum electronics", *Rev. Mod. Phys.*, vol. 85, pp. 961–1019, 2013.

[18] D. Loss and D. P. DiVincenzo, "Quantum computation with quantum dots", *Phys. Rev. A*, vol. 57, pp. 120–126, 1998.

[19] J. Elzerman, R. Hanson, L. W. Van Beveren, B. Witkamp, L. Vandersypen, and L. P. Kouwenhoven, "Single-shot read-out of an individual electron spin in a quantum dot", *nature*, vol. 430, no. 6998, p. 431, 2004.

[20] F. H. L. Koppens, C. Buizert, K. J. Tielrooij, I. T. Vink, K. C. Nowack, T. Meunier, L. P. Kouwenhoven, and L. M. K. Vandersypen, "Driven coherent oscillations of a single electron spin in a quantum dot." *Nature*, vol. 442, no. August, pp. 766–771, 2006.

[21] P. Cerfontaine, T. Botzem, S. Humpohl, D. Schuh, D. Bougeard, and H. Bluhm, "Feedback-tuned noise-resilient gates for encoded spin qubits", 2014. arXiv: 1606.01897.

[22] B. E. Kane, "A silicon-based nuclear spin quantum computer", *Nature*, vol. 393, no. 6681, p. 133, 1998.

[23] C. B. Simmons, M. Thalakulam, N. Shaji, L. J. Klein, H. Qin, R. H. Blick, D. E. Savage, M. G. Lagally, S. N. Coppersmith, and M. A. Eriksson, "Single-electron quantum dot in Si/SiGe with integrated charge sensing", *Applied Physics Letters*, vol. 91, no. 21, p. 213 103, 2007.

[24] A. Morello, J. J. Pla, F. A. Zwanenburg, K. W. Chan, K. Y. Tan, H. Huebl, M. Möttönen, C. D. Nugroho, C. Yang, J. A. Van Donkelaar, A. D. Alves, D. N. Jamieson, C. C. Escott, L. C. Hollenberg, R. G. Clark, and A. S. Dzurak, "Single-shot readout of an electron spin in silicon", *Nature*, vol. 467, no. 7316, pp. 687–691, 2010.

[25] M. Veldhorst, J. C. C. Hwang, C. H. Yang, A. W. Leenstra, B. De Ronde, J. P. Dehollain, J. T. Muhonen, F. E. Hudson, K. M. Itoh, A. Morello, and A. S. Dzurak, "An addressable quantum dot qubit with fault-tolerant control- fi delity", *Nature Nanotechnology*, vol. 9, pp. 981–985, 2014.

[26] W. Huang, C. H. Yang, K. W. Chan, T. Tanttu, B. Hensen, R. C. C. Leon, M. A. Fogarty, J. C. C. Hwang, F. E. Hudson, K. M. Itoh, A. Morello, A. Laucht, and A. S. Dzurak, "Fidelity benchmarks for two-qubit gates in silicon", 2018. arXiv: 1805.05027.

[27] E. Kawakami, P. Scarlino, D. R. Ward, F. R. Braakman, D. E. Savage, M. G. Lagally, M. Friesen, S. N. Coppersmith, M. A. Eriksson, and L. M. Vandersypen, "Electrical control of a long-lived spin qubit in a Si/SiGe quantum dot", *Nature Nanotechnology*, vol. 9, pp. 666–670, 2014.

[28] R. Maurand, X. Jehl, D. Kotekar-Patil, A. Corna, H. Bohuslavskyi, R. Laviéville, L. Hutin, S. Barraud, M. Vinet, M. Sanquer, and S. De Franceschi, "A CMOS silicon spin qubit", *Nature Communications*, vol. 7, pp. 3–8, 2016.

[29] T. F. Watson, S. G. Philips, E. Kawakami, D. R. Ward, P. Scarlino, M. Veldhorst, D. E. Savage, M. G. Lagally, M. Friesen, S. N. Coppersmith, M. A. Eriksson, and L. M. Vandersypen, "A programmable two-qubit quantum processor in silicon", *Nature*, vol. 555, pp. 633–637, 2018.

[30] J. T. Muhonen, J. P. Dehollain, A. Laucht, F. E. Hudson, R. Kalra, T. Sekiguchi, K. M. Itoh, D. N. Jamieson, J. C. McCallum, A. S. Dzurak, and A. Morello, "Storing quantum information for 30 seconds in a nanoelectronic device", *Nature Nanotechnology*, vol. 9, no. 12, pp. 986–991, 2014.

[31] F. Borjans, D. M. Zajac, T. M. Hazard, and J. R. Petta, "Single-Spin Relaxation in a Synthetic Spin-Orbit Field", 2018. arXiv: `1811.00848v1`.

[32] A. Hollman and L. Schreiber, Non published data, Conference presentation, 2018.

[33] B. Weber, Y.-L. Hsueh, T. F. Watson, R. Li, A. R. Hamilton, L. C. L. Hollenberg, R. Rahman, and M. Y. Simmons, "Spin-orbit coupling in silicon for electrons bound to donors", *npj Quantum Information*, vol. 4, p. 61, 2018.

[34] D. P. DiVincenzo, "The physical implementation of quantum computation", *Fortschritte der Physik: Progress of Physics*, vol. 48, no. 9-11, pp. 771–783, 2000.

[35] T. Brown, H. Eugene LeMay Jr., B. Bursten, C. Murphy, P. Woodward, S. Langford, D. Sagatys, and A. Goeroge, *Chemistry: The Central Science*. Pearson Australia, 2018.

[36] W. Kohn and J. M. Luttinger, "Theory of donor states in silicon", *Phys. Rev.*, vol. 98, pp. 915–922, 1955.

[37] A. L. Saraiva, A. Baena, M. Calderón, and B. Koiller, "Theory of one and two donors in silicon", *Journal of Physics: Condensed Matter*, vol. 27, no. 15, p. 154 208, 2015.

[38] G. Lansbergen, R. Rahman, C. Wellard, I. Woo, J. Caro, N. Collaert, S. Biesemans, G. Klimeck, L. Hollenberg, and S. Rogge, "Gate-induced quantum-confinement transition of a single dopant atom in a silicon finfet", *Nature Physics*, vol. 4, no. 8, p. 656, 2008.

[39] R. Rahman, C. J. Wellard, F. R. Bradbury, M. Prada, J. H. Cole, G. Klimeck, and L. C. L. Hollenberg, "High precision quantum control of single donor spins in silicon", *Phys. Rev. Lett.*, vol. 99, p. 036 403, 2007.

[40] J. J. Pla, K. Y. Tan, J. P. Dehollain, W. H. Lim, J. J. L. Morton, D. N. Jamieson, A. S. Dzurak, and A. Morello, "A single-atom electron spin qubit in silicon", *Nature*, vol. 489, no. 7417, pp. 541–544, 2012.

[41] J. J. Pla, K. Y. Tan, J. P. Dehollain, W. H. Lim, J. J. L. Morton, F. Zwanenburg, D. N. Jamieson, A. S. Dzurak, and A. Morello, "High-fidelity readout and control of a nuclear spin qubit in silicon." *Nature*, vol. 496, no. 7445, pp. 334–8, 2013.

[42] J. P. Dehollain, J. T. Muhonen, R. Blume-Kohout, K. M. Rudinger, J. K. Gamble, E. Nielsen, A. Laucht, S. Simmons, R. Kalra, and A. S. Dzurak, "Optimization of a solid-state electron spin qubit using gate set tomography", *New Journal of Physics*, vol. 18, no. 10, p. 103 018, 2016.

[43] A. Morello, C. C. Escott, H. Huebl, L. H. Willems van Beveren, L. C. L. Hollenberg, D. N. Jamieson, A. S. Dzurak, and R. G. Clark, "Architecture for high-sensitivity single-shot readout and control of the electron spin of individual donors in silicon", *Phys. Rev. B*, vol. 80, p. 081 307, 2009.

[44] Y. V. Nazarov and Y. M. Blanter, *Quantum Transport*. Cambridge University Press, 2009.

[45] M. A. Ali Ahmed, G. A. Álvarez, and D. Suter, "Robustness of dynamical decoupling sequences", *Phys. Rev. A*, vol. 87, p. 042 309, 2013.

[46] R. Kalra, "The building blocks of a quantum computer based on donor spins in silicon", Ph.D. thesis, University of New South Wales, Australia, 2016.

[47] T. F. Watson, B. Weber, Y.-L. Hsueh, L. C. L. Hollenberg, R. Rahman, and M. Y. Simmons, "Atomically engineered electron spin lifetimes of 30s in silicon", *Science Advances*, vol. 3, no. 3, 2017.

[48] R. Loudon, *The Quantum Theory of Light*. Oxford University Press, 2000.

[49] C. Gerry and P. Knight, *Introductory Quantum Optics*. Cambridge University Press, 2005.

[50] A. Bienfait, "Magnetic Resonance with Quantum Microwaves", Ph.D. thesis, University of Paris-Saclay, France, 2016.

[51] M. H. Devoret, "Quantum fluctuations in electrical circuits", Quantum Fluctuations: Les Houches Session LXIII, June 27 - July 28, 1995, Elsevier Science B.V., 1995.

[52] K. Kurokawa, "Power waves and the scattering matrix", *IEEE Transactions on Microwave Theory and Techniques*, vol. 13, no. 2, pp. 194–202, 1965.

[53] C. W. Gardiner and M. J. Collett, "Input and output in damped quantum systems: Quantum stochastic differential equations and the master equation", *Phys. Rev. A*, vol. 31, pp. 3761–3774, 1985.

[54] A. Blais, R.-S. Huang, A. Wallraff, S. M. Girvin, and R. J. Schoelkopf, "Cavity quantum electrodynamics for superconducting electrical circuits: An architecture for quantum computation", *Phys. Rev. A*, vol. 69, p. 062 320, 2004.

[55] B. M. Terhal, "Quantum error correction for quantum memories", *Rev. Mod. Phys.*, vol. 87, pp. 307–346, 2015.

[56] A. G. Fowler, M. Mariantoni, J. M. Martinis, and A. N. Cleland, "Surface codes: Towards practical large-scale quantum computation", *Phys. Rev. A*, vol. 86, p. 032 324, 2012.

[57] A. M. Stephens, "Fault-tolerant thresholds for quantum error correction with the surface code", *Phys. Rev. A*, vol. 89, p. 022 321, 2014.

[58] E Knill, "Quantum computing with realistically noisy devices", *Nature*, vol. 434, no. 7029, pp. 39–44, 2005.

[59] N. H. Nickerson, Y. Li, and S. C. Benjamin, "Topological quantum computing with a very noisy network and local error rates approaching one percent", *Nature communications*, vol. 4, p. 1756, 2013.

[60] K. Saeedi, S. Simmons, J. Z. Salvail, P. Dluhy, H. Riemann, N. V. Abrosimov, P. Becker, H.-J. Pohl, J. J. L. Morton, and M. L. W. Thewalt, "Room-temperature quantum bit storage exceeding 39 minutes using ionized donors in silicon-28", *Science*, vol. 342, no. 6160, pp. 830–833, 2013.

[61] J. Yoneda, K. Takeda, T. Otsuka, T. Nakajima, M. R. Delbecq, G. Allison, T. Honda, T. Kodera, S. Oda, Y. Hoshi, N. Usami, K. M. Itoh, and S. Tarucha, "A quantum-dot spin qubit with coherence limited by charge noise and fidelity higher than 99.9 %", *Nature Nanotechnology*, vol. 13, no. February, pp. 102–106, 2018.

[62] X. Xue, T. F. Watson, J. Helsen, D. R. Ward, D. E. Savage, M. G. Lagally, S. N. Coppersmith, M. A. Eriksson, S Wehner, and L. M. K. Vandersypen, "Benchmarking Gate Fidelities in a Si/SiGe Two-Qubit Device", 2018. arXiv: 1811.04002v1.

[63] S. Gorman and M. Simmons, Non published data, Conference presentation, 2018.

[64] D. M. Zajac, A. J. Sigillito, M. Russ, F. Borjans, J. M. Taylor, G. Burkard, and J. R. Petta, "Resonantly driven cnot gate for electron spins", *Science*, 2018.

[65] K. M. Itoh, "Isotope engineering of silicon and diamond for quantum computing and sensing applications", *MRS Communications*, vol. 4, pp. 143–157, 2014.

[66] B. Koiller, X. Hu, and S. Das Sarma, "Exchange in silicon-based quantum computer architecture", *Phys. Rev. Lett.*, vol. 88, p. 027 903, 2001.

[67] Y. Song and S Das Sarma, "Statistical exchange-coupling errors and the practicality of scalable silicon donor qubits", *Applied Physics Letters*, vol. 109, no. 25, p. 253 113, 2016.

[68] J. P. Dehollain, J. T. Muhonen, K. Y. Tan, A. Saraiva, D. N. Jamieson, A. S. Dzurak, and A. Morello, "Single-Shot Readout and Relaxation of Singlet and Triplet States in Exchange-Coupled 31P Electron Spins in Silicon", *Phys. Rev. Lett.*, vol. 112, p. 236 801, 2014.

[69] M. F. Gonzalez-Zalba, A. Saraiva, M. J. Calderón, D. Heiss, B. Koiller, and A. J. Ferguson, "An exchange-coupled donor molecule in silicon", *Nano letters*, vol. 14, no. 10, pp. 5672–5676, 2014.

[70] B. Weber, Y. H. Tan, S. Mahapatra, T. F. Watson, H. Ryu, R. Rahman, L. C. Hollenberg, G. Klimeck, and M. Y. Simmons, "Spin blockade and exchange in Coulomb-confined silicon double quantum dots", *Nature Nanotechnology*, vol. 9, pp. 430–435, 2014.

[71] R. Kalra, A. Laucht, C. D. Hill, and A. Morello, "Robust two-qubit gates for donors in silicon controlled by hyperfine interactions", *Phys. Rev. X*, vol. 4, p. 021 044, 2014.

[72] C. D. Hill, E. Peretz, S. J. Hile, M. G. House, M. Fuechsle, S. Rogge, M. Y. Simmons, and L. C. L. Hollenberg, "A surface code quantum computer in silicon", *Science Advances*, vol. 1, no. 9, 2015.

[73] L. C. L. Hollenberg, A. D. Greentree, A. G. Fowler, and C. J. Wellard, "Two-dimensional architectures for donor-based quantum computing", *Phys. Rev. B*, vol. 74, p. 045 311, 2006.

[74] F. A. Mohiyaddin, R. Kalra, A. Laucht, R. Rahman, G. Klimeck, and A. Morello, "Transport of spin qubits with donor chains under realistic experimental conditions", *Phys. Rev. B*, vol. 94, p. 045 314, 2016.

[75] J. J. Morton, "A silicon-based cluster state quantum computer", 2009. arXiv: 0905.4008v1.

[76] L. Trifunovic, F. L. Pedrocchi, and D. Loss, "Long-distance entanglement of spin qubits via ferromagnet", *Phys. Rev. X*, vol. 3, p. 041 023, 2013.

[77] J. O'Gorman, N. H. Nickerson, P. Ross, J. J. Morton, and S. C. Benjamin, "A silicon-based surface code quantum computer", *npj Quantum Information*, vol. 2, p. 15 019, 2016.

[78] G. Pica, B. W. Lovett, R. N. Bhatt, T. Schenkel, and S. A. Lyon, "Surface code architecture for donors and dots in silicon with imprecise and nonuniform qubit couplings", *Phys. Rev. B*, vol. 93, p. 035 306, 2016.

[79] R. Rahman, G. P. Lansbergen, S. H. Park, J. Verduijn, G. Klimeck, S. Rogge, and L. C. L. Hollenberg, "Orbital stark effect and quantum confinement transition of donors in silicon", *Phys. Rev. B*, vol. 80, p. 165 314, 2009.

[80] M. J. Calderón, A. Saraiva, B. Koiller, and S. Das Sarma, "Quantum control and manipulation of donor electrons in si-based quantum computing", *Journal of Applied physics*, vol. 105, no. 12, p. 122 410, 2009.

[81] G. Klimeck, S. S. Ahmed, H. Bae, N. Kharche, S. Clark, B. Haley, S. Lee, M. Naumov, H. Ryu, F. Saied, M. Prada, M. Korkusinski, T. B. Boykin, and R. Rahman, "Atomistic Simulation of Realistically Sized Nanodevices Using NEMO 3-D—Part I: Models and Benchmarks", *IEEE Transactions on Electron Devices*, vol. 54, no. 9, pp. 2079–2089, 2007.

[82] G. Klimeck, S. S. Ahmed, N. Kharche, M. Korkusinski, M. Usman, M. Prada, and T. B. Boykin, "Atomistic Simulation of Realistically Sized Nanodevices Using NEMO 3-D—Part II: Applications", *IEEE Transactions on Electron Devices*, vol. 54, no. 9, pp. 2090–2099, 2007.

[83] P. Harvey-Collard, N. T. Jacobson, M. Rudolph, J. Dominguez, G. A. Ten Eyck, J. R. Wendt, T. Pluym, J. K. Gamble, M. P. Lilly, M. Pioro-Ladrière, and M. S. Carroll, "Coherent coupling between a quantum dot and a donor in silicon", *Nature Communications*, vol. 8, no. 1029, 2017.

[84] G. Feher, "Electron spin resonance experiments on donors in silicon. i. electronic structure of donors by the electron nuclear double resonance technique", *Phys. Rev.*, vol. 114, pp. 1219–1244, 1959.

[85] S. J. Hile, L. Fricke, M. G. House, E. Peretz, C. Y. Chen, Y. Wang, M. Broome, S. K. Gorman, J. G. Keizer, R. Rahman, and M. Y. Simmons, "Addressable electron spin resonance using donors and donor molecules in silicon", *Science Advances*, vol. 4, no. 7, 2018.

[86] J. L. Ivey and R. L. Mieher, "Ground-state wave function for shallow-donor electrons in silicon. ii. anisotropic electron-nuclear-double-resonance hyperfine interactions", *Phys. Rev. B*, vol. 11, pp. 849–857, 1975.

[87] P. Boross, G. Széchenyi, and A. Pályi, "Valley-enhanced fast relaxation of gate-controlled donor qubits in silicon", *Nanotechnology*, vol. 27, p. 314 002, 2016.

[88] J. Van Donkelaar, C. Yang, A. Alves, J. McCallum, C. Hougaard, B. Johnson, F. Hudson, A. Dzurak, A. Morello, and D. Spemann, "Single atom devices by ion implantation", *Journal of Physics: Condensed Matter*, vol. 27, p. 154 204, 2015.

[89] M. Garwood and L. DelaBarre, "The return of the frequency sweep: Designing adiabatic pulses for contemporary NMR", *Journal of Magnetic Resonance*, vol. 153, no. 2, pp. 155–177, 2001.

[90] G. Wolfowicz, A. M. Tyryshkin, R. E. George, H. Riemann, N. V. Abrosimov, P. Becker, H.-j. Pohl, M. L. W. Thewalt, S. A. Lyon, and J. J. L. Morton, "Atomic clock transitions in silicon-based spin qubits", *Nature Nanotechnology*, vol. 8, pp. 561–564, 2013.

[91] C. Chicone, *Ordinary Differential Equations with Applications*. Springer, 2006.

[92] L. Gammaitoni, P. Hänggi, P. Jung, and F. Marchesoni, "Stochastic resonance", *Rev. Mod. Phys.*, vol. 70, pp. 223–287, 1998.

[93] S. Oh, Y.-P. Shim, J. Fei, M. Friesen, and X. Hu, "Resonant adiabatic passage with three qubits", *Phys. Rev. A*, vol. 87, p. 022 332, 2013.

[94] B. C. Johnson, J. C. Mccallum, L. H. W. V. Beveren, and E. Gauja, "Deep level transient spectroscopy study for the development of ion-implanted silicon fi eld-effect transistors for spin-dependent transport", *Thin Solid Films*, vol. 518, no. 9, pp. 2524–2527, 2010.

[95] E. Paladino, Y. M. Galperin, G. Falci, and B. L. Altshuler, "1/f noise: Implications for solid-state quantum information", *Rev. Mod. Phys.*, vol. 86, pp. 361–418, 2014.

[96] D. Kim, D. Ward, C. Simmons, J. K. Gamble, R. Blume-Kohout, E. Nielsen, D. Savage, M. Lagally, M. Friesen, and S. Coppersmith, "Microwave-driven coherent operation of a semiconductor quantum dot charge qubit", *Nature nanotechnology*, vol. 10, no. 3, p. 243, 2015.

[97] B. Thorgrimsson, D. Kim, Y.-C. Yang, L. Smith, C. Simmons, D. R. Ward, R. H. Foote, J. Corrigan, D. Savage, and M. Lagally, "Extending the coherence of a quantum dot hybrid qubit", *npj Quantum Information*, vol. 3, no. 1, p. 32, 2017.

[98] B. M. Freeman, J. S. Schoenfield, and H. Jiang, "Comparison of low frequency charge noise in identically patterned Si/SiO2 and Si/SiGe quantum dots", *Applied Physics Letters*, vol. 108, no. 253108, 2016.

[99] O. E. Dial, M. D. Shulman, S. P. Harvey, H. Bluhm, V. Umansky, and A. Yacoby, "Charge noise spectroscopy using coherent exchange oscillations in a singlet-triplet qubit", *Phys. Rev. Lett.*, vol. 110, p. 146 804, 2013.

[100] C. Henkel, S. Pötting, and M. Wilkens, "Loss and heating of particles in small and noisy traps", *Applied Physics B*, vol. 69, no. 5-6, pp. 379–387, 1999.

[101] A. Poudel, L. S. Langsjoen, M. G. Vavilov, and R. Joynt, "Relaxation in quantum dots due to evanescent-wave johnson noise", *Phys. Rev. B*, vol. 87, p. 045 301, 2013.

[102] J. Bylander, S. Gustavsson, F. Yan, F. Yoshihara, K. Harrabi, G. Fitch, D. G. Cory, Y. Nakamura, J.-S. Tsai, and W. D. Oliver, "Noise spectroscopy through dynamical decoupling with a superconducting flux qubit", *Nature Physics*, vol. 7, no. 7, p. 565, 2011.

[103] O. Astafiev, Y. A. Pashkin, Y. Nakamura, T. Yamamoto, and J. S. Tsai, "Quantum noise in the josephson charge qubit", *Phys. Rev. Lett.*, vol. 93, p. 267 007, 2004.

[104] A. Shnirman, G. Schön, I. Martin, and Y. Makhlin, "Low- and high-frequency noise from coherent two-level systems", *Phys. Rev. Lett.*, vol. 94, p. 127 002, 2005.

[105] A. Laucht, R. Kalra, S. Simmons, J. P. Dehollain, J. T. Muhonen, F. A. Mohiyaddin, S. Freer, F. E. Hudson, K. M. Itoh, D. N. Jamieson, J. C. Mccallum, A. S. Dzurak, and A. Morello, "A dressed spin qubit in silicon", *Nature Nanotechnology*, vol. 12, pp. 61–66, 2016.

[106] F. Yan, S. Gustavsson, J. Bylander, X. Jin, F. Yoshihara, D. G. Cory, Y. Nakamura, T. P. Orlando, and W. D. Oliver, "Rotating-frame relaxation as a noise spectrum analyser of a superconducting qubit undergoing driven evolution", *Nature Communications*, vol. 4, p. 2337, 2013.

[107] S. Ravets, H. Labuhn, D. Barredo, L. Béguin, T. Lahaye, and A. Browaeys, "Coherent dipole–dipole coupling between two single rydberg atoms at an electrically-tuned förster resonance", *Nature Physics*, vol. 10, p. 12, 2014.

[108] R. Li, L. Petit, D. P. Franke, J. P. Dehollain, J. Helsen, M. Steudtner, N. K. Thomas, Z. R. Yoscovits, K. J. Singh, S. Wehner, L. M. K. Vandersypen, J. S. Clarke, and M. Veldhorst, "A crossbar network for silicon quantum dot qubits", *Science Advances*, vol. 4, no. 7, 2018.

[109] L. M. K. Vandersypen, H. Bluhm, J. S. Clarke, A. S. Dzurak, R. Ishihara, A. Morello, D. J. Reilly, L. R. Schreiber, and M. Veldhorst, "Interfacing spin qubits in quantum dots and donors - hot, dense and coherent", *npj Quantum Information*, vol. 3, no. 34, 2016.

[110] M. Veldhorst, H. G. Eenink, C. H. Yang, and A. S. Dzurak, "Silicon CMOS architecture for a spin-based quantum computer", *Nature Communications*, vol. 8, no. 1766, 2017.

[111] L. Childress, A. S. Sørensen, and M. D. Lukin, "Mesoscopic cavity quantum electrodynamics with quantum dots", *Phys. Rev. A*, vol. 69, p. 042 302, 2004.

[112] Z.-L. Xiang, S. Ashhab, J. Q. You, and F. Nori, "Hybrid quantum circuits: Superconducting circuits interacting with other quantum systems", *Rev. Mod. Phys.*, vol. 85, pp. 623–653, 2013.

[113] X. Mi, J. V. Cady, D. M. Zajac, P. W. Deelman, and J. R. Petta, "Strong coupling of a single electron in silicon to a microwave photon", *Science*, vol. 355, no. 6321, pp. 156–158, 2017.

[114] G. Tosi, F. A. Mohiyaddin, H. Huebl, and A. Morello, "Circuit-quantum electrodynamics with direct magnetic coupling to single-atom spin qubits in isotopically enriched 28si", *AIP Advances*, vol. 4, no. 8, p. 087 122, 2014.

[115] P. Haikka, Y. Kubo, A. Bienfait, P. Bertet, and K. Mølmer, "Proposal for detecting a single electron spin in a microwave resonator", *Phys. Rev. A*, vol. 95, p. 022 306, 2017.

[116] X. Hu, Y.-x. Liu, and F. Nori, "Strong coupling of a spin qubit to a superconducting stripline cavity", *Phys. Rev. B*, vol. 86, p. 035 314, 2012.

[117] J. J. Viennot, M. C. Dartiailh, A. Cottet, and T. Kontos, "Coherent coupling of a single spin to microwave cavity photons", *Science*, vol. 349, no. 6246, pp. 408–411, 2015.

[118] N. Samkharadze, A. Bruno, P. Scarlino, G. Zheng, D. P. DiVincenzo, L. DiCarlo, and L. M. K. Vandersypen, "High-kinetic-inductance superconducting nanowire resonators for circuit qed in a magnetic field", *Phys. Rev. Applied*, vol. 5, p. 044 004, 2016.

[119] M. Castellanos-Beltran, K. Irwin, G. Hilton, L. Vale, and K. Lehnert, "Amplification and squeezing of quantum noise with a tunable josephson metamaterial", *Nature Physics*, vol. 4, no. 12, p. 929, 2008.

[120] R. Barends, J. Kelly, A. Megrant, A. Veitia, D. Sank, E. Jeffrey, T. C. White, J. Mutus, A. G. Fowler, B. Campbell, Y. Chen, Z. Chen, B. Chiaro, A. Dunsworth, C. Neill, P. O'Malley, P. Roushan, A. Vainsencher, J. Wenner, A. N. Korotkov, A. N. Cleland, and J. M. Martinis, "Superconducting quantum circuits at the surface code threshold for fault tolerance", *Nature*, vol. 508, no. 7497, pp. 500–503, 2014.

[121] M. H. Devoret and R. J. Schoelkopf, "Superconducting circuits for quantum information: An outlook", *Science*, vol. 339, no. 6124, pp. 1169–1174, 2013.

[122] F. Motzoi, J. M. Gambetta, P. Rebentrost, and F. K. Wilhelm, "Simple pulses for elimination of leakage in weakly nonlinear qubits", *Phys. Rev. Lett.*, vol. 103, p. 110 501, 2009.

[123] J. Ghosh, S. N. Coppersmith, and M. Friesen, "Pulse sequences for suppressing leakage in single-qubit gate operations", *Phys. Rev. B*, vol. 95, p. 241 307, 2017.

[124] J. Werschnik and E. K. U. Gross, "Quantum Optimal Control Theory", *J. Phys. B: At. Mol. Opt. Phys.*, vol. 40, no. R175, 2007.

[125] C. D. Hill, "Robust controlled-not gates from almost any interaction", *Phys. Rev. Lett.*, vol. 98, p. 180 501, 2007.

[126] T. Van der Sar, Z. Wang, M. Blok, H. Bernien, T. Taminiau, D. Toyli, D. Lidar, D. Awschalom, R. Hanson, and V. Dobrovitski, "Decoherence-protected quantum gates for a hybrid solid-state spin register", *Nature*, vol. 484, no. 7392, p. 82, 2012.

[127] J. J. Morton, A. M. Tyryshkin, R. M. Brown, S. Shankar, B. W. Lovett, A. Ardavan, T. Schenkel, E. E. Haller, J. W. Ager, and S. Lyon, "Solid-state quantum memory using the 31 p nuclear spin", *Nature*, vol. 455, no. 7216, p. 1085, 2008.

[128] S. Freer, S. Simmons, A. Laucht, J. T. Muhonen, J. P. Dehollain, R. Kalra, F. A. Mohiyaddin, F. E. Hudson, K. M. Itoh, J. C. Mccallum, D. N. Jamieson, A. S. Dzurak, and A. Morello, "A single-atom quantum memory in silicon", *Quantum Science and Technology*, vol. 2, no. 1, p. 015 009, 2017.

[129] M. Jenkins, D. Zueco, O. Roubeau, G. Aromí, J. Majer, and F. Luis, "A scalable architecture for quantum computation with molecular nanomagnets", *Dalton Transactions*, vol. 45, no. 42, 2016.

[130] B. Sarabi, P. Huang, and N. M. Zimmerman, "Possible hundredfold enhancement in the direct magnetic coupling of a single atomic spin to a circuit resonator", 2018. arXiv: `1702.02210v3`.

[131] M. Pioro-Ladriere, T. Obata, Y. Tokura, Y.-S. Shin, T. Kubo, K Yoshida, T. Taniyama, and S. Tarucha, "Electrically driven single-electron spin resonance in a slanting zeeman field", *Nature Physics*, vol. 4, no. 10, p. 776, 2008.

[132] Z. Shi, C. B. Simmons, J. R. Prance, J. K. Gamble, T. S. Koh, Y.-P. Shim, X. Hu, D. E. Savage, M. G. Lagally, M. A. Eriksson, M. Friesen, and S. N. Coppersmith, "Fast hybrid silicon double-quantum-dot qubit", *Phys. Rev. Lett.*, vol. 108, p. 140 503, 2012.

[133] M. Russ and G. Burkard, "Three-electron spin qubits", *Journal of Physics: Condensed Matter*, vol. 29, no. 39, p. 393 001, 2017.

[134] J. Salfi, J. A. Mol, D. Culcer, and S. Rogge, "Charge-insensitive single-atom spin-orbit qubit in silicon", *Phys. Rev. Lett.*, vol. 116, p. 246 801, 2016.

[135] J. Bateman, A. Xuereb, and T. Freegarde, "Stimulated raman transitions via multiple atomic levels", *Phys. Rev. A*, vol. 81, p. 043 808, 2010.

[136] P. Kok and B. Lovett, *Introduction to Optical Quantum Information Processing*. Cambridge University Press, 2010.

[137] J. J. Bollinger, J. D. Prestage, W. M. Itano, and D. J. Wineland, "Laser-cooled-atomic frequency standard", *Phys. Rev. Lett.*, vol. 54, pp. 1000–1003, 1985.

[138] A. J. Sigillito, A. M. Tyryshkin, T. Schenkel, A. A. Houck, and S. A. Lyon, "Electrically driving nuclear spin qubits with microwave photonic bangap resonators", 2017. arXiv: 1701.06650v1.

[139] P. London, J. Scheuer, J.-M. Cai, I. Schwarz, A. Retzker, M. B. Plenio, M. Katagiri, T. Teraji, S. Koizumi, J. Isoya, R. Fischer, L. P. McGuinness, B. Naydenov, and F. Jelezko, "Detecting and polarizing nuclear spins with double resonance on a single electron spin", *Phys. Rev. Lett.*, vol. 111, p. 067 601, 2013.

[140] A. Laucht, S. Simmons, R. Kalra, G. Tosi, J. P. Dehollain, J. T. Muhonen, S. Freer, F. E. Hudson, K. M. Itoh, D. N. Jamieson, J. C. McCallum, A. S. Dzurak, and A. Morello, "Breaking the rotating wave approximation for a strongly driven dressed single-electron spin", *Phys. Rev. B*, vol. 94, p. 161 302, 2016.

[141] J. Pachos and H. Walther, "Quantum computation with trapped ions in an optical cavity", *Phys. Rev. Lett.*, vol. 89, p. 187 903, 2002.

[142] Z.-B. Feng, "Coupling charge qubits via raman transitions in circuit qed", *Phys. Rev. A*, vol. 78, p. 032 325, 2008.

[143] M. Abanto, L. Davidovich, B. Koiller, and R. L. de Matos Filho, "Quantum computation with doped silicon cavities", *Phys. Rev. B*, vol. 81, p. 085 325, 2010.

[144] A. Angerer, T. Astner, D. Wirtitsch, H. Sumiya, S. Onoda, J. Isoya, S. Putz, and J. Majer, "Collective strong coupling with homogeneous rabi frequencies using a 3d lumped element microwave resonator", *Applied Physics Letters*, vol. 109, no. 3, p. 033 508, 2016.

[145] K. Fischer, M. Agostinelli, C. Allen, D. Bahr, M. Bost, P. Charvat, V. Chikarmane, Q. Fu, C. Ganpule, and M. Haran, "Low-k interconnect stack with multi-layer air gap and tri-metal-insulator-metal capacitors for 14nm high volume manufacturing", *IEEEexplore*, vol. 7325600, 2015.

[146] D. P. Franke, J. S. Clarke, and M. Veldhorst, "Rent's rule and extensibility in quantum computing", 2018. arXiv: 1806.02145v1.

[147] M. A. Nielsen and I. L. Chuang, *Quantum computation and quantum information*. Cambridge University Press, 2000.

[148] S. J. Devitt, W. J. Munro, and K. Nemoto, "Quantum error correction for beginners", *Reports on Progress in Physics*, vol. 76, no. 7, p. 076 001, 2013.

[149] A. M. Steane, G. Casati, D. L. Shepelyansky, P. Zoller, and G. Benenti, "Quantum Computers, Algorithms and Chaos", vol. 32, pp. 1–32, 2006, Proceedings of the International School of Physics "Enrico Fermi", course CLXII.

[150] D. Gottesman, "Class of quantum error-correcting codes saturating the quantum hamming bound", *Phys. Rev. A*, vol. 54, pp. 1862–1868, 1996.

[151] D. M. Greenberger, M. A. Horne, A. Shimony, and A. Zeilinger, "Bell's theorem without inequalities", *American Journal of Physics*, vol. 58, pp. 1131–1143, 1990.

[152] H. J. Briegel and R. Raussendorf, "Persistent entanglement in arrays of interacting particles", *Phys. Rev. Lett.*, vol. 86, pp. 910–913, 2001.

[153] D. Bacon, "Operator quantum error-correcting subsystems for self-correcting quantum memories", *Phys. Rev. A*, vol. 73, p. 012 340, 2006.

[154] P. Aliferis and A. W. Cross, "Subsystem fault tolerance with the bacon-shor code", *Phys. Rev. Lett.*, vol. 98, p. 220 502, 2007.

[155] A. G. Fowler, C. D. Hill, and L. C. L. Hollenberg, "Quantum-error correction on linear-nearest-neighbor qubit arrays", *Phys. Rev. A*, vol. 69, p. 042 314, 2004.

[156] A. M. Stephens and Z. W. E. Evans, "Accuracy threshold for concatenated error detection in one dimension", *Phys. Rev. A*, vol. 80, p. 022 313, 2009.

[157] Y. Tomita and K. M. Svore, "Low-distance surface codes under realistic quantum noise", *Phys. Rev. A*, vol. 90, p. 062 320, 2014.

[158] C. Jones, M. A. Fogarty, A. Morello, M. F. Gyure, A. S. Dzurak, and T. D. Ladd, "Logical qubit in a linear array of semiconductor quantum dots", *Phys. Rev. X*, vol. 8, p. 021 058, 2018.

[159] P. W. Shor, "Scheme for reducing decoherence in quantum computer memory", *Phys. Rev. A*, vol. 52, R2493–R2496, 1995.

[160] E. Campbell, A. Khurana, and A. Montanaro, "Applying quantum algorithms to constraint satisfaction problems", 2018. eprint: `1810.05582`.

[161] Y. Li and S. C. Benjamin, "One-dimensional quantum computing with a 'segmented chain' is feasible with today's gate fidelities", *npj Quantum Information*, vol. 4, no. 1, p. 25, 2018.

[162] M. J. Curry, T. D. England, N. C. Bishop, G. Ten-Eyck, J. R. Wendt, T. Pluym, M. P. Lilly, S. M. Carr, and M. S. Carroll, "Cryogenic preamplification of a single-electron-transistor using a silicon-germanium heterojunction-bipolar-transistor", *Applied Physics Letters*, vol. 106, no. 203505, 2015.

[163] Jani Electronics, "Coplanar waveguide calculator", 2018.

[164] R. N. Simons, *Coplanar Waveguide Circuits, Components, and Systems*. Wiley, 2004, pp. 15–21.

[165] A. Palacios-Laloy, "Superconducting qubit in a resonator : test of the Leggett-Garg inequality and single-shot readout", Ph.D. thesis, University of Paris-Saclay, France, 2010.

[166] N. Samkharadze, G. Zheng, N. Kalhor, D. Brousse, A. Sammak, U. C. Mendes, A. Blais, G. Scappucci, and L. M. K. Vandersypen, "Strong spin-photon coupling in silicon", *Science*, 2018.

[167] D. R. McCamey, M. Francis, J. C. McCallum, A. R. Hamilton, A. D. Greentree, and R. G. Clark, "Donor activation and damage in Si-SiO2from low-dose, low-energy ion implantation studied via electrical transport in MOSFETs", *Semiconductor Science and Technology*, vol. 20, no. 5, pp. 363–368, 2005.

[168] K. L. Brower, "Passivation of paramagnetic Si/SiO2 interface states with molecular hydrogen", *Applied Physics Letters*, vol. 53, no. 6, pp. 508–510, 1988.

[169] BlueFors, "BlueFors LD400 Manual", 2018.

[170] J. B. Johnson, "Thermal agitation of electricity in conductors", *Phys. Rev.*, vol. 32, pp. 97–109, 1928.

[171] H. Nyquist, "Thermal agitation of electric charge in conductors", *Phys. Rev.*, vol. 32, pp. 110–113, 1928.

[172] Morello group, "SilQ", Advanced qubit control and measurement python package, 2016.

[173] Microsoft Corporation and Kobenhavns Universitet, "QCoDes", Qubit control and measurement python package, 2013.

[174] C. Macklin, K. O'Brien, D. Hover, M. E. Schwartz, V. Bolkhovsky, X. Zhang, W. D. Oliver, and I. Siddiqi, "A near–quantum-limited josephson traveling-wave parametric amplifier", *Science*, vol. 350, no. 6258, pp. 307–310, 2015.

[175] A. Laucht, J. T. Muhonen, F. A. Mohiyaddin, R. Kalra, J. P. Dehollain, S. Freer, F. E. Hudson, M. Veldhorst, R. Rahman, G. Klimeck, K. M. Itoh, D. N. Jamieson, J. C. McCallum, A. S. Dzurak, and A. Morello, "Electrically controlling single-spin qubits in a continuous microwave field", *Science Advances*, vol. 1, no. 3, 2015.

[176] J. Dehollain, J. Pla, E Siew, K. Tan, A. Dzurak, and A Morello, "Nanoscale broadband transmission lines for spin qubit control", *Nanotechnology*, vol. 24, no. 1, p. 015 202, 2012.

[177] D. C. Mattis and J. Bardeen, "Theory of the anomalous skin effect in normal and superconducting metals", *Phys. Rev.*, vol. 111, pp. 412–417, 1958.

[178] N. C. Carvalho, Y. Fan, and M. E. Tobar, "Piezoelectric tunable microwave superconducting cavity", *Review of Scientific Instruments*, vol. 87, no. 9, 2016.

[179] D. K. Wilson and G. Feher, "Electron Spin Resonance Experiments on Donors in Silicon. III. Investigation of Excited States by the Application of Uniaxial Stress and Their Importance in Relaxation Processes", *Phys. Rev.*, vol. 124, pp. 1068–1083, 1961.

[180] J. Gordon and K. Bowers, "Microwave spin echoes from donor electrons in silicon", *Physical Review Letters*, vol. 1, no. 10, p. 368, 1958.

[181] A. M. Tyryshkin, S. Tojo, J. J. Morton, H. Riemann, N. V. Abrosimov, P. Becker, H.-J. Pohl, T. Schenkel, M. L. Thewalt, K. M. Itoh, *et al.*, "Electron spin coherence exceeding seconds in high-purity silicon", *Nature materials*, vol. 11, no. 2, p. 143, 2012.

[182] L. A. Tracy, T.-M. Lu, N. Bishop, G. Ten Eyck, T Pluym, J. Wendt, M. Lilly, and M. Carroll, "Electron spin lifetime of a single antimony donor in silicon", *Applied Physics Letters*, vol. 103, no. 14, p. 143 115, 2013.

[183] T. F. Watson, B. Weber, M. G. House, H. Büch, and M. Y. Simmons, "High-fidelity rapid initialization and read-out of an electron spin via the single donor d- charge state", *Phys. Rev. Lett.*, vol. 115, p. 166 806, 2015.

[184] F. Yan, S. Gustavsson, A. Kamal, J. Birenbaum, A. P. Sears, D. Hover, T. J. Gudmundsen, D. Rosenberg, G. Samach, S. Weber, J. L. Yoder, T. P. Orlando, J. Clarke, A. J. Kerman, and W. D. Oliver, "The flux qubit revisited to enhance coherence and reproducibility", *Nature Communications*, vol. 7, p. 12 964, 2016.

[185] A. Cottet, "Implementation of a quantum bit in a superconducting circuit", Ph.D. thesis, University of Paris VI, France, 2003.

[186] C. Herring and E. Vogt, "Transport and deformation-potential theory for many-valley semiconductors with anisotropic scattering", *Phys. Rev.*, vol. 101, pp. 944–961, 1956.

[187] H. Hasegawa, "Spin-lattice relaxation of shallow donor states in ge and si through a direct phonon process", *Phys. Rev.*, vol. 118, pp. 1523–1534, 1960.

[188] L. M. Roth, "G factor and donor spin-lattice relaxation for electrons in germanium and silicon", *Phys. Rev.*, vol. 118, pp. 1534–1540, 1960.

[189] H. B. Callen and T. A. Welton, "Irreversibility and generalized noise", *Phys. Rev.*, vol. 83, pp. 34–40, 1951.

[190] A. I. Volokitin and B. N. J. Persson, "Near-field radiative heat transfer and noncontact friction", *Rev. Mod. Phys.*, vol. 79, pp. 1291–1329, 2007.

[191] V. N. Premakumar, M. G. Vavilov, and R. Joynt, "Evanescent-wave johnson noise in small devices", *Quantum Science and Technology*, vol. 3, p. 015 001, 2018.

[192] P. Huang and X. Hu, "Electron spin relaxation due to charge noise", *Phys. Rev. B*, vol. 89, p. 195 302, 19 2014.

[193] U. Güngördü and J. Kestner, "Indications of a soft cutoff frequency in the charge noise of a si/sige quantum dot spin qubit", *arXiv preprint arXiv:1811.06082*,

[194] I. Martin, D Mozyrsky, and H. Jiang, "A scheme for electrical detection of single-electron spin resonance", *Physical review letters*, vol. 90, no. 1, p. 018 301, 2003.

[195] A. Laucht, R. Kalra, J. T. Muhonen, J. P. Dehollain, F. A. Mohiyaddin, F. Hudson, J. C. McCallum, D. N. Jamieson, A. S. Dzurak, and A. Morello, "High-fidelity adiabatic inversion of a 31p electron spin qubit in natural silicon", *Applied Physics Letters*, vol. 104, no. 9, p. 092 115, 2014.

[196] R. Serway, *Principles of Physics*. Saunders College Pub., 1998.

[197] N. W. Ashcroft and N. D. Mermin, *Solid State Physics*. Saunders College Pub., 1976.

[198] T. Thorbeck and N. M. Zimmerman, "Formation of strain-induced quantum dots in gated semiconductor nanostructures", *AIP Advances*, vol. 5, no. 8, p. 087 107, 2015.

[199] J. J. Pla, A. Bienfait, G. Pica, J. Mansir, F. A. Mohiyaddin, Z. Zeng, Y. M. Niquet, A. Morello, T. Schenkel, J. J. L. Morton, and P. Bertet, "Strain-induced spin-resonance shifts in silicon devices", *Phys. Rev. Applied*, vol. 9, p. 044 014, 4 2018.

[200] J. Mansir, P. Conti, Z. Zeng, J. J. Pla, P. Bertet, M. W. Swift, C. G. Van de Walle, M. L. W. Thewalt, B. Sklenard, Y. M. Niquet, and J. J. L. Morton, "Linear hyperfine tuning of donor spins in silicon using hydrostatic strain", *Phys. Rev. Lett.*, vol. 120, p. 167 701, 16 2018.

[201] C. Tahan, M. Friesen, and R. Joynt, "Decoherence of electron spin qubits in si-based quantum computers", *Phys. Rev. B*, vol. 66, p. 035 314, 2002.

[202] V. N. Golovach and D. Loss, "Transport through a double quantum dot in the sequential tunneling and cotunneling regimes", *Phys. Rev. B*, vol. 69, p. 245 327, 2004.

[203] K. MacLean, S. Amasha, I. P. Radu, D. M. Zumbühl, M. A. Kastner, M. P. Hanson, and A. C. Gossard, "Energy-dependent tunneling in a quantum dot", *Phys. Rev. Lett.*, vol. 98, p. 036 802, 2007.

[204] T. Otsuka, T. Nakajima, M. R. Delbecq, S. Amaha, J. Yoneda, K. Takeda, G. Allison, P. Stano, A. Noiri, T. Ito, D. Loss, A. Ludwig, A. D. Wieck, and S. Tarucha, "Higher-order spin and charge dynamics in a quantum dot-lead hybrid system", *Scientific Reports*, vol. 7, p. 12 201, 2017.

[205] F. Qassemi, W. A. Coish, and F. K. Wilhelm, "Stationary and transient leakage current in the pauli spin blockade", *Phys. Rev. Lett.*, vol. 102, p. 176 806, 2009.

[206] N. S. Lai, W. H. Lim, C. H. Yang, F. A. Zwanenburg, W. A. Coish, F. Qassemi, A. Morello, and A. S. Dzurak, "Pauli spin blockade in a highly tunable silicon double quantum dot", *Scientific Reports*, vol. 1, p. 110, 2011.

[207] D. M. Zumbühl, C. M. Marcus, M. P. Hanson, and A. C. Gossard, "Cotunneling spectroscopy in few-electron quantum dots", *Phys. Rev. Lett.*, vol. 93, p. 256 801, 25 2004.

[208] L. Viola, E. Knill, and S. Lloyd, "Dynamical decoupling of open quantum systems", *Phys. Rev. Lett.*, vol. 82, pp. 2417–2421, 12 1999.

[209] K. Khodjasteh, D. A. Lidar, and L. Viola, "Arbitrarily accurate dynamical control in open quantum systems", *Phys. Rev. Lett.*, vol. 104, p. 090 501, 9 2010.

[210] D. Sabbagh, N. Thomas, J. Torres, R. Pillarisetty, P. Amin, H. C. George, K. Singh, A. Budrevich, D. Merrill, L. Ross, J. Roberts, L. Lampert, L. Massa, S. Amitonov, J. Boter, G. Droulers, J. Eenink, M. V. Hezel, D. Donelson, M. Veldhorst, L. M. K. Vandersypen, J. S. Clarke, and G. Scappucci, "Wafer-scale silicon for quantum computing", 2018. arXiv: `1810.06521v1`.

[211] IBM, "The future is quantum", 2018.

[212] S. Boixo, S. V. Isakov, V. N. Smelyanskiy, R. Babbush, N. Ding, Z. Jiang, M. J. Bremner, J. M. Martinis, and H. Neven, "Characterizing quantum supremacy in near-term devices", *Nature Physics*, vol. 14, no. 6, pp. 595–600, 2018.

"The mountains are calling and I must go."

John Muir